Delft University of Technology

CH4 and CO2 utilisation by unsteady-state operation

Pinto, D.

DOI
10.4233/uuid:ea8f3652-39aa-4305-98f3-9cefc17f0498

Publication date
2023

Document Version
Final published version

Citation (APA)
Pinto, D. (2023). *CH4 and CO2 utilisation by unsteady-state operation*. [Dissertation (TU Delft), Delft University of Technology]. https://doi.org/10.4233/uuid:ea8f3652-39aa-4305-98f3-9cefc17f0498

Important note
To cite this publication, please use the final published version (if applicable).
Please check the document version above.

CH$_4$ and CO$_2$ utilisation by unsteady-state operation

Dissertation

for the purpose of obtaining the degree of doctor

at Delft University of Technology

by the authority of the Rector Magnificus prof.dr.ir. T.H.J.J. van der Hagen

chair of the Board for Doctorates

to be defended publicly on

Friday 22 September 2023 at 10:00 o'clock

by

Donato PINTO

Dottore magistrale in Scienza dei Materiali

Università degli studi di Padova, Italy

born in Altamura, Italy

This dissertation has been approved by the promotors.

Composition of the doctoral committee:

Table of Contents

Summary

CH_4 and CO_2 are ideal candidates in the context of C1 chemistry as alternatives to oil-based feedstocks for chemicals and fuels production, due to their abundancy, low cost and potential to develop a closed carbon cycle.

Large scale utilisation of CO_2 in the chemical industry is currently limited to a few applications (e.g. synthesis of urea, carboxylic acids, food industry) and generally requires high purity feedstock. Integrated processes that combine CO_2 capture from diluted sources (e.g. industrial flue gases, air) and its conversion to value-added chemicals represent a solution to enhance the utilisation of CO_2 and mitigate its emissions. CH_4 is an abundant hydrocarbon with diversified sources ranging from fossil-based (natural gas, shale gas) to renewable ones (biomass, biogas), which can potentially substitute oil for the synthesis of valuable chemicals and fuels, including higher hydrocarbons. At the moment, however, CH_4 utilisation is circumscribed to combustion for heat and energy production or energy-intensive production of H_2 and syngas ($H_2 + CO$) via steam reforming, resulting in a high carbon footprint.

In general, the thermodynamic stability of CO_2 and CH_4 molecules imposes severe limitations to their exploitation as chemical feedstocks, in terms of low conversion efficiencies and control on the selectivity of products. Their efficient conversion requires harsh reaction conditions (high temperatures and pressures, highly chemically reactive substances) at which the stability of the desired products is threatened, resulting in low selectivity. In this scenario, catalysis is essential to identify functional materials and develop new catalytic processes able to maximise the selective conversion of CO_2 and CH_4 feedstocks to value-added products.

Unsteady-state operation in catalysis is an option to overcome the thermodynamic constraints imposed by the conventional steady-state operation. Integrated CO_2 capture and conversion, sorption-enhanced reactions, chemical looping combustion are examples of intrinsically unsteady-state catalytic processes that demonstrated enhanced performances compared to their steady state analogues. Moreover, the analysis of the transient catalytic behaviour developed in unsteady-state conditions leads to a deeper understanding of the catalytic processes in terms of identification of specific reactant-catalyst interactions, the steps involved in products formation and the mechanism of catalyst deactivation.

This dissertation deals with the catalytic activation of CO_2 and CH_4 molecules targeting at their valorisation to important chemical commodities as CO (syngas) and light hydrocarbons. Unsteady-state catalysis is explored as a means to overcome thermodynamic constraints associated to the conventional CO_2 and CH_4 conversion routes.

Chapters 2-3 focus on the utilisation of CO_2 in integrated capture and conversion processes employing bifunctional catalytic materials. Chapter 4 deals with the selective activation of CH_4 on simple metal oxides, identifying the key catalytic properties at play during its valorisation to oxidative C-C coupling products. Chapter 5 combines the insights obtained on the unsteady-state reaction with the evaluation of the steady-state oxidative coupling of CH_4 in terms of temperature and gas concentration gradients developed inside the reactor.. Lastly, combined utilisation of CO_2 and CH_4 is explored in Chapter 6, where an unsteady-state operation for dry reforming of methane is proposed and investigated.

Catalytic testing, traditional characterisation techniques together with advanced *in situ*/*operando* methodologies are combined in the investigation of the catalytic reactions. Important insights into the mechanism of CO_2 and CH_4 activation are obtained by the analysis of the transient evolution of intermediates and products in the unsteady-state reaction conditions. The results obtained and approaches disclosed in this dissertation open new directions for the catalytic exploitation of CO_2 and CH_4 as chemical feedstocks in view of the transition towards more carbon neutral, oil-free economy and industry.

Chapter 2 explores CO_2 capture and reduction (CCR) reaction on a K-promoted Cu/Al_2O_3 catalyst. CCR is an isothermal unsteady-state process that alternates the capture of CO_2 from diluted streams on a catalytic sorbent and its selective reduction by H_2 to CO, resulting in the formation of a syngas in the product stream. Bifunctional catalysts that can guarantee both capture functionality, enabled byalkaline metals, and selective conversion of the captured CO_2 in H_2, enabled by transition metals, at isothermal conditions are needed. The results obtained on the $Cu-K/Al_2O_3$ reveal a synergy between the Cu and K phases to sequestrate CO_2 from diluted CO_2 streams and promote its conversion to CO in H_2, while regenerating the activity towards CO_2 capture at a temperature of 350 °C. Compared to other metal oxide supports (ZrO_2, TiO_2), γ-Al_2O_3 guarantees high dispersion and destabilisation of the potassium phase resulting in the highest CO_2 capture capacity.

In **Chapter 3**, a mechanistic investigation of CCR on the $Cu-K/Al_2O_3$ system is performed. Spatiotemporal *operando* methodologies are designed to follow the dynamic variation of temperature, gas concentration and reactive surface species in the CCR reactor while monitoring the reaction progress. The results indicate that exothermic capture of CO_2 takes place on a unique potassium state to form surface carbonates, which can be rapidly reduced to CO under H_2 atmosphere. Exploiting the versatility of unsteady-state operation, designed catalytic experiments were conducted to demonstrate the active involvement of CO in the capture mechanism and the CO_2 capture capability in presence of an oxidised catalyst surface, expanding the CCR perspectives to treatment of complex effluent streams.

In **Chapter 4**, the activation of CH_4 is inspected for a series of single metal oxides (La_2O_3, Nd_2O_3, Y_2O_3, MgO, TiO_2) in unsteady-state operation, alternating CH_4 and O_2 pulses at high temperatures. In absence of gaseous oxygen, high temperatures (900 °C) are needed to observe formation of C_2 products. The analysis of the transient evolution of products in the CH_4 pulse reveals the existence of a peculiar selectivity for the different simple metal oxides associated with the nature of the lattice oxygen species present in the catalysts. In particular, rare-earth metal oxides exhibit high initial activity towards partial oxidation products (CO, H_2), while unique selectivity towards coupling products (C_2H_6 and C_2H_4) is found for MgO. TiO_2 provides selective activation of CH_4 to CO thanks to a continuous supply of lattice oxygen species, effectively preventing accumulation of carbon deposits.

La_2O_3 and MgO are further investigated in the oxidative coupling of methane (OCM) in **Chapter 5**. Interestingly, the intrinsic activity towards CH_4 activation shown by those systems in Chapter 4 contrasts with results obtained in steady-state OCM conditions, where La_2O_3 and MgO exhibit very similar selectivity and conversion trends with temperature. The highly oxidative conditions of steady-state OCM promote the development of unselective total oxidation paths ultimately leading to undesired formation of CO_2 and H_2O. Spatially-resolved *operando* analysis reveals the development of temperature and concentration gradients along the catalytic bed, caused by the activation of highly exothermic paths in OCM conditions.

Formation of huge hotspots at the front of the catalytic bed are unavoidable due to the presence of gaseous O_2 and H_2 deriving from methane activation. The local increase in temperature strongly controls the conversion and selectivity of the simple metal oxide catalytic bed, limiting the yield of C_2 products and favouring total oxidation products (CO_2, H_2O). Catalyst modification by addition of promoters (Li, Sr) has a positive effect in suppressing the unselective exothermic oxidation paths, reducing the formation of hotspots and favouring the release of the desired C_2 products.

Finally, in **Chapter 6**, the combined utilisation of CH_4 and CO_2 in dry reforming of methane is explored in a new unsteady-state catalytic concept coined as 'dynamic coke-mediated dry reforming of methane' (DC-DRM). Contrarily to the steady-state process, separation of the reactants and products streams and suppression of the undesired reverse water-gas shift reaction are intrinsically achieved in unsteady-state configuration. In DC-DRM operation, CH_4 and CO_2 feeds are periodically alternated to the reactor bed targeting the extensive coking of a Ni-based catalyst in the reducing CH_4 pulse and the complete gasification of the coke with regeneration of activity in the subsequent CO_2 pulse. A La-promoted Ni/ZrO_2 catalyst exhibits excellent and stable catalytic performance at 800 °C approaching complete conversion of the CH_4 and CO_2 reactant pulses in the reaction loop, and separation of the H_2 and CO product streams. Thanks to the flexibility of the process, the use of reducible metal oxides supports as TiO_2 enables the activation of an additional redox route to directly obtain a H_2-rich syngas mixture with tunable H_2/CO ratio in the CH_4 pulse.

Samenvatting

CH_4 en CO_2 zijn ideale kandidaten in de context van de C1-chemie als alternatieven voor op olie gebaseerde grondstoffen voor chemicaliën- en brandstofproductie omwille van hun overvloed, lage kosten en de mogelijkheid om een gesloten koolstofcyclus te ontwikkelen.

Grootschalig gebruik van CO_2 in de chemische industrie is op dit moment beperkt tot enkele toepassingen (b.v. synthese van ureum, carbonzuren, voedselindustrie) en vereist over het algemeen een zeer zuiver basismateriaal. Geïntegreerde processen waarbij CO_2-afvang uit verdunde bronnen (b.v. industriële rookgassen, lucht) en de omzetting ervan in chemicaliën met toegevoegde waarde vormen een oplossing om het gebruik van CO_2 te verbeteren en de CO uitstoot te beperken. CH_4 is een overvloedige koolwaterstof met uiteenlopende bronnen, variërend van fossiele oorsprong (aardgas, schaliegas) tot hernieuwbare bronnen (biomassa, biogas), die potentieel olie kan vervangen voor de synthese van waardevolle chemicaliën en brandstoffen, waaronder hogere koolwaterstoffen. Momenteel is het gebruik van CH_4 echter beperkt tot verbranding voor warmte- en energieproductie of energie-intensieve productie van H_2 en syngas (H_2 + CO) via stoomreforming, met als gevolg een grote koolstofvoetafdruk.

In het algemeen stelt de thermodynamische stabiliteit van CO_2- en CH_4-moleculen ernstige beperkingen aan hun exploitatie als chemische grondstoffen, in termen van lage conversie en controle op de selectiviteit van de producten. Hun efficiënte omzetting vereist harde reactieomstandigheden (hoge temperaturen en druk, zeer actieve reactanten) waarbij de stabiliteit van de gewenste producten in het gedrang komt, wat resulteert in een lage selectiviteit. In dit scenario is katalyse essentieel om functionele materialen te individualiseren en nieuwe katalytische processen te ontwikkelen die de selectieve omzetting van CO_2 en CH_4 in producten met toegevoegde waarde bewerkstelligd.

Operatie in een niet-stationaire toestand bij katalyse is een optie om de thermodynamische beperkingen van de conventionele stationaire werking te overkomen. Geïntegreerde CO_2-opvang en -omzetting, met sorptie versterkte reacties, chemische looping-verbranding zijn voorbeelden van intrinsieke niet-stationaire katalytische processen die aantoonbaar verbeterde prestaties in vergelijking met hun analogen in stationaire toestand. Bovendien is het begrip van katalytische processen gebaat bij analyse van het transiënte katalytische gedrag dat in niet-stationaire omstandigheden wordt ontwikkeld, waardoor specifieke reactant-katalysatorinteracties, de stappen betrokken bij productvorming en het mechanisme van katalysatordeactivatie kunnen worden geïdentificeerd.

Dit proefschrift behandelt de katalytische activering van CO_2- en CH_4-moleculen met als doel hun valorisatie tot belangrijke chemische grondstoffen zoals CO, syngas en lichte olefinen. Niet-stationaire katalyse wordt onderzocht als een middel om de thermodynamische beperkingen van de conventionele CO_2- en CH_4-omzettingsroutes te overwinnen, om een hoge omzettingsefficiëntie en productselectiviteit te bereiken.

De hoofdstukken 2-3 richten zich op het gebruik van CO_2 in geïntegreerde afvang- en omzettingsprocessen waarbij gebruik wordt gemaakt van bifunctionele katalytische materialen. Hoofdstuk 4 behandelt de selectieve activering van CH_4 op eenvoudige metaaloxiden, waarbij de belangrijkste katalytische eigenschappen die een rol spelen bij de valorisatie tot oxidatieve C-C-koppelingsproducten, die in hoofdstuk 5 worden geëvalueerd.

Ten slotte wordt het gecombineerde gebruik van CO_2 en CH_4 onderzocht in hoofdstuk 6, waar een alternatieve werking in niet-stationaire toestand voor droge hervorming van methaan wordt voorgesteld en onderzocht.

Bij het onderzoek van de katalytische reacties worden katalytische tests, traditionele karakteriseringstechnieken en geavanceerde *in situ/operando* methodologieën gecombineerd. Belangrijke inzichten in het mechanisme van CO_2 en CH_4 activering worden verkregen door de analyse van de transiënte evolutie van tussenproducten en producten in de niet-stationaire reactieomstandigheden. De in dit proefschrift verkregen resultaten openen nieuwe wegen voor de katalytische exploitatie van CO_2 en CH_4 als chemische grondstoffen met het oog op de overgang naar een meer koolstofneutrale, olievrije economie en industrie.

Hoofdstuk 2 onderzoekt de CO_2 afvang en reductie (CCR) reactie op een K-gepromote Cu/Al_2O_3 katalysator. CCR is een isothermisch unsteady-state proces waarbij CO_2 uit een verdunde stroom wordt afgevangen op een katalytisch sorbent en selectief wordt gereduceerd door H_2 tot CO, wat resulteert in de vorming van syngas in de productstroom. Er is behoefte aan bifunctionele katalysatoren die zowel afvangfunctionaliteit (alkalimetalen) als selectieve omzetting van het afgevangen CO_2 in H_2 (overgangsmetalen) onder isotherme omstandigheden kunnen garanderen. De resultaten verkregen op de $Cu-K/Al_2O_3$ katalysator onthullen een synergie tussen de Cu- en K-fasen om CO_2 uit verdunde stromen vast te leggen en de omzetting ervan in CO in H_2 te bevorderen, terwijl de activiteit voor CO_2-opvang bij een temperatuur van 350 °C wordt geregenereerd. Vergeleken met andere metaaloxidedragers (ZrO_2, TiO_2) garandeert γ-Al_2O_3 een hoge dispersie en destabilisatie van de kaliumfase, hetgeen resulteert in de hoogste CO_2-opvangcapaciteit.

In **Hoofdstuk 3** wordt een mechanistisch onderzoek van CCR op het $Cu-K/Al_2O_3$-systeem uitgevoerd. Ruimte en tijd opgehelderde *operando* methoden zijn ontworpen om de dynamische variatie van temperatuur, gasconcentratie en reactieve oppervlaktespecies in de CCR-reactor te volgen terwijl de voortgang van de reactie wordt gevolgd. De resultaten geven aan dat exotherme opvang van CO_2 plaatsvindt op een unieke kaliumtoestand om oppervlaktecarbonaten te vormen, die snel kunnen worden gereduceerd tot CO onder H_2 atmosfeer. Door gebruik te maken van de veelzijdigheid van de werking in niet-stationaire toestand werden specifieke katalytische experimenten uitgevoerd om de actieve betrokkenheid van CO in het afvangmechanisme en het vermogen om CO_2 af te vangen in aanwezigheid van een geoxideerd katalysatoroppervlak aan te tonen, waardoor de CCR-perspectieven worden uitgebreid tot de behandeling van complexe afvalwaterstromen.

In **Hoofdstuk 4** wordt de activering van CH_4 onderzocht op een reeks eenvoudige metaaloxiden (La_2O_3, Nd_2O_3, Y_2O_3, MgO, TiO_2) in niet-stationaire toestand, waarbij CH_4- en O_2-pulsen bij hoge temperaturen elkaar afwisselen. Bij afwezigheid van gasvormige zuurstof zijn hoge temperaturen (900 °C) nodig om de vorming van C_2-producten waar te nemen. De analyse van de voorbijgaande evolutie van producten in de CH_4-puls toont het bestaan aan van een bijzondere selectiviteit voor de verschillende eenvoudige metaaloxiden die samenhangt met de aard van de in de katalysatoren aanwezige raster zuurstofsoorten. Met name zeldzame aardmetaaloxiden vertonen een hoge initiële activiteit ten aanzien van partiële oxidatieproducten (CO, H_2), terwijl voor MgO een unieke selectiviteit ten aanzien van koppelingsproducten (C_2H_6 en C_2H_4) wordt gevonden. TiO_2 zorgt voor selectieve activering van CH_4 of CO dankzij een continue toevoer van raster zuurstofsoorten, waardoor accumulatie van koolstofafzetting effectief wordt voorkomen.

La$_2$O$_3$ en MgO worden in **Hoofdstuk 5** verder onderzocht in de oxidatieve koppeling van methaan (OCM). Interessant is dat de intrinsieke activiteit voor CH$_4$-activering die deze systemen in Hoofdstuk 4 vertonen, in contrast staat met de resultaten die zijn verkregen in OCM-omstandigheden in stationaire toestand, waarin La$_2$O$_3$ en MgO zeer vergelijkbare selectiviteits- en omzettingstrends met de temperatuur vertonen. De sterk oxidatieve omstandigheden van OCM in stationaire toestand bevorderen de ontwikkeling van niet-selectieve totale oxidatiepaden die uiteindelijk leiden tot ongewenste vorming van CO$_2$ en H$_2$O. Ruimtelijk geresolveerde *operando*-analyse toont de ontwikkeling van temperatuur- en concentratiegradiënten langs het katalytische bed, veroorzaakt door de activering van zeer exotherme paden in OCM-condities. De vorming van enorme hotspots aan de voorzijde van het katalytische bed is onvermijdelijk door de aanwezigheid van gasvormig O$_2$ en H$_2$ afkomstig van methaanactivering. De plaatselijke verhoging van de temperatuur regelt sterk de omzetting en selectiviteit van het eenvoudige metaaloxide katalysatorbed, waarbij de opbrengst van C$_2$-producten wordt beperkt en de totale oxidatieproducten (CO$_2$, H$_2$O) worden bevorderd. Katalysatormodificatie door toevoeging van promotors (Li, Sr) heeft een positief effect op de onderdrukking van de niet-selectieve exotherme oxidatietrajecten, vermindert de vorming van hotspots en bevordert het vrijkomen van de gewenste C$_2$-producten.

Ten slotte wordt in **Hoofdstuk 6** het gecombineerde gebruik van CH$_4$ en CO$_2$ bij de droge hervorming van methaan onderzocht in een nieuw katalytisch concept in niet-stationaire toestand, genaamd dynamische cokes gemedieerde droge hervorming van methaan (DC-DRM). In tegenstelling tot het stationaire proces worden de scheiding van reactanten en producten en de onderdrukking van de ongewenste omgekeerde water-gasverschuivingsreactie intrinsiek bereikt in een configuratie in niet-stationaire toestand. Bij DC-DRM worden CH$_4$ en CO$_2$ periodiek afwisselend naar het reactorbed gevoerd, met als doel uitgebreide verkoking van een op Ni-gebaseerde katalysator in de dalende CH$_4$-puls en volledige vergassing van de cokes met regeneratie van de activiteit in de daaropvolgende CO$_2$-puls. Een La-gepromote Ni/ZrO$_2$-katalysator vertoont uitstekende en stabiele katalytische prestaties bij 800 °C en benadert de volledige omzetting van de CH$_4$- en CO$_2$-reactorpulsen in de reactiekring en de scheiding van de H$_2$- en CO-productstromen. Dankzij de flexibiliteit van het proces kan het gebruik van reduceerbare metaaloxiden als TiO$_2$ de activering van een extra redoxroute mogelijk maken om rechtstreeks een H$_2$-rijk syngasmengsel te verkrijgen met een instelbare H$_2$/CO-verhouding in de CH$_4$-puls.

Chapter 1

Introduction

1.1   C1 chemistry and catalysis

A demanded scientific task of our age is guiding our world from a fossil fuels-based economy and industry towards an environmentally and ecologically sustainable system. The present production of chemicals and fuels heavily depends on fossil fuels-derived feedstocks. The limited reserves of fossil fuels and the concentrated production by few international actors are a source of instability for price and availability. The non-renewable character of fossil fuels-derived sources is also associated with high emissions of CO_2 as waste and translates into production of fuels and chemicals with high carbon footprint.[1, 2]

For the 'green' transition to take place, it is crucial to diversify fuel and chemical sources by selecting alternative feedstocks and processes to fossil fuels-based ones in the short-term and eventually replace them fully in the future. Those alternatives must also comply with the urgent need of reducing the carbon footprint of chemical industry and enabling circular processes by implementing the use of abundant and renewable feedstocks.[3-5] Complete decarbonisation of the chemical industry remains a big challenge, being the sector heavily-dependent on non-renewable fossil fuels feedstocks. In the last decades, fossil fuels-based feedstocks (mainly ethane and naphtha) represented about 74% of the sources of chemicals, and still dominate the production of highly valuable chemical building blocks such as light olefins and aromatics.[6]

In principle, most of the carbon-based chemicals and fuels can be derived from abundant and economic one-carbon-containing (C1) molecules (Figure 1.1). Some important examples of C1 molecules are CO, CO_2, CH_4, CH_3OH and HCOOH, which can be obtained from abundant and diversified sources alternative to crude oil.[7-9] Apart from traditional fossil sources as natural gas, shale gas and coal, C1 molecules can be obtained from renewable biomass, solid wastes and emitted CO_2, enabling mitigation of the carbon footprint and circularity in the chemical industry.

In particular, CO_2 and CH_4 are key players in the C1 chemistry scenario since they represent abundant and easily available sources of C.[10] Rising emissions of CO_2, responsible for the greenhouse effect, derive mainly from burning of fossil fuels for the production of energy and heat. In the present fossil fuels based economy, CO_2 is treated as a waste and readily released to the atmosphere. However, as a C-containing molecule, CO_2 can act as carbon-feedstock for the production of various chemicals and fuels.[11] Recycling CO_2 from waste sources (e.g. flue gases) or even capturing CO_2 from air and utilising it can significantly reduce the carbon footprint of the existing chemical industry.[12] CH_4, instead, represents an ideal molecule to

transition between the present fossil fuels based industry to a carbon neutral one. As main constituent of natural gas, it is the most abundant hydrocarbon on earth, with a ready infrastructure and technology. The high H/C ratio compared to oil and coal makes it an optimal source of H_2. Moreover, gradual substitution of fossil sources with renewable ones (biogas, gasified biomass) can supply CH_4 with reduced carbon footprint.[13]
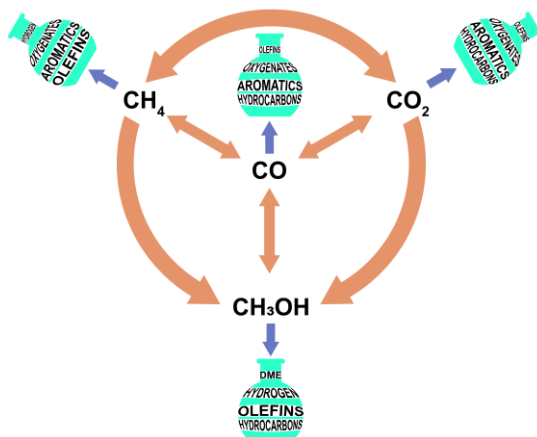

Figure 1.1: Schematic of C1 chemistry pathways for the production of chemicals and fuels.[14]

Direct valorisation of CO_2 and CH_4 to high valuable products (e.g. liquid fuels, oxygenates, light olefins, aromatics) may revolutionise the current chemical industry, imprinting an advance towards the closure of the carbon cycle. However, the activation and selective transformation of CO_2 and CH_4 molecules is complicated by their thermodynamic stability. At the harsh reaction conditions (temperatures, pressures and highly reactive reactants) necessary to achieve efficient conversions, selectivity is generally low.[10, 14, 15] Thus, current utilisation of CH_4 and CO_2 as C1 feedstocks goes preferentially through their transformation to valuable intermediates as CO and CH_3OH, which are further processed into chemicals and fuels.[16] Synthesis gas, a mixture of H_2 and CO mainly generated from reforming of natural gas, can be readily processed into valuable molecules as methanol (in combination with CO_2) or higher hydrocarbons via Fischer-Tropsch reaction.[15, 17] On the other hand, CH_3OH is a versatile commodity for the chemical industry since it can act as fuel, feedstock for chemicals production (methanol to olefins process) and intermediate species for storage and transportation of H_2 in liquid form.[18-20]
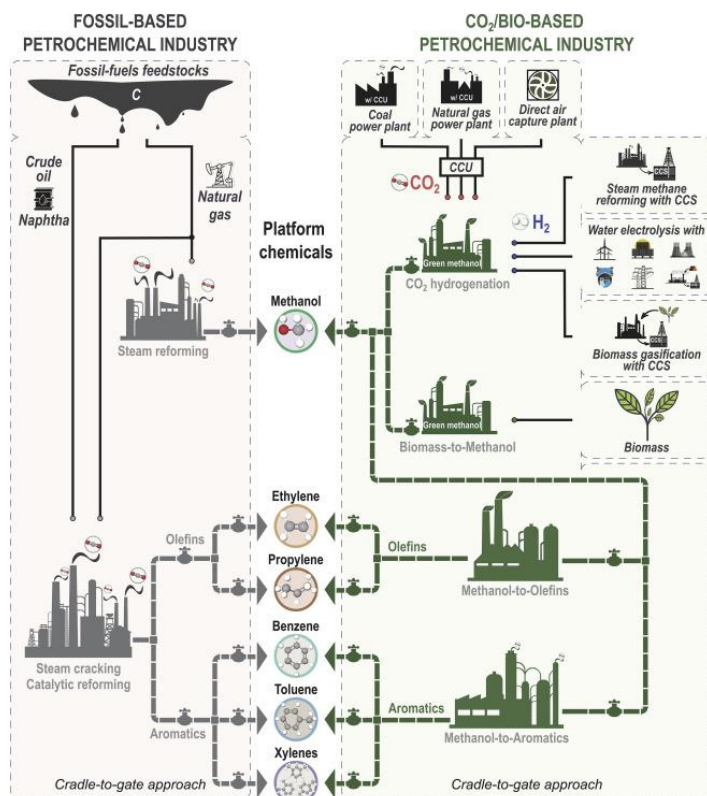
Figure 1.2: Overview of fossil fuels-based processes and alternative renewable feedstocks for petrochemical industry.[3]

Catalysis is fundamental for C1 chemistry to achieve high conversion efficiencies at mild reaction conditions and to drive the reactions towards the desired products with high selectivity. The large scale of fuels and chemicals production and the need of continuous operation make heterogeneous catalytic processes preferrable, thanks to the easiness of product separation. Two important directions for the C1 catalysis are i) the development of materials with functionalisation to promote specific conversion and selectivity and ii) the design of new catalytic processes capable of overcoming the thermodynamic constraints and limitations associated with the transformation of stable and relatively inert molecules as CO_2 and CH_4.

In the next paragraphs, the state of the art of CO_2 and CH_4 catalysis in view of their employment as chemicals and fuel feedstocks is briefly introduced, together with the main challenges associated with their utilisation in catalytic processes. The role of unsteady-state operation in catalysis is then discussed together with its potentialities to facilitate selective conversion of CO_2 and CH_4.

1.2 CO$_2$ - from waste to resource

A substantial share of the CO$_2$ released in the atmosphere is attributed to the energy sector for power and heat generation and the industry, accountable for 34% and 24% of global greenhouse gas emissions, respectively.[21] The roadmap for global warming control relies on the urgent application of diverse measures to target the abatement of anthropogenic CO$_2$ emission.[22-25] Given its large-scale potential, carbon capture and storage (CCS) is considered one of the leading strategies for the decarbonisation of energy plants and industries[26-28] Among carbon capture technologies, amine scrubbing has been long utilised to remove CO$_2$ from natural gas and it is now applied for large-scale post-combustion capture in coal-fired power plants.[29, 30] As an alternative to solvent-based chemical CO$_2$ capture, physical and chemical CO$_2$ adsorption on solid sorbents[26, 31] have been developed on a variety of systems including alkali-metals supported on metal oxides,[32, 33] carbonaceous materials,[34, 35] zeolites,[34, 36, 37] metal organic frameworks (MOFs).[33, 38] Their employment eliminates the technological concerns associated to large volumes of liquids of amine scrubbing processes, and promises increased adsorption capacity and reduced energy penalty for regeneration. Due to their less volatile nature as solids, they can operate in a wider range of pressure and temperature working conditions with a possibility to deal with low concentration CO$_2$, as represented by direct air capture (DAC) applications.[39] Recently, polymer-based materials, ionic liquids and solids containing ionic-liquid moieties have emerged as new promising sorbent materials.[26, 40-43] Despite the technical maturity, in 2018 only 37 large scale CCS plants existed at different development and demonstration stages[26]. Widely debated and critical aspects associated with CCS are on the risk of leakages and environmental impact for the designated sequestration sites (e.g. geological sites, or ocean storage).[44, 45] The energy penalty due to the regeneration of the solvents used for CO$_2$ absorption, the need of adequate transportation grid and related infrastructure are the major causes of low cost-effectiveness.[46] According to the IPCC[27], CO$_2$ capture costs for a post-combustion electric power plant increase the energy requirement by 24-42%, and the estimated cost for CO$_2$ capture in a fossil fuel power plant is 15-75\$ per ton of CO$_2$.[47] Moreover, such processes cannot enable circular carbon economy, since fixed CO$_2$ is not recycled to other valuable chemicals and fuels.[48, 49]

Combining CO$_2$ capture with its utilisation as chemical feedstock would provide not only a solution for limiting the release of CO$_2$ into the atmosphere, but also make CO$_2$ a valuable resource for chemical industry, adding 'green' value to the existing processes in the direction of achieving carbon neutrality. Despite its abundancy, CO$_2$ utilisation in chemical industry is limited, less than 1% of the annual CO$_2$ emitted worldwide.[50] Principal applications cover the synthesis of urea, methanol, carboxylic acids and employment in food industry.[51, 52]

Being the most oxidised state of carbon and having the low energy level ($\Delta H^0_f = -393.5$ kJ mol^{-1}), the first obvious limitation of CO$_2$ for wide employment as chemical feedstock is the thermodynamical stability and consequent relative inertness of the CO$_2$ molecule.[53] To activate and reduce CO$_2$ into useful chemicals, a large input of energy has to be provided either by high-energy reactants (H$_2$, unsaturated compounds, organometallics compounds at a high energy state) or by harsh reactions conditions (high temperature and pressure), penalising the product selectivity.[11, 54] Energy to chemically reduce CO$_2$ molecule can be also supplied by light and electricity in photo- and electro-chemical pathways, which in turn suffer from low efficiencies and challenging scale up.[53, 55] Despite the thermodynamic stability of

the molecule, the presence of polar C=O bonds leads to electron-deficiency on the carbon, resulting in high affinity towards nucleophiles and electron donors.[11] For example, basic compounds can quickly react with CO_2 and such functionalities are fundamental to design active CO_2 sorbents.

Another strong limitation of CO_2 utilisation comes from the requirements of feedstock purity and pressure for industrial processing. Apart from a few exceptions, CO_2 purity is generally too low in flue gases (<40 %). By contrast, most of the CCU technologies require pure and pressurised CO_2 feedstock, which translates into higher costs and energy consumption that often make utilisation of CO_2 economically unfeasible and increases the carbon footprint.[56] In this perspective, strategies that *combine* the capture of CO_2 from diluted sources with its conversion to valuable chemicals are effective solutions to decrease the energy penalty associated with the purification and pressurisation steps.[54, 57] By reacting with H_2 produced with green energies (e.g. water electrolysis driven by renewable electricity), CO_2 can be valorised to C1 molecules of higher industrial interest such as CH_4 through methanation reaction, methanol or CO, the main constituent of syngas, through the reverse water-gas shift (RWGS) reaction.[53, 58-61]

CO_2 methanation (Reaction 1.1) is an exothermic reaction, thermodynamically favourable at low temperatures. At those reaction conditions, however, the reaction becomes kinetically limited, inhibiting the achievement of high conversions efficiency for its industrialisation. Direct CO_2 hydrogenation to methanol (Reaction 1.2) also benefits from low temperatures and high pressure conditions.

$$CO_2 + 4H_2 \rightleftharpoons CH_4 + 2H_2O \qquad \Delta H_{298}^0 = -164\ kJ\ mol^{-1} \qquad (1.1)$$

$$CO_2 + 3H_2 \rightleftharpoons CH_3OH + H_2O \qquad \Delta H_{298}^0 = -49.5\ kJ\ mol^{-1} \qquad (1.2)$$

$$CO_2 + H_2 \rightleftharpoons CO + H_2O \qquad \Delta H_{298}^0 = 41.2\ kJ\ mol^{-1} \qquad (1.3)$$

CO is derived from RWGS (Reaction 1.3), constituting one of the most promising processes for large-scale utilisation of CO_2. CO, upon mixing with H_2 (i.e. resulting in syngas), has high potential for its further utilisation as building block for fossil fuels-free chemicals via methanol synthesis and Fischer-Tropsch processes to produce a range of hydrocarbons, as widely practiced in industry.[53, 62] Due to its endothermic nature, RWGS suffers from thermodynamic limitations, requiring high temperatures (e.g. 800 °C) to reach satisfying conversion with high energy cost.

Development of functional catalysts is fundamental to selectively activate CO_2 and drive the reaction towards the desired products at favourable reaction conditions. Rational design of catalyst materials is a priority research direction, which implies a deep fundamental knowledge of the mechanism of CO_2 activation on catalytic surfaces, the type and stability of reactive intermediates and the properties controlling the product selectivity.

1.3   CH$_4$ - a molecule for the transition

Due to its abundance and compatibility with the present industrial infrastructure, methane is a key molecule for the transition to a more sustainable energy and chemistry. Methane provides higher energy density and a higher H/C ratio (4) compared to oil and coal, meaning lower amount of CO_2 released per unit of energy produced and suitability to represent a convenient H_2 source. By using methane for energy production, reduction of CO_2 emission are estimated to be 27% compared to oil and 47% compared to coal.[63] Apart from its usage as energy source, methane has a large potential as chemical feedstock and it is not well-explored yet.

Methane is the main component of natural gas. Recently, the extent of its proved reserves has sharply increased and doubled in the last two decades.[64] A major part of these reserves is located in the Earth core, with a significant share concentrated in Russia and Middle East regions (Figure 1.3). An even higher amount is expected to be present in the form of gas hydrates stored in permafrost region or sea sediments.[65] The primary extraction techniques involve horizontal drilling and hydraulic fracturing ('fracking') of shale rocks. Especially the recent exploitation of shale gas[66] led to a steep increase in the production of natural gas, causing the fall of its market price and making it a competitive alternative to oil. Nevertheless, the higher transportation costs compared to oil and coal substantially limits the expansion of its usage.[67] At the same time, fracking has been disputed for its environmental impact concerning the pollution of water resources and the disposal of wastewaters,[68] and for the possible correlation with induced seismicity events.[69, 70] Together with the expanding activity of its extraction, increasing concentration of methane in the atmosphere has risen the concern in the scientific community, due to its high global warming potential estimated as 25 times the impact of an equivalent emission of CO_2.[71, 72] To date, the majority of natural gas is combusted for the production of thermal and mechanical energy or electricity.[73] To avoid its release to the atmosphere, around 150 billion m^3 of gas are flared at oil production sites as a waste, contributing to greenhouse gas emissions with 350 million tons of CO_2 yearly released in the atmosphere.[74, 75] Accordingly, a strong effort should be taken not only in the exploitation of the natural reserves but more significantly in making proficient use of this valuable natural resource. A consistent portion of the natural gas is extracted in remote regions, and the availability and price of methane is heavily affected by the cost of transportation infrastructure. On-site conversion of methane to value-added, easily transportable chemicals in liquid form represents a valid direction to expand the accessibility of alternatives to oil-derived materials. Developing efficient and innovative strategies for methane utilisation represents a realistic possibility to start an energetic transition while satisfying the increasing energy demand.

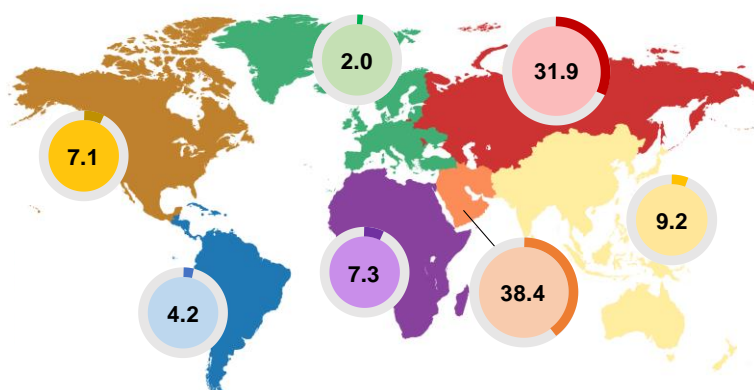**Distribution of Natural Gas Reserves**

Figure 1.3: Geographic distribution of proved natural gas reserves (%). Data from BP Statistical Review of World Energy 2019 © BP p.l.c. 20192. Map created with mapchart.net©.

From a chemical point of view, selective activation of methane represents a severe challenge. The high stability of the molecule is expressed by the high energy required for cleavage of the first C-H bond (439 kJ mol^{-1}).[76] The molecule presents a high symmetry which is reflected in the low polarisability and the absence of a dipole moment. As a consequence, high temperature conditions or aggressive reactants are usually needed, leading to unselective conversion paths, since most of the targeted derivative molecules exhibit lower bond dissociation energies. To tackle the challenge of selective conversion of methane, heterogeneous catalytic processes have been developed intensively.[77, 78]
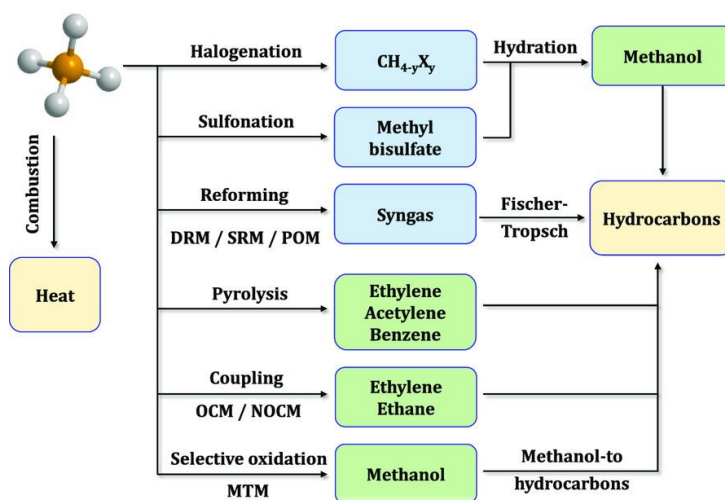

Figure 1.4: Overview of strategies for methane utilisation.[79]

1.3.1 Indirect routes of CH$_4$ utilisation

The commercial processes for large scale utilisation of CH$_4$ are mainly based on its conversion to synthesis gas ('syngas'), a mixture of H$_2$ and CO representing a key player for the natural gas to liquid fuel route (GTL). Currently, the principal sectors for syngas utilisation comprise ammonia, H$_2$, methanol production, Fischer-Tropsch (FT) synthesis of hydrocarbons and its employment as fuel.[80] The market size for syngas is expected to strongly increase in the coming years, due to the predictable measures against global warming that will lead to the decline of oil-based chemistry.[81] Systemic employment of synthetic fuels derived from syngas will introduce several environmental benefits. These fuels are intrinsically free from heteroatoms (S, N), which are removed upfront in the process. Thus, their combustion in vehicles and engines results in a lower levels of hazardous gases in the exhaust.[82] FT synthesis is the only technology commercially available for direct conversion of syngas to light olefins. However, the large scale conversion of natural gas into FT product is greatly affected by the cost of syngas and the poor selectivity represents still a limitation for extensive use of FT.[83-85] The stoichiometric ratio of the components in syngas, SN = (H$_2$ – CO$_2$)/(CO-CO$_2$), is an essential property for its further transformation, thus its tunability is a key factor to design versatile processes for valuable transformation of methane and CO$_2$-containing flue gases.

Up to date, steam reforming of natural gas accounts for the majority of syngas production (steam reforming of methane (SRM), Reaction 1.4).

$$CH_4 + H_2O \rightarrow CO + 3H_2 \qquad \Delta H^0_{298} = +206\ kJ\ mol^{-1} \qquad (1.4)$$

From a thermodynamic point of view, the reaction is endothermic and a large amount of heat is required to drive the reaction. In order to avoid coke deposition on the Ni-based catalysts and increase their stability, higher H$_2$O/CH$_4$ ratios in the feed are used, bringing technological issues associated with the hot steam management and lower purity of the product due to the unconverted steam.[84] For the production of H$_2$, the process is coupled with the reversible exothermic water-gas shift reaction (WGS, the reverse reaction of Reaction 1.3), where the CO$_2$ generated by WGS is separated and treated as a waste and contributes to the carbon footprint of the process. The theoretical H$_2$/CO ratio in SRM would be close to 3, thus additional purification and separation steps are required. To meet the requirements of the downstream processes, SRM is usually combined with partial oxidation to decrease the steam to carbon ratio and achieve a SN close to 2, which is ideal for methanol synthesis. Greener routes for production of syngas from CH$_4$ must involve the direct utilisation of CO$_2$ and an efficient recovery of the thermal energy deriving from methane oxidation. Strategies with simultaneous utilisation of CH$_4$ and CO$_2$ exhibit a high potential in lowering the environmental impact of fuel and chemicals production processes.[86]

To produce a more sustainable H$_2$, different options have been evaluated in order to decarbonise SRM. Reducing emissions of 60% by integration of CO$_2$ capture in SRM is considered a threshold for the transition from grey to blue H$_2$.[87] Nevertheless, the present technology for carbon dioxide capture and utilisation/storage (CCUS) represents a significant cost voice for a SRM plant, by increasing of 50% the capital expenditure (CAPEX) and almost doubling the operational costs (OPEX).[88] Another complication is added by the management of the captured CO$_2$. The storage of the excess CO$_2$ requires the individuation of secure geological sites and brings an additional cost of transportation. A potential economic reward by the alternative utilisation of CO$_2$ as chemical feedstock (CCU). Developing more advanced CO$_2$ capture technologies may be a direction to decrease the capture cost and speed up the

integration in the present process. Novel processes as integrated CO_2 capture and conversion offer the possibility to capture low CO_2 concentrations in the flue streams and directly convert it to syngas or methane.[31, 89, 90]

A greener perspective is offered by the gradual substitution of natural gas with renewable methane source as biogas. Originated from agricultural or municipal waste, biogas plants has limited capacities compared to the typical steam reformers. In addition, the specific composition of the biogas is variable and richer than the natural gas in CO_2 and sulphur compounds. Typical CO_2 concentration ranges between 20 and 55%, thus adequate separation steps and good flexibility of the reforming process are required.[91, 92] In this regard, reforming processes that directly use CO_2 to target syngas production appears more suitable for biogas utilisation.[93]

Alternative CH_4 reforming strategies have been proposed, by changing the oxidant species (CO_2, H_2O, O_2) and the composition of the feed. This results in the activation of either endothermic (steam or dry reforming) or exothermic processes (autothermal reforming, partial oxidation) and ultimately tuning of the H_2/CO ratio can be realized.

1.3.2 Alternative reforming reactions

The utilisation of CO_2 as reforming agent offers the possibility of reducing carbon footprint of syngas production. Converting two greenhouse gases by simultaneous utilisation of CO_2 and CH_4, dry reforming (DRM) has attracted great scientific and industrial interests. In this process, CH_4 acts as a reducing agent for CO_2, leading to the formation of syngas with ideal H_2/CO ratio of 1 (Reaction 1.5).

$$CH_4 + CO_2 \rightarrow 2CO + 2H_2 \qquad \Delta H^0_{298K} = +247 \; kJ \; mol^{-1} \qquad (1.5)$$
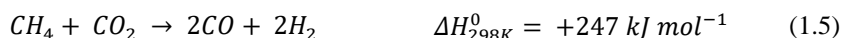
Thanks to the effective consumption of CO_2, the process has potentially a lower carbon footprint. Nevertheless, DRM is even more endothermic than SRM and the global warming impact of the whole process is mostly dependent on the heat supply necessary to drive the reaction. In a future scenario of fully renewable electricity sources to power the reactor heating, DRM will strongly reduce its environmental impact[94] and stand as a potential source for large-scale production of greener H_2 and syngas. From the viewpoint of the catalytic reaction, some major challenges regarding the catalyst deactivation by coke deposition on the active Ni-based materials and sintering phenomena remain unresolved. In that respect, materials engineering has traced a path in the direction of bimetallic catalysts (Ni-Fe, Ni-Co) to improve the long-term catalytic activity and stability.[95, 96] The addition of steam mitigates the formation of coke, whilst CO_2 is actively converted in the process, known as bireforming (Reaction 1.6).[97, 98] The resulting H_2/CO ratio in the syngas can be tuned by proper optimization of the H_2O/CO_2 ratio in the feed. A H_2/CO ratio of 2 has been reported, matching the needs of relevant downstream application like Fischer-Tropsch and methanol syntheses.[99, 100]

$$CH_4 + 2H_2O + CO_2 \rightarrow 4CO + 8H_2 \qquad \Delta H^0_{298K} = +220 \; kJ \; mol^{-1} \qquad (1.6)$$

In order to produce syngas with lower environmental impact, exothermic reaction routes can make a significant contribution by lowering the energy cost of the whole processes.[101] Partial oxidation of methane (Reaction 1.7) is a mildly exothermic route, considered as an alternative to steam reforming to produce synthesis gas with H_2/CO ratio of 2. The catalytic reaction

faces severe technological challenges. The presence of oxygen in the feed causes the activation of total oxidation reaction (Reaction 1.8) that causes the formation of huge hotspots in the catalyst bed and the development of intense temperature gradients in fixed-bed reactors.[102] Besides, purification cost for the feed O_2 and poor control on hotspot formation are additional obstacle for the scale-up.[103]

$$CH_4 + \frac{1}{2}O_2 \rightarrow CO + 2H_2 \qquad\qquad \Delta H^0_{298} = -36\ kJ\ mol^{-1} \qquad (1.7)$$

$$CH_4 + 2O_2 \rightarrow CO_2 + 2H_2O \qquad\qquad \Delta H^0_{298} = -803\ kJ\ mol^{-1} \qquad (1.8)$$

Nonetheless, integrating exothermicity in the aforementioned methane reforming reactions reduces the required thermal energy and helps to overcome the limitations of steam and dry reforming in terms of catalyst deactivation by coking.[104] The inclusion of exothermicity is at the basis of autothermal reforming of methane,[105] a combination of endothermic reforming routes (Reaction 1.4) and exothermic partial oxidation (Reaction 1.7), the latter providing in-situ generation of the heat required for the former. How to precisely control the partial and total oxidation and thus to control CO/CO_2 ratio for a desired downstream process, is a major challenge.

Trireforming represents an extension of the concept of autothermal strategies to combine methane activation with utilisation of CO_2 directly from flue gas. It is a highly relevant process to meet the requirements of waste CO_2 valorisation, formation of syngas with lower carbon footprint and optimization of the process by controlled inclusion of exothermic reactions. The purpose of this strategy is to combine synergistically catalytic steam and dry reforming, together with partial or total oxidation of methane, by proper mixing of CH_4 with CO_2, H_2O and O_2 in the same reactor.[106] Exothermic oxidation routes (Reactions 1.7 and 1.8) are activated in the presence of oxygen, providing in-situ generation of the heat required for the reforming reactions. Significant reduction of carbon deposits on the catalyst material is achieved,[107] increasing the stability of the catalyst and improving the process control.

Flue gas from fossil fuels plants can be a valid source of the H_2O, CO_2 and O_2 mixtures, after removal of poisoning agent as NO_x and SO_x. Natural gas power plants or coal-fired power station are readily available sources of flue gas and heat to promote further reactions. Thus, trireforming can be directly implemented to make valuable utilisation of the wastes. Since the flue gas composition is specific for each plant, a highly flexible process is required to deal with varying feed composition and desired product specification.

The syngas produced has a theoretical H_2/CO ratio of 2, which is an optimum value for downstream methanol production or Fischer-Tropsch processes. Catalytic experiments of trireforming showed promising tuning of the final H_2/CO ratio depending on the different feed compositions.[108-110] The process opens a path in the direction of connecting the flue gas management and valorisation together with the production of a readily available syngas with adjustable ratio. By tuning of the catalytic process, the syngas generated can be optimised for the downstream processes of interest, potentially removing any further separation step.

1.3.3 Thermodynamics of CH₄ reforming

Although limited to thermodynamic conversions assuming constant temperature and pressure, the theoretical investigation by means of Gibbs energy minimisation provides important insights into the key challenges of methane reforming to syngas. Thermodynamic equilibrium composition using different CH_4 reforming strategies (Figure 1.5) shows that, independently of the oxidant choice, high temperatures are needed to achieve complete conversion of methane. In dry reforming of methane (Figure 1.5A), the complete substitution of steam with carbon dioxide as oxidant results in extensive carbon deposition. CO_2 is not very efficient in oxidising solid carbon species. On the contrary, the thermodynamic stability of carbon deposits is undermined by utilisation of strong oxidant (O_2, H_2O) as in the case of partial oxidation (Figure 1.5D) and autothermal reforming (Figure 1.5E). Thus, blending CO_2 feed with strong oxidants (O_2, H_2O) can be beneficial to overcome the thermodynamic limitation by improving carbon gasification. Thus, combined reforming strategies as bi- and trireforming (Figures 1.5B-C) are able to balance the needs of higher process stability while providing efficient CO_2 utilisation.
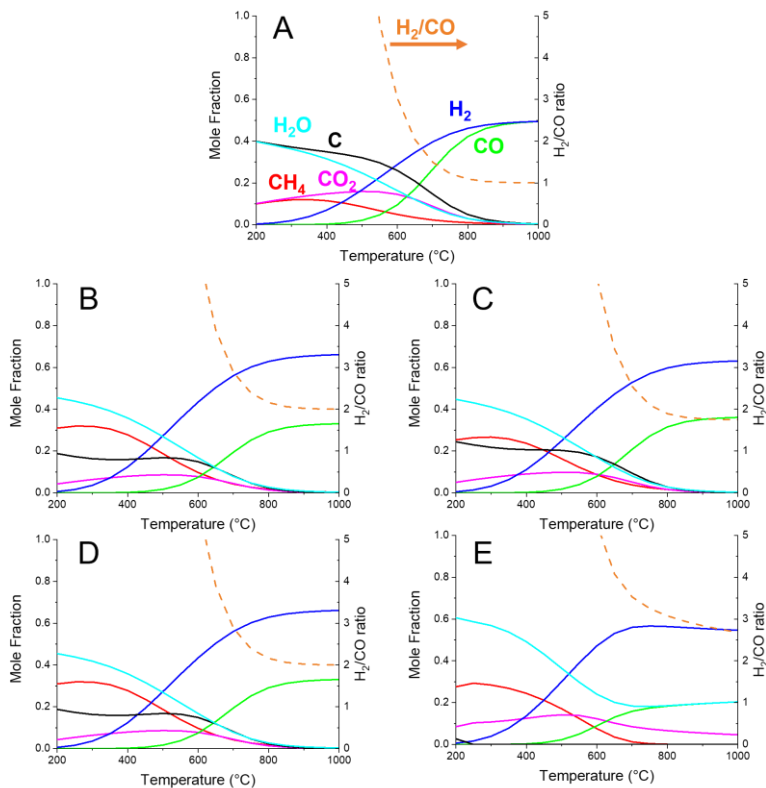

Figure 1.5: Thermodynamic equilibrium composition at 1 bar for different CH_4 reforming strategies calculated by Gibbs free energy minimization (Aspen Plus, ideal gas equation of state). The starting feed composition (feed molar ratio) is the stoichiometric reactant ratio for dry reforming and partial oxidation, while feed ratios in the range of reported processes are chosen for the remaining ones. A) dry reforming (feed molar ratio CH_4:CO_2 = 1:1), B) bireforming (CH_4:CO_2:H_2O = 3:1:2), C) trireforming (CH_4:CO_2:H_2O:O_2 = 1:0.475:0.475:0.1), D) partial oxidation (CH_4:O_2 = 1:0.5), E) authothermal reforming (CH_4:H_2O:O_2 = 1:0.5:0.5).

In the perspective of efficient utilising methane and CO_2, an ideal process should combine the versatility towards the feed composition, i.e. flue gas from power plants, and the capacity of producing a desired H_2/CO ratio in order to adapt to the downstream processes, meanwhile reducing additional costs of separation/purification and compression steps. In this regard, targeted and adjustable oxidant mixtures (CO_2, H_2O, O_2) translate into higher H_2/CO ratio in the product, that is a more attractive and valuable syngas (Figure 1.6).
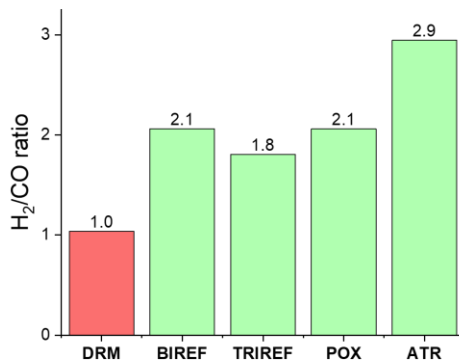

Figure 1.6: H_2/CO ratio extracted from the thermodynamic equilibrium composition at 1 bar and 850 °C for different CH_4 reforming strategies. Dry reforming of methane (DRM), bireforming (BIREF), trireforming (TRIREF), partial oxidation (POX) and autothermal reforming (ATR).

1.3.4 Direct routes of CH_4 utilisation

Direct routes rely on the direct conversion of CH_4 to chemicals. Chemicals with relevant market sizes as methanol, formaldehyde, ethylene, halogenated compounds and aromatics can be in principle obtained by direct methane conversion.[111-115] The promising benefits of a single-step synthesis have to face the reality of low yields, that complicate the commercialisation. In the case of methanol and formaldehyde, two strong candidates as liquid hydrogen carriers, the direct synthesis from methane will eliminate the intermediate step involving syngas, significantly improving the overall energy efficiency of an industrial process. However, in most of the oxidative reaction paths for direct methane conversion, such products are more easily oxidised than methane and driven to total oxidation (CO_2) at reaction conditions.[116] Activation of methane is achieved at the interaction with catalytic surfaces, where a symmetry or structure deformation of the molecule is indicated by the appearance of the infrared-forbidden symmetric stretch vibrational mode.[117, 118] Methyl radicals are formed by homolytic cleavage of the C-H bond. For metal oxides catalysts, the homolytic bond splitting takes place on an oxygen center on the surface, resulting in a methyl radical and an hydroxyl species.[78] However, radical reactions are difficult to control. After the first oxidation of C-H bond in methane, the intermediate products are exposed to overoxidation and, unless readily separated from the reaction environment, they end up in the chemically more stable and economically less valuable CO and CO_2.

Non-radical pathways of methane activation have been evaluated with the promise of an improved selective activation and functionalization. Alkanes are prone to react with strong electrophiles. Electrophilic activation of methane to functionalised alkanes can take place in strong polar media as superacids, where the stability of the products is challenged.[119] High one-pass yield (70%) of methane to methyl bisulfate by Periana et al.[120] remains an isolate report in the field. Platinum and other transition metal complexes (including Rh, Ir and Fe) activates methane throughout oxidative addition reactions, in which the metal increases its oxidation state to promote the heterolytic cleavage of the C-H bond.[121, 122] Other recognised pathways as sigma-bond metathesis, metalloradical activation with metal-porphyrin complexes broaden the spectra of methane activation chemistry.[123] Nonetheless, all these strategies suffer from the intrinsic limitations of homogenous catalytic process, and a major impulse to the efficient utilisation of methane will come by the implementation of efficient heterogeneous catalytic processes.

1.3.5   Oxidative coupling of CH_4

Among derivatives of methane, ethylene has one of the biggest market size and value for its high demand as chemical feedstock especially as the building block in plastic industry. Upon compression, it becomes an easily transportable liquid. Currently, ethylene is produced by steam cracking of naphtha or using the ethane fraction separated from the natural gas. Due to the endothermicity of the reactions involved, these processes are energy intensive and 1-2 tons of CO_2 emitted per ton of ethylene are estimated.[124, 125] In the past decades, an ideal reaction attracted a lot of research interest for the possibility of converting methane to ethane and ethylene over inexpensive metal oxides catalysts. This reaction is called oxidative coupling of methane (OCM, Reaction 9).

$$2CH_4 + O_2 \rightarrow C_2H_4 + 2H_2O \qquad\qquad \Delta H^0_{298K} = -281\ kJ\ mol^{-1} \qquad (1.9)$$

The complexity of OCM derives from its radical nature. The proposed mechanism involves the heterogeneous activation of methane molecule on the catalyst, typically a metal oxide, with formation of a methyl radical as intermediate.[126, 127] Then, this radical can be desorbed and combine in the gas phase, to form ethane and, after a subsequent dehydrogenation step, ethylene. The radical nature of the reaction, together with the multiple paths involving reactions in both heterogeneous (catalyst surface) and homogeneous (gas) phase, increases the complexity of the process. The reaction is held at high temperature to promote the activation of the methane molecule, requiring catalysts with high thermal stability. The amount of research could identify many active catalysts for the reaction, most of them based on abundant metal oxides with strong basic sites.[128, 129] The presence of gaseous oxygen in the feed activates unselective exothermic routes as partial and total oxidation, finally leading to thermodynamically more favourable products as CO and CO_2.[130] This thermodynamic limitation ultimately leads to a low methane to C_2 (ethane and ethylene) yield below 30%,[131-133] which makes the process economically unattractive due to the cost of downstream separation and recycling of unconverted gas.

Approaching a future in which oil needs are progressively substituted by those of gas, the interest on this reaction route is fully restored. The state of art of OCM technology is expected to become competitive with current petrochemical processes within the next two decades.[134] Different research approaches have been adopted to increase OCM performance, involving the optimisation of reaction conditions as temperature and high pressure,[135] or the

investigation of alternative reactor configurations.[136, 137] Fundamental knowledge about the OCM catalysis, the nature of the product selectivity limitation and the possibility to overcome it is still required to speed up its access to industry as a valid and profitable alternative for ethylene production.

1.4 Unsteady-state operation in catalysis

The high thermodynamic stability of molecules such as CO_2 and CH_4 imposes severe limitations to their use as feedstock for chemicals and fuels production. At the extreme conditions required for their efficient conversion (highly reactive species, high temperatures and pressures), the less valuable, more thermodynamically favoured products prevail. Catalytic research is primarily oriented to the development of more active and selective catalyst materials for existing processes as a way to maximise conversion and selectivity towards the desired products. The catalytic processes involving heterogeneous catalysts are commonly conducted in steady-state conditions, with reaction inputs like temperature, pressure, reactants concentration fixed to optimized values for the whole duration of the process. Alternative catalytic technologies that rely on unsteady-state operation offer a possibility to overcome thermodynamic constraints and enhance the catalytic performance.

Unsteady-state operation is typically achieved through the periodic variation of feed composition. Temperature, flow rate and direction, pressure are other examples of reaction inputs that can be modified to develop unsteady-state operation. As a result of these periodic perturbations, conditions to exceed steady-state performance in terms of conversion, yield and selectivity can be identified and isolated.[138]

Several successful examples of catalytic processes demonstrated that dynamical changes of the reaction inputs provided an effective increase of the catalytic performance. NO_x storage and reduction mechanism in catalysts for automotive is based on unsteady-state operation, with alternation of NO_x species storage in lean (oxidising) conditions and regeneration of the catalyst in a short fuel-enriched (reducing) pulse in which release of the stored NO_x species and their reduction to N_2 take place.[139, 140] Similarly, higher NO_x conversion by NH_3 are obtained in unsteady-state conditions.[141]

For reaction limited by thermodynamic equilibrium, sorption-enhanced processes can enhance the reactant conversions in accordance to Le Châtelier's principle. A sorbent material is used to selectively remove the undesired byproduct, driving the reaction towards the targeted compounds and obtaining a purified product stream. Periodic regeneration of the sorbent takes place *in situ* by modification of the reaction inputs (e.g. flow composition, temperature, pressure-swing adsorption), enabling continuous operation. Popular examples are reactions involving formation of undesired H_2O in the product stream, as CO_2 hydrogenation to methane and reverse water-gas shift to CO.[142, 143] Alternatively, the water-gas shift equilibrium can be driven to the formation of pure H_2 with high yields by removing the CO_2 product with basic sorbent materials (alkali-, alkaline earth metal oxides).[144]
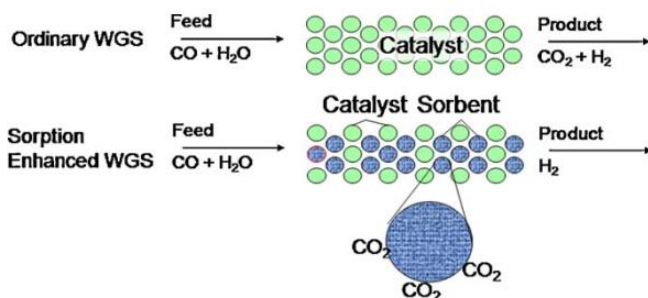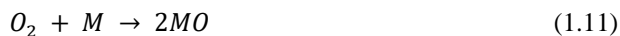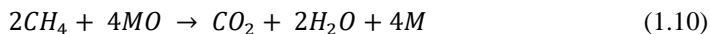
Figure 1.7: Schematic of sorption-enhanced water-gas shift reaction for the production of H_2.[145]

Chemical looping is another approach that consists in the subdivision of a chemical reaction into different reaction (redox) steps, facilitating product separation and overcoming thermodynamic constraints imposed by the steady-state reactive atmosphere. This is often enabled by making use of a solid material which directly intervenes in the reaction mechanism as an intermediate between the different phases of process operation. In the case of oxygen storage materials as cerium oxide and iron oxide, a redox reaction can take place. A reductive reactant (reducing agent) is converted to a desired product by interacting with the solid oxide while in the subsequent step the reduced metal oxide is regenerated by air or oxygen-rich feeds.[146, 147]

Chemical looping strategies were initially approached as an opportunity to achieve efficient and economic CO_2 capture in combustion processes.[148] Chemical looping combustion of CH_4 is performed by interaction of the fuel with the activated oxygen available on/in a solid carrier (Reaction 1.10, where CH_4 is used as fuel and M denotes metal atom in a generic form without proper accounts of oxidation states) in a flameless O_x-free manner.[149] Upon removal of the water, the CO_2 is efficiently purified, since it is intrinsically separated from the air flow by the process.[150] After the fuel oxidation step, the reduced solid material is regenerated (oxidized) by exposure to oxygen or air (Reaction 1.11) or by CO_2 to utilise CO_2 and at the same time produce valuable CO (Reaction 1.12).[149]

$$2CH_4 + 4MO \rightarrow CO_2 + 2H_2O + 4M \qquad (1.10)$$

$$O_2 + M \rightarrow 2MO \qquad (1.11)$$

$$CO_2 + M \rightarrow CO + MO \qquad (1.12)$$

The approach is highly flexible; such a process can thus be optimized for CO production, CO_2 utilisation and efficient use of heat. Promising stability of some solid materials under multiple redox cycles has also been reported.[151, 152] The same concept has been extended to reforming strategies.[146] Thanks to the combination of sorption-enhancement and chemical looping operation, an unsteady-state dry reforming of methane operation was developed to intensify CO_2 utilisation and obtain high yields of CO as product.[31, 153] However, chemical looping processes increase the technological complexity and cost associated to the need of fluidized reactor beds with high circulation rates and degradation of the solid carriers.

In summary, unsteady-state operation stands as a valid opportunity to tackle the challenges related to conventional CO_2 and CH_4 activation routes, when the technological efforts are justified by remarkable advantages compared to the steady-state alternatives.

Unsteady-state techniques are also widely employed as a powerful investigation tool to obtain fundamental mechanistic insights into the catalytic reactions by transient analysis of products and intermediates. Catalytic properties which have a minor effect in steady-state conditions become fundamental in unsteady-state operation (energy of reactant-surface bond, specific active surface, amount and strength of active sites).[144] The interaction between the catalyst and one reactant molecule can change whether the other reactant is present or not, resulting in selectivities that can be completely different compared to the steady-state operation. In this perspective, apart from its valuable technological impact, there is also a more fundamental interest in using this methodology approach, related to the investigation of the catalytic behaviour of the materials. In fact, the possibility of the catalyst to explore different set of conditions, allows identifying the key properties responsible of the catalytic activity. Spatiotemporal *operando* methodologies become fundamental to investigate the catalytic processes with high mechanistic detail. These advanced methodologies, including spectroscopies, chromatography and imaging techniques, permits to monitor the influences of the periodic changes on the input with high time resolution and at different positions in the catalyst bed. This can represent a fundamental step towards a rational design and functionalization of the catalytic materials.[154]

1.5   Scope of the thesis

This thesis focuses on the catalytic conversion of CO_2 and CH_4 in view of their utilisation as abundant and economic C1 feedstocks alternative to fossil fuels for chemicals and fuels production. Due to the thermodynamic stability of CO_2 and CH_4 molecules, the need of energy-intensive processes and the unsatisfactory product selectivity limit their utilisation as chemical feedstock. In this regard, unsteady-state catalytic processes offer the possibility to overcome the thermodynamic constraints of the conventional steady-state operation and, at the same time, provide fundamental insights into the catalytic processes.

Integrated CO_2 capture and conversion to value-added molecules is a promising catalytic strategy to utilise CO_2 as chemical feedstock and mitigate its emissions. **Chapters 2 - 3** of this thesis report an examination of CO_2 capture and reduction (CCR) catalysis. CCR is a catalytic, isothermal, unsteady-state process for the combined capture of CO_2 from diluted streams and reduction in H_2. A bifunctional catalyst is required to develop the capture functionality (alkali metal) and the selective reduction (transition metal) of the captured CO_2. In **Chapter 2**, a K-promoted Cu/y-Al_2O_3 catalyst is chosen as model system for CCR aiming at selective conversion of CO_2 to CO. Objective of the research is to determine the reactive conditions that develop the continuous CCR activity and to identify the catalytic roles of the K promoter, metallic Cu and γ-Al_2O_3 support.

In the highly dynamic conditions of CCR reaction, the identification of the catalytically active state is challenging. An in-depth investigation of the CCR catalysis on the K-promoted Cu y-Al_2O_3 is carried on in **Chapter 3**, with the aim of exploring the mechanism of the capture and

reduction reactions. *Operando* surface infrared spectroscopy and spatiotemporal sampling of gas concentration and temperature along the catalytic bed are used to detect the evolution of intermediates and products along the catalytic bed.

Thanks to their thermal stability, simple metal oxides are frequently used as catalytic support material for high temperature oxidation of CH_4. Furthermore, it is recognised that some of them (MgO, La_2O_3) possess remarkable activity towards the oxidative coupling of CH_4 (OCM) to C_2H_6 and C_2H_4. In **Chapter 4**, the intrinsic catalytic activity of a series of simple metal oxides (MgO, La_2O_3, Y_2O_3, Nd_2O_3, TiO_2) towards CH_4 conversion is studied. Unsteady-state operation and transient analysis of the catalytic reaction products are employed to reveal the presence of specific active sites and selectivity paths for CH_4 conversion.

The insights gained from unsteady-state activation of CH_4 on MgO and La_2O_3 are integrated in the investigation of OCM reaction of **Chapter 5.** In steady-state reaction conditions, the co-presence of CH_4 and O_2 in the reactant feed at high temperature causes a loss of selectivity towards C_2 products and favours the formation of undesired CO_x species. Spatial sampling is employed as powerful tool to monitor the development of temperature and concentration gradients along the catalytic bed during OCM reaction conditions. Similarly, the beneficial effect of metal promoters (Li-, Sr-) towards C_2 selectivity in OCM is also examined.

Combined utilisation of CH_4 and CO_2 in the dry reforming of methane (DRM) would play an important role in decreasing the carbon footprint of the reforming processes for synthesis gas generation. However, steady-state DRM suffers from severe limitations, including the loss of valuable H_2 in the reverse water-gas shift side reaction, a consequent low H_2/CO ratio in the product and the unavoidable accumulation of solid carbon deposits that ultimately leads to catalyst deactivation and fouling. **Chapter 6** investigates the dynamic coke-mediated dry reforming of methane (DC-DRM), an unsteady-state process realised by periodic alternation of the CH_4 and CO_2 feeds to the catalyst bed. The reaction operates with fast coking of the catalyst during the CH_4 pulse and efficient gasification of the C deposits to CO in the CO_2 pulse. Ni-based catalysts are screened in order to individuate the best combination of support material and promoter to ensure high conversions of CH_4 and CO_2, high H_2 and CO product yields and maintain high performance stability along multiple cycles.

This doctoral thesis takes advantage of the unique conditions of unsteady-state operation to develop pathways for the activation of CO_2 and CH_4 and to obtain, with the aid of catalytic investigation and *operando* analytic techniques, unique insights into the catalytic processes involving those two key C1 molecules.

References

1. A. Isella and D. Manca, *Journal*, 2022, **15**.
2. IEA, *Technology Roadmap - Energy and GHG Reductions in the Chemical Industry via Catalytic Processes*, IEA, Paris, 2013.
3. Á. Galán-Martín, V. Tulus, I. Díaz, C. Pozo, J. Pérez-Ramírez and G. Guillén-Gosálbez, *One Earth*, 2021, **4**, 565-583.
4. S. Teske, T. Pregger, S. Simon and C. Harpprecht, in *Achieving the Paris Climate Agreement Goals : Part 2: Science-based Target Setting for the Finance industry — Net-Zero Sectoral 1.5˚C Pathways for Real Economy Sectors*, ed. S. Teske, Springer International Publishing, Cham, 2022, DOI: 10.1007/978-3-030-99177-7_9, pp. 225-246.
5. J. P. Lange, *Energy Environ. Sci.*, 2021, **14**, 4358-4376.
6. IEA, *The Future of Petrochemicals*, Paris, 2021.
7. W. Keim, *Pure Appl. Chem.*, 1986, **58**, 825-832.
8. C. Du, P. Lu and N. Tsubaki, *ACS Omega*, 2020, **5**, 49-56.
9. I. Yarulina, A. D. Chowdhury, F. Meirer, B. M. Weckhuysen and J. Gascon, *Nature Catalysis*, 2018, **1**, 398-411.
10. M. He, Y. Sun and B. Han, *Angew. Chem. Int. Ed.*, 2013, **52**, 9620-9633.
11. T. Sakakura, J.-C. Choi and H. Yasuda, *Chem. Rev.*, 2007, **107**, 2365-2387.
12. F. Kazemifar, *Greenhouse Gases: Science and Technology*, 2022, **12**, 200-230.
13. E. F. Sousa-Aguiar, L. G. Appel and C. Mota, *Catal. Today*, 2005, **101**, 3-7.
14. J. Bao, G. Yang, Y. Yoneyama and N. Tsubaki, *ACS Catal.*, 2019, **9**, 3026-3053.
15. W. Zhou, K. Cheng, J. Kang, C. Zhou, V. Subramanian, Q. Zhang and Y. Wang, *Chem. Soc. Rev.*, 2019, **48**, 3193-3228.
16. C. Mesters, *Annual Review of Chemical and Biomolecular Engineering*, 2016, **7**, 223-238.
17. Y. An, T. Lin, F. Yu, Y. Yang, L. Zhong, M. Wu and Y. Sun, *Science China Chemistry*, 2017, **60**, 887-903.
18. P. Tian, Y. Wei, M. Ye and Z. Liu, *ACS Catal.*, 2015, **5**, 1922-1938.
19. V. Dieterich, A. Buttler, A. Hanel, H. Spliethoff and S. Fendt, *Energy Environ. Sci.*, 2020, **13**, 3207-3252.
20. B. Lee, H. Lee, D. Lim, B. Brigljević, W. Cho, H.-S. Cho, C.-H. Kim and H. Lim, *Appl. Energy*, 2020, **279**, 115827.
21. W. F. Lamb, *Environ. Res. Lett.*, 2021, **16**, 073005.
22. S. J. Davis, K. Caldeira and H. D. Matthews, *Science*, 2010, **329**, 1330-1333.
23. S. J. Davis, N. S. Lewis, M. Shaner, S. Aggarwal, D. Arent, I. L. Azevedo, S. M. Benson, T. Bradley, J. Brouwer, Y.-M. Chiang, C. T. M. Clack, A. Cohen, S. Doig, J. Edmonds, P. Fennell, C. B. Field, B. Hannegan, B.-M. Hodge, M. I. Hoffert, E. Ingersoll, P. Jaramillo, K. S. Lackner, K. J. Mach, M. Mastrandrea, J. Ogden, P. F. Peterson, D. L. Sanchez, D. Sperling, J. Stagner, J. E. Trancik, C.-J. Yang and K. Caldeira, *Science*, 2018, **360**, eaas9793.
24. E. Benhelal, G. Zahedi, E. Shamsaei and A. Bahadori, *J. Clean. Prod.*, 2013, **51**, 142-161.
25. S. Griffiths, B. K. Sovacool, J. Kim, M. Bazilian and J. M. Uratani, *Energy Res. Soc. Sci.*, 2022, **89**, 102542.
26. M. Bui, C. S. Adjiman, A. Bardow, E. J. Anthony, A. Boston, S. Brown, P. S. Fennell, S. Fuss, A. Galindo, L. A. Hackett, J. P. Hallett, H. J. Herzog, G. Jackson, J. Kemper, S. Krevor, G. C. Maitland, M. Matuszewski, I. S. Metcalfe, C. Petit, G.

Puxty, J. Reimer, D. M. Reiner, E. S. Rubin, S. A. Scott, N. Shah, B. Smit, J. P. M. Trusler, P. Webley, J. Wilcox and N. Mac Dowell, *Energy Environ. Sci.*, 2018, **11**, 1062-1176.

27. B. D. Metz, O; de Coninck, HC; Loos, M; Meyer, LJ, *IPCC (2005) Special report on carbon dioxide capture and storage.*, Cambridge, 2005.

28. A. Raza, R. Gholami, R. Rezaee, V. Rasouli and M. Rabiei, *Petroleum*, 2019, **5**, 335-340.

29. G. T. Rochelle, in *Absorption-Based Post-combustion Capture of Carbon Dioxide*, ed. P. H. M. Feron, Woodhead Publishing, 2016, DOI: https://doi.org/10.1016/B978-0-08-100514-9.00003-2, pp. 35-67.

30. L. M. Romeo, I. Bolea and J. M. Escosa, *Appl. Therm. Eng.*, 2008, **28**, 1039-1046.

31. S. M. Kim, P. M. Abdala, M. Broda, D. Hosseini, C. Copéret and C. Müller, *ACS Catal.*, 2018, **8**, 2815-2823.

32. J. M. Lee, Y. J. Min, K. B. Lee, S. G. Jeon, J. G. Na and H. J. Ryu, *Langmuir*, 2010, **26**, 18788-18797.

33. A. Samanta, A. Zhao, G. K. H. Shimizu, P. Sarkar and R. Gupta, *Ind. Eng. Chem. Res.*, 2012, **51**, 1438-1463.

34. S. Sjostrom and H. Krutka, *Fuel*, 2010, **89**, 1298-1306.

35. T. C. Drage, O. Kozynchenko, C. Pevida, M. G. Plaza, F. Rubiera, J. J. Pis, C. E. Snape and S. Tennison, *Energy Procedia*, 2009, **1**, 599-605.

36. R. V. Siriwardane, M.-S. Shen, E. P. Fisher and J. Losch, *Energy Fuels*, 2005, **19**, 1153-1159.

37. O. Cheung and N. Hedin, *RSC Adv.*, 2014, **4**, 14480-14494.

38. C. A. Trickett, A. Helal, B. A. Al-Maythalony, Z. H. Yamani, K. E. Cordova and O. M. Yaghi, *Nat. Rev. Mater.*, 2017, **2**, 17045.

39. E. S. Sanz-Pérez, C. R. Murdock, S. A. Didas and C. W. Jones, *Chem. Rev.*, 2016, **116**, 11840-11876.

40. M. Ramdin, T. W. de Loos and T. J. H. Vlugt, *Ind. Eng. Chem. Res.*, 2012, **51**, 8149-8177.

41. Y. Han and W. S. W. Ho, *J. Membr. Sci.*, 2021, **628**, 119244.

42. R. Dawson, D. J. Adams and A. I. Cooper, *Chem. Sci.*, 2011, **2**, 1173-1177.

43. S. Zulfiqar, M. I. Sarwar and D. Mecerreyes, *Polym. Chem.*, 2015, **6**, 6435-6451.

44. M. C. Payán, B. Verbinnen, B. Galan, A. Coz, C. Vandecasteele and J. R. Viguri, *Environ. Pollut.*, 2012, **162**, 29-39.

45. H. Deng, J. M. Bielicki, M. Oppenheimer, J. P. Fitts and C. A. Peters, *Clim. Change*, 2017, **144**, 151-163.

46. E. S. Rubin, J. E. Davison and H. J. Herzog, *Int. J. Greenh. Gas Control*, 2015, **40**, 378-400.

47. L.-S. Fan, L. Zeng, W. Wang and S. Luo, *Energy & Environmental Science*, 2012, **5**, 7254-7280.

48. M. Aresta, A. Dibenedetto and E. Quaranta, *J. Catal.*, 2016, **343**, 2-45.

49. A. Rafiee, K. Rajab Khalilpour, D. Milani and M. Panahi, *J. Environ. Chem. Eng.*, 2018, **6**, 5771-5794.

50. M. Mikkelsen, M. Jørgensen and F. C. Krebs, *Energy Environ. Sci.*, 2010, **3**, 43-81.

51. M. Aresta and I. Tommasi, *Energy Convers. Manage.*, 1997, **38**, S373-S378.

52. E. Alper and O. Yuksel Orhan, *Petroleum*, 2017, **3**, 109-126.

53. A. Álvarez, A. Bansode, A. Urakawa, A. V. Bavykina, T. A. Wezendonk, M. Makkee, J. Gascon and F. Kapteijn, *Chem. Rev.*, 2017, **117**, 9804-9838.

54. F. Marocco Stuardi, F. MacPherson and J. Leclaire, *Curr. Opin. Green Sustain. Chem.*, 2019, **16**, 71-76.

55.   Y. Yan, J. Gu, E. L. Zeitler and A. B. Bocarsly, in *Carbon Dioxide Utilisation*, eds. P. Styring, E. A. Quadrelli and K. Armstrong, Elsevier, Amsterdam, 2015, DOI: https://doi.org/10.1016/B978-0-444-62746-9.00012-8, pp. 211-233.
56.   H.-J. Ho, A. Iizuka and E. Shibata, *Ind. Eng. Chem. Res.*, 2019, **58**, 8941-8954.
57.   L. Zhang, Y. Song, J. Shi, Q. Shen, D. Hu, Q. Gao, W. Chen, K.-W. Kow, C. Pang, N. Sun and W. Wei, *Advances in Atmospheric Sciences*, 2022, **39**, 1252-1270.
58.   S. Rönsch, J. Schneider, S. Matthischke, M. Schlüter, M. Götz, J. Lefebvre, P. Prabhakaran and S. Bajohr, *Fuel*, 2016, **166**, 276-296.
59.   Y. A. Daza and J. N. Kuhn, *RSC Adv.*, 2016, **6**, 49675-49691.
60.   A. Bansode and A. Urakawa, *J. Catal.*, 2014, **309**, 66-70.
61.   A. Jangam, S. Das, N. Dewangan, P. Hongmanorom, W. M. Hui and S. Kawi, *Catal. Today*, 2020, **358**, 3-29.
62.   G. Centi, E. A. Quadrelli and S. Perathoner, *Energy Environ. Sci.*, 2013, **6**, 1711-1731.
63.   S. R. Golisz, T. Brent Gunnoe, W. A. Goddard, J. T. Groves and R. A. J. C. L. Periana, 2011, **141**, 213-221.
64.   *BP Statistical Review of World Energy*, 2019.
65.   T. S. Collett, *American Association of Petroleum Geologists Bulletin*, 2002, **86**, 1971-1992.
66.   Q. Wang, X. Chen, A. N. Jha and H. Rogers, *Renewable and Sustainable Energy Reviews*, 2014, **30**, 1-28.
67.   E. McFarland, *Science*, 2012, **338**, 340.
68.   D. Costa, J. Jesus, D. Branco, A. Danko and A. Fiúza, *Environmental Science and Pollution Research*, 2017, **24**, 14579-14594.
69.   X. Bao and D. W. Eaton, *Science*, 2016, **354**, 1406.
70.   J.-Y. Lee, M. Weingarten and S. Ge, *Geosci. J.*, 2016, **20**, 137-148.
71.   H. Rodhe, *Science*, 1990, **248**, 1217.
72.   M. Etminan, G. Myhre, E. J. Highwood and K. P. Shine, *Geophys. Res. Lett.*, 2016, **43**, 12,614-612,623.
73.   Energy Information Administration, http://www.eia.gov/dnav/ng/ng_cons_sum_dcu_nus_a.html).
74.   O. Ismail and G. Umukoro, *Energy and Power Engineering*, 2012, **4**, 290-302.
75.   The World Bank, Global Gas Flaring Reduction Partnership, https://www.worldbank.org/en/programs/gasflaringreduction#7).
76.   S. J. Blanksby and G. B. Ellison, *Acc. Chem. Res.*, 2003, **36**, 255-263.
77.   R. Horn and R. Schlögl, *Catal. Lett.*, 2015, **145**, 23-39.
78.   P. Schwach, X. Pan and X. Bao, *Chem. Rev.*, 2017, **117**, 8497-8520.
79.   L. Sun, Y. Wang, N. Guan and L. Li, *Energy Technology*, 2020, **8**, 1900826.
80.   K. Aasberg-Petersen, I. Dybkjær, C. V. Ovesen, N. C. Schjødt, J. Sehested and S. G. Thomsen, *J. Nat. Gas Sci. Eng.*, 2011, **3**, 423-459.
81.   G. Centi and S. Perathoner, *Catal. Today*, 2020, **342**, 4-12.
82.   M. A. Pen˜a, J. P. Gómez and J. L. G. Fierro, *Appl. Catal. A: Gen.*, 1996, **144**, 7-57.
83.   J. R. Rostrup-Nielsen, *Catal. Today*, 2002, **71**, 243-247.
84.   S. Luo, L. Zeng, D. Xu, M. Kathe, E. Chung, N. Deshpande, L. Qin, A. Majumder, T.-L. Hsieh, A. Tong, Z. Sun and L.-S. Fan, *Energy Environ. Sci.*, 2014, **7**, 4104-4117.
85.   F. Jiao, J. Li, X. Pan, J. Xiao, H. Li, H. Ma, M. Wei, Y. Pan, Z. Zhou, M. Li, S. Miao, J. Li, Y. Zhu, D. Xiao, T. He, J. Yang, F. Qi, Q. Fu and X. Bao, *Science*, 2016, **351**, 1065.
86.   A. Sternberg, C. M. Jens and A. Bardow, *Green Chem.*, 2017, **19**, 2244-2259.
87.   M. Noussan, P. P. Raimondi, R. Scita and M. Hafner, *Sustainability*, 2021, **13**.

88.   IEA, *The Future of Hydrogen*, IEA, Paris, 2019.
89.   L. F. Bobadilla, J. M. Riesco-García, G. Penelás-Pérez and A. Urakawa, *J. CO2 Util.*, 2016, **14**, 106-111.
90.   F. Kosaka, Y. Liu, S.-Y. Chen, T. Mochizuki, H. Takagi, A. Urakawa and K. Kuramoto, *ACS Sustain. Chem. Eng.*, 2021, **9**, 3452-3463.
91.   L. B. Braga, J. L. Silveira, M. E. da Silva, C. E. Tuna, E. B. Machin and D. T. Pedroso, *Renewable and Sustainable Energy Reviews*, 2013, **28**, 166-173.
92.   A. Capa, R. García, D. Chen, F. Rubiera, C. Pevida and M. V. Gil, *Renewable Energy*, 2020, **160**, 575-583.
93.   D. Pham Minh, T. J. Siang, D.-V. N. Vo, T. S. Phan, C. Ridart, A. Nzihou and D. Grouset, in *Hydrogen Supply Chains*, ed. C. Azzaro-Pantel, Academic Press, 2018, DOI: https://doi.org/10.1016/B978-0-12-811197-0.00004-X, pp. 111-166.
94.   A. Sternberg and A. Bardow, *ACS Sustain. Chem. Eng.*, 2016, **4**, 4156-4165.
95.   S. M. Kim, P. M. Abdala, T. Margossian, D. Hosseini, L. Foppa, A. Armutlulu, W. van Beek, A. Comas-Vives, C. Copéret and C. Müller, *Journal of the American Chemical Society*, 2017, **139**, 1937-1949.
96.   S. A. Theofanidis, V. V. Galvita, H. Poelman and G. B. Marin, *ACS Catal.*, 2015, **5**, 3028-3039.
97.   G. A. Olah, A. Goeppert, M. Czaun and G. K. S. Prakash, *Journal of the American Chemical Society*, 2013, **135**, 648-650.
98.   N. Kumar, M. Shojaee and J. J. Spivey, *Current Opinion in Chemical Engineering*, 2015, **9**, 8-15.
99.   D. Qin, J. Lapszewicz and X. Jiang, *J. Catal.*, 1996, **159**, 140-149.
100.   G. A. Olah, G. K. S. Prakash and A. Goeppert, *Journal of the American Chemical Society*, 2011, **133**, 12881-12898.
101.   Y. S. Seo, A. Shirley and S. T. Kolaczkowski, *J. Power Sources*, 2002, **108**, 213-225.
102.   F. Basile, G. Fornasari, F. Trifirò and A. Vaccari, *Catal. Today*, 2001, **64**, 21-30.
103.   Y. H. Hu and E. Ruckenstein, in *Advances in Catalysis*, Academic Press, 2004, vol. 48, pp. 297-345.
104.   P. W. Song C., Srimat S.T. , *Tri-reforming of Natural Gas Using CO2 in Flue Gas of Power Plants without CO2 Pre-separation for Production of Synthesis Gas with Desired H2/CO Ratios*, Springer, Boston, MA, 2002.
105.   Y. Matsuo, Y. Yoshinaga, Y. Sekine, K. Tomishige and K. Fujimoto, *Catal. Today*, 2000, **63**, 439-445.
106.   C. Song and W. Pan, *Catal. Today*, 2004, **98**, 463-484.
107.   S.-H. Lee, W. Cho, W.-S. Ju, B.-H. Cho, Y.-C. Lee and Y.-S. Baek, *Catal. Today*, 2003, **87**, 133-137.
108.   A. V. Paladino Lino, C. B. Rodella, E. M. Assaf and J. M. Assaf, *Int. J. Hydrogen Energy*, 2020, **45**, 8418-8432.
109.   A. J. Majewski and J. Wood, *Int. J. Hydrogen Energy*, 2014, **39**, 12578-12585.
110.   D. M. Walker, S. L. Pettit, J. T. Wolan and J. N. Kuhn, *Appl. Catal. A: Gen.*, 2012, **445-446**, 61-68.
111.   Z. Zakaria and S. K. Kamarudin, *Renewable and Sustainable Energy Reviews*, 2016, **65**, 250-261.
112.   Z. R. Ismagilov, E. V. Matus and L. T. Tsikoza, *Energy Environ. Sci.*, 2008, **1**, 526-541.
113.   T. Shimamura, K. Okumura, K. Nakagawa, T. Ando, N.-o. Ikenga and T. Suzuki, *J. Mol. Catal. A: Chem.*, 2004, **211**, 97-102.
114.   K. Tabata, Y. Teng, T. Takemoto, E. Suzuki, M. A. Bañares, M. A. Peña and J. L. G. Fierro, *Catal. Rev.*, 2002, **44**, 1-58.

115. K. Otsuka and M. Hatano, *J. Catal.*, 1987, **108**, 252-255.
116. M. Ravi, M. Ranocchiari and J. A. van Bokhoven, *Angew. Chem. Int. Ed.*, 2017, **56**, 16464-16483.
117. C. Li, G. Li and Q. Xin, *J. Phys. Chem.*, 1994, **98**, 1933-1938.
118. C. Li, W. Yan and Q. Xin, *Catal. Lett.*, 1994, **24**, 249-256.
119. G. A. Olah, *Acc. Chem. Res.*, 1987, **20**, 422-428.
120. R. A. Periana, D. J. Taube, S. Gamble, H. Taube, T. Satoh and H. Fujii, *Science*, 1998, **280**, 560.
121. A. E. Shilov and A. A. Shteinman, *Coord. Chem. Rev.*, 1977, **24**, 97-143.
122. J. A. Labinger and J. E. Bercaw, *Nature*, 2002, **417**, 507-514.
123. V. N. Cavaliere and D. J. Mindiola, *Chem. Sci.*, 2012, **3**, 3356-3365.
124. M. Ghanta, D. Fahey and B. Subramaniam, *Applied Petrochemical Research*, 2014, **4**, 167-179.
125. Y. Gao, L. Neal, D. Ding, W. Wu, C. Baroi, A. M. Gaffney and F. Li, *ACS Catal.*, 2019, **9**, 8592-8621.
126. K. Takanabe and E. Iglesia, *J. Phys. Chem. C*, 2009, **113**, 10131-10145.
127. K. D. Campbell, E. Morales and J. H. Lunsford, *Journal of the American Chemical Society*, 1987, **109**, 7900-7901.
128. S. Lacombe, C. Geantet and C. Mirodatos, *J. Catal.*, 1995, **151**, 439-452.
129. S. Kuś, M. Otremba and M. Taniewski, *Fuel*, 2003, **82**, 1331-1338.
130. L. Hu, D. Pinto and A. Urakawa, in *Catalysis: Volume 32*, The Royal Society of Chemistry, 2020, vol. 32, pp. 203-223.
131. U. Zavyalova, M. Holena, R. Schlögl and M. Baerns, *ChemCatChem*, 2011, **3**, 1935-1947.
132. J. A. Labinger, *Catal. Lett.*, 1988, **1**, 371-375.
133. Y. S. Su, J. Y. Ying and W. H. Green, *J. Catal.*, 2003, **218**, 321-333.
134. A. Cruellas, J. J. Bakker, M. van Sint Annaland, J. A. Medrano and F. Gallucci, *Energy Convers. Manage.*, 2019, **198**, 111789.
135. B. Beck, V. Fleischer, S. Arndt, M. G. Hevia, A. Urakawa, P. Hugo and R. Schomäcker, *Catalysis Today*, 2014, **228**, 212-218.
136. S. Bhatia, C. Y. Thien and A. R. Mohamed, *Chem. Eng. J.*, 2009, **148**, 525-532.
137. S. Jašo, H. R. Godini, H. Arellano-Garcia, M. Omidkhah and G. Wozny, *Chem. Eng. Sci.*, 2010, **65**, 6341-6352.
138. P. Silveston, R. R. Hudgins and A. Renken, *Catal. Today*, 1995, **25**, 91-112.
139. E. Fridell, H. Persson, B. Westerberg, L. Olsson and M. Skoglundh, *Catal. Lett.*, 2000, **66**, 71-74.
140. N. Takahashi, H. Shinjoh, T. Iijima, T. Suzuki, K. Yamazaki, K. Yokota, H. Suzuki, N. Miyoshi, S.-i. Matsumoto, T. Tanizawa, T. Tanaka, S.-s. Tateishi and K. Kasahara, *Catal. Today*, 1996, **27**, 63-69.
141. E. S. Borisova, A. S. Noskov and L. N. Bobrova, *Catal. Today*, 1997, **38**, 97-105.
142. B. T. Carvill, J. R. Hufton, M. Anand and S. Sircar, *AlChE J.*, 1996, **42**, 2765-2772.
143. R. Delmelle, R. B. Duarte, T. Franken, D. Burnat, L. Holzer, A. Borgschulte and A. Heel, *Int. J. Hydrogen Energy*, 2016, **41**, 20185-20191.
144. A. Zagoruiko, *Russian Chemical Reviews - RUSS CHEM REV-ENGL TR*, 2007, **76**, 639-654.
145. G. Manzolini, E. Macchi, M. Binotti and M. Gazzani, *Int. J. Greenh. Gas Control*, 2011, **5**, 200-213.
146. X. Zhu, Q. Imtiaz, F. Donat, C. R. Müller and F. Li, *Energy Environ. Sci.*, 2020, **13**, 772-804.
147. L. Zeng, Z. Cheng, J. A. Fan, L.-S. Fan and J. Gong, *Nature Reviews Chemistry*, 2018, **2**, 349-364.

148.   E. Jerndal, T. Mattisson and A. Lyngfelt, *Chem. Eng. Res. Des.*, 2006, **84**, 795-806.
149.   M. Najera, R. Solunke, T. Gardner and G. Veser, *Chem. Eng. Res. Des.*, 2011, **89**, 1533-1543.
150.   J. Adanez, A. Abad, F. Garcia-Labiano, P. Gayan and L. F. de Diego, *Prog. Energy Combust. Sci.*, 2012, **38**, 215-282.
151.   S. Bhavsar, M. Najera and G. Veser, *Chem. Eng. Technol.*, 2012, **35**, 1281-1290.
152.   A. Löfberg, T. Kane, J. Guerrero-Caballero and L. Jalowiecki-Duhamel, *Chem. Eng. Process.*, 2017, **122**, 523-529.
153.   L. C. Buelens, V. V. Galvita, H. Poelman, C. Detavernier and G. B. Marin, *Science*, 2016, **354**, 449.
154.   A. Urakawa, *Current Opinion in Chemical Engineering*, 2016, **12**, 31-36.

Chapter 2

Role of γ-Al₂O₃ support, unique state of potassium and synergy with copper at the basis of the integrated CO₂ capture and reduction catalysis

Abstract

Carbon dioxide capture and reduction (CCR) process emerges as an efficient catalytic strategy for CO_2 capture and conversion to valuable chemicals. K-promoted Cu/Al_2O_3 catalysts exhibited promising CO_2 capture efficiency and highly selective conversion to syngas (CO + H_2). The dynamic nature of the Cu-K system at reaction conditions complicates the identification of the catalytically active phase and surface sites. The present work aims at more precise understanding of theroles of the potassium and copper and the contribution of the metal oxide support. While Al_2O_3 guarantees high dispersion and destabilisation of the potassium phase, potassium and copper act synergistically to remove CO_2 from diluted streams and promote fast regeneration of the active phase for CO_2 capture releasing CO while passing H_2. A temperature of 350 °C is found necessary to activate H_2 dissociation and generate the active sites for CO_2 capture. The effects of synthesis parameters on the CCR activity are also described by combination of *ex-situ* characterisation of the materials and catalytic testing.

2.1   Introduction

Drastic actions to abate CO_2 emissions are required in the short term to prevent global warming while transitioning towards a more carbon neutral industry and economy.

Carbon capture and storage (CCS) strategies are technologically mature options to abate emissions from highly emitting sectors as industry and energy production, by CO_2 sequestration and storage in geological sites.[1, 2] Current implementation of CCS strategies, however, is too slow to act as realistic solution for the abatement of CO_2 emissions.[3] The principal bottlenecks are the energy penalties and high costs associated to sorbent regeneration, compression and transportation steps. In addition, the CO_2 is essentially treated as a waste, thus CCS processes do not generate any economic return and ultimately fail to develop a closed carbon cycle.

In this regard, carbon capture and utilisation (CCU) strategies stand as favourable solutions to recover the captured CO_2 and valorise it as a feedstock for production of more carbon neutral chemical and fuels.[4-6] Despite its abundance, CO_2 utilisation in chemical industry is scarce due to its thermodynamic stability and relative inertness. A half of the CO_2 utilised as feedstock in industry is used in urea synthesis, but it is also employed in synthesis of carboxylic acids, in the CO hydrogenation to methanol and as an additive in food industry. However, these applications currently utilise a limited amount of CO_2, less than 1% of the CO_2 emitted every year from anthropogenic sources.[7]

In order to extend the utilisation of CO_2 as feedstock, it is desirable to convert it into more reactive C1 building blocks (e.g., CO, CH_4, CH_3OH), which can be exploited in existing industrial processes.[8] However, methanol synthesis and reverse water-gas shift to CO suffer from thermodynamic limitation, requiring harsh conditions (temperature, pressure) to obtain adequate conversions, while exothermic methanation is favoured at low temperature where yields are kinetically limited.[9, 10] Moreover, conventional catalytic processes put a strong requirement on the purity and compression of the CO_2 feedstock, incrementing the total costs and energy requirements.

Recently, a new CCU strategy referred to as 'integrated CO_2 capture and conversion' or 'CO_2 capture and reduction' (CCR) was demonstrated. This approach effectively integrates in one process the separation of CO_2 from diluted streams (e.g. flue gases, air) with its conversion to more valuable molecules as CO and CH_4. Farrauto group proposed a bifunctional catalytic materials based on Ru and CaO with the ability of capturing CO_2 and converting it to CH_4 by use of green H_2.[11] Urakawa group demonstrated the activity of catalysts made of earth-abundant elements in terms of CO_2 capture efficiency and selective conversion to syngas (CO + H_2).[12, 13] The overall reaction can be thought as a reverse water-gas shift reaction (RWGS) performed in an unsteady-state operation. A CO_2-containing feed is sent to the catalytic bed for CO_2 capture followed by a H_2 feed that reduces the captured CO_2 and releases it as CO. Thanks to the reversibility of the sorption, the capture and reduction processes are operated at same temperature and pressure, eliminating the need of sorbent (catalyst) regeneration step and potentially lowering energy requirements. Moreover, continuous CCR operation with excellent performances can be obtained in circulating fluidised bed reactors. Kosaka et al.[14] demonstrated that CO_2 can be captured from low concentration feed (2%) and converted into high concentration CH_4 stream (20%) with high capture efficiency and H_2 conversion.

Bifunctional catalyst materials exhibiting the abilities to capture CO_2 from flue gas and selectively convert it to the desired product are needed.[11] CaO is well-known for the CO_2 capture ability through carbonation reaction, but it needs high temperature for regeneration and generally shows poor stability over the capture-regeneration cycles.[15, 16] It has been reported that other alkali/alkaline-earth metals (Li, Na, K, Cs, Ba) are stable and effective promoters, increasing the CO_2 sorption capacity of the base materials.[13, 17-20] Among them, K shows unique promotion properties by ensuring highly efficient CO_2 capture and reactive desorption of captured CO_2 to CO under H_2 atmosphere at isothermal conditions in the temperature range of 300-500 °C.[12, 21, 22] Besides the alkali promoter, the introduction of transition metals in the catalytic systems is fundamental to ensure the conversion of the captured CO_2. The choice of the active metal greatly affects the reduction products. The use of Ni or Ru promotes catalytic methanation[11, 23, 24] of the captured CO_2, while Cu brings high selectivity towards CO.[12, 13] The latter case is attractive for the versatility of the technology and product, since the presence of product CO and unconverted H_2 during the reduction phase results in the production of a syngas, with H_2/CO ratio tuneable by changing operation conditions and further adding H_2 in the product stream.

Considering the relevance of designing efficient catalytic systems, it is fundamental to understand the catalytic role of the different promoters and their participation in the CCR process. In reaction conditions, the two functionalities interplay in a highly dynamic system. Hyakutake et al.[13] attempted to elucidate the role of K and its interaction with Cu by means of *operando* XRD analysis and reported the generation of a highly dynamic state in reaction conditions, with a profound change in the crystalline structure of the material. However, the dynamic nature of the catalyst and catalytic process set the barrier high for detailed investigations on the roles of K and its synergistic interaction with Cu. Another question mark regards the role of the support material and its contribution to the CCR activity. Studies about the influence of support material on the mechanism of RWGS reaction led to the distinction between irreducible oxides (Al_2O_3, SiO_2) promoting activation of CO_2 via formate route and reducible oxides (TiO_2, CeO_2) activating CO_2 through oxygen vacancies.[25] Employment of γ-Al_2O_3 and MgO-Al_2O_3 mixtures as supports ensured high CCR performance in various catalytic systems.[12, 24, 26] Modification of Al_2O_3 with basic metal oxides is known to increase the heat of CO_2 adsorption and, in particular, a strong interaction between the acidic γ-Al_2O_3 support and the basic K_2CO_3 is expected.[27] Hu et al.[23] reported activity in integrated CO_2 capture and methanation for a ZrO_2-supported catalyst. However, their role as supports in bifunctional catalysts for integrated CO_2 capture and conversion have not been clarified yet.

In this work, we employed K-promoted Cu/γ-Al_2O_3 catalysts as the model system to identify the fundamental catalytic properties to develop the CCR activity. Catalysts with variable composition were prepared and tested to elucidate the roles of potassium promotion and of the Cu active metal as well as their synergetic behaviour to develop efficient CO_2 capture and selective reduction to CO. Synthesis parameters, including the choice of the potassium precursors and the conditions of the impregnation synthesis, were evaluated to clarify their influence on the formation of the active CCR phase. Besides, the peculiarities of the γ-Al_2O_3 as support were investigated in comparison to TiO_2 rutile and ZrO_2 counterparts. Temperature-dependent catalytic activity was studied to identify the conditions for the formation of the catalytically active phase for CCR. The empirical evidences collected in this work suggest that an highly amorphous state of potassium, whose formation is favoured by

high dispersion on the γ-Al_2O_3 support, interacts with the metallic Cu phase to synergistically develop the unique CCR catalytic activity.

2.2   Experimental

2.2.1   Catalyst synthesis

Aluminum oxide (γ-phase, Alfa Aesar, catalyst support), titanium oxide (rutile, Alfa Aesar, >99.5%) and zirconium oxide (monoclinic, Alfa Aesar, catalyst support) were employed as support material. Cu and K were introduced by incipient wetness impregnation using copper nitrate trihydrate (Merck Sigma, >99.5%) and potassium carbonate anhydrous (Merck Sigma, >99.0%) as precursors. Potassium nitrate (ACS reagent, Merck Sigma, >99.0%) and potassium bicarbonate (Merck Sigma, >99.5%) were also employed as potassium precursors. A two-step impregnation procedure was used. First, the support material was impregnated with the aqueous solution of copper nitrate, dried overnight at 80 °C and calcined at 500 °C for 5h in air. Then, the resulting catalyst was further impregnated with an aqueous solution of the potassium precursor, followed again by overnight drying at 80 °C and calcination at 500 °C for 5h in air.

2.2.2   Catalyst characterisation

Powder X-ray diffractograms were acquired on a Bruker D8 Advance diffractometer with Bragg-Brentano geometry using monochromatic Co Kα radiation ($\lambda = 1.7902$ Å) or Cu Kα radiation ($\lambda = 1.5405$ Å). BET surface area of the catalysts was determined from N_2 adsorption isotherms at 77 K using a Micromeritics TriStar II 3020 instrument. H_2 temperature programmed reduction (H_2-TPR) was carried out in a dedicated set-up, consisting of a tubular furnace in which a 6 mm internal diameter quartz tube for holding the sample is inserted and equipped with thermal conductivity detector (TCD) to monitor H consumption. Experiments were performed using a diluted H_2 stream (10 vol% in Ar) with a 30 mL min^{-1} flow rate. 100 mg of sample were charged in the tube, and its temperature was raised from 25 to 800 °C with a ramp rate of 10 °C min^{-1}. Scanning electron microscopy and energy dispersive X-ray spectroscopy (SEM-EDS) measurements were carried out on a JEOL JSM-6010LA *InTouchScope* operated in high vacuum mode, with acceleration voltage set at 20 kV. Transmission electron microscopy was carried out on a Jeol JEM1400 plus TEM.

2.2.3   Catalytic reaction

The catalytic testing was carried on a dedicated setup, in a configuration similar to the one reported in previous works.[13] A schematic representation of the reaction setup is presented in Figure 2.1. The inlet feed was controlled by a system of mass flow controllers (MFCs, Bronkhorst) and two electric 4-way valves to switch among different gas flows at the inlets. The reactor consisted of a tubular quartz tube reactor (4 mm ID, 6 mm OD), loaded with 200 mg of catalyst material, pelletized, crushed and sieved in 200-300 μm range. Prior to each reaction, the catalyst underwent an activation treatment consisting of 50 mL min^{-1} of pure H_2 at 450 °C for 1 h. The temperature of the bed was controlled by a thermocouple inserted in the quartz reactor. The catalytic performance was evaluated under CCR conditions at different temperatures (300, 350, 400 and 450 °C) and ambient pressure. A typical reaction cycle consisted of the alternation of 25 mL min^{-1} of 10 vol% CO_2 in He, to a reduction phase consisting of 50 mL min^{-1} of H_2 (100 vol%). An inert phase of He (80 mL min^{-1}, 100 vol%)

was flushed between the CO_2 and H_2 phases (and *vice versa*). The composition of the product gas mixture was evaluated quantitatively by Fourier transform infrared (FTIR) spectroscopy (ALPHA Bruker) with a time resolution of 5 s. Valve switching and spectral acquisition were synchronised by LabView software. The data presented resulted from the average of multiple cycles of stable operation, after a reproducible activity was achieved.
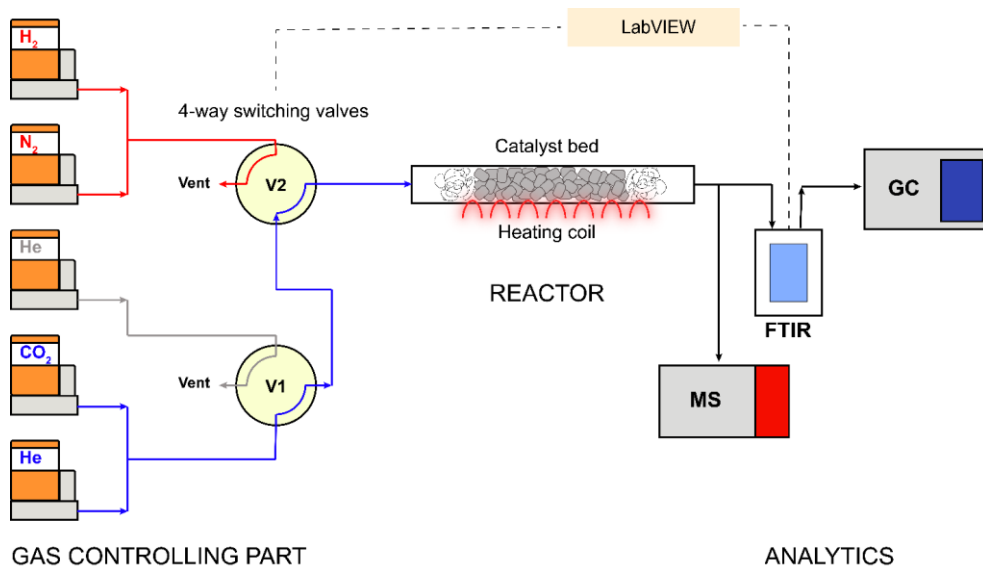

Figure 2.1 Schematic representation of the reaction testing setup. The inlet gas feed controlling part (left) is composed of five mass flow controllers (MFCs) for a total of three inlet feeds (reducing (red), oxidising (blue) and He flushing (grey) lines). The combination of two 4-way switching valves (V1, V2) permits the alternate of the feeds at the inlet of the reactor. The reactor furnace (middle) consists of a refractory brick with a compartment for the reactor quartz tube and the heating coil. A metal jacket surrounds the quartz tube in correspondence of the catalyst bed to ensure uniform distribution of heat. The analytic equipment (right) consists of a Fourier Transform Infrared (FTIR) spectrometer, a mass spectrometer (MS) and a gas chromatograph (GC); the latter one is utilised to calibrate the IR signals and permit quantitative *operando* FTIR analysis. During reaction, a LabVIEW software controls the switching of the valves to periodically change the inlet feed, in synchronisation with the FTIR spectra acquisition.

Quantitative comparison of the CCR activity of different catalyst was made on the basis of the capture capacity, defined as the total amount of CO released during the reducing H_2 pulse (H_2, s = start, $H_{2,e}$ = end of the pulse) per gram of catalyst.[24]

$$\text{capture capacity} = \frac{\int_{H_{2,s}}^{H_{2,e}} CO}{g_{cat}} \quad [\mu mol\ g^{-1}] \tag{2.1}$$

2.3   Results and discussion

CO_2 capture and reduction was performed experimentally by exposing the catalytic bed to the periodic alternation of a diluted CO_2 feed (10 vol% in He) and pure H_2. The gas composition of the reactor outlet stream was analysed by FTIR. The gaseous concentration profile for a blank CCR experiment is reported in Figure 2.2. Each CCR cycle of operation consisted of a CO_2 pulse (0-420 s), followed by the reducing H_2 pulse (570-990 s). For the purposes of this investigation, inert flushing phases (He, 420-570 s and 990-1140 s) were introduced between the CO_2 and H_2 pulses to avoid mixing of the reactants phases, to eliminate possible side reactions activated in co-feed conditions and to univocally identify the role of the catalytic materials in the capture and reduction phases.
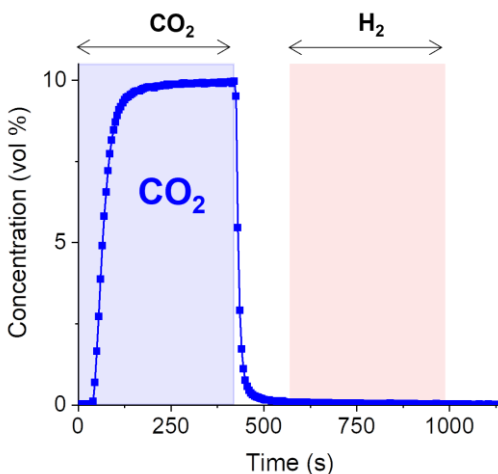
Figure 2.2: Reactor outlet CO_2 concentration obtained by FTIR spectroscopy during a blank CCR experiment on a Cu-K/Al$_2$O$_3$ catalyst (11 wt% Cu, 10wt% K) at room temperature. CCR cycle consists of the alternation of diluted CO_2 feed (blue region, 25 mL min^{-1}, 10 vol% in He, 0-420 s), He flush (50 mL min^{-1}, 420-570 s), pure H_2 feed (red region, 50 mL min^{-1}, 570-990 s), He flush (50 mL min^{-1}, 990-1140 s).

2.3.1   Catalytic role of potassium

Bifunctional materials guarantee the activity in CO_2 capture and reduction reactions (CCR), introducing both the strong affinity to CO_2 and the selectivity towards the desired carbon products. Following the previous contribution,[13] we employed a Cu-K/Al$_2$O$_3$ catalyst (Cu 11 wt%, K 10 wt%) as a model system to investigate the catalytic roles of the two promoters.

The X-ray diffractograms acquired on the synthesised materials are reported in Appendix A1 (Figure A1). Potassium would be expected in the carbonate form, considering its employment as precursor for the synthesis and the calcination performed in air. However, no K_2CO_3 reflexes were detected. Similar results were obtained by Bansode et al.[28], which pointed out the existence of a highly dispersed K phase in the form of nanocrystallites or thin layers. The appearance of narrow metallic Cu reflexes in the XRD reflects a sintering phenomenon, indicating that the amount of copper employed exceeds the conditions to obtain a uniform dispersion of nanocrystals.

To isolate the promotional effect of potassium, we compared the catalytic performance of the catalysts at increasing potassium loadings (Figure 2.3).
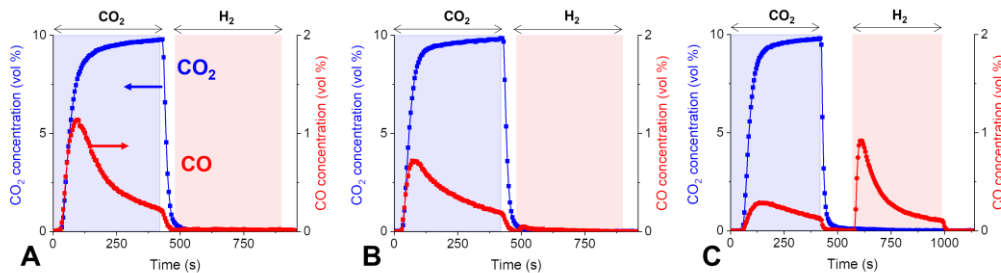

Figure 2.3: Concentration profiles of CO_2 (blue) and CO (red) during CCR at 350 °C, 1 bar with 10% CO_2 in He (blue region) at 25 mL min^{-1} vs. 100% H_2 (red region) at 50 mL min^{-1} over A) Cu/Al$_2$O$_3$ (Cu 11 wt%), B) Cu-K/Al$_2$O$_3$ (Cu 11 wt%, K 2 wt%), C) Cu-K/Al$_2$O$_3$ (Cu 11 wt%, K 10 wt%). He flush phase at 80 mL min^{-1} in between the CO_2 and H_2 pulses.

Figure 2.3A shows that the unpromoted catalyst (11 wt.% Cu / Al$_2$O$_3$) does not possess the ability to capture CO_2. During the CO_2 pulse, CO was produced from the direct interaction with the reduced catalyst. No CO_x species were released in the H_2 pulse, indicating that the capture of CO_2 is not active in absence of potassium. Low loadings of potassium are not sufficient to develop the active phase for CO_2 capture, as indicated by the results obtained in Figure 2.3B for a K-promoted Cu/Al$_2$O$_3$ catalyst (11 wt% Cu, 2 wt% K,). However, the presence of potassium undermined the CO_2 reduction responsible for CO produced in the CO_2 pulse, indicating an interaction between the copper and potassium phases. At higher loading of K (10 wt% K, 11 wt% Cu), the emergence of the typical CCR catalytic activity was noticed (Figure 2.3C). CO_2 was sequestrated from the feed, and then selectively converted and released as CO in the H_2 pulse. No other carbon-containing products were detected within the detection limit. The results indicated that an optimum loading of potassium exists and high CCR catalytic activity may be obtained when particular conditions of high dispersion of potassium phase and intimate contact with copper are fulfilled.

To gain insights into the interaction between Cu and K phase in the catalytic system, H_2 temperature programmed reduction (H_2-TPR) analysis was conducted (Figure 2.4). For the unpromoted Cu/Al$_2$O$_3$ catalyst, complete Cu(II) reduction to metallic Cu(0) is achieved at 300 °C. The profile presents a main peak at around 235 °C with a small shoulder centered at around 270 °C. The first peak can be assigned to the presence of highly dispersed CuO nanoparticles, while the shoulder can be related to bulk oxidation of bigger agglomerates.[29] Compared to the unpromoted Cu/Al$_2$O$_3$ catalyst, the reduction peak of CuO shifted towards higher temperatures in presence of potassium, from ca. 235 °C to 325 °C in case of 10 wt% K loading. Conversely, the decomposition of K$_2$CO$_3$ was enhanced at lower temperatures thanks to the formation of metallic Cu. In fact, the reduction profile peaked at around 570 °C observed for the K/Al$_2$O$_3$ catalyst (10 wt% K) was lost in the catalyst containing Cu in favour of a wide reduction shoulder between 390 and 690 °C detected in the Cu-K/Al$_2$O$_3$ system (10 wt% K, 11 wt% Cu).
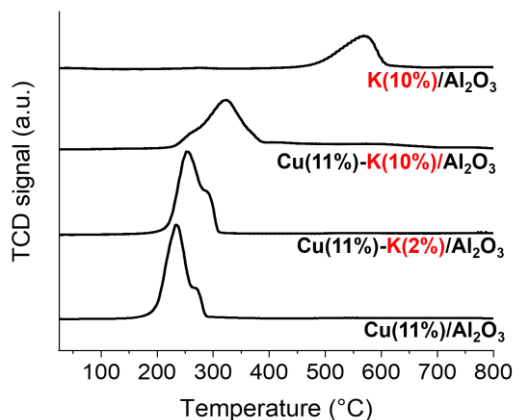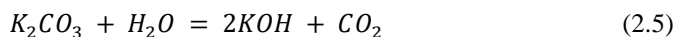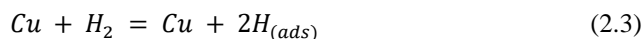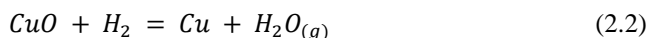
Figure 2.4: H_2-TPR profiles of y-Al_2O_3 supported catalysts. Sample were treated under H_2 flow (10 vol% in Ar, 30 mL min^{-1}) and heating rate of 10 °C min^{-1}.

The decomposition of K_2CO_3, a crucial step for the activation of the catalyst towards CO_2 capture, can be depicted as the results of a dynamic interplay of reactions. When the catalyst is exposed to H_2 feed and heated, the reduction of CuO produce H_2O (Reaction 2.2). The resulting metallic Cu activates the H_2 molecule (Reaction 2.3), making H species available on the catalyst surface ($H_{(ads)}$).[30] As suggested by TPR profiles of Figure 2.4 for the promoted Cu-K/Al_2O_3 catalyst, the K_2CO_3 decomposition (Reaction 2.4) is significantly enhanced in presence of water release from CuO reduction (Reaction 2.5).[31] When the CuO is fully reduced, as in CCR reaction conditions, H species from H_2 dissociation on metallic copper can drive K_2CO_3 decomposition further (Reaction 2.6).

$$CuO + H_2 = Cu + H_2O_{(g)} \qquad (2.2)$$

$$Cu + H_2 = Cu + 2H_{(ads)} \qquad (2.3)$$

$$K_2CO_3 = K_2O + CO_2 \qquad (2.4)$$

$$K_2CO_3 + H_2O = 2KOH + CO_2 \qquad (2.5)$$

$$K_2CO_3 + 2H_{(ads)} = 2KOH + CO \qquad (2.6)$$

During the catalyst activation step in H_2, the reduction of CuO triggers the decomposition of K_2CO_3 initially as an effect of water release and then by continuous supply of H species from dissociation of gaseous H_2 on metallic Cu.

Cu and K phases interact strongly in reaction conditions. *In situ* XRD measurements performed by Hyakutake et al.[13] on a similar system, revealed that in reaction conditions a highly dynamic state is generated, with a profound change in the crystalline structure. They noticed the absence of crystalline CuO or metallic Cu reflexes, and addressed this phenomenon to a nanodispersion induced by the contact with the highly dynamic K phase. Transmission electron microscopy images collected for the Cu-K/Al_2O_3 catalyst (10 wt% K,

11 wt% Cu) after 50 CCR cycles at 350 °C, shown in Figure 2.5, support the previous observation. While CuO nanoparticles up to 10 nm diameter are clearly observed in the fresh sample, small dispersed Cu nanoparticles (2-3 nm) are observed in the sample after reaction condition.
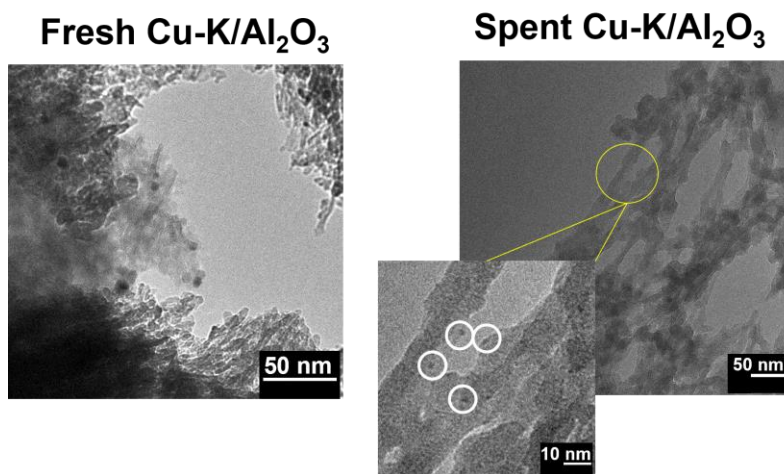

Figure 2.5: TEM images for the Cu-K/Al$_2$O$_3$ (Cu 11 wt%, K 10 wt%) fresh (left) and spent after 50 CCR cycles at 350 °C (right).

Luo et al.[32] reported similar behaviour on a K-promoted Pt/Al$_2$O$_3$, for which they related the formation of finely dispersed Pt species under thermal aging to the interaction with an extremely mobile K phase. Preliminary investigation by *in situ* soft-X-ray absorption spectroscopy (Appendix A2) also revealed a change in the state of K in reaction conditions possibly due to the generation of a highly disordered potassium phase with increased dispersion on the γ-Al$_2$O$_3$ support. Such high dispersion and the intimate contact between the metallic Cu and the K phase are expected to play a key role for the activity of the catalyst towards CCR.

2.3.2 Influence of synthesis conditions

The extremely dynamic nature of the catalytic system in reaction conditions challenges the identification of the potassium active phase for developing CCR catalysis. The nature of this potassium phase, however, is independent of the K precursor employed in the synthesis. In this work, three Cu-K/Al$_2$O$_3$ catalysts (Cu 10 wt%, K 10 wt%) were synthesized employing different K precursors, namely potassium carbonate, bicarbonate and nitrate. Those salts were chosen in view of their different thermal stability. Bulk KNO$_3$ decomposition is reported at temperatures higher than the calcination temperature of 500 °C employed in this work,[33, 34] while KHCO$_3$ starts decomposing to K$_2$CO$_3$ already at temperatures as low as 100 °C.[35]

Interestingly, though the as-synthesized materials exhibited some differences in terms of structural and morphological properties (Appendix A3, Table A1), the CCR activity was preserved and similar catalytic behaviour was observed for all the samples. Catalytic activity (Appendix A3, Figure A5) indicated that the active K phase was generated in reaction conditions for all the catalysts, independently of the K precursor employed during the synthesis. The results suggest that, during catalyst activation and CCR reaction, a similar

potassium state was generated for all the samples. Such indication was confirmed by the X-ray diffractograms of the spent samples (Figure A6), that showed comparable patterns after CCR reaction.

The potassium-derived catalytically active phase is crucial in the generation of CO_2 capture and reduction activity, thus it appears meaningful to investigate its dependence on synthesis conditions. To this scope, we synthesized and tested 4 different Cu-K/Al_2O_3 (Cu 11 wt%, K 10 wt%). Each catalyst was synthesized using an increasing amount of water in the potassium impregnation step, with the objective of transitioning from the incipient wetness impregnation regime to conditions closer to wet impregnation synthesis. For incipient wetness impregnation synthesis, the volume of potassium precursor solution matches the pore volume of the powder to be impregnated (defined here as 1 unit of pore volume). In this case, capillary forces drive the solution inside the pores maximising the dispersion of K.

Employing an excess of water (2, 3 and 5 units of pore volume in this work) in the impregnation, the deposition of the solute inside the material pores is expected to be mainly governed by diffusional forces, requiring longer times to achieve an equilibrium composition.[36] X-ray diffractograms of the samples showed similar patterns (Figure A7). Only low intensity broad reflexes associated to dispersed CuO nanocrystallites and the γ-Al_2O_3 support were detected. The absence of K-related reflexes confirmed the low crystalline character of the phase. SEM-EDX composition analysis (Table A2) suggested that excess of water in the K impregnation leads to a lower concentration of potassium in the catalyst bulk, preventing uniform dispersion and possibly favouring surface segregation of the potassium phase. Both BET surface area and pore volume of the catalysts increased with the amount of water employed in the potassium impregnation step, indicating that, approaching wet impregnation synthesis conditions, pore filling with the potassium solution and deposition of the potassium phase were avoided (Table A3). Figure 2.6 shows the performance of the different catalysts in terms of CO_2 capture capacity, as defined in the Experimental section (Reaction 2.1).
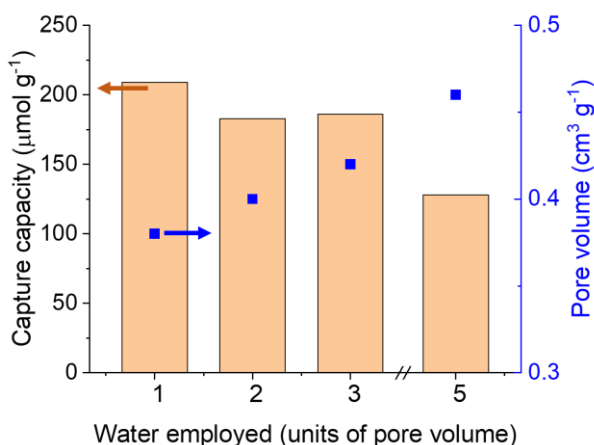

Figure 2.6: Capture capacity and pore volume for Cu-K/Al_2O_3 (Cu 10 wt%, K 10 wt%) synthesized with different amount of water in potassium impregnation step (1-5× pore volume of support).

The employment of excess water in the K impregnation step undermined the activity of the Cu-K/Al$_2$O$_3$ catalysts. The reproducibility of the synthesis procedure was tested, and the catalytic activity results were confirmed (Table A4), with the descending trend of capture capacity at increasing water amount in the K impregnation. The catalyst prepared with incipient wetness impregnation (i.e. 1 unit of pore volume of water solution) showed the highest performance, indicating that, besides exhibiting lower surface area and pore volume, the uniform dispersion of potassium and the maximisation of contact with the copper phase are decisive properties to maximise CCR activity.

2.3.3 Catalytic role of copper

The role of transition metals in bifunctional materials for the integrated capture and conversion of CO$_2$ is promoting the reduction of the captured CO$_2$ and selectively driving its conversion towards the desired products (CO or CH$_4$). Copper, especially, is known to provide high selectivity towards CO$_2$ conversion to CO. For this reason, Cu-based catalysts are frequently employed for CO$_2$ reduction reactions, as the reverse water-gas shift (RWGS).[37] Reduced copper species are reported to dissociate gaseous H$_2$ and provide active H species that increase the reducibility of CO$_2$ and selectively form CO.[38, 39] In this section, we investigate the role of copper in the development of the CO$_2$ capture and reduction activity.

A K/Al$_2$O$_3$ catalyst (K 10 wt%) was synthesized to investigate the catalytic behaviour in absence of copper. The activation pretreatment of the catalyst in H$_2$ (1 h at 450 °C) leads to the decomposition of the K phase generating active sites for capture. After that, capture of CO$_2$ from the feed was noticed during the first cycle of CCR operation at 350 °C (Appendix A4, Figure A8). However, the regeneration of the active phase is kinetically slow at reaction temperature and the short duration of the H$_2$ pulse in operating conditions (420 s) prevented the full regeneration of the catalyst after the first cycle. As shown in Figure 2.7A, the ability to capture CO$_2$ was drastically abated in the following reaction cycles and continuous CCR activity could not be achieved. In absence of copper, only a limited portion of the potassium phase can be decomposed at low reaction temperature. As a consequence, the catalyst exhibits very low CO$_2$ capture capacity (65.5 µmol g^{-1}).

A substantial enhancement of the activity in reduction of captured CO$_2$ was obtained already at low Cu loadings (Cu 1 wt%, K 10 wt%), as shown in Figure 2.7B. During the H$_2$ pulse (570 – 990 s), the high release of CO indicates that kinetic of reduction was clearly boosted, resulting in a drastic improvement of CCR performance in terms of CO$_2$ capture capacity (210.2 µmol g^{-1}). Metallic copper introduced the selective reduction of the captured CO$_2$ and promoted fast regeneration of the active phase for capture, key properties to develop isothermal cyclic CCR operation. H species generated by H$_2$ activation on Cu appear to be decisive for the decomposition of the potassium phase and the selective release of CO. Figure 2.7C shows that increasing the loading of copper (Cu 11 wt%, K 10 wt%) does not play a decisive role in enhancing the performance of the catalytic system, since only a minor increase in capture capacity was detected (227.5 µmol g^{-1}). More than the absolute loading of copper, a decisive role seems to be played by the dispersion of K and Cu and the optimal contact between the two phases at reaction conditions. In analogy with a proposed mechanism for RWGS reaction,[37] the close contact between the phases may favour the spillover of H species from the metallic copper to the capture sites, providing the reduction of CO$_2$ to CO.[40]
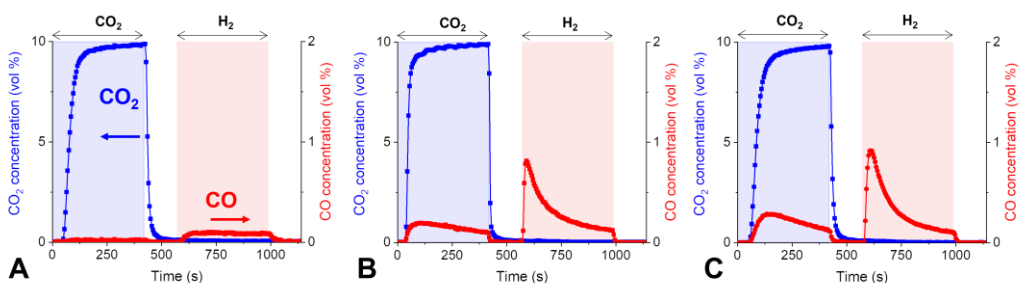
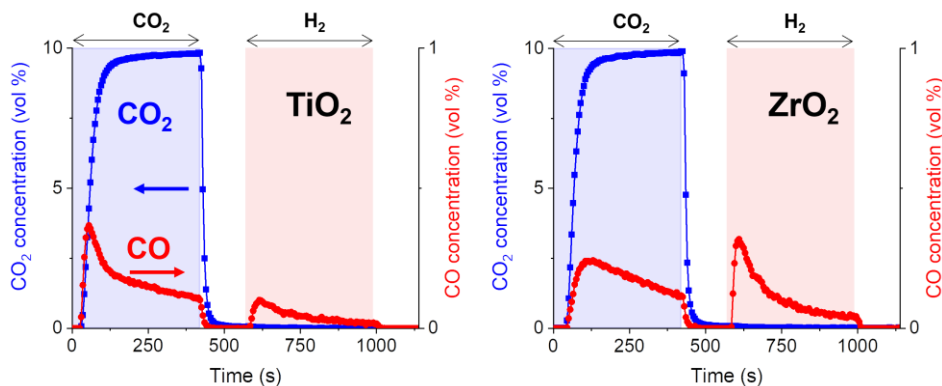**Figure 2.7:** Concentration profiles of CO_2 (blue) and CO (red) during CCR at 350 °C, 1 bar with 10% CO_2 in He (blue region) at 25 mL min^{-1} vs. 100% H_2 (red region) at 50 mL min^{-1} over A) K/Al$_2$O$_3$ (K 10 wt%), B) Cu-K/Al$_2$O$_3$ (Cu 1 wt%, K 10 wt%), C) Cu-K/Al$_2$O$_3$ (Cu 11 wt%, K 10 wt%). He flush phase at 80 mL min^{-1} in between the CO_2 and H_2 pulses.

2.3.4 Contribution of metal oxide support to CCR catalysis

In the previous sections, the role of Cu and K in the development of the CO_2 capture and reduction catalysis has been elucidated. In the attempt of determining the role of the metal oxide support in generating the catalytically active phase for CCR, we investigated the reaction on similar Cu-K catalytic systems supported on TiO_2 (rutile) and ZrO_2 (Cu 10 wt%, K 10 wt%). XRD of the catalysts are reported in Appendix A5 (Figure A9). The catalytic activity results are shown in Figure 2.8.

Figure 2.8: Concentration profiles of CO_2 (blue) and CO (red) during CCR at 350 °C, 1 bar with 10% CO_2 in He (blue region) at 25 mL min^{-1} vs. 100% H_2 (red region) at 50 mL min^{-1} over (left) Cu-K/TiO$_2$ (Cu 10 wt%, K 10 wt%) and (right) Cu-K/ZrO$_2$ (Cu 10 wt%, K 10 wt%). He flush phase at 80 mL min^{-1} in between the CO_2 and H_2 pulses.

Negligible activity in CO_2 capture is noticed for the TiO_2-supported catalyst, as reflected in the low amount of CO evolved in the H_2 pulse. The formation of a K-Ti mixed oxide phase, which is stable in reaction conditions, may explain the inability of the catalyst in generating an active potassium state for CO_2 capture (Appendix A5). Although showing some activity, the ZrO_2-supported catalyst performed significantly worse than its γ-Al$_2$O$_3$-based counterpart (Figure 2.3C). Figure 2.9 reports the CO_2 capture capacities of the three catalytic systems measured at 350 °C and their BET surface area. The results suggest that, thanks to its high

49

surface area, γ-Al_2O_3 support markedly enhances the CCR activity ensuring adequate dispersion of the Cu nanoparticles and maximizing the contact between Cu and K phases.

Comparing different support materials employed for RWGS reaction, Jurkovic et al.[41] found high dispersion of Cu on Al_2O_3 and ZrO_2 on catalysts prepared by deposition precipitation method, with Cu/Al_2O_3 exhibiting the highest catalytic activity. Relations between the catalytic activity and the acidity of metal oxides should also be considered. γ-Al_2O_3 exhibit strong Lewis acid sites while weaker acidity is found for the amphoteric TiO_2 and ZrO_2.[42-44] Addition of potassium promoter is known to strongly interact with acidic supports,[28, 45] causing their neutralisation. In this sense, the acidity of γ-Al_2O_3 can promote a peculiar interaction with the K_2CO_3. The fine dispersion and the strong interaction with Al_2O_3 have been shown to enhance the K_2CO_3 decomposition at lower temperatures in comparison with bulk K_2CO_3,[22, 27] as also detected in the TPR results of Figure 2.4. Such increased destabilisation of the K_2CO_3 phase helps to generate the potassium active state for CO_2 capture and reduction.
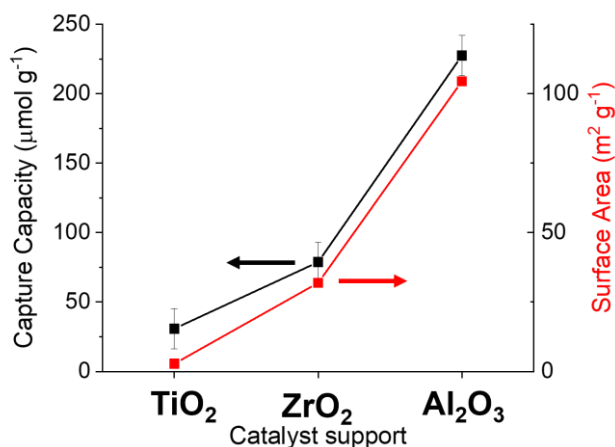
Figure 2.9: Capture capacity (black, left y axis) and respective surface area (red, right y axis) for Cu-K catalysts supported on different metal oxides (TiO_2 rutile, ZrO_2 and γ-Al_2O_3).

2.3.5   Temperature and generation of the catalytically active phase

Figure 2.10 reports the catalytic activity results obtained for the Cu-K/Al_2O_3 catalyst (Cu 11 wt%, K 10 wt%) in four different experiments at varying reaction temperatures. Looking at the catalytic behaviour, the typical CCR activity was noticed starting from a temperature of 350 °C. A significant change in the reduction mechanism was observed at this temperature. The higher CO formation detected at 350 °C during both CO_2 and H_2 pulses revealed an enhancement of direct CO_2 hydrogenation and captured CO_2 reduction, respectively. The results indicate that a temperature of 350 °C is decisive for the formation of the active phase for CO_2 capture and reduction in the Cu-K/Al_2O_3 system. The TPR profiles of Figure 2.4 also displayed an increased H_2 consumption in this temperature range, assignable to both CuO reduction and K_2CO_3 decomposition. In reaction conditions, with the copper already in its metallic state, 350 °C is necessary to activate H_2 dissociation.[46] At this temperature, the increased availability of surface H species promotes the decomposition of the potassium phase

generating the catalytically active state for CO_2 capture. At higher temperatures, a kinetic enhancement of the CO_2 reduction was registered, in agreement with the endothermic nature of the reaction and in similarity with the RWGS.[47] As a result, the CO_2 capture capacity of the catalyst increased with temperature and the profiles of CO release in the H_2 pulse exhibited a higher and narrower initial peak. From the point of view of the process development, temperature stands out as a key operating parameter to control the duration of the CO_2 and H_2 pulses. Higher temperatures can in fact shorten the H_2 pulse for regenerating the catalyst and at the same time, by concentrating the CO release in time, can tune the H_2/CO ratio in the syngas product to flexibly target the needs of the downstream processes.
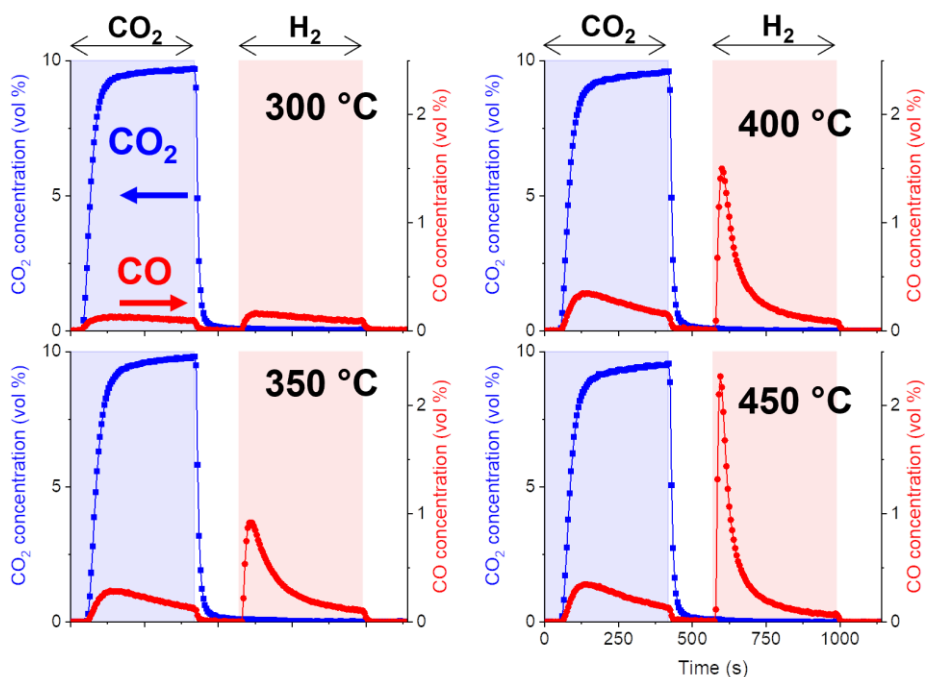
Figure 2.10: Concentration profiles of CO_2 (blue) and CO (red) during CCR at 350 °C, 1 bar with 10% CO_2 in He (blue region) at 25 mL min^{-1} vs. 100% H_2 (red region) at 50 mL min^{-1} over Cu-K/Al$_2$O$_3$ (Cu 11 wt%, K 10 wt%) at different reaction temperatures. He flush phase at 80 mL min^{-1} in between the CO_2 and H_2 pulses.

2.4 Conclusions

The activity towards CO_2 capture and selective reduction to CO derives from a complex interaction between the Cu and K promoters and the γ-Al_2O_3 support. Potassium introduces the CO_2 affinity, but its intimate interaction with the metallic Cu is vital to generate the active phase for capture. The γ-Al_2O_3 excels as catalyst support, providing high surface area end ensuring high dispersion of potassium and intimate contact with the Cu phase. A strong interaction between the acidic sites of γ-Al_2O_3 and the basic potassium carbonate enhances the decomposition of the potassium-derived phase, generating active sites for CO_2 capture. The formation of the active phase for CO_2 capture was found to be independent of the type of potassium precursor employed in the synthesis. However, the high dispersion and intimate contact between copper and potassium phases proved to be key parameters for the activity towards CCR. The generation of active capture sites in H_2, was found to be activated at a temperature between 300 and 350 °C in presence of copper. Metallic Cu activates H_2 dissociation and provides H species that enhance the decomposition of the potassium phase. In such a dynamic state, the synergy between Cu and K permits to aggressively capture CO_2 from the feed and selectively releasing CO when exposed to H_2, providing at the same time fast regeneration of the CO_2 capture active sites. These results furnish insights for improved catalyst design of bifunctional catalysts for integrated CO_2 capture and reduction processes.

Appendix A

A1. X-Ray diffraction analysis

Assignment of the crystalline phases was made by search-match analysis based on PDF database. X-ray diffractograms of unpromoted Cu/Al_2O_3 (Cu 11 wt%), K/Al_2O_3 (K 10 wt%) and $Cu-K/Al_2O_3$ (Cu 11 wt%, K 10wt%) are shown in Figure A1. Reflexes of CuO tenorite (PDF 45-0937) are identified in the Cu-containing samples. The other reflexes are assigned to the γ-Al_2O_3 support (PDF 48-0367).
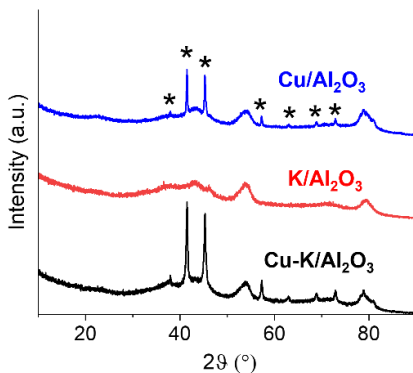

Figure A1: X-ray diffractograms of Cu/Al_2O_3 (Cu 11 wt%) (top, blue line), K/Al_2O_3 (K 10 wt%) (middle, red line) and $Cu-K/Al_2O_3$ (Cu 11 wt%, K 10wt%) (bottom, black line). Phase identification: CuO tenorite (*).

A2. *In situ* soft-XAS – State of potassium at reaction conditions.

Metallic copper, with its reducing properties and the ability to dissociate H_2, and the highly dynamic potassium phase generated in reaction conditions interacts synergistically to develop the continuous catalytic capture and conversion of CO_2. However, the exact identification of the active potassium state during CCR is challenging.

Investigation of the potassium crystalline state in reaction environment is scarce and only few works reported *in situ* soft-XAS studies of potassium promoted catalysts.[48, 49] The need of low energy X-rays poses a high technical barrier for the design of proper reactor cells and for the signal to noise of the acquisition. In this work, we found evidences that the generation of the active catalytic state for CCR is facilitated by the dispersion of potassium on the Al_2O_3 support and by the intimate interaction with the reduced Cu, which promotes H_2 dissociation and potassium carbonate decomposition.

To visualize the effect of the CCR reactive conditions on the crystalline state of potassium, an explorative *in situ* XAS experiment was designed and performed. A Cu-K/Al_2O_3 catalyst (Cu 11 wt%, K 10 wt%) was loaded into a quartz capillary (OD 1 mm, thickness 0.01 mm) connected to a gas flowing system similar to the one employed for the catalytic activity tests. The capillary was then mounted on a heated plate and placed into the vacuum chamber for soft X-ray absorption. A schematic of the reactor cell shown in Figure A2.
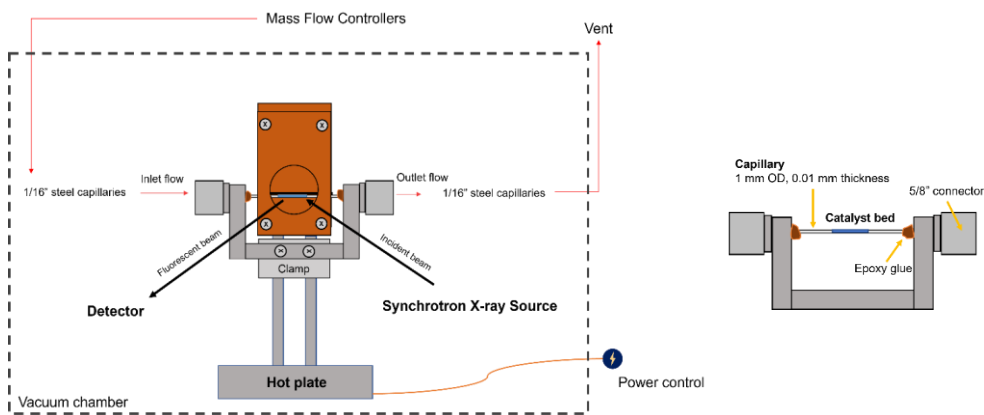

Figure A2: Schematic of in situ XAS reaction cell setup (left) and detail of the capillary holder (right).

Despite the low signal to noise ratio, due to the attenuation of the SiO_2 capillary and the dilution of the potassium absorbent in the system, differences in the potassium K-edge absorption spectra obtained at working conditions (400 °C, CO_2 / H_2 pulses) compared to the spectra acquired at room temperature were clearly observable (Figure A3).

Changes in the peaks related to electronic transitions[50] (A and B) suggest a possible transition in the state of potassium. However, the low signal to noise ratio obtained in this experimental configuration impeded its rigorous identification. At working conditions (400 °C, CO_2 / H_2 pulses), peak C generated from transitions to a continuum state, strongly decreased in intensity compared to the room temperature. Such band highlights changes in long-range order and can be attributed to the generation of a highly disordered potassium phase.
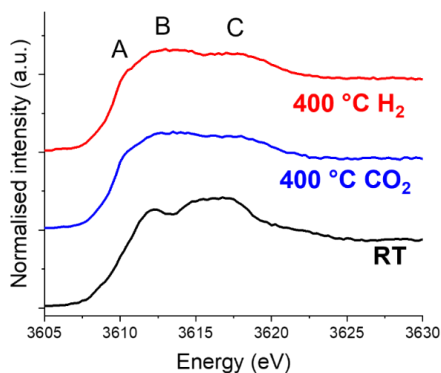
54

Figure A3: *In situ* potassium K-edge XANES of Cu-K/Al_2O_3 catalyst (Cu 11 wt%, K 10 wt%) at room temperature (RT) and in reaction conditions averaged during 5 h at 400 °C in H_2 (10% in He) and 4 h at 400 °C in CO_2 (1 % in He).

Davies et al.[48] conducted an *operando* X-ray absorption investigation on a potassium-promoted α-Al_2O_3 catalyst for soot oxidation. With the aid of XANES simulations, they were able to identify changes in the local structure of potassium upon heating, with increased mobility and dispersion on the Al_2O_3 support. In the CCR system, the presence of metallic Cu introduces additional complexity to the investigation of the local structure.[49] However, these preliminary results seem to confirm the increased dispersion and the amorphous character of the potassium phase in reaction conditions.

A loss in short-range crystalline order may be also suggested by EXAFS result (Figure A4). The identification of possible phase mixtures and monitoring of subtle changes of the potassium state with the reaction pulses were unsuccessful and need future improvements of the reactor to increase the signal to noise ratio of the spectra.
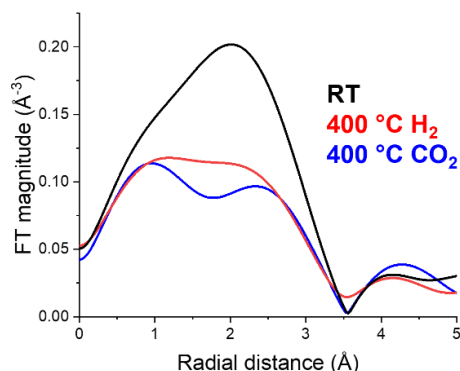

Figure A4: Fourier transforms (FT) of k^2-weighted EXAFS of Cu-K/Al_2O_3 catalyst (Cu 11 wt%, K 10 wt%) at room temperature (RT) and in reaction conditions averaged during 5 h at 400 °C in H_2 (10% in He) and 4 h at 400 °C in CO_2 (1% in He).

A3. Influence of synthesis conditions

Effect of potassium precursor in the synthesis

Figure A5 shows the profiles of gas composition in the effluent stream from the reactor during CCR performed at 350 °C on three Cu-K/Al$_2$O$_3$ catalysts (Cu 10 wt%, K 10 wt%) synthesized with different potassium precursors. A summary of the CO$_2$ capture capacity for the different systems, together with their BET surface area and pore volume is reported in Table S1.
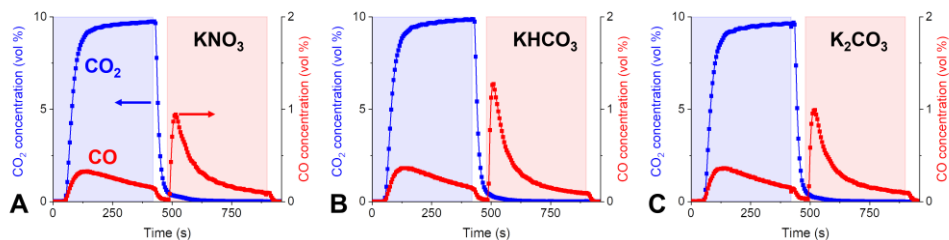

Figure A5: concentration profiles of CO$_2$ (blue) and CO (red) during CCR at 350 °C, 1 bar with 10% CO$_2$ in He (blue region) at 25 mL min^{-1} vs. 100% H$_2$ (grey region) at 50 mL min^{-1} over Cu-K//Al$_2$O$_3$ (Cu 10 wt%, K 10 wt%) synthesized with different K precursors: A) KNO$_3$, B) KHCO$_3$, C) K$_2$CO$_3$.

The catalyst synthesized with impregnation of a potassium bicarbonate solution (B_Cu-K/Al$_2$O$_3$), exhibited slightly better performance in terms of capture capacity at 350 °C and 450 °C. Differences in surface area and pore volume can partly explain such results, considering the higher surface area and pore volume compared to the K$_2$CO$_3$ – derived catalyst (C_Cu-K/Al$_2$O$_3$. In the case of KNO$_3$-derived catalyst (N_Cu-K/Al$_2$O$_3$), however, comparable surface area and pore volume didn't result in similar performance. The lower activity of the N_Cu-K/Al$_2$O$_3$ catalyst can be explained by the presence of a certain degree of crystallinity in the fresh sample (Figure A6), that indicates a non-ideal dispersion of the potassium phase on the catalyst support. Such discrepancy stresses the importance of the dispersion of K phase, which is critical factor to generate the CCR activity.

Table A1: Capture capacity and properties of Cu-K/Al$_2$O$_3$ synthesized with different K precursors

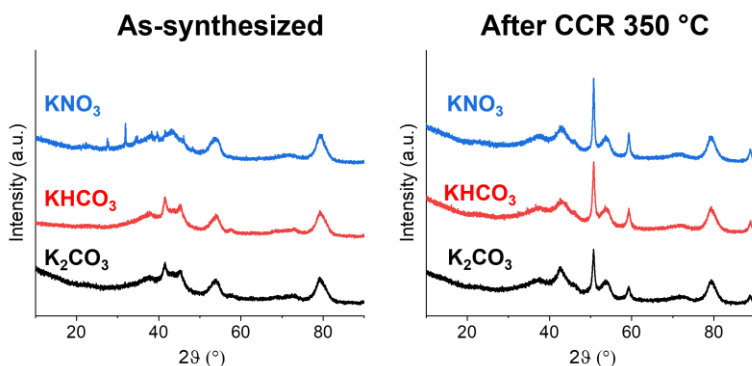| Catalyst	Capture capacity (µmol g^{-1}) at 350 °C	Capture capacity (µmol g^{-1}) at 450 °C	BET Surface Area (m^2 g^{-1})	Pore volume (cm^3 g^{-1})
N_Cu-K/Al$_2$O$_3$	214	292	118	0.39
B_Cu-K/Al$_2$O$_3$	235	306	114	0.42
C_Cu-K/Al$_2$O$_3$	214	283	99	0.31

Figure A6: X-ray diffractograms of Cu-K/Al$_2$O$_3$ (Cu 10 wt%, K 10 wt%) synthesized with different K precursors, as-synthesized (left) and after CCR at 350 °C (right)

Effect of amount of water in the potassium impregnation step

X-ray diffractograms of the samples prepared with different amount of water in the potassium impregnation step showed similar patterns (Figure A7). Only low intensity broad reflexes, associated to the CuO phase, and the γ-Al$_2$O$_3$ support were detected. The absence of potassium-related reflexes confirmed the low crystalline character of the phase.
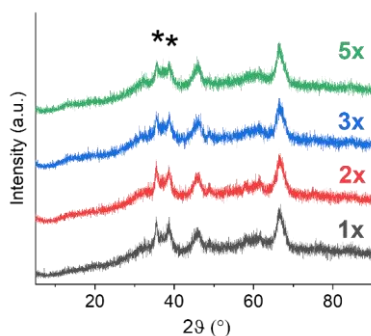
Figure A7: X-ray diffractograms of Cu-K//Al$_2$O$_3$ (Cu 10 wt%, K 10 wt%) synthesized with different amount of water in K impregnation step (1-5× pore volume of support). Phase identification: CuO tenorite (*). XRD acquired employing Cu Kα wavelength.

Table A2: SEM-EDX compositional analysis. Effect of water amount employed (referred to pore volume of the impregnated support material).

Water amount	1×	2×	3×	5×
C (mass %)	10	37	ND	ND
O (mass %)	43	40	47	41
Al (mass %)	27	14	37	38
K (mass %)	9	4	7	6
Cu (mass %)	11	5	11	15
Cu:K ratio	1.2	1.3	1.7	2.7

57

Table A3: Capture capacity at 350 °C, surface area and pore volume. Effect of water amount employed (referred to pore volume of the impregnated support material).

Water amount	Capture capacity (μmol g^{-1}) at 350 °C	BET Surface Area (m^2 g^{-1})	Pore volume (cm^3 g^{-1})
1×	209	102	0.38
2×	183	107	0.4
3×	186	121	0.42
5×	128	132	0.46

Table A4: Capture capacity, surface area and pore volume. 2nd batch of catalysts. Effect of amount of water employed (referred to pore volume of the impregnated support material).

Water amount	Capture capacity (μmol g^{-1}) at 350 °C
1×	201
2×	196
3×	187

A4. Catalytic role of copper

Figure A8 shows the catalytic activity results obtained during the 1st cycle of CCR operation at 350 °C on a K/Al_2O_3 catalyst (K 10 wt%), in absence of Cu. By comparison with the blank CO_2 profile, it is evident that catalyst was able to capture CO_2 after the extensive activation pretreatment in H_2 (50 mL min^{-1}, 1 h at 450 °C). However, in the short H_2 pulse at reaction conditions, the catalyst is not able to convert the captured CO_2 and regenerate the sites for CCR activity, undermining the activity in the following cycles of operation.
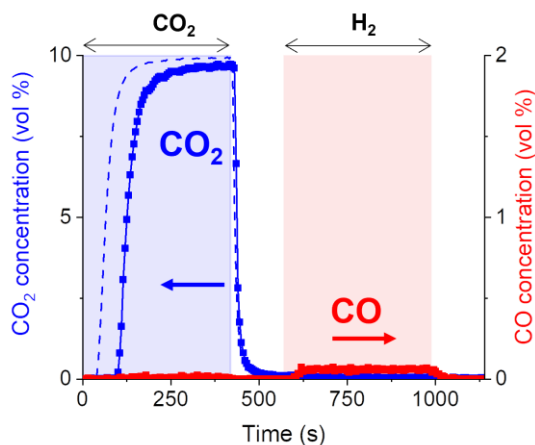
Figure A8: Concentration profiles of CO_2 (blue) and CO (red) during 1st cycle of CCR at 350 °C, 1 bar with 10% CO_2 in He (blue region) at 25 mL min^{-1} vs. 100% H_2 (grey region) at 50 mL min^{-1} over K/Al_2O_3 (K 10 wt%). Dashed line represents blank CO_2 profile at room temperature.

A5. Contribution of metal oxide support to CCR catalysis

X-ray diffractograms of Cu-K/TiO_2 (Cu 10 wt%, K 10 wt%) are shown in Figure A9a. Reflexes of CuO tenorite (41°, 45°, PDF 45-0937) were identified. The low-intensity broad reflex at 13° was assigned to a K-Ti mixed oxide phase (PDF 41-1100). The other reflexes were assigned to TiO_2 rutile phase (PDF 78-1508). After CCR reaction (top, red line), the copper was found only in metallic state (51°, 59°, PDF 85-1326). The reflex at 13° was still visible after reaction, indicating the stability of the phase towards reducing treatments.

Together with the low surface area, the K-Ti mixed oxide phase observed in the XRD can explain the low CCR activity of the TiO_2-supported catalyst. In a work from Salinas et al.,[51] a similar low 2θ reflex was detected for an anatase TiO_2 impregnated with K, after calcination at 600°C. They assigned it to a phase transformation towards potassium titanate, that was formed at 700 °C. In Figure A9a, additional minor reflections were visible at 34°, 56° and 57°, indicating the presence of a single potassium titanium oxide, or a mixture of different phases with variable stoichiometry (PDF 41-1100, PDF 46-0224).[52, 53] Importantly, these phases were found also in the spent catalyst powders. This suggests that potassium may be blocked in a stable crystalline oxide phase, reducing its availability for CO_2 capture and preventing its interaction with the Cu sites to form the active phase for CCR.

Figure A9b shows the diffractogram of 10Cu-10K/ZrO_2. Reflexes of monoclinic ZrO_2 baddeleyite (PDF 07-0343) are identified together with CuO tenorite (PDF 45-0937). No minor phases are detected.
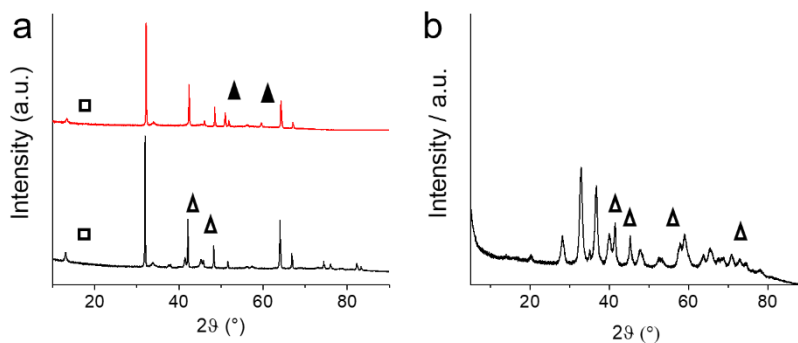

Figure A9: X-ray diffractograms of a) 10Cu-10K/TiO_2 fresh (bottom, black line) and used (top, red line). b) 10Cu-10K/ZrO_2. Phase identification: CuO tenorite (Δ), metallic Cu (▲), K-Ti mixed oxide (□).

References

1.   F. Marocco Stuardi, F. MacPherson and J. Leclaire, *Curr. Opin. Green Sustain. Chem.*, 2019, **16**, 71-76.
2.   R. S. Haszeldine, S. Flude, G. Johnson and V. Scott, *Philos. Trans. Royal Soc. A*, 2018, **376**, 20160447.
3.   E. S. Rubin, J. E. Davison and H. J. Herzog, *Int. J. Greenh. Gas Control*, 2015, **40**, 378-400.
4.   J. Leclaire and D. J. Heldebrant, *Green Chem.*, 2018, **20**, 5058-5081.
5.   J. R. Fernández, S. Garcia and E. S. Sanz-Pérez, *Ind. Eng. Chem. Res.*, 2020, **59**, 6767-6772.
6.   M. Aresta, A. Dibenedetto and A. Angelini, *Chem. Rev.*, 2014, **114**, 1709-1742.
7.   M. Mikkelsen, M. Jørgensen and F. C. Krebs, *Energy Environ. Sci.*, 2010, **3**, 43-81.
8.   W. Keim, *Pure Appl. Chem.*, 1986, **58**, 825-832.
9.   X. Cui and S. K. Kær, *Ind. Eng. Chem. Res.*, 2019, **58**, 10559-10569.
10.   K. Stangeland, D. Kalai, H. Li and Z. Yu, *Energy Procedia*, 2017, **105**, 2022-2027.
11.   M. S. Duyar, M. A. A. Treviño and R. J. Farrauto, *Appl. Catal., B*, 2015, **168-169**, 370-376.
12.   L. F. Bobadilla, J. M. Riesco-García, G. Penelás-Pérez and A. Urakawa, *J. CO2 Util.*, 2016, **14**, 106-111.
13.   T. Hyakutake, W. van Beek and A. Urakawa, *J. Mater. Chem. A*, 2016, **4**, 6878-6885.
14.   F. Kosaka, T. Sasayama, Y. Liu, S.-Y. Chen, T. Mochizuki, K. Matsuoka, A. Urakawa and K. Kuramoto, *Chem. Eng. J.*, 2022, **450**, 138055.
15.   T. Shimizu, T. Hirama, H. Hosoda, K. Kitano, M. Inagaki and K. Tejima, *Chem. Eng. Res. Des.*, 1999, **77**, 62-68.
16.   J. C. Abanades, *Chem. Eng. J.*, 2002, **90**, 303-306.
17.   S. Cimino, F. Boccia and L. Lisi, *J. CO2 Util.*, 2020, **37**, 195-203.
18.   M. d. Arco, E. Hernández, C. Martín and V. Rives, *Spectrosc. Lett.*, 1989, **22**, 1183-1191.
19.   E. L. G. Oliveira, C. A. Grande and A. E. Rodrigues, *Sep. Purif. Technol.*, 2008, **62**, 137-147.
20.   A. Roesch, E. P. Reddy and P. G. Smirniotis, *Ind. Eng. Chem. Res.*, 2005, **44**, 6485-6490.
21.   J. M. Lee, Y. J. Min, K. B. Lee, S. G. Jeon, J. G. Na and H. J. Ryu, *Langmuir*, 2010, **26**, 18788-18797.
22.   S. Walspurger, L. Boels, P. D. Cobden, G. D. Elzinga, W. G. Haije and R. W. van den Brink, *ChemSusChem*, 2008, **1**, 643-650.
23.   L. Hu and A. Urakawa, *J. CO2 Util.*, 2018, **25**, 323-329.
24.   F. Kosaka, Y. Liu, S.-Y. Chen, T. Mochizuki, H. Takagi, A. Urakawa and K. Kuramoto, *ACS Sustain. Chem. Eng.*, 2021, **9**, 3452-3463.
25.   M. Zhu, Q. Ge and X. Zhu, *Trans. Tianjin Univ.*, 2020, **26**, 172-187.
26.   M. A. Arellano-Treviño, N. Kanani, C. W. Jeong-Potter and R. J. Farrauto, *Chem. Eng. J.*, 2019, **375**, 121953.
27.   M. Kantschewa, E. V. Albano, G. Etrtl and H. Knözinger, *Appl. Catal.*, 1983, **8**, 71-84.
28.   A. Bansode, B. Tidona, P. R. von Rohr and A. Urakawa, *Catal. Sci. Technol.*, 2013, **3**, 767-778.

29. M.-F. Luo, P. Fang, M. He and Y.-L. Xie, *J. Mol. Catal. A: Chem.*, 2005, **239**, 243-248.
30. K. Christmann, *Prog. Surf. Sci.*, 1995, **48**, 15-26.
31. Y. Duan, D. R. Luebke and H. H. Pennline, *Int. J. Clean Coal Energ.*, 2012, **1**, 1-11.
32. J. Luo, F. Gao, D. H. Kim and C. H. F. Peden, *Catal. Today*, 2014, **231**, 164-172.
33. M. R. Udupa, *Thermochim. Acta*, 1976, **16**, 231-235.
34. S. Gordon and C. Campbell, *Anal. Chem.*, 1955, **27**, 1102-1109.
35. M. Hartman, K. Svoboda, B. Čech, M. Pohořelý and M. Šyc, *Ind. Eng. Chem. Res.*, 2019, **58**, 2868-2881.
36. E. Marceau, X. Carrier and M. Che, in *Synthesis of Solid Catalysts*, Wiley-VCH, 2009, DOI: 10.1002/9783527626854.ch4, pp. 59-82.
37. M. D. Porosoff, B. Yan and J. G. Chen, *Energy Environ. Sci.*, 2016, **9**, 62-73.
38. C.-S. Chen, W.-H. Cheng and S.-S. Lin, *Catal. Lett.*, 2000, **68**, 45-48.
39. K.-H. Ernst, C. T. Campbell and G. Moretti, *J. Catal.*, 1992, **134**, 66-74.
40. W. C. Conner and J. L. Falconer, *Chem. Rev.*, 1995, **95**, 759-788.
41. D. L. Jurković, A. Pohar, V. D. B. C. Dasireddy and B. Likozar, *Chem. Eng. Technol.*, 2017, **40**, 973-980.
42. A. Álvarez, A. Bansode, A. Urakawa, A. V. Bavykina, T. A. Wezendonk, M. Makkee, J. Gascon and F. Kapteijn, *Chem. Rev.*, 2017, **117**, 9804-9838.
43. C. Lahousse, A. Aboulayt, F. Maugé, J. Bachelier and J. C. Lavalley, *J. Mol. Catal.*, 1993, **84**, 283-297.
44. L. Ferretto and A. Glisenti, *Chem. Mater.*, 2003, **15**, 1181-1188.
45. G. Garcia Cortez, J. L. G. Fierro and M. A. Bañares, *Catal. Today*, 2003, **78**, 219-228.
46. J. A. Rodriguez, J. Y. Kim, J. C. Hanson, M. Pérez and A. I. Frenkel, *Catal. Lett.*, 2003, **85**, 247-254.
47. Y. A. Daza and J. N. Kuhn, *RSC Adv.*, 2016, **6**, 49675-49691.
48. C. J. Davies, A. Mayer, J. Gabb, J. M. Walls, V. Degirmenci, P. B. J. Thompson, G. Cibin, S. Golunski and S. A. Kondrat, *Phys. Chem. Chem. Phys.*, 2020, **22**, 18976-18988.
49. G. P. Huffman, N. Shah, J. M. Zhao, F. E. Huggins, T. E. Hoost, S. Halvorsen and J. G. Goodwin, *J. Catal.*, 1995, **151**, 17-25.
50. C. Sugiura and S. Muramatsu, *Phys. Status Solidi B*, 1985, **132**, K111-K115.
51. D. Salinas, P. Araya and S. Guerrero, *Appl. Catal., B*, 2012, **117-118**, 260-267.
52. E. A. Z. González, M. García-Guaderrama, M. R. Villalobos, F. L. Dellamary, S. Kandhual, N. P. Rout, H. Tiznado and G. G. C. Arizaga, *Powder Technol.*, 2015, **280**, 201-206.
53. S.-O. Kang, H.-S. Jang, Y.-I. Kim, K.-B. Kim and M.-J. Jung, *Mater. Lett.*, 2007, **61**, 473-477.

Chapter 3

Mechanistic insights into the CO_2 capture and reduction on K-promoted Cu/Al_2O_3 by spatiotemporal *operando* methodologies

Abstract

Integrated CO_2 capture and conversion processes bring the promise of drastic abatement of CO_2 emission together with its valorisation to chemical building blocks such as CH_4 and CO. Isothermal CO_2 capture and reduction (CCR) on a K-promoted Cu/Al_2O_3 was recognised as an effective catalytic strategy for removing CO_2 from diluted stream and converting it to syngas (H_2 + CO) employing green H_2 as reducing agent. The dual functionality of the catalyst is the key of this dynamic process, in which the alkaline metal introduces the capture functionality and copper ensures the selective conversion of the captured CO_2 to CO. However, the highly dynamic state of the catalyst at reaction conditions represents a barrier for the identification of the catalytic mechanism of CCR, which is vital for rational process improvement and design. In this work, we conducted a mechanistic investigation of CCR by means of spatiotemporal *operando* methodologies, gaining insights into dynamic variation of temperature, gas concentration and reactive surface species in the CCR reactor. The results show that the unique potassium state exothermically captures CO_2 as surface carbonates which can be reduced to CO rapidly under H_2 atmosphere. When the surface carbonates are transformed to formates the reaction path is altered and the reduction to CO becomes slower. By designing controlled catalytic experiments, we further demonstrate the active involvement of CO in the capture mechanism and the effectiveness of CO_2 capture in presence of an oxidised surface, extending the perspectives and suitability of CCR to treat actual complex effluent streams.

3.1 Introduction

The urgency of reducing anthropogenic emissions of CO_2 has given impulse to the elaboration of carbon capture and utilisation (CCU) strategies. Such strategies are designed to substantially reduce the CO_2 emissions of industrial processes and power plants by separating CO_2 from exhaust gases and, after purification and compression, making it available as feedstock for chemicals and fuels production. Compared to the alternative carbon capture and storage (CCS) that treat CO_2 as a waste, CCU technologies extract value from the captured CO_2 by employing it as a carbon source to produce carbon-neutral commodities.[1-4]

Several technological options have been investigated and developed for CO_2 capture, including amine-based liquid solutions, solid sorbents, separation membranes, ionic liquids, cryogenic separation and biological systems among others.[5-8] Technologies employing amine-based solutions, in particular monoethanolamine, are available at commercial stage, although their employment put some constraints on the capture process.[9] The flue gases containing CO_2 need to be cooled down to an optimal temperature of operation, which is around 40-60 °C for amines. Moreover, O_2, dust, NO_x and SO_x compounds often have to be separated from the flue gas, since they act as poisoning agent provoking the decomposition of the solvent. After saturation of the solution with CO_2, an energy-intensive CO_2 desorption and solvent regeneration has to be performed.

Solid sorbents, including metal oxides, zeolites, carbon, polymers and metal organic frameworks, partially overcome the constraints introduced by an absorbent in the liquid phase, with great promises to reduce capital costs and energy requirements for regeneration.[10-12] Alkaline metal oxides, especially CaO, present high affinity towards CO_2 capture and are tested in carbonation cycles.[13] However, their thermal regeneration requires high temperatures, leading to particle sintering and capture efficiency losses.

Despite the promising readiness of the available technologies, the operational costs related to CO_2 capture still represent the main limitation. Such costs become prohibitive to capture diluted CO_2, as in the case of flue gases emitted by power plants, cement and steel industry, in which the capture cost can exceed 100 USD per ton of CO_2.[14] Furthermore, high purity CO_2 needs to be separated and compressed to be sourced to the chemical industry. The current CO_2 utilisation involves mainly urea synthesis and other small-scale applications (food industry, methanol, carboxylic acids synthesis, etc.), that accounts for transforming an amount of CO_2 equivalent to 0.5% of its annual emissions.[15, 16] Consequently, it is more desirable to design processes which can directly and successfully handle diluted sources of CO_2, as flue gases from power plants, or even make use of the hundreds of ppm concentration in air, in order to reduce the costs related to purification and compression steps.

Anticipating wider availability of economic green H_2 in the near future, the combination of CO_2 capture with its direct conversion to more appealing carbon-containing molecules, can bring additional value to the product. In the last decade, several research groups have proposed and demonstrated integrated CO_2 capture and conversion processes. By using a properly functionalized solid catalyst, CO_2 from diluted streams is captured and stored in the material. Successively, employing H_2 as a reducing agent, the captured CO_2 can be selectively converted to more appealing carbon-containing molecules like CO and CH_4 with a wider

range of applications in chemical industry than CO_2. With economic green H_2 availability, such processes will become competitive options to close the carbon-cycle.

Farrauto and coworkers[17] proved the feasibility of the concept by means of a bifunctional catalyst, in which a combination of alkaline metal oxide (CaO) and transition metal (Ru) supported on γ-Al_2O_3 provided efficient capture of CO_2 from diluted streams and its subsequent conversion to CH_4 when the atmosphere was switched to H_2. A key characteristic of the process is that both capture and conversion steps can take place at the same pressure and in isothermal conditions. Thanks to the nanodispersion of the alkali component on the support, the regeneration of the sorbent in H_2 was achieved at temperatures as low as ~300 °C, permitting to reduce the energy requirements compared to the case of bulk CaO regeneration. A similar integrated process, referred to as CO_2 capture and reduction (CCR), was demonstrated by our research group employing catalysts containing abundant chemical elements.[18] Potassium was introduced as efficient promoter for CO_2 sorption, while the combination of Fe, Cu and Cr exhibited high performance targeting the selective formation of CO, in view of obtaining a valuable syngas mixture (H_2 + CO) in the product stream.

The interest in the catalytic process has grown recently with the exploration of alternative catalytic formulations. Several alkali (Li, Na, K, Cs) and alkali earth promoters (Ca, Ba) can be employed to introduce the CO_2 capture functionality.[19-22] The conversion of the captured CO_2 is selectively driven towards the desired product by proper selection of the active metal phase. In particular, Cu-based catalysts exhibited selective reduction to CO,[23, 24] while Ru and Ni were employed for methanation.[25-27]

Recently, Kosaka et al.[28] demonstrated the beneficial effect of increasing reaction pressures (up to 9 bar) to enhance the performances of direct CO_2 capture at the level of the atmosphere and CH_4 formation on a Na-promoted Ni/Al_2O_3 catalyst.

Despite a trending research directed towards optimisation of CCR processes, knowledge regarding the fundamental catalytic mechanism is still limited. Ex-situ investigation of the catalytic materials inherently lacks information about the active catalytic state. Hyakutake et al.[23] employed a K-promoted Cu/Al_2O_3 catalyst as model systems to investigate the peculiar characteristics of the active phase for CO_2 capture and reduction. *Operando* diffuse reflectance infrared Fourier transform spectroscopy (DRIFTS) suggested the formation of surface intermediates assigned to formates on potassium, while *operando* XRD analysis revealed a highly dynamic system in reaction conditions, with a complex state composed of an highly amorphous potassium state and nanodispersed copper. At the operation temperatures, the dynamic nature of the catalytic system varies in time and space, requiring spatiotemporal analytical techniques to elucidate the CCR chemistry and to identify the catalytic roles played by the K and Cu phases.

In this contribution, we aimed to deepen the comprehension on the catalytic mechanism responsible for CO_2 capture and reduction on a K-promoted Cu/Al_2O_3 system, by identifying active reaction paths of the CCR catalysis. Spatiotemporal sampling of temperature and gas composition along the catalytic bed were used, while *operando* DRIFTS was used to identify spatiotemporal variations of reactive surface species. Unprecedented mechanistic insights were gained by the substitution of CO_2 with CO at the inlet stream and from the evaluation of how CCR operates when Cu is oxidised.

3.2   Experimental

3.2.1   Catalyst synthesis

Aluminum oxide (γ-phase, Thermo Fischer, catalyst support), was employed as support material. Cu and K were added by incipient wetness impregnation using copper nitrate trihydrate (Merck, >99.5%) and potassium carbonate anhydrous (Sigma, >99.0%) as precursors. Copper nitrate was first impregnated on the support, the resulting mixture was dried overnight at 80 °C and then calcined at 500 °C for 5 h. The obtained Cu/Al_2O_3 material was further impregnated with a K_2CO_3 aqueous solution to obtain the final composition ($Cu/K/Al_2O_3$, 11/10/79 wt%).

3.2.2   Catalyst characterization

Powder X-ray diffractograms were acquired on a Bruker D8 Advance Diffractometer with Bragg-Brentano geometry using monochromatic Co kα radiation (λ = 1.7902 Å). BET surface area of the catalysts was determined from N_2 adsorption isotherms at 77 K using a Micromeritics TriStar II 3020 instrument.

3.2.3   Catalytic testing

The reaction setup configuration was similar to the one described in Chapter 2 (Figure 2.1) and previous works.[23] The gas controlling part consisted of mass flow controllers (MFCs, Bronkhorst) and two electric 4-way valves to switch among different gas flows at the inlets. After being pelletized, crushed and sieved in 200-300 µm range, 250 mg of catalyst material were placed in a tubular quartz tube reactor (4 mm ID, 6 mm OD). Blank experiments were conducted by passing the reaction gas mixture on the fresh, non-activated catalyst at room temperature. Prior to the catalytic experiment, the catalyst was activated by reduction under 50 mL min^{-1} of pure H_2 at 450 °C. The temperature of the bed was controlled by a thermocouple inserted in the quartz reactor. Catalytic performance was evaluated under CCR conditions at 350, 400 and 450 °C and ambient pressure. 15 mL min^{-1} of 9.9 vol% CO_2 in He, referred to as capture phase, was alternated to a reduction phase consisting of 15 mL min^{-1} of H_2 (100 vol%). An inert phase of He (30 mL min^{-1}, 100 vol%) was flushed between the capture and reducing phases (and vice versa). The effluent gas mixture composition was quantified by FT-IR spectroscopy (ALPHA Bruker) with a time resolution of 5 s. Valve switching and spectral acquisition were synchronized by LabView software. The data presented were obtained from the average of multiple cycles of operation, after a stable and reproducible composition of the effluent was achieved.

3.2.4   Spatiotemporal sampling of temperature and gas composition

For the spatiotemporal analysis of temperature and gas composition along the catalyst bed, the reaction setup was modified introducing a stainless steel capillary in the reactor through the centre of the packed bed. The capillary (inner diameter = 500 µm, outer diameter = 700

µm, REACNOSTICS GmbH) had 4 holes for gas sampling, equally distanced at the same axial position, with diameter of 50 µm. For measuring the temperature at the sampling position, a thermocouple was inserted through the capillary, with the tip aligned with the sampling holes. The capillary end was sealed with epoxy glue, fixing the thermocouple in place. The other end of the capillary was connected to a mass spectrometer (Omnistar Pfeiffer Vacuum). The reactor effluent was analysed by the FT-IR as explained previously. The same experimental conditions employed for the catalytic testing were applied.

3.2.5 Operando DRIFTS

The DRIFTS measurements were carried out in a custom-made reaction cell, similar to a previously reported design,[29] mounted in a Harrick praying mantis optical system. The reaction cell consisted of a 2x2 mm rectangular channel, sealed with a ZnSe window on the top, which limited the operation temperature to 350 °C. A catalyst pellet mass of 160 mg was tested, which translated to a bed length in the reaction cell of ca. 14 mm. Acquiring DRIFT spectra at different positions on the catalytic bed was possible by moving the entire reactor cell, mounted on an actuator. Prior to the reaction, the catalyst was reduced at 350 °C for 1 h in H_2 (30 mL min^{-1}, 100 vol%). For the regular CCR experiments, CO_2 (10 mL min^{-1}, 1 vol % in He, 420 s), He (30 mL min^{-1}, 100 vol%, 175 s) and H_2 (10 mL min^{-1}, 100 vol%, 420 s) and He (30 mL min^{-1}, 100 vol%, 175 s) phases were alternatingly passed to the reactor. CO (10 mL min^{-1}, 0.5 vol% in He, 420 s) and O_2 (30 mL min^{-1}, 5 vol% in He, 175 s) phases were also employed in dedicated experiments. Spectra were acquired using a Bruker INVENIO R FT-IR spectrometer, equipped with a liquid-nitrogen-cooled MCT detector. Before measurements, a background was taken over the completely reduced catalyst. DRIFT spectra were averaged over consecutive, reproducible cycles to improve signal to noise ratio (S/N). The reactor effluent was analysed by means of FT-IR spectroscopy as explained previously.

3.3 Results and discussion

3.3.1 CO₂ capture and reduction catalysis

A Cu-K/γ-Al$_2$O$_3$ catalyst (11 wt% Cu, 10 wt% K) was synthesised by a two-step incipient wetness impregnation method, following the procedure already reported for similar materials.[23] The successful outcome of the synthesis was verified by X-ray diffraction (Appendix B1, Figure B1).

Figure 3.1 shows a representative concentration profile during the CCR catalytic test performed at 350 °C on the Cu-K/γ-Al$_2$O$_3$ catalyst.

In a typical CCR catalytic test, 0.25 g of catalyst are first activated by exposure to a reducing stream at 450 °C (100 % H$_2$, 50 mL min^{-1}, 1 h). During this pretreatment, CuO is fully reduced to metallic Cu, while the highly dispersed K$_2$CO$_3$ phase is partially decomposed. The presence of copper enhances the decomposition of K$_2$CO$_3$ at lower temperature compared to bulk K$_2$CO$_3$ or K/Al$_2$O$_3$ system, as confirmed by TGA analysis (Appendix B3, Figure B3). As a result, active sites for the capture of CO$_2$ are generated. Then, the catalyst is cyclically exposed to the alternating reactive gases. First, a CO$_2$ feed (10% in He, 15 mL min^{-1}) is passed to the catalyst bed, from which CO$_2$ is captured until saturation of the active sites. For this catalytic test (Figure 3.1), an excess of CO$_2$, compared to the CO$_2$ capture capacity of the catalyst, is passed to the reactor in order to study the reaction paths before and after catalyst saturation. It is possible to maximize the full CO$_2$ capture period by adjusting gas flow rate, catalyst amount and CO$_2$ concentration. An inert flush phase (He, 30 mL min^{-1}) is then introduced to the reactor to remove weakly-adsorbed species and avoid mixing of reactants and related gas-phase reactions for more precise mechanistic studies. After that, H$_2$ is introduced to the reactor (100%, 15 mL min^{-1}) to remove the adsorbed CO$_2$ in the form of CO
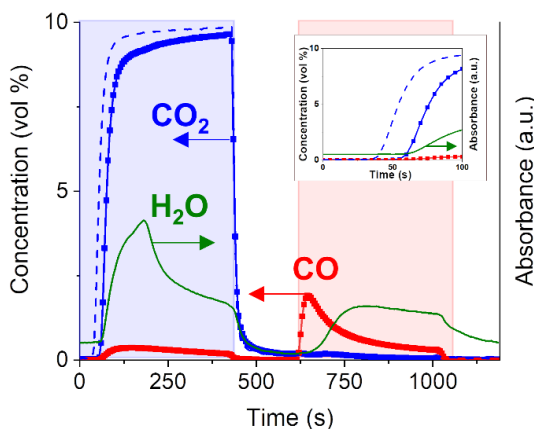

Figure 3.1: Outlet gas concentrations during CCR performed at 350 °C. 1 CCR cycle consists of CO$_2$ feed (0-420 s, 15 mL min^{-1}, 10% in He), inert flush (420-595 s, 30 mL min^{-1}, He), H$_2$ (595-1015 s, 15 mL min^{-1}, 100%), inert flush (1015-1190 s, 30 mL min^{-1}, He) and the cycle is repeated. Results are averaged over 18 CCR cycles. CO$_2$ blank signal (dotted line) obtained as average of 2 CCR cycles during blank experiment at room temperature. The inset shows the concentration profiles during the initial phase of the CO$_2$ capture phase (0-100 s).

and regenerate the catalytically active phase, followed by an additional inert flush phase (He, 30 mL min^{-1}). Figure 3.1 reports the average of the cycles with stable catalytic activity achieved after the first non-reproducible cycle. Compared to the CO_2 profile obtained for a blank experiment performed on the inactive catalyst bed at room temperature, the delay in the appearance of CO_2 at the outlet (20 s) suggests that CO_2 is aggressively captured by the catalyst. Quantitative evaluation of the outlet stream composition clarifies that ca. 100% of CO_2 was captured during this initial period. No CO signal is detected in this time interval within the detection limit (ca. 100 ppm), resulting in virtually a CO_x-free reactor effluent.

Once saturation of the capture sites is achieved, most of the CO_2 entering the reactor is directly released to the reactor outlet apart from a small fraction reacting to produce CO. The detection of CO only after the end of the initial active capture period suggests that the active sites generated on this catalyst may be active for both CO_2 and CO capture. Interestingly, the outlet gas analysis (Figure 3.1) highlighted the formation of water during the capture phase. The formation of water in the CO_2 atmosphere indicates the presence of active H or OH species, generated during catalyst exposure to gaseous H_2 and stored on the catalyst surface. The identification of such species seems directly related to the catalytically active phase and will be targeted in the following sections.

Upon switching to the reduction (H_2) feed, the captured CO_2 is instantaneously and selectively reduced to CO and no other carbon-containing products such as CH_4 are observed within the detection limit (Figure 3.1). The sharp peak of CO detected at the outlet is not accompanied by water formation. The water signal starts to rise with a significant delay (ca. 60 s) compared to the start of the H_2 phase (595 s). This excludes a direct correlation of water formation to the main reduction mechanism of captured CO_2 towards CO formation.

The presence of unconverted H_2 and CO in the effluent stream generates a syngas, whose quality, after separation of water in the product stream, is generally defined by the H_2/CO ratio. The beauty of the CCR is the flexibility of the process, since this ratio can be tuned by the H_2 flow rate, the reduction period, the reduction rate defined by the catalyst and also the reaction temperature.

3.3.2   Effect of reaction temperature

In general, reaction temperature is one of the process parameters greatly affecting CCR performance. Figure 3.2 compares the CCR activity at three different temperatures, namely 350, 400 and 450 °C. At higher temperatures, the CO_2 is detected in the reactor effluent during the capture phase increasingly delayed, revealing an higher capture capacity of the material. Increasing the temperature is beneficial for the CCR reaction. At higher temperature, a larger portion of potassium active sites for capture is likely regenerated in H_2 atmosphere at each cycle. This is in line with the increased weight loss detected at 450 °C during H_2-TGA, which is related to decomposition of the potassium phase (Figure B3). As a consequence, the amount of CO_2 removed from the feed gas increases from 54 μmol g_{cat}^{-1} (350 °C), 95 μmol g_{cat}^{-1} (400 °C) to 130 μmol g_{cat}^{-1} (450 °C).
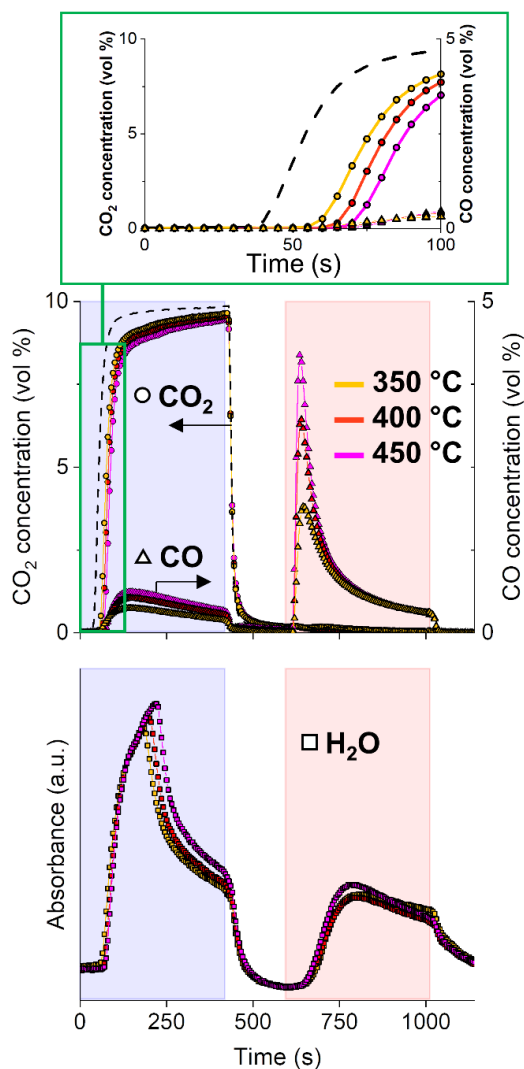
Figure 3.2: Outlet gas concentrations of CO_2 ($\circ$) and CO ($\triangle$) and signal of H_2O ($\square$) during CCR performed at 350 °C (yellow profiles), 400 °C (red profiles), 450 °C (magenta profiles). Results are averaged of 18 CCR cycles. CO_2 blank signal (dotted line) obtained as average of 2 CCR cycles

After the initial active capture, the amount of CO produced by direct interaction of CO_2 with the catalyst slightly increases with temperature. Some considerations can be made from the qualitative analysis of the water signals evolved during the CO_2 stream at different temperatures. On the one hand, the slight increase in water signal with temperature, associated to the increased amount of CO formation, indicates that a CO_2 hydrogenation path to CO is active, which is enhanced at higher temperatures in accordance with the endothermic RWGS reaction.[30] As mentioned earlier, CO is only detected after saturation of the capture sites, when the CO_2 signal starts to rise. The initial absence of CO detection suggests that CO has affinity towards the capture sites and may directly participate in the capture mechanism.
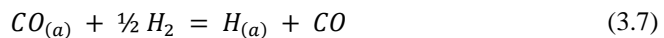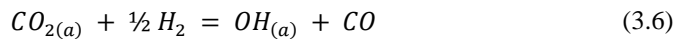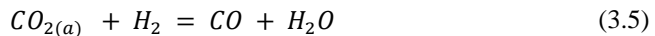
The analysis of the gaseous species at the reactor outlet permits to identify three main reactions taking place during the CO_2 capture phase:

$$CO_2 + \square = CO_2\,(a) + H_2O \qquad (3.1)$$

$$CO_2 + 2H_{(a)} = CO + H_2O \qquad (3.2)$$

$$CO + \square = CO_{(a)} \qquad (3.3)$$
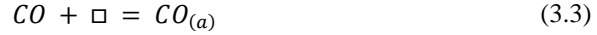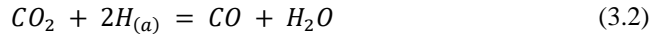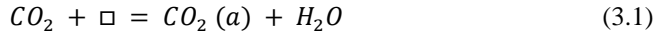
where ($\square$) represent an active sites for CO_x capture on the catalyst. $CO_{2(a)}$ and $CO_{(a)}$ do not necessarily indicate simple adsorbed states of the respective molecules, but rather molecules trapped in the form of surface/bulk chemical species like carbonate. Determining the type of adsorbed species formed during CO_x capture is crucial to identify the active sites for CCR and such studies are described in the following sections.

When the feed gas is switched to H_2, the comparison of the catalytic activity profiles at different temperatures clarifies the presence of two distinct mechanisms involved in the formation of CO.

The first mechanism is associated with the initial fast release of CO. At higher temperatures, the peak of CO reaches higher values, consistent with the higher amount of CO_2 captured. Interestingly, this initial CO release is not accompanied by any water formation (*vide supra*). The absence of a marked release of water at this stage suggests the absence of CuO formation during the CO_2 capture stage, as evidenced in a previous work.[23] This also excludes the relevance of a redox reaction involving a Cu/Cu_xO cycle as mechanism for CO_2 reduction for this catalytic system. Rather, CO_2 is reduced by active H species formed by H_2 dissociation on Cu (Reaction 3.4). However, this reaction does not follow a standard hydrogenation path (RWGS, Reaction 3.5) leading to CO and water release as a consequence of CO_2 reduction. Rather, during the initial reduction phase of CCR, the excess of active H species generated in the reduction phase may induce the destabilisation of the surface intermediates formed during CO_2 capture, provoking the fast selective release of CO (Reactions 3.6 and 3.77). Results from the investigation of surface species and their dynamics in capture and reduction phases are fundamental to elucidate the type of mechanism involved.

$$H_2 = 2H_{(a)} \qquad (3.4)$$

$$CO_{2(a)} + H_2 = CO + H_2O \qquad (3.5)$$

$$CO_{2(a)} + \tfrac{1}{2}\,H_2 = OH_{(a)} + CO \qquad (3.6)$$

$$CO_{(a)} + \tfrac{1}{2}\,H_2 = H_{(a)} + CO \qquad (3.7)$$

After the fast initial release, a second mechanism is responsible for the long tailing in the CO signal. This slowly decaying CO signal seems to be correlated with the water signal. Interestingly, both CO and water profiles deriving from this mechanism are not affected by change in reaction temperature. This contrasts with the hypothesis of a reverse water-gas shift type of reaction which would in turn be favoured at higher temperatures. Mass transfer limitations generated in the packed bed reactor, as well as the presence of less active catalytic sites may be responsible for this reaction. However, the analysis of the outlet stream composition lacks of spatial resolution to answer the question.

3.3.3 Spatiotemporal *operando* studies of temperature, concentration and surface species in the reactor

The analysis of the catalytic activity profiles characterised by the outlet stream concentrations offers relevant indications on the type of reactions involved in CCR. However, the information retrieved at the reactor outlet lacks spatial resolution, potentially missing any temperature or concentration gradients developed in the reactor bed. Moreover, such results are detached from any consideration on the catalyst state and dynamic of surface species involved in the capture of CO_2 and selective conversion to CO. In particular for the Cu-K/Al_2O_3 system, the unique catalytic state reached in operation conditions does not permit to make conclusive statements based on ex situ data.[23] To obtain deeper understanding of the reaction mechanisms involved in CCR, we performed *operando* spatiotemporal sampling of temperature and gas concentration along the reactor bed. In addition, with the aim of identifying the surface reaction mechanisms involved in the CCR reaction, we performed spatiotemporal *operando* DRIFTS and compared the dynamics of surface species with the evolution of the catalytic activity.

Figure 3.3 contains the results obtained from spatiotemporal sampling of concentration and temperature by means of a moving capillary system under CCR with Cu-K/γ-Al_2O_3 at 350 °C. The reaction condition employed was identical to that of the experiment shown in Figure 3.1. A schematic of the sampling positions is represented in Figure 3.3A. The sampling positions inside the bed are indicated with the relative position, where Positions 0 and 1 correspond to quartz wool at the front and after the catalyst bed, respectively. Figure 3.3B highlights the evolution of CO_2 sampled at different positions along the catalyst bed during the initial stages of the capture phase and analysed by mass spectrometry.
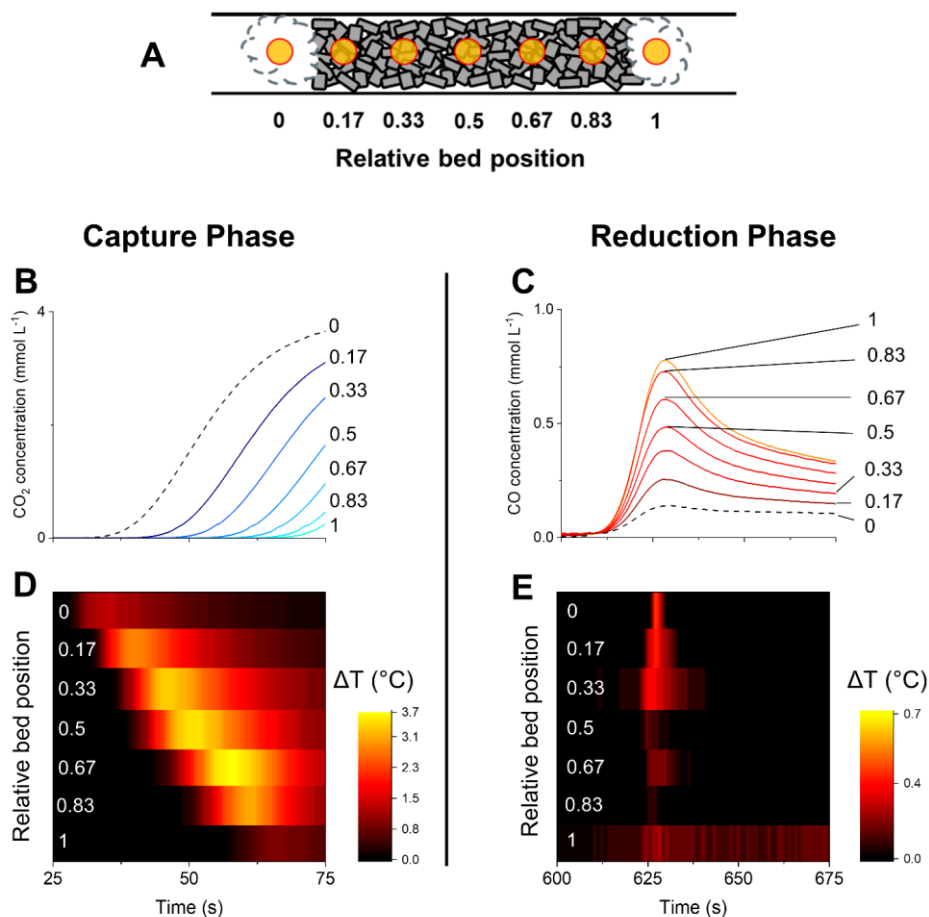
Figure 3.3: Spatiotemporal profiling of temperature and gas phase composition (MS) along the catalyst bed during CCR at 350 °C. Schematic of different sampling positions (A) shown in the relative position (0: beginning of the catalyst bed, 1: end of the catalyst bed). Position 0 and 1 correspond to quartz wool at the front and after the catalyst bed, respectively. CO_2 (B) and CO (C) concentration profiles obtained for the initial stage of the capture phase and reduction phase, respectively. Dashed black line correspond to the signal collected at position 0 in the quartz wool in front of the bed. Temperature of the catalyst bed sampled at different positions from the front to the end of the catalyst bed during the initial stage of the capture phase (D) and reduction phase (E).

Moving along the bed (relative position from 0 to 1), the CO_2 is detected at progressively increasing times, confirming the existence of an active adsorption front proceeding until saturation of the active sites at each position.

At the same time, a temperature increase is detected before the detection of gaseous CO_2 at each position (Figures 3.3D vs. 3.3B). The capture is then associated with an exothermic process which can result from the adsorption of CO_2 from the gas phase. This is consistent with the exothermic reaction of CO_2 with K_2O or KOH to form carbonate or bicarbonate species (Reactions 3.8-11).[31] However, the generation of water during the capture reaction suggests that the mechanism of CO_2 capture may involve a potassium hydroxide phase with formation of carbonates species (Reaction 3.10).

$$K_2O + CO_2 = K_2CO_3 \qquad \Delta H_{300K} = -386\ kJ\ mol^{-1} \qquad (3.8)$$

$$K_2O + 2CO_2 + H_2O = 2KHCO_3 \qquad \Delta H_{300K} = -176\ kJ\ mol^{-1} \qquad (3.9)$$

$$2KOH + CO_2 = K_2CO_3 + H_2O \qquad \Delta H_{300K} = -154\ kJ\ mol^{-1} \qquad (3.10)$$

$$KOH + CO_2 = KHCO_3 \qquad \Delta H_{300K} = -156\ kJ\ mol^{-1} \qquad (3.11)$$

In order to verify this, the analysis of the dynamics of surface species during an analogous CCR experiment is reported in Figures 3.4A-D, in comparison with the reactor outlet gas stream concentrations (Figure 3.4E). To optimise the temporal behaviour of the surface species analysis, the inlet flow condition for these experiments were set to 10 mL min^{-1} for the CO_2 feed (1% in He) and the H_2 feed, while the He flush was kept at 30 mL min^{-1}. The spectra are the average of 8 cycles after achieving a stable operation (quasi steady-state). The last spectrum of the cycle, collected at the end of the inert flushing phase, is used as the background to calculate the absorbance.

When CO_2 is fed to the catalyst bed (0-420 s), we observe the rise of specific vibrations in the CO stretching region (ν(CO) = 1640 and 1290 cm^{-1}). The outlet stream concentrations (Figure 3.4E) clarify that those species are appearing on the surface before the rise of CO_2 signal at the outlet (ca. 200 s). When the saturation is reached at one position of the bed, the surface intermediates start forming at positions further in the bed. The delay observed at each position for the appearance of the ν(CO) stretching bands reproduces quite well the spatially-resolved profile of CO_2 along the catalytic bed obtained with *operando* gas sampling experiments (Figure 3.3B). This confirms that those signals are directly related to the surface intermediates formed during CO_2 capture.

Such species were previously assigned to specific formates on potassium. Contrarily to what happens in $H_2 + CO_2$ cofeed operation,[32] the rise of CH stretching bands (2900-2700 cm^{-1}) during the CO_2 capture is not observed here, indicating that formates may be not a stable intermediate for the capture process. This is in line with the indication of low thermal stability of potassium formate species on Al_2O_3-supported catalysts, which would decompose to carbonates at temperature lower than 350 °C.[33, 34] A similar consideration applies to eventual bicarbonate groups on potassium.[35] Rather, the absorption bands centered at 1640 and 1290 cm^{-1}, arising during CO_2 capture, reflect the splitting of the doubly degenerated asymmetric CO stretching vibration of carbonates, as a result of the lowered symmetry when coordinated to a surface metal cation. The high value of the splitting $\Delta\nu > 300$ cm^{-1}, reported for similar catalytic systems,[36, 37] identifies the observed surface species as bidentate carbonates.[38, 39] This represents a strong indication that the principal capture mechanism consists of the exothermic reaction of a KOH phase and CO_2 to form carbonates and water (Reaction 10). When the atmosphere is switched to inert flushing (at 420 s), neither a temperature change nor massive CO_x release is detected by spatial sampling (Appendix B4, Figure B4), confirming a strong chemical interaction stabilising the adsorbed CO_x species on the catalyst surface. Nevertheless, a slight decrease in intensity of the DRIFTS bands is observed, indicating that the inert flushing may provoke only a limited removal of the surface intermediates formed during capture.
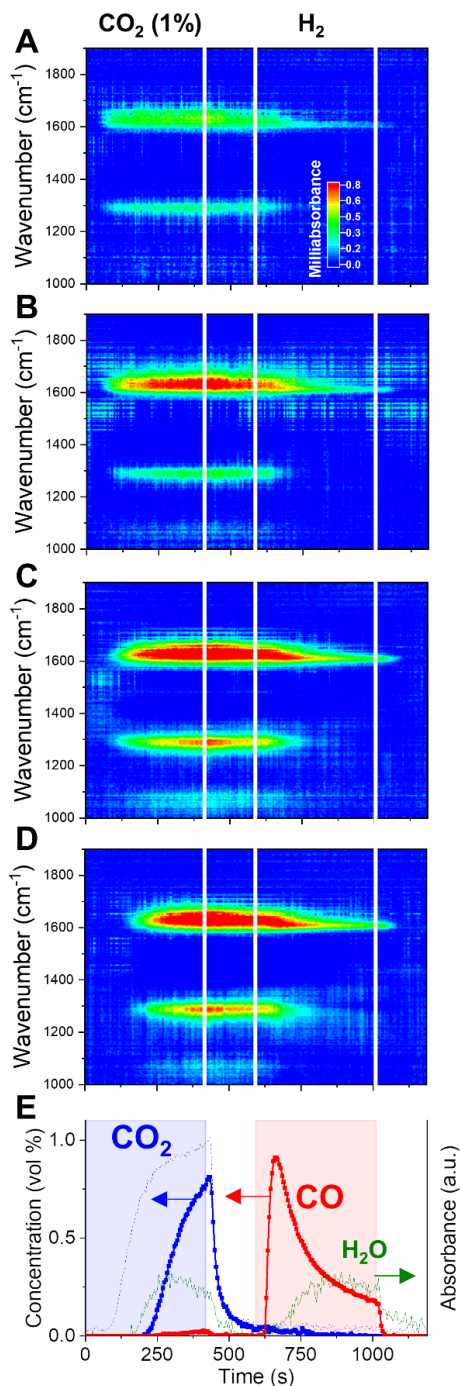
Figure 3.4: Dynamic evolution of surface species elucidated by *operando* DRIFTS during CCR at 350 °C at different positions (A = 3.3 mm, B = 6.4 mm, C = 9.5 mm, D = 12.6 mm) of the catalyst bed from front (A) to back (D). Outlet gas composition (E) obtained by averaging 5 cycles at 350 °C. CO_2 blank signal (dotted line) obtained as average of 2 CCR cycles during a blank experiment at room temperature.

H_2 is essential to remove the surface species generated during CO_2 capture. Switching to H_2 flow (Figure 3.3C), a sudden release of CO is detected instantaneously for each position along the catalytic bed. The removal of adsorbed CO_2 in the form of CO is a fast process. Spatiotemporal sampling of temperature during the reduction phase (Figure 3.3E) indicates that the CO release is associated with only limited exothermicity and temporally confined at the beginning of the reduction phase. Such results confirm the absence of a redox cycle involving extensive copper oxidation, which would have in turn resulted in a highly exothermic reaction. Rather, H_2 is activated on the catalyst by dissociation on Cu and provokes the fast decomposition of the CO_2-derived surface intermediates.

In terms of surface species, it can be observed from the DRIFTS data in Figure 3.4 that, at the switching to H_2 atmosphere (595 s), the bidentate carbonates formed during the capture phase are rapidly decomposed, as indicated by the fast decrease in the intensity of the corresponding $\nu(CO)$ stretching bands centered at 1640 and 1290 cm^{-1}. The fast removal of the surface intermediates for capture matches temporarily the fast release of CO detected in the outlet stream (Figure 3.4E). Thus, a fast decomposition of the surface carbonates, induced by the presence of H_2, constitutes the principal route for the fast CO production in CCR and the regeneration of the active KOH phase (Reaction 3.12).

$$K_2CO_3 + H_2 = 2KOH + CO \qquad (3.12)$$
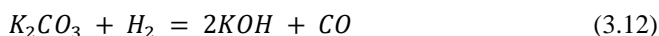
After the fast release of CO, a long tailing of CO formation is observed. In DRIFTS, such tailing is associated with a narrow band in the CO stretching region centered around 1610 cm^{-1}. At the same time, IR absorption bands in the C-H stretching region appear at 2760 and 2670 cm^{-1} (Appendix B5, Figure B5), at vibrational frequencies comparable with formates species on potassium.[40, 41] Such bands indicate that, in presence of excess H_2, accumulation of formates on the surface may occur, which slowly decompose to CO and H_2O. In fact, formates were proposed as intermediates for CO formation in reverse-water gas shift catalysis, where CO_2 and H_2 are simultaneously fed.[42] However, in CCR conditions formate intermediates do not seem to be involved in the capture and fast reduction of captured CO_2. The slightly higher intensity of the formates bands for position towards the end of the bed (Figure B5) may indicate their accumulation due to limitations specific of the plug flow configuration, which can limit the efficient release of CO and the fast regeneration of the catalyst.

3.3.4 CO capture

To prove the participation of CO in the capture mechanism, we designed a CCR experiment in which the CO_2 phase is substituted by a diluted CO stream (0.5 % in He) and performed *operando* DRIFTS. A direct comparison of dynamic surface species in presence of CO_2 or CO as reagents is aimed by employing the same catalyst bed of the experiment in Figure 3.4 and analysing the position at 9.5 mm from the front end of the catalyst bed (the Figure 3.4C position, the total bed length of 14 mm). The position was selected for providing the best combination in terms of higher absorbance intensity and temporal resolution to discriminate the dynamic evolution of surface species, compared to positions at the front of the bed.

The results are reported in Figure 3.5. When the inlet CO_2 is substituted by a CO stream, to our surprise, very similar catalytic behaviour and surface species dynamics are observed. During the capture phase (0-420 s), CO is effectively captured from the inlet stream. Such

result indicates that the active sites on the catalyst surface, formed during the activation of potassium phase in H_2, have high affinity for both CO_2 and CO.

Figure 3.5A reports the *operando* DRIFTS spectra obtained for one position towards the end of the catalyst bed. The CO capture is accompanied by the rise of the same absorption bands in the CO stretching region as observed during CO_2 capture (Figure 3.4) and assigned to bidentate carbonates. At this position, such bands rise with a significant delay (ca. 200 s) with respect to the start of the CO feed, confirming the progress of a capture front along the bed until saturation of the active sites.
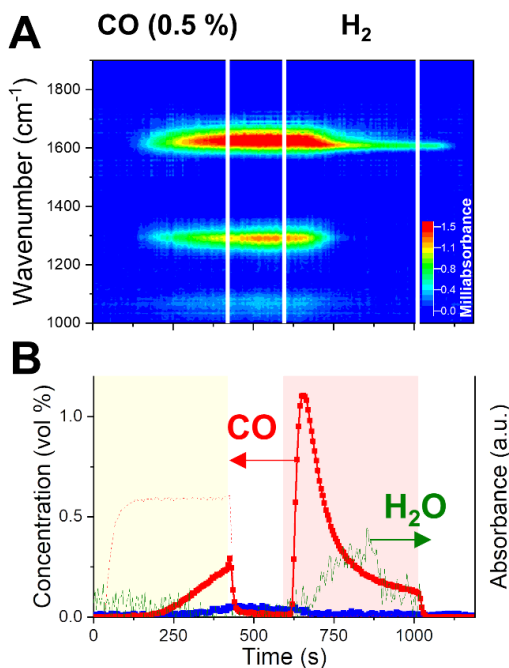
Figure 3.5: Dynamic evolution of surface species elucidated by *operando* DRIFTS (A) during CO-CCR performed at 350 °C. Outlet gas composition (B) was obtained from averaging 5 cycles. CO blank signal (dotted line) obtained as average of 2 CCR cycles during a blank experiment at room temperature.

In contrast to the CO_2 capture (Figure 3.4E), the absence of water release upon CO capture indicates a different type of interaction between CO and the catalytic surface. Alkali hydroxides such as NaOH and KOH are known to efficiently react with CO to form K_2CO_3 with release of H_2 (Reaction 3.13).[43, 44]

$$2KOH + CO = K_2CO_3 + H_2 \qquad (3.13)$$
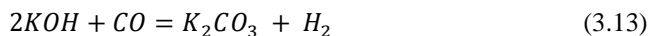
Similarities to the CO_2-based CCR experiment are evidenced also in the reduction phase. When H_2 is sent to the reactor (595 s), a fast intense release of CO is detected at the outlet, associated with a drastic decrease in intensity of the surface carbonates bands. After that, a long tailing in the CO signal at the outlet is linked to the slow decay of a narrow band at 1610 cm^{-1}.

Simultaneously, the same bands appear in the $\nu(CH)$ stretching region (Figure B6) as observed in the CO_2-CCR experiment (Figure B5) and they are assigned to potassium formates species. However, contrary to the CO_2 experiment, the water signal rise is limited and drops before the end of the H_2 phase, implying the importance of extra oxygen atom in CO_2 for water formation.

3.3.5 CO_2 capture on oxidised catalytic surface

Previous *operando* XRD investigation by Hyakutake et al.[23] elucidated that, during CCR operation, a highly dispersed K phase is generated and strongly interacts with the metallic Cu, provoking its nanodispersion. The combination of dispersed potassium phase and metallic copper has been proven a critical property to induce the efficient CCR catalytic activity. Metallic Cu provides sites for H_2 dissociation and ensures the regeneration of the catalytically active phase by enhancing the decomposition of the potassium carbonate phase. However, it is not clear whether Cu is playing a fundamental role in the CO_2 capture mechanism. To answer this, we performed a modified CCR experiment by introducing a diluted O_2 flow (5% in He) instead of the inert flushing phase of the end of each cycle. At the reaction temperature, it is expected that the introduction of oxygen in the reactor leads to the complete oxidation of the copper phase, while keeping intact the active potassium phase generated by decomposition of the potassium carbonate precursor in H_2. As a consequence, CO_2 capture takes place on a oxidised surface, which contains CuO.

Operando DRIFTS results obtained at a single position (9.5 mm in the bed, similar to Figure 3.5A) are presented in Figure 6A. Importantly, the capture of CO_2 is still observed in presence of an oxidised catalytic surface, as demonstrated by the delayed appearance of CO_2 at the reactor outlet. In terms of surface species, the typical CO stretching bands associated to bidentate carbonates are observed in the capture phase, apart for the band centered at 1650 cm^{-1}, whose peak presents a blue-shift compared to the experiments with CO_2 or CO capture on a reduced surface. This result may indicate a specific influence of metallic Cu in the bonding of carbonates species to the surface.

The amount of CO_2 captured and the evolution of the H_2O signal at the outlet are comparable to the ones observed in the regular CCR experiment. In contrast, there is no CO detected when CO_2 interacts with an oxidised Cu surface. No modifications of the potassium phase are expected as a consequence of the oxygen treatment. The temperature of the reaction and the cyclic exposure to the highly reducing H_2 phase may not induce dehydration of KOH to K_2O, for which only limited evidences were reported.[45, 46] The short O_2 treatment (175 s) employed in this experiment is not expected to specifically promote such phase transition. In agreement with the regular CCR operation, H_2O is detected during CO_2 capture and appears as a specific product of the capture reaction. KOH species are then expected to react with CO_2 to form potassium carbonates species observed on the surface and to release water (Reaction 10).

Furthermore, no detected CO in the capture phase indicates that the responsible reaction path is prohibited in presence of CuO. Since no evidences of extensive copper oxidation were found during regular CCR operation in this work and previous work, we are tempted to assign the CO formation in normal CCR to an hydrogenation reaction (Reaction 2), resulting from the interaction of CO_2 with specific H species activated on Cu. Such species may be oxidised during the forced Cu oxidation in the experiment shown in Figure 6. Proof of this oxidation process is the water release observed at the reactor outlet during the O_2 flushing phase (1015-1190s).

Upon switching to H_2 (at 595 s), the presence of CuO activates its reduction accompanying significant production of water. Notably, no CO is released, and only removal of the captured species in the form of CO_2 is observed. The extensive release of water may destabilise the surface intermediate and promoting a water-gas shift type of reaction resulting in the removal of unconverted CO_2.
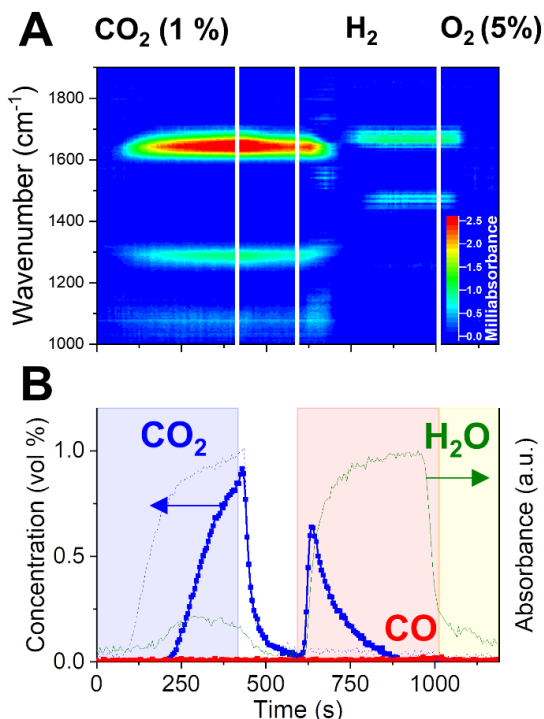

Figure 3.6: Dynamic evolution of surface species elucidated by *operando* DRIFTS (A) during CCR performed at 350 °C with substitution of last He gas phase with O_2 (5% in He). Outlet gas composition (B) was obtained from averaging 5 cycles at 350 °C. CO_2 blank signal (blue dotted line) obtained as average of 2 CCR cycles during a blank experiment at room temperature.

The most important observation is that the selective conversion of captured CO_2 to CO is lost in presence of oxidised Cu. *Operando* DRIFTS clarifies that, after the fast removal of surface carbonates and corresponding evolution of CO_2, new surface bands appear on the catalyst surface, which can be possibly assigned to adsorbed water due to high amount of water released from CuO reduction. However, it is proved that the Cu-K-based catalyst is able to efficiently capture CO_2 in presence of oxygen and water in the stream,[18] which is a functionality of interest for realistic application as the removal of CO_x species from flue gases in combustion and chemical plants.

3.4 Conclusions

This work investigated a Cu-K/Al_2O_3 catalyst with the aim of clarifying the principal reaction routes active in the CO_2 capture and its selective reduction to CO. The results indicate that the catalytically active phase for capture, first generated during activation in H_2 at 450 °C, may consist of highly dispersed KOH species. *Operando* sampling of gaseous concentration and temperature inside the catalyst bed revealed that, when the catalyst is exposed to CO_2 atmosphere, an exothermic reaction takes place progressively along the bed until saturation of the active site, accompanying a release of water. In addition, spatiotemporal *operando* DRIFTS confirmed that CO_2 is fixated on the catalyst surface in the form of bidentate carbonates species. During the CO_2 capture, the presence of metallic Cu and reactive hydrogen stored in the catalyst stimulates a CO_2 hydrogenation path to CO as side reaction. This side reaction takes place after completion of the active CO_2 capture period. By substituting CO_2 with CO in the feed, we demonstrated that CO can be also effectively captured by the catalyst material. However, this capture step does not involve the formation of water.

Switching the reactant feed to H_2, the regeneration of the catalyst and the selective release of CO take place. Combination of the spatiotemporal *operando* methodologies revealed that surface carbonates are rapidly decomposed, selectively generating CO and restoring the active phase for CO_2 capture. No water is released during the fast removal of surface carbonates, in agreement with a K_2CO_3 decomposition route and excluding the intervention of extensive copper oxidation in the reaction. After the initial fast release of CO, a tailing CO release is observed. This slow CO formation is caused by the decomposition of the surface formates formed on the potassium-containing species.

Intentionally oxidising the surface by O_2 before CO_2 capture, we proved that CO_2 capture can still take place in presence of CuO with formation of surface carbonates and release of water, reinforcing the hypothesis that the active phase for capture consists of KOH species. However, in the H_2 atmosphere, the excess water generated by CuO reduction leads to carbonates decomposition with release of unconverted CO_2. These insights have practical implications in designing better CCR catalysts and defining feed gas composition and operation conditions.

Appendix B

B1. X-Ray diffraction analysis

Ex-situ X-ray diffraction patterns were acquired to determine the crystal structure of the synthesised catalyst and to verify the outcome of the synthetic procedure.

Figure B1 reports the result obtained for the Cu-K/Al$_2$O$_3$ catalyst (Cu/K/Al$_2$O$_3$, 11/10/79 wt%). In line with previous results obtained for similar materials,[23, 32] the diffraction pattern shows reflexes typical of CuO tenorite phase (PDF 45-0937) and γ-Al$_2$O$_3$ (PDF 48-0367). The absence of strong reflexes of K$_2$CO$_3$, employed as potassium precursor in the synthesis, indicate that potassium is highly dispersed and forming an highly amorphous phase. Small broad reflexes at low angles, compatible with a KAlCO$_3$(OH)$_2$ phase (PDF 21-0979), indicate a strong interaction between the potassium phase and the γ-Al$_2$O$_3$ support. Such phase results from reaction of potassium carbonate with surface γ-Al$_2$O$_3$ and water absorbed on the surface during the synthesis.[47] However, this phase is crystalline at room temperature and, due to the small particle size, it is suspected to become amorphous at T = 200 °C and finally decomposing to form a K$_2$CO$_3$ phase.[48]
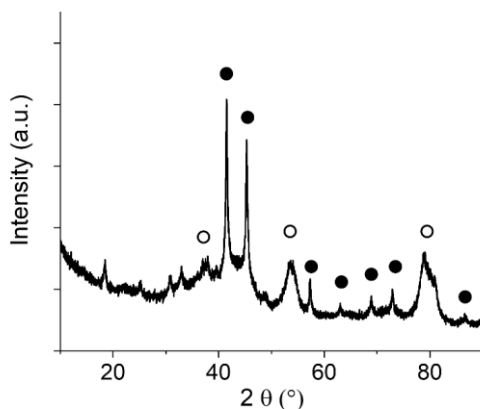

Figure B1: X-ray diffractogram of as-synthetised K-promoted Cu/Al$_2$O$_3$ (K 10 wt%, Cu 11 wt%) catalyst obtained at room temperature. Reflexes from γ-Al$_2$O$_3$ (○) and CuO tenorite (●)

B2. BET Surface Area

The surface area of the Cu-K/Al$_2$O$_3$ was estimated by BET analysis of the fresh sample, obtaining a value of 135 m^2 g^{-1}. The surface area is considerably lower than for the unpromoted Cu/Al$_2$O$_3$ sample (Cu 12.2 wt%), for which a value of 191 m^2 g^{-1} was found. The corresponding N$_2$ adsorption-desorption isotherms obtained for the two samples are reported in Figure B2. Indeed, the impregnation of the potassium phase on highly porous material is expected to provoke pore blocking and the decrease in the catalyst surface area.[49, 50]
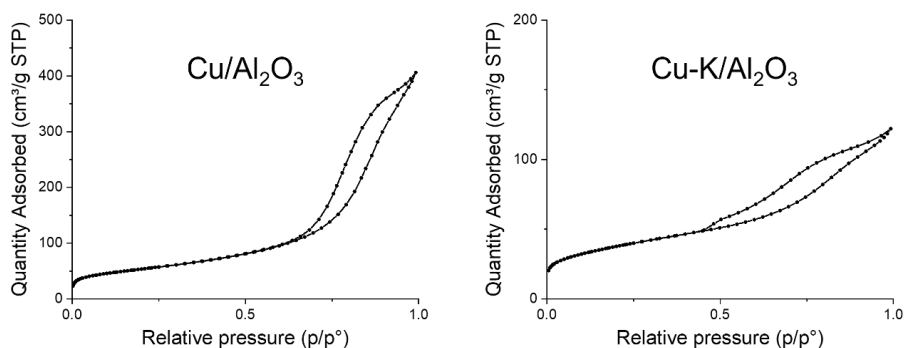
Figure B2: N$_2$ adsorption-desorption isotherms for unpromoted (left) and K-promoted (right) Cu/Al$_2$O$_3$ catalysts.

B3. Thermogravimetric analysis

Figure B3 reports the results obtained from thermogravimetric analysis performed on the K$_2$CO$_3$ precursor, the unpromoted Cu/Al$_2$O$_3$ catalyst (Cu 12.2 wt%) and the promoted Cu-K/Al$_2$O$_3$ catalyst (11 wt% Cu, 10 wt% K). The analysis was performed by keeping the samples under H$_2$ flow (100 mL min^{-1} 5 vol% in Ar) in order to evaluate the weight loss induced by the reduction of the samples.

After 10 minutes flushing at room temperature, the samples were heated up at at a rate of 10°C min^{-1} up to 800 °C. For the pure K$_2$CO$_3$, after a significative weight loss around 100°C related to evaporation of water adsorbed from air exposure, no weight changes are noticed until very high temperature (> 700 °C). In the Al$_2$O$_3$-supported catalysts, a weight loss from water removal from the support is associated with the contribute of CuO reduction which starts at temperatures above 250 °C.
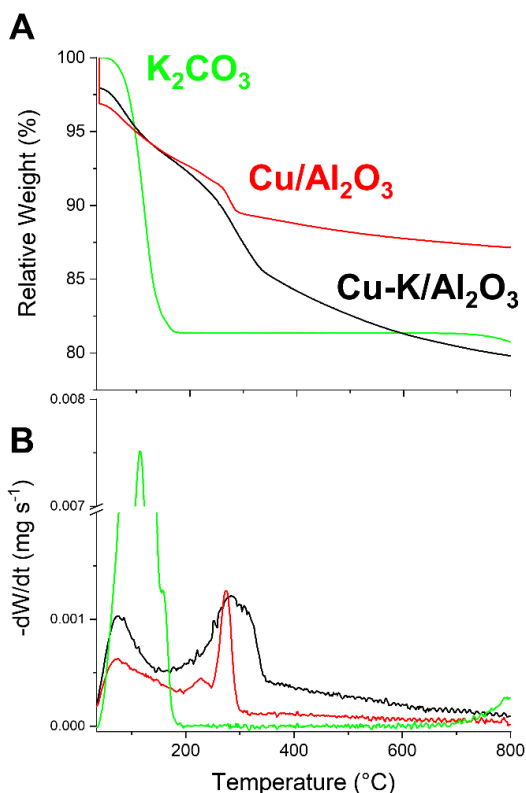
Figure B3: Thermogravimetric analysis of K_2CO_3 precursor, Cu/Al_2O_3 and $Cu-K/Al_2O_3$ catalysts under H_2 stream (5 vol% in Ar, 100 mL min^{-1}). Sample is kept 10 min at room temperature then heated up at 10 °C min^{-1} rate until 800°C. A) Relative weight change over temperature and B) derivative of weight loss with respect to time over temperature.

In Figure B2-B, the derivative of the weight change with respect to time (dW/dT) is plotted against the sample temperature. For the unpromoted Cu/Al_2O_3 catalyst, the peak of weight loss derivative at 275 °C represents a maximum in the reduction rate ascribable to the CuO reduction process. In the $Cu-K/Al_2O_3$ catalyst, the presence of potassium broadens the CuO reduction peak and shifts it to higher temperatures. This phenomenon, frequently reported in literature,[51, 52] is an effect of the intimate interaction between the potassium and copper phases. After the peak referred to CuO reduction, a continuous weight loss takes place in the temperature range 350 – 800 °C, which is ascribable to the decomposition of the K_2CO_3 – derived phase on the catalyst. For the pure K_2CO_3 sample, the decomposition in H_2 starts at temperature higher than 700 °C. However, in the complete catalyst, the high dispersion of potassium on γ-Al_2O_3 and the presence of metallic Cu, activating H_2, favour the decomposition of carbonates at substantially lower temperatures compared to the bulk K_2CO_3 sample.[53, 54]

B4. Spatial sampling of temperature and concentration

Figure B4 reports the complete profile of CO_2, CO and temperature measured by spatial sampling at different position in the catalytic bed. The CCR experiment was performed at 350 °C, employing 0.25 g of Cu-K/Al_2O_3 catalyst.
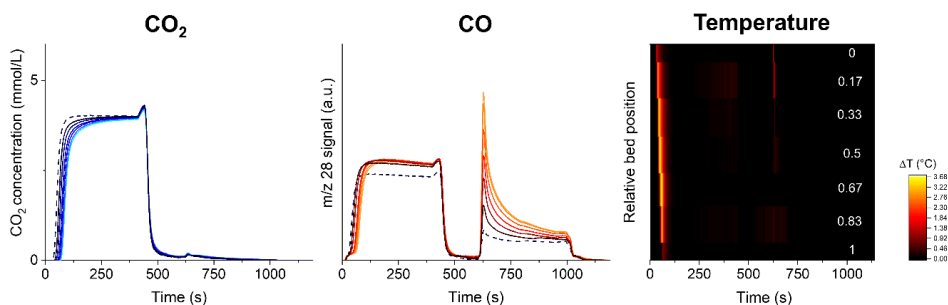

Figure B4: Spatiotemporal profile of CO_2 (left), CO (middle), and temperature (right) along the catalyst bed during CCR at 350 °C. Position 0 and 1 correspond to quartz wool at the beginning and at the end of the catalyst bed, respectively. All the positions are expressed in relative position. Profiles of different position are depicted with a colour scale from inlet of the bed (darker profile, relative position 0) towards the end of the catalytic bed (lighter profile, relative position 1).

The CO_2 concentration is evaluated by calibration of the signal at mass to charge ratio m/z = 44 of the mass spectrometer. Fragmentation of the CO_2 gives signal at m/z = 28, interfering with the detection of the CO. Due to the unsteady-state nature of the pulsed experiment, it was not possible to quantify the amount of CO released in the capture phase (0 – 420 s). In contrast, the limited evolution of CO_2 in H_2 atmosphere (595 – 1015 s) permitted to use the m/z = 28 signal for quantification of the CO produced in the reduction phase, as reported in the main text.

The complete temperature profile at different position of the bed (from inlet position 0 to outlet position 1) confirms that temperature gradients are confined in the early stages of the CO_2 pulse (0 - 420 s), where the exothermic CO_2 capture takes place.

B5. *Operando* DRIFTS

Figure B5 reports the result of *operando* DRIFT spectroscopy in the ν(CH) stretching region during CCR operation at 350 °C. During the CO_2 stream (0 – 420 s), the absence of bands in the ν(CH) stretching region excludes the intervention of formate species as stable intermediates derived from CO_2 capture. After switching the feed to H_2 (595 – 1015 s), bands centered at 2670 and 2760 cm^{-1} rise with a delay compatible with the slow release of CO detected at the outlet (see main text Figure 3.4). Such bands are assignable to formate species on potassium,[40, 41] which would be involved in a slow hydrogenation reaction provoking the release of CO and H_2O observed at the outlet. Despite the low signal to noise ratio, the bands appear more intense toward the end of the bed, indicating that some gradient in the distribution of the surface species can be generated due to the packed bed configuration.

Figure B6 reports the result of *operando* DRIFT spectroscopic study in the ν(CH) stretching region for the CCR experiment in which the CO_2 stream is substituted with a CO stream (0.5 vol% in He). The results are obtained on the same catalytic bed of Figure B4, at the same position of the results reported in Figure B4-C. As can be noticed, very similar surface species dynamic is observed, with the rise of bands centered at 2670 and 2760 cm^{-1} in the H_2 atmosphere, associated to the tailing in the CO released by the catalyst (see main text Figure 3.5).
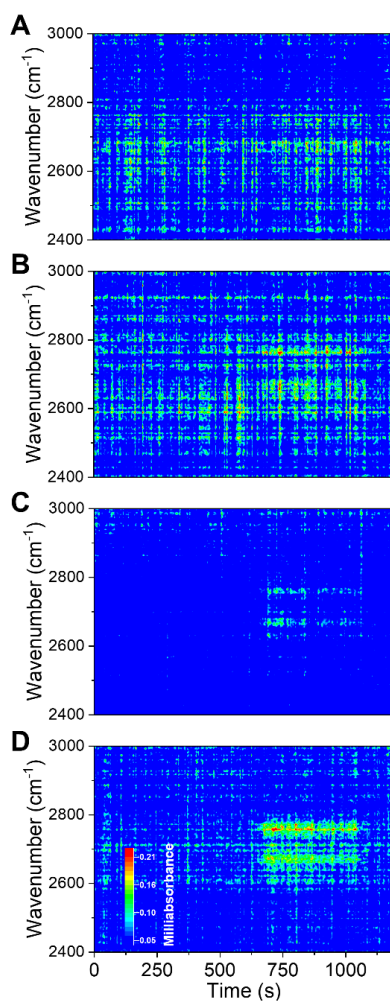

Figure B5: Spatiotemporal profile of CO_2 (left), CO (middle), and temperature (right) along the catalyst bed during CCR at 350 °C. Position 0 and 1 correspond to quartz wool at the beginning and at the end of the catalyst bed, respectively. All the positions are expressed in relative position. Profiles of different position are depicted with a colour scale from inlet of the bed (darker profile, relative position 0) towards the end of the catalytic bed (lighter profile, relative position 1).
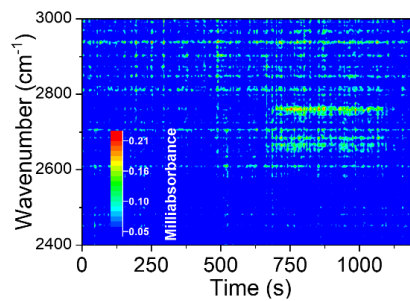
Figure B6: Dynamic evolution of surface species in the ν(CH) stretching region from operando DRIFT spectroscopy during CCR at 350 °C with substitution of CO_2 with CO at the inlet.

References

1. M. Peters, B. Köhler, W. Kuckshinrichs, W. Leitner, P. Markewitz and T. E. Müller, *ChemSusChem*, 2011, **4**, 1216-1240.
2. C. J. Quarton and S. Samsatli, *Appl. Energy*, 2020, **257**, 113936.
3. M. Aresta, A. Dibenedetto and A. Angelini, *Chem. Rev.*, 2014, **114**, 1709-1742.
4. A. Otto, T. Grube, S. Schiebahn and D. Stolten, *Energy Environ. Sci.*, 2015, **8**, 3283-3297.
5. M. Bui, C. S. Adjiman, A. Bardow, E. J. Anthony, A. Boston, S. Brown, P. S. Fennell, S. Fuss, A. Galindo, L. A. Hackett, J. P. Hallett, H. J. Herzog, G. Jackson, J. Kemper, S. Krevor, G. C. Maitland, M. Matuszewski, I. S. Metcalfe, C. Petit, G. Puxty, J. Reimer, D. M. Reiner, E. S. Rubin, S. A. Scott, N. Shah, B. Smit, J. P. M. Trusler, P. Webley, J. Wilcox and N. Mac Dowell, *Energy Environ. Sci.*, 2018, **11**, 1062-1176.
6. M. Ramdin, T. W. de Loos and T. J. H. Vlugt, *Ind. Eng. Chem. Res.*, 2012, **51**, 8149-8177.
7. W. Gao, S. Liang, R. Wang, Q. Jiang, Y. Zhang, Q. Zheng, B. Xie, C. Y. Toe, X. Zhu, J. Wang, L. Huang, Y. Gao, Z. Wang, C. Jo, Q. Wang, L. Wang, Y. Liu, B. Louis, J. Scott, A.-C. Roger, R. Amal, H. He and S.-E. Park, *Chem. Soc. Rev.*, 2020, **49**, 8584-8686.
8. S.-i. Nakao, K. Yogo, K. Goto, T. Kai and H. Yamada, *Advanced CO2 capture technologies: absorption, adsorption, and membrane separation methods*, Springer, 2019.
9. P. Markewitz, W. Kuckshinrichs, W. Leitner, J. Linssen, P. Zapp, R. Bongartz, A. Schreiber and T. E. Müller, *Energy Environ. Sci.*, 2012, **5**, 7281-7305.
10. J. Wang, L. Huang, R. Yang, Z. Zhang, J. Wu, Y. Gao, Q. Wang, D. O'Hare and Z. Zhong, *Energy Environ. Sci.*, 2014, **7**, 3478-3518.
11. Y. Belmabkhout, V. Guillerm and M. Eddaoudi, *Chem. Eng. J.*, 2016, **296**, 386-397.
12. L.-C. Lin, A. H. Berger, R. L. Martin, J. Kim, J. A. Swisher, K. Jariwala, C. H. Rycroft, A. S. Bhown, M. W. Deem, M. Haranczyk and B. Smit, *Nat. Mater.*, 2012, **11**, 633-641.
13. J. Blamey, E. J. Anthony, J. Wang and P. S. Fennell, *Prog. Energy Combust. Sci.*, 2010, **36**, 260-279.
14. IEA, *CCUS in Clean Energy Transitions,*, International Energy Agency, Paris, 2020.
15. M. Mikkelsen, M. Jørgensen and F. C. Krebs, *Energy Environ. Sci.*, 2010, **3**, 43-81.
16. H.-J. Ho, A. Iizuka and E. Shibata, *Ind. Eng. Chem. Res.*, 2019, **58**, 8941-8954.
17. M. S. Duyar, M. A. A. Treviño and R. J. Farrauto, *Appl. Catal., B*, 2015, **168-169**, 370-376.
18. L. F. Bobadilla, J. M. Riesco-García, G. Penelás-Pérez and A. Urakawa, *J. CO2 Util.*, 2016, **14**, 106-111.
19. S. Cimino, F. Boccia and L. Lisi, *J. CO2 Util.*, 2020, **37**, 195-203.
20. E. L. G. Oliveira, C. A. Grande and A. E. Rodrigues, *Sep. Purif. Technol.*, 2008, **62**, 137-147.
21. A. Porta, R. Matarrese, C. G. Visconti, L. Castoldi and L. Lietti, *Ind. Eng. Chem. Res.*, 2021, **60**, 6706-6718.
22. H. Sun, J. Wang, J. Zhao, B. Shen, J. Shi, J. Huang and C. Wu, *Appl. Catal., B*, 2019, **244**, 63-75.
23. T. Hyakutake, W. van Beek and A. Urakawa, *J. Mater. Chem. A*, 2016, **4**, 6878-6885.
24. L. Proaño, E. Tello, M. A. Arellano-Trevino, S. Wang, R. J. Farrauto and M. Cobo, *Appl. Surf. Sci.*, 2019, **479**, 25-30.

25. A. Porta, C. G. Visconti, L. Castoldi, R. Matarrese, C. Jeong-Potter, R. Farrauto and L. Lietti, *Appl. Catal., B*, 2021, **283**, 119654.
26. A. Bermejo-López, B. Pereda-Ayo, J. A. González-Marcos and J. R. González-Velasco, *J. CO2 Util.*, 2019, **34**, 576-587.
27. L. Hu and A. Urakawa, *J. CO2 Util.*, 2018, **25**, 323-329.
28. F. Kosaka, Y. Liu, S.-Y. Chen, T. Mochizuki, H. Takagi, A. Urakawa and K. Kuramoto, *ACS Sustain. Chem. Eng.*, 2021, **9**, 3452-3463.
29. A. Urakawa, N. Maeda and A. Baiker, *Angew. Chem. Int. Ed. Engl.*, 2008, **47**, 9256-9259.
30. Y. A. Daza and J. N. Kuhn, *RSC Adv.*, 2016, **6**, 49675-49691.
31. Y. Duan, D. R. Luebke, H. W. Pennline, B. Li, M. J. Janik and J. W. Halley, *J. Phys. Chem. C*, 2012, **116**, 14461-14470.
32. A. Bansode, B. Tidona, P. R. von Rohr and A. Urakawa, *Catal. Sci. Technol.*, 2013, **3**, 767-778.
33. K. Kobl, L. Angelo, Y. Zimmermann, S. Sall, K. Parkhomenko and A.-C. Roger, *Comptes Rendus Chimie*, 2015, **18**, 302-314.
34. P. Baraldi, *Spectrochim. Acta*, 1979, **35**, 1003-1007.
35. M. Hartman, K. Svoboda, B. Čech, M. Pohořelý and M. Šyc, *Ind. Eng. Chem. Res.*, 2019, **58**, 2868-2881.
36. K. Coenen, F. Gallucci, B. Mezari, E. Hensen and M. van Sint Annaland, *J. CO2 Util.*, 2018, **24**, 228-239.
37. N. D. Parkyns, *J. Chem. Soc. A*, 1969, DOI: 10.1039/J19690000410, 410-417.
38. G. Busca and V. Lorenzelli, *Mater. Chem.*, 1982, **7**, 89-126.
39. G. J. Millar, C. H. Rochester and K. C. Waugh, *J. Chem. Soc., Faraday Trans.*, 1992, **88**, 1477-1488.
40. G. J. Millar, C. H. Rochester and K. C. Waugh, *J. Catal.*, 1995, **155**, 52-58.
41. I. L. C. Freriks, P. C. de Jong-Versloot, A. G. T. G. Kortbeek and J. P. van den Berg, *J. Chem. Soc., Chem. Commun.*, 1986, DOI: 10.1039/C39860000253, 253-255.
42. C.-S. Chen, W.-H. Cheng and S.-S. Lin, *Catal. Lett.*, 2000, **68**, 45-48.
43. M. C. Boswell and J. V. Dickson, *J. Am. Chem. Soc.*, 1918, **40**, 1779-1786.
44. S. Kumar, V. Drozd and S. K. Saxena, *Catalysts*, 2012, **2**.
45. C. Di Blasi, A. Galgano and C. Branca, *Energy Fuels*, 2009, **23**, 1045-1054.
46. T. Otowa, R. Tanibata and M. Itoh, *Gas Sep. Purif.*, 1993, **7**, 241-245.
47. J. V. Veselovskaya, V. S. Derevschikov, T. Y. Kardash, O. A. Stonkus, T. A. Trubitsina and A. G. Okunev, *Int. J. Greenh. Gas Control*, 2013, **17**, 332-340.
48. S. C. Lee and J. C. Kim, *Catal. Surv. Asia*, 2007, **11**, 171-185.
49. J. M. Lee, Y. J. Min, K. B. Lee, S. G. Jeon, J. G. Na and H. J. Ryu, *Langmuir*, 2010, **26**, 18788-18797.
50. X. Yang, X. Su, X. Chen, H. Duan, B. Liang, Q. Liu, X. Liu, Y. Ren, Y. Huang and T. Zhang, *Appl. Catal., B*, 2017, **216**, 95-105.
51. G. Jacobs, T. K. Das, Y. Zhang, J. Li, G. Racoillet and B. H. Davis, *Appl. Catal. A: Gen.*, 2002, **233**, 263-281.
52. D. Courcot, C. Pruvost, E. A. Zhilinskaya and A. Aboukaïs, *Kinet. Catal.*, 2004, **45**, 580-588.
53. S. Walspurger, L. Boels, P. D. Cobden, G. D. Elzinga, W. G. Haije and R. W. van den Brink, *ChemSusChem*, 2008, **1**, 643-650.
54. M. Kantschewa, E. V. Albano, G. Etrtl and H. Knözinger, *Appl. Catal.*, 1983, **8**, 71-84.

Chapter 4

Specific selectivity of simple oxides towards CH_4 activation

Abstract

Often employed as support material due to their stability at high temperatures, simple metal oxides exhibit noticeable catalytic activity in methane conversion reactions. Highly oxidative conditions needed for the conversion of methane often pose strong limitations on the product selectivity, favouring the formation of undesired total oxidation products (CO_2, H_2O) and the development of temperature and concentration gradients in the catalytic bed. The harsh reaction conditions, combined with the complexity of catalyst formulations, complicate the understanding and identification of the role played by the catalyst for the activation of CH_4 and its selective conversion to more valuable products (CO, H_2, olefins). In this sense, transient studies of the direct interaction of CH_4 with relatively simple catalytic systems can give unbiased information on the specific role and selectivity of the catalytically active sites. In this work, we perform an unsteady-state catalytic investigation of CH_4 activation on diverse monometallic oxides including rare-earth (La_2O_3, Nd_2O_3, Y_2O_3), alkali-earth (MgO) and reducible (TiO_2) metal oxides, by alternation of CH_4 and O_2 feeds to the catalytic bed at high temperatures. The transient analysis of the product stream composition reveals peculiar selectivity for the different oxides, demonstrating the direct involvement of lattice oxygen species in the activation of the CH_4 molecule. Rare-earth metal oxides show high initial activity towards partial oxidation products (CO, H_2), while MgO possess unique selectivity towards coupling products (C_2H_6 and C_2H_4) with remarkable activity in dehydrogenation reactions. A continuous supply of lattice oxygen species for the selective oxidation of CH_4 to CO is provided by TiO_2, which can effectively prevent accumulation of C deposits. The results explicitly indicate the roles played by the metal oxide materials and can serve as a basis for rational design of catalytic systems and reaction conditions for the selective conversion of CH_4.

4.1 Introduction

As main component of the natural gas, methane represents a valid opportunity to substitute oil in the short-term as energy and chemical feedstock. Apart from energy generation, a major process for CH_4 utilisation is its reforming with H_2O to produce a valuable mixture of H_2 and CO (syngas). Syngas is an effective intermediate for additional chemical processes as methanol synthesis or hydrocarbons production via Fischer-Tropsch synthesis.[1] Developing direct conversion of methane into value-added products would substantially reduce the energy and economic requirements of the indirect routes, however several challenges are associated with its selective conversion to chemicals.[2-4] From a thermodynamical point of view, methane is the most stable hydrocarbon in a wide temperature range (up to 1030 °C).[5] The high stability of the molecule, and the deriving challenges to its activation, are related to the high symmetry of its tetrahedral structure, with equally spaced H atoms surrounding the C in the centre. In a radical reaction path, a first C-H bond breaking is necessary to activate the molecule and generate an active methyl radical. The high energy of the bond (439 kJ mol^{-1}) makes the activation highly endothermic, requiring extreme conditions to drive the reaction.[4] In homogeneous gas-phase reactions, C-C and C-H bond cleavage is observed at only very high temperatures (1200 °C).[5] The use of strong oxidants can alter the overall reaction exothermic, often at the cost of low selectivity, by the formation of undesired oxidation products as H_2O and CO_2. In order to lower the energetic requirements for methane activation and, at the same time, controlling the selectivity of the products, the employment of a catalyst is fundamental. Strong interaction with a catalyst surface reduces the symmetry of the molecule and facilitates the activation of the molecule by electron transfer.[6]

With the promise of single-process conversion of CH_4 to olefins, and simultaneously cutting the process chain and its costs, the first oxidative coupling of methane (OCM) works were received with enthusiasm in the early 1980s.[7] Several works reported screening of simple oxides focusing the attention on their performance in OCM.[8-10] Alkaline-earth and rare-earth metal oxides exhibited often the best results, and there is a general agreement about the positive influence of the oxide basicity on the formation of coupling products.[9, 11] However, a limit on the maximum C_2 products yield was found (< 30 %),[12] which inhibited the commercialisation of the process so far. Several attempts have been made to determine the mechanism in OCM reaction conditions.[13, 14] It is generally agreed that the reaction starts with activation of CH_4 molecule by abstraction of a H atom from the catalyst and formation of a methyl radical ($CH_3^•$). Methyl radicals will then couple to form C_2H_6, and subsequent dehydrogenation yields C_2H_4. Alternatively, C_2 species can be further oxidised to undesired CO and CO_2.[4, 15] However, in terms of identifying the catalytically active sites and establishing the nature of the C_2 selectivity on simple metal oxide catalysts, the information retrieved at those conditions are often inconclusive.

Understanding the mechanism of methane activation in highly oxidative conditions is complicated by the presence of highly reactive oxidant species (molecular oxygen, peroxide ion, superoxide radical, hydroxyl radicals)[16, 17] that can react further leading to nonselective exothermic pathways, often associated with temperature and concentration gradients in the catalytic bed. On the contrary, unsteady-state operation permits to intrinsically separate the reducing and oxidising feeds, inhibiting the development of highly exothermic and

unselective total oxidation pathways and highlighting the specific role and selectivity of the catalytically active sites.[18-20]

In this chapter, the specific selectivity of a series of simple metal oxide catalysts towards CH_4 activation is investigated. The studied catalysts include rare-earth metal oxides (La_2O_3, Nd_2O_3, Y_2O_3), which are known for their activity in methane oxidation reactions,[21] MgO, a model catalytic system for OCM investigation,[4] and TiO_2, commonly employed as support material for its redox properties.[22, 23] Unsteady-state operation experiments are performed by alternatively passing CH_4 and O_2 feeds to the catalytic bed at temperatures up to 900 °C, to evaluate the peculiar activity towards CH_4 activation and regenerating the active oxygen of the catalyst in the subsequent O_2 pulse. The transient evolution of products in the reactant pulses is analysed by means of fast FTIR spectroscopy (5 s temporal resolution) and mass spectrometry. The results reveal distinct selectivity of the different metal oxides at 900 °C towards partial oxidation of CH_4 to CO and H_2 and towards coupling of CH_4 to C_2H_6 and C_2H_4. Information on the extent of coke deposition was derived by analysis of the CO_x product evolved in the O_2 pulse. Insights into the participation of active lattice oxygen species are obtained and verified by thermogravimetric analysis of the catalysts.

4.2 Experimental

4.2.1 Catalyst materials

La_2O_3 (99.99%, Alfa Aesar), MgO ($\geq$ 99% trace metal basis, Sigma Aldrich), Nd_2O_3 (Nanografi, nanoparticles 25-40 nm, 99.95%), TiO_2 (Alfa Aesar, rutile, 99.5%) and Y_2O_3 (Aldrich, 99.99%) were used as simple metal oxide catalysts without any further treatment.

4.2.2 Thermogravimetric analysis

Thermogravimetric analysis (TGA) of the samples was carried out in a METTLER TOLEDO SF/1100 thermogravimetric analyser by heating at a rate of 10 °C min^{-1} up to 1000 °C. The simple metal oxides samples were analysed under 100 mL min^{-1} flow of pure N_2 or diluted H_2 (5 vol% in N_2). Physical mixtures of 10 wt% carbon black (Vulcan XC 72R) on simple metal oxides were prepared for TGA analysis in N_2.

4.2.3 Catalytic testing

200 mg of catalyst material (pelletised, crushed and sieved to the size range of 300-400 μm) was loaded into a quartz tube reactor (6 mm OD, 4 mm ID), fixed between quartz wool layers. The temperature of the bed was monitored by a thermocouple inserted in the quartz wool in contact with the end of the catalytic bed. Gas feeds were controlled by a system of mass flow controllers (Bronkhorst) and two 4-way switching valves (VICI Valco) controlled by software. Each cycle of operation consists of alternation of diluted O_2 (25 vol% in He, 0-150 s), He flush (150-300 s) and CH_4 (300-450 s) feeds (50 mL min^{-1}) to the reactor. The data presented were obtained from the average of at least 3 cycles of operation, after a stable and reproducible composition of the effluent was achieved. The composition of the reactor effluent was analysed by combination of FTIR spectroscopy (ALPHA, Bruker) and mass spectrometry (Omnistar Pfeiffer Vacuum). The quantification of C_2H_6, calibration of the MS signal (m/z 30) was performed at reaction conditions by gas chromatography injections taken at different moments of the CH_4 pulse performed across multiple stable cycles of operations.

4.3   Results and discussion

4.3.1   Thermogravimetric analysis

Thermogravimetric analysis is employed to characterise the catalyst samples and reveal the presence of active lattice oxygen species that can take part in the selective activation of methane. Three different experiments are conducted for each metal oxide catalyst. On the metal oxide samples, TGA is performed heating up the catalyst in N_2 atmosphere (blue lines) or in a reducing H_2 atmosphere (red lines) up to 1000 °C (Figure 4.1). In H_2 atmosphere, a prominent decrease in the catalyst weight would be observed in correspondence by the abstraction of O species from the catalyst, at the temperatures at which the surface and bulk reduction processes are activated. In addition, a physical mixture of metal oxide and C black is prepared and tested for TGA in N_2 (black lines). In those condition, an additional weight loss is introduced, corresponding to the gasification of the solid carbon operated by oxygen species which are thermally activated during the TGA heating ramp. By comparing the profiles obtained, the presence of active oxygen species in the catalysts lattice and their activity for both the oxidation of H_2 and gasification of C can be tested.

La₂O₃

Figure 4.1A shows the TGA profiles obtained for La_2O_3. All the three TGA experiments showed similar weight loss profiles, with the highest extent observed for the N_2-TGA on the pure La_2O_3. In the case of C/La_2O_3, the smaller weight loss can be explained by the additional presence of solid C in the sample (10 wt% C on metal oxide), the significantly lower weight loss observed during the H_2-TGA indicates a possible instrumental limitation. To take into account the buoyancy effect, TGA of empty crucibles are conducted prior to each experiment and subtracted from the corresponding TGA profiles. An expansion of the La_2O_3 powders in the crucibles during TGA is detected, possibly connected with the cause of the discrepancy in the N_2 and H_2-TGA profiles. For the purpose of this investigation, however, qualitative information can be retrieved by the analysis of the first derivative of the weight loss profiles with respect to temperature, shown in Figure 4.1B. The derivative profiles express the rate of weight change and their minima characterise the temperatures at which weight loss processes reach their maximum rate. It is clear that two main weight loss phenomenon takes place on the La_2O_3 sample with a peak around 300 and 500 °C. At around 600 °C, an additional peak is detected in the derivative profiles, with the H_2-TGA profile showing a slightly lower temperatures. Exposure of La_2O_3 to air at ambient conditions is known to promote bulk hydration and carbonation.[24] The important weight loss experienced by the La_2O_3 samples is independent from the gaseous atmosphere or the presence of C, suggesting that the phenomenon is associated with thermal decomposition of hydroxide and carbonate phases. Similar TGA profiles for La_2O_3 have been reported, although diverging decomposition temperatures are obtained on different samples.[25, 26] In general, low temperature decomposition involves dehydration followed, at higher temperatures, by the decomposition of $LaO(OH)$ and $La_2O_2CO_3$ species to La_2O_3.

It has to be noted that decomposition of the La hydroxide and carbonate may hide the presence of additional less-significant weight loss processes. In particular, evolution of water and CO_2 could provoke the gasification of the C black employed for the N_2-TGA of the C/La_2O_3 sample. However, at temperatures higher than 600 °C, the TGA profile of C/La_2O_3 sample

experiences a slow weight loss until it reaches a sudden acceleration approaching 1000 °C, as evidenced in the corresponding derivative profile. The singularity of this weight loss phenomenon, which is not observed in the C-free samples, reveals the presence of a limited amount of oxygen species which are able to selectively activate C gasification.

MgO

Similar to the La_2O_3 case, three relevant weight loss processes occur for MgO (Figure 4.1C) with derivative peaks at around 100, 300 and 580 °C (Figure 4.1D). Evaporation of adsorbed water can take place during the first one, while the followings are explained by the decomposition of Mg hydroxides and carbonates which were formed upon prolonged air exposure at ambient conditions.[27] Contrarily to the La_2O_3 case, none of the three TGA profiles of MgO reaches a plateau. A small but continuous weight decrease is observed under all conditions at temperatures above 600 °C with a slight acceleration in the C/MgO sample at temperatures approaching 1000 °C, indicating contribution of C gasification processes. After the last intense weight loss at temperatures higher than ca. 900 °C, an additional weight loss process starts to be activated exclusively for the sample containing C black, indicating the presence of oxygen species active in C gasification at this temperature.

Nd_2O_3

The TGA profiles of Nd_2O_3 (Figure 4.1E-F) show two pronounced weight loss steps with derivative peaks between 550 and 750 °C, assignable to the progressive dehydration and decarbonation of hydroxide and carbonate phases.[28] Also for this system, the derivative of weight change of the C/Nd_2O_3 sample shows a slight acceleration at temperatures close to 1000 °C, indicating activation of C gasification.

Y_2O_3, TiO_2

The TGA profiles of Y_2O_3 (Figure 4.1G) and TiO_2 (Figure 4.1H) do not show any relevant weight loss at low temperatures, implying that the samples are present in the form of pure oxides. The limited extent of weight change, below 1% of the initial weight, resulted in noisy flat derivatives (not shown here). However, the absence of bulk phase decomposition processes increases the sensitivity of the technique regarding the discrimination of specific interaction of oxygen species with H_2 and solid C. At high temperatures, the profiles of H_2-TGA and N_2-TGA on the C-containing sample start to diverge from the N_2-TGA profile. The trends reveal an additional weight loss in presence of gaseous hydrogen or solid carbon, which identifies the participation of lattice oxygen in the oxidation of hydrogen and gasification of C, respectively.

In the case of Y_2O_3, the divergence of the TGA profiles start at around 650 °C and the weight loss is accentuated in the presence of H_2 atmosphere. This result demonstrates the presence of reducible oxygen species, seemingly confined at the surface of the catalyst, which can react with H_2 at and, at higher temperatures, activate C gasification. Temperature programmed reduction studies confirmed the limited reducibility of Y_2O_3 support and the possibility of removing oxygen species from the lattice in highly reducing conditions.[29]

Least weight loss (<0.05 wt%) was detected on the TiO_2 sample (Figure 4.1H). Although TiO_2 is known for the excellent redox properties in photocatalytic application, it usually displays low reducibility in temperature programmed reduction experiments. Rutile TiO_2, in particular,

shows very limited reducibility in H_2 and at higher temperatures compared to anatase TiO_2.[30] At temperatures higher than 800 °C, an increased weight loss is noticed for the H_2-TGA profile and the N_2-TGA on the C-containing sample. Above this temperature, oxygen species of the TiO_2 lattice are active for the oxidation of H_2 and C. Contrarily to the case of Y_2O_3, the higher weight loss observed in presence of C black seems to suggest a preferential activity of oxygen species in TiO_2 towards the oxidation of solid C species.
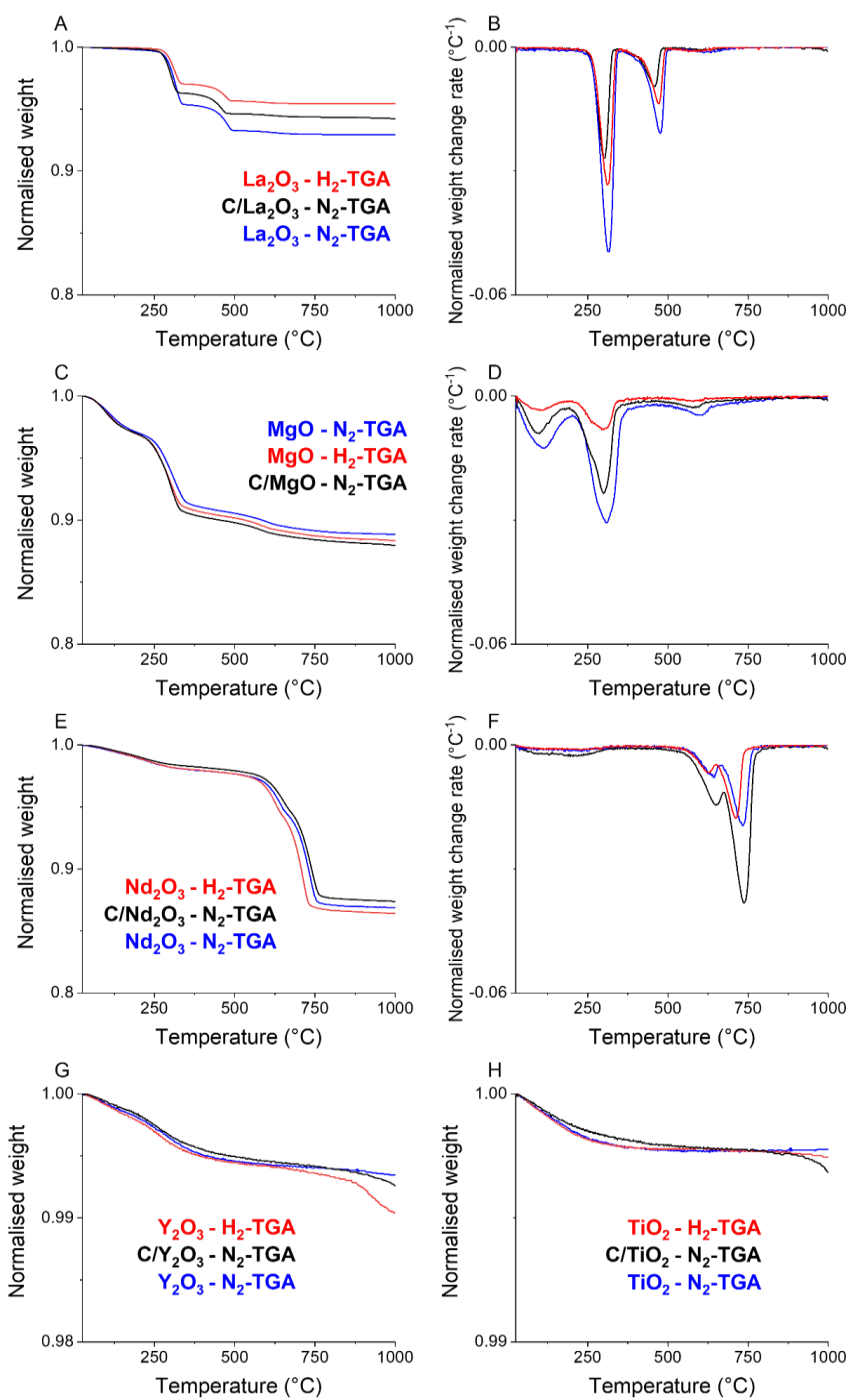
Figure 4.1: Thermogravimetric analysis (TGA) of the different metal oxide catalysts (30-1000 °C, 10 °C min^{-1} heating rate) performed under N_2 (blue profiles), H_2 (red profiles). TGA profiles of C/metal oxide (C black 10 wt%) physical mixtures under N_2 (black profiles). Derivative of weight change is included for samples undergoing prominent weight losses. La_2O_3 (A-B), MgO (C-D), Nd_2O_3 (E-F), Y_2O_3 (G) and TiO_2 (H).

99

4.3.2 Catalytic activity – Transient analysis of products

The catalytic activity tests were performed by exposing the catalyst bed to the alternation of gas feed atmospheres at different temperatures (300, 500, 700, 900 °C). The results presented are average of multiple stable cycles of operation, each cycle consisting of an oxidant pulse (0-150 s, 25 vol% O_2 in He), an inert flushing pulse (150-300 s, pure He) and a reducing pulse (300-450s, pure CH_4), fed at constant flow rate (50 mL min^{-1}).

To observe the evolution of reaction products deriving from CH_4 activation, a minimum temperature of 700 °C was needed, indicating that the lattice oxygen is activated only above this temperature. Figure 4.2 reports the profile of CO evolved in the CH_4 pulse (300-450 s) at 700 °C. Interestingly, CO was the only C product detected for the different simple metal oxide catalysts at 700 °C. To enhance the activation of CH_4 in the non-oxidative conditions of the catalytic test and clearly observe an evolution of C-containing products, higher temperatures are necessary (*vide infra*).
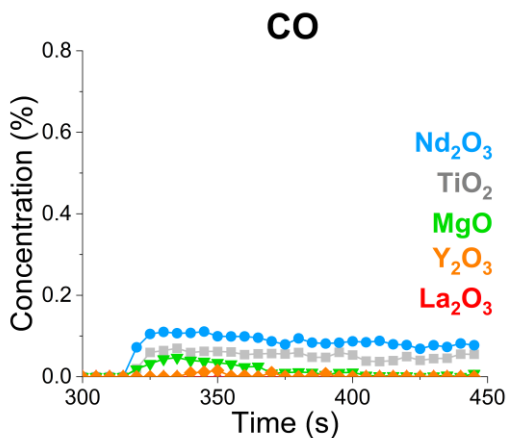
Figure 4.2: Transient analysis of CO (FTIR) evolved during the CH_4 pulse (300-450 s) of the catalytic tests performed at 700 °C. The results are averaged over multiple stable cycles of operation. Results for Y_2O_3 (orange ◊), La_2O_3 (red ▲), Nd_2O_3 (blue ●), MgO (green ▼), TiO_2 (grey ■).

Above 700 °C, C_2 products are increasingly observed at higher temperatures. Figure 4.3 reports the evolution of products for the different metal oxide catalysts during the CH_4 pulse (300-450 s) in the catalytic tests conducted at 900 °C. No CO_2 was produced in the reducing pulse for all the catalyst, excluding the promotion of total oxidation of CH_4 by the lattice oxygen of the simple metal oxides in absence of gaseous O_2.
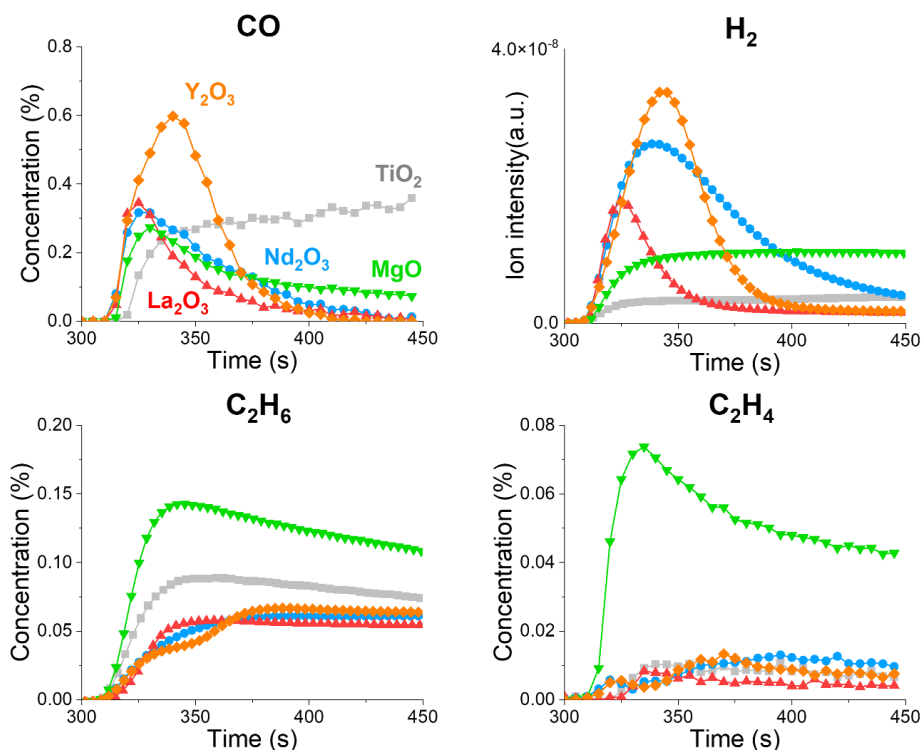

Figure 4.3: Transient analysis of products (FTIR + MS) during the CH_4 pulse (300-450 s) of the catalytic tests performed at 900 °C. The results are averaged over multiple stable cycles of operation. Results for Y_2O_3 (orange ◊), La_2O_3 (red ▲), Nd_2O_3 (blue ●), MgO (green ▼), TiO_2 (grey ■).

Y_2O_3, La_2O_3

Y_2O_3 and La_2O_3 display similar catalytic behaviour, producing CO with high selectivity. The characteristic peak shape of the CO profile demonstrate the presence of reactive oxygen species in the oxides lattice, which undergo fast reaction with CH_4 at 900 °C until complete depletion. Those O species are restored in the subsequent O_2 pulse together with the activity of the catalyst. The signal of H_2 evolved in the CH_4 pulse well reproduces the CO trend, indicating that a mechanism of partial oxidation of methane is involved (Reaction 4.1, where $O_{(l)}$ stands for lattice oxygen).

$$CH_4 + O_{(l)} = 2H_2 + CO \tag{4.1}$$

101

This oxygen is depleted in the interval of the reductive pulse of CH_4, indicating that it is possibly involving coordinatively unsaturated surface sites or oxygen species confined in the surface layers of the lattice. Ekstrom et al.[31] conducted isotopic studies of partial oxidation on rare earth metal oxides at 700 °C. They found that the isotopic composition of reaction products instantaneously followed the change in the isotopic composition of the methane feed. Presence of a small number of highly active sites was postulated, which are responsible for the instantaneous conversion of CH_4. The hypothesis was confirmed by the observation of rapid oxygen exchange between gas-phase and lattice oxygen atoms at 700 °C, which led to identify the active sites as oxygen atom in a vacancy site at the catalyst surface. In agreement with these results, Dixit et al.[32] observed H_2 and CO as main products during temperature programmed reduction of La_2O_3 in CH_4. By addition of gaseous oxygen, they noticed the increase in CH_4 conversion, with decrease in H_2 production and rise of CO_2 as main product. Those results reinforce the evidence of an intrinsic selectivity of the lattice oxygen in Y_2O_3 and La_2O_3 towards CH_4 partial oxidation (Reaction 4.1). Such selective behaviour is lost in presence of gaseous oxygen, where the extremely oxidative conditions promote exothermic reaction leading to total oxidation of CH_4 to CO_2 and H_2O.

Higher activity exhibited by Y_2O_3, corresponding to a larger amount of available oxygen species for CH_4 partial oxidation, can be explained as follows. A first naive consideration is on basis of the experimental conditions of the catalytic test, for which a fixed amount of catalyst was loaded into the reactor (0.2 g). Being Y a lighter element than La, a larger amount of oxygen is available in the Y_2O_3 catalytic bed. However, interpretation of the trends of the moles of CO produced with respect to the total oxygen available in the catalyst (Appendix C, Figure C1) is not obvious. Another factor is the lower surface oxygen vacancy formation energy of Y_2O_3 compared to La_2O_3, which can explain the higher availability of reactive oxygen species and the better performance in CH_4 partial oxidation.[33] This consideration is in agreement with the results obtained from TGA, which showed enhanced reducibility of Y_2O_3 (Figure 4.1G) in presence of H_2 and C at high temperatures. Poor activity towards C_2 product is observed for both Y_2O_3 and La_2O_3, with C_2H_6 detected as the main C_2 product. Although La_2O_3 is an active catalytic system for OCM, its activity towards C_2 species in the non-oxidative conditions of the CH_4 pulse is minimal. In the case of Y_2O_3, both profiles of C_2H_6 and C_2H_4 experience a rise after 350 s. This time fits well with the moment of the drop of the CO and H_2 signals and seems related to the depletion of the active oxygen species in the catalyst. The scarcity of highly active oxygen species can prevent the oxidation of the CH_x intermediates to CO, favour non-oxidative processes for the decomposition of methane and resulting in an increased formation of C_2 species.

Nd_2O_3

When tested for catalytic oxidation of CH_4, rare-earth metal oxides generally exhibit similar products distribution and selectivity trends.[10] Evidence of isotopic exchange of oxygen on rare-earth metal oxides revealed a high lattice oxygen mobility. The active participation of lattice oxygen in oxidation reactions was confirmed by the similar activation energy found for both $^{18}O_2$-exchange and H_2 oxidation processes.[21] Thus, it is not surprising to find high partial oxidation activity also for Nd_2O_3 (Figure 4.3), in agreement with the behaviour exhibited by Y_2O_3 and La_2O_3. However, differences are noticed in particular regarding the formation of H_2, whose signal is surprisingly high for Nd_2O_3 and decays more slowly than the

corresponding CO signal. Although the literature on the activity of pure Nd_2O_3 is scarce, addition of Nd as catalytic promoter for the conversion of CH_4 is reported to enhance the activity towards partial oxidation products and especially H_2 selectivity at high temperatures.[34, 35] Moreover, among a series of lanthanides, Campbell et al.[9] reported the highest activity in the oxidative coupling of methane on Nd_2O_3.

In absence of gaseous oxygen, a reaction route responsible for the surplus of H_2 can be identified in the catalytic decomposition of CH_4 (Reaction 4.2), which proceeds through progressive dehydrogenation steps (Reaction 4.2a) until solid carbon ($C_{(ads)}$) is deposited on the surface of the catalyst and H_2 released from the surface (Reaction 4.2b). The analysis of the C deposition extent can be performed on the basis of the CO_x species evolved during the O_2 pulse of the unsteady-state experiment (Figure 4.4) The formation of CO_x species over Nd_2O_3 is substantially higher than over Y_2O_3 and La_2O_3, indicating the presence of carbon deposits in larger amount. Thus, Nd_2O_3 proves to be highly active for the decomposition of CH_4. From these results, it can be concluded that partial oxidation products are readily formed at the beginning of the CH_4 pulse, when there is abundance of surface oxygen species. After depletion of this active oxygen, methane decomposition is more prominently activated on Nd_2O_3 and proceeds by stepwise dehydrogenation steps leading to accumulation of solid C and release of H_2.
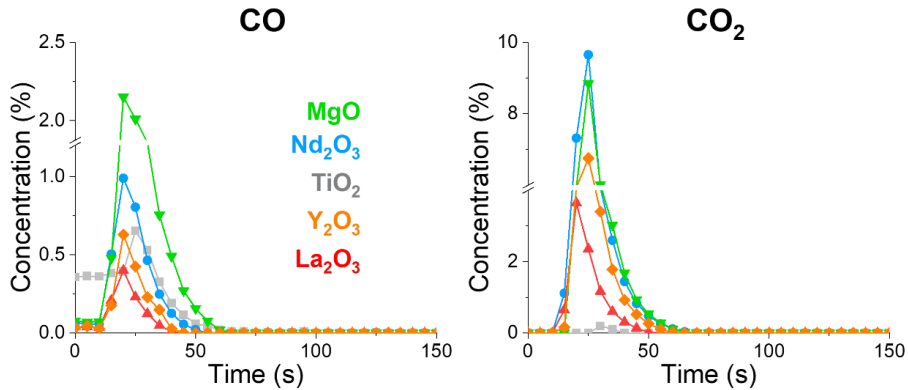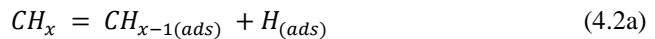
$$CH_4 = C_{(ads)} + 2H_2 \qquad (4.2)$$

$$CH_x = CH_{x-1(ads)} + H_{(ads)} \qquad (4.2a)$$

$$2H_{(ads)} = H_2 \qquad (4.2b)$$

Figure 4.4: Transient analysis of CO_x products (FTIR) evolved during the O_2 pulse (300-450 s, 25 vol% O_2 in He) of the catalytic tests performed at 900 °C. The results are averaged over multiple stable cycles of operation. Results for Y_2O_3 (orange ◊), La_2O_3 (red ▲), Nd_2O_3 (blue ●), MgO (green ▼), TiO_2 (grey ■).

The enhanced activity in CH_4 decomposition is not directly associated with general increase in the production of C_2 species. The profiles of C_2 species (Figure 4.3) visibly indicates that the ratio of C_2H_4 to C_2H_6 is higher in the case of Nd_2O_3, confirming an intrinsic catalytic activity towards dehydrogenation reactions. However, such predisposition towards dehydrogenation reactions ultimately favours the formation of solid C and H_2 products rather than intermediates C_2 species.

MgO shows a unique intrinsic activity for the selective conversion of CH_4 to C_2 species (Figure 4.3). The CO release rises slowly at the beginning of the CH_4 pulse, without a pronounced peaked profile. The signal then progressively decays, maintaining an almost constant release of CO until the end of the pulse. $^{18}O/^{16}O$ isotopic transient kinetics experiments on MgO revealed oxygen exchange with the first surface layers of the catalyst activated at around 600 °C.[36] Contrary to what have been shown for rare earth metal oxides, the profiles of CO and H_2 do not match for MgO. The H_2 signal do not present any peak and, after the initial rise, maintains a constant value for all the duration of the CH_4 pulse.

Lattice O species are available, as confirmed by the continuous release of CO. Those oxygen species are not depleted in an initial fast process to partially oxidise CH_4, but supplied at a constant rate for the formation of CO. Considering the constant value of H_2, it appears that MgO can continuously activate the decomposition of the CH_4 molecules to C and H_2. While the H_2 is instantaneously released, the C deposits are oxidised to CO by the lattice oxygen at a slower rate. Such mechanism would favour the accumulation of carbon deposits.

The slow rate of methane partial oxidation promoted by the lattice oxygen can also explain the high selectivity observed for C_2 products. Instead of rapidly converting CH_4 to CO by means of active surface oxygen species, $CH_3^{\bullet}$ radicals are formed on MgO and allowed to couple in the gas phase to form C_2H_6 (Reaction 4.3) without undergoing further oxidation steps.[37, 38] The activity towards the dehydrogenation of methane is reflected also in high activity towards selective dehydrogenation of C_2H_6 to C_2H_4 (Reaction 4,4), which is detected in exceptionally high concentration among the metal oxides screened.

$$2CH_4 = C_2H_6 + H_2 \qquad\qquad (4.3)$$

$$C_2H_6 = C_2H_4 + H_2 \qquad\qquad (4.4)$$

The dehydrogenation of C_2H_6 to C_2H_4 also contributes to an additional release of H_2, which explains its constant signal detected along the whole CH_4 pulse.

The highly redox properties of TiO_2 (rutile) are clearly observed in the catalytic CH_4 activation (Figure 4.3). At 900 °C, a constant formation of CO is detected, which proceeds until the end of the CH_4 pulse. Towards the end of the reductive CH_4 pulse, the concentration of CO is extremely high compared to the other mixed oxides, indicating a constant supply of oxygen species from the catalyst lattice. Although the profiles of CO and H_2 match in shape, the release of H_2 is substantially lower when compared with the other simple oxides investigated. This observation suggests poor activity towards dehydrogenation reactions for TiO_2. It is possible that H atoms abstracted from the CH_4 molecules adsorb in the form of surface hydroxyl groups and promote the release of water.[39] Due to the presence of a water condenser at the reactor outlet, no information about the amount of water release could be derived from the present data. On the other hand, a significant release of C_2H_6 is noticed, which is found higher than the Y_2O_3, La_2O_3 and Nd_2O_3 cases. Very low selectivity towards C_2H_4 further indicates a poor activity towards dehydrogenation reactions. The remarkably low release of CO_x species during the O_2 pulse (Figure 4.4) indicates that accumulation of carbon deposits on TiO_2 is prevented by the high availability of reactive lattice oxygen species.

Due to the long-lasting release of active lattice oxygen observed for MgO and TiO_2, a similar catalytic experiment with an extended CH_4 pulse duration (900 s) was performed. The results (Figure C2) confirm the selectivity trends observed with the short reducing pulse, with preferential generation of CO on TiO_2 and C_2 products on MgO. In terms of coking, the exposure of the catalysts to a longer CH_4 pulse is expected to favour the accumulation of carbon deposits on the catalyst surface, resulting in a larger release of CO_x products in the oxidant pulse. The CO and CO_2 profiles obtained during the O_2 pulse (Figure 4.5) shows that the amounts of CO and CO_2 released on the MgO catalyst drastically increase compared to the short CH_4 pulse case (Figure 4.4). The ability of MgO to activate CH_4 and promote dehydrogenation, together with the absence of reactive oxygen species for its oxidation to CO, favour the accumulation of carbon deposits, and the release of C_2 species. For the TiO_2 catalyst, in contrast, the release of CO_x species in the O_2 pulse is limited. The high availability of lattice oxygen for the oxidation of CH_4 prevented the accumulation of solid carbon by directly promoting its selective oxidation to CO. Interestingly, the residual carbon deposits removed in O_2 are selectively gasified to CO, with very limited CO_2 formation. This peculiar selectivity of TiO_2 towards the oxidation of solid carbon deposits makes it an interesting support for the design of catalysts for selective CH_4 conversion.
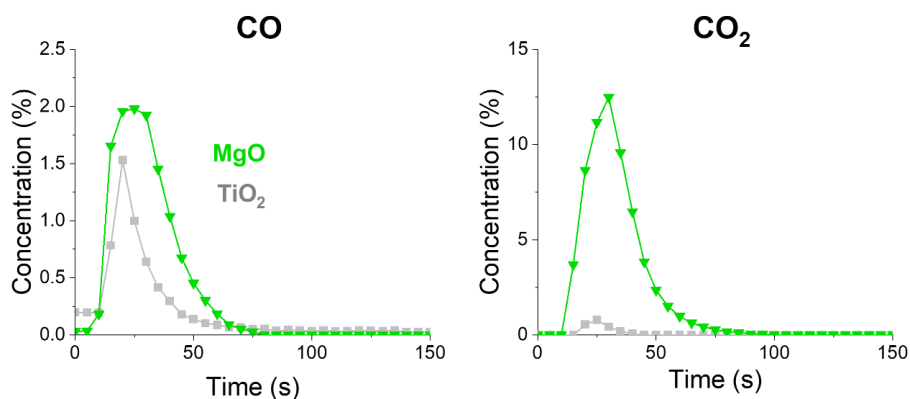

Figure 4.5: Transient analysis of CO_x products (FTIR) evolved during the O_2 pulse (0-150 s, 25 vol% O_2 in He) of the catalytic tests performed at 900 °C with extended CH_4 pulse duration (900 s). The results are averaged over multiple stable cycles of operation. Results for MgO (green ▼) and TiO_2 (grey ■).

4.4   Conclusions

The intrinsic activity of simple metal oxides towards CH_4 activation has been revealed by unsteady-state operation catalysis and transient analysis of the product stream. In unsteady-state conditions, i.e. CH_4 and O_2 alternatively fed to the reactor, temperatures higher than 700 °C are necessary to activate the conversion of CH_4. A specific reactive lattice oxygen species activates partial oxidation of CH_4 to CO and H_2 with high selectivity in rare-earth metal oxides (Y_2O_3, La_2O_3 and Nd_2O_3) at 900 °C. Among those, Nd_2O_3 also exhibits high activity in decomposition of CH_4 that contributes to additional H_2 formation and enhanced formation of solid C. The best performances in terms of C_2 coupling products is found for the MgO catalyst, on which less pronounced reactivity of lattice oxygen species allows continuous C_2H_6 and C_2H_4 formation without undergoing further oxidation steps. On the other hand, the high redox properties of TiO_2 intervene in the CH_4 oxidation by selectively oxidising it to CO. A constant supply of active O from TiO_2 lattice is detected, which make the system an ideal support to prevent accumulation of carbon deposits in CH_4 conversion reactions. Thermogravimetric analysis of the simple metal oxides in H_2 and in presence of solid C confirmed the direct participation of lattice oxygen in the oxidation reactions at high temperature.

The results here presented clarify the specific role of simple metal oxides in the activation of CH_4, which appears closely related to the nature of their surface oxygen species. It is suggested that, in oxidative conditions, the development of highly exothermic reaction routes, promoted by the presence of molecular oxygen, can enhance the rate of unselective total oxidation paths and ultimately control the distribution of products.

Appendix C

C1. Catalytic activity – Amount of O employed in CO formation

As an indication of the amount of lattice O directly involved in the conversion of CH_4, Figure C1 reports the amount of CO produced during the CH_4 pulse (300 – 450 s) of the catalytic tests conducted at 900 °C with respect to the estimated amount of O present in the metal oxide catalysts. For the estimation of the total amount of oxygen in the metal oxides, the weight of the catalyst loaded in the reactor is corrected for the experienced weight loss at 900 °C during TGA in N_2.
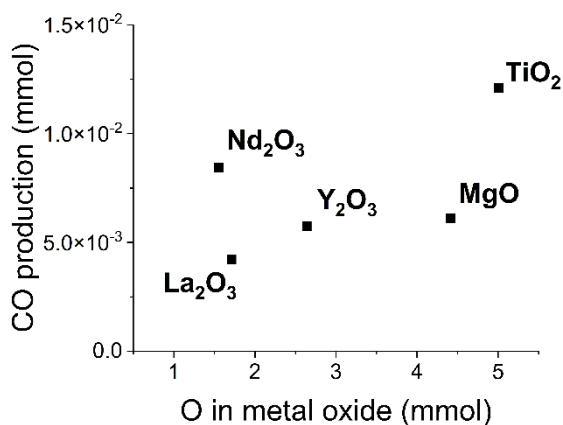
Figure C1: Amount of CO produced in the CH_4 pulse at 900 °C versus total amount of O available in the catalytic bed.

C2. Catalytic activity – Extended CH_4 pulse test

For the extended CH_4 pulse experiment, duration of the reducing pulse was 900 s instead of 150 s. The test permits to evaluate the long-term evolution of the products, in particular focusing on the C_2 evolution in MgO and CO in TiO_2. After an initial peak, the C_2 signals in MgO experience a decay until reaching a steady-state formation, indicating a limited but continuous ability to activate CH_4 and the subsequent coupling of the methyl radicals.

TiO_2, instead, maintained a high rate of CO formation by participation of lattice oxygen. The redox property of the material are confirmed in terms of high lattice oxygen mobility. Considering the low surface area of the TiO_2 rutile material (3.8 m^2 g^{-1}), it is expected that bulk oxygen is involved in the selective conversion of CH_4 to CO.
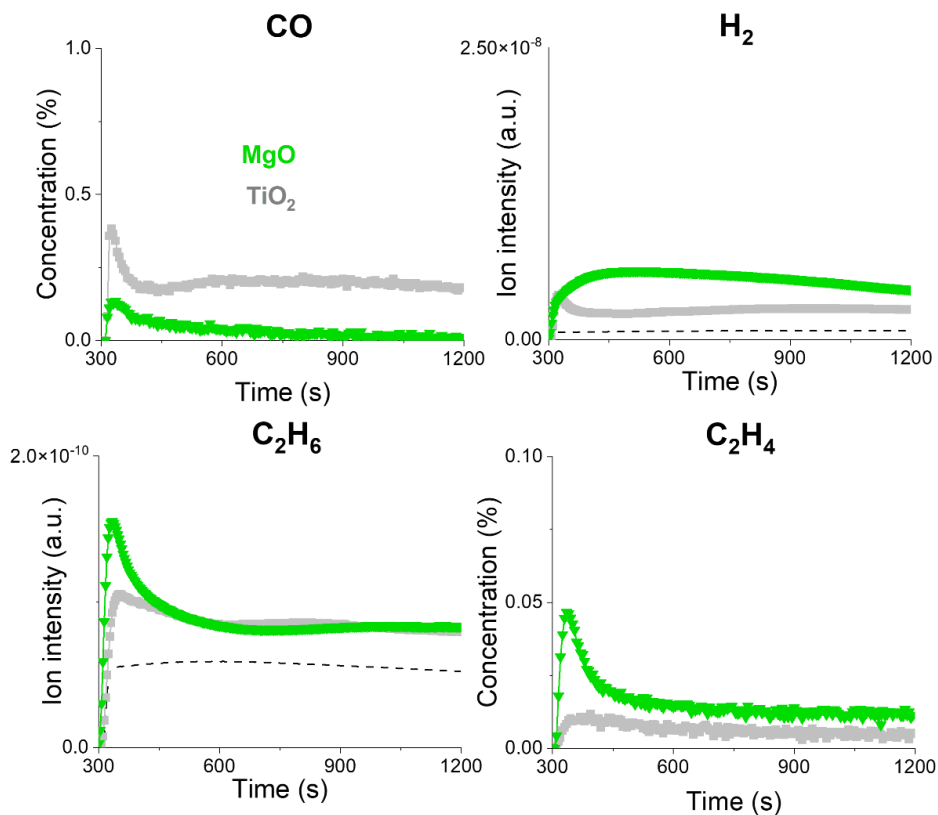
Figure C2: Transient analysis of products (FTIR + MS) evolved during the CH_4 pulse (300-1200 s) of the catalytic tests performed at 900 °C with extended CH_4 pulse duration (900 s). The results are averaged over multiple stable cycles of operation. Results for MgO (green ▼) and TiO_2 (grey ■). Dotted line represent MS signal of H_2 and C_2H_6 during a blank experiment at room temperature.

References

1. K. Aasberg-Petersen, I. Dybkjær, C. V. Ovesen, N. C. Schjødt, J. Sehested and S. G. Thomsen, *J. Nat. Gas Sci. Eng.*, 2011, **3**, 423-459.
2. C. Hammond, S. Conrad and I. Hermans, *ChemSusChem*, 2012, **5**, 1668-1686.
3. A. A. Latimer, A. Kakekhani, A. R. Kulkarni and J. K. Nørskov, *ACS Catal.*, 2018, **8**, 6894-6907.
4. P. Schwach, X. Pan and X. Bao, *Chem. Rev.*, 2017, **117**, 8497-8520.
5. T. V. Choudhary, E. Aksoylu and D. Wayne Goodman, *Catal. Rev.*, 2003, **45**, 151-203.
6. C. Li, G. Li and Q. Xin, *J. Phys. Chem.*, 1994, **98**, 1933-1938.
7. G. E. Keller and M. M. Bhasin, *J. Catal.*, 1982, **73**, 9-19.
8. J. M. DeBoy and R. F. Hicks, *Ind. Eng. Chem. Res.*, 1988, **27**, 1577-1582.
9. K. D. Campbell, H. Zhang and J. H. Lunsford, *J. Phys. Chem.*, 1988, **92**, 750-753.
10. K. Otsuka, K. Jinno and A. Morikawa, *J. Catal.*, 1986, **100**, 353-359.
11. S. Sato, R. Takahashi, M. Kobune and H. Gotoh, *Appl. Catal. A: Gen.*, 2009, **356**, 57-63.
12. Y. S. Su, J. Y. Ying and W. H. Green, *J. Catal.*, 2003, **218**, 321-333.
13. S. B. F. Da Ros, T.; Schwaab, M.; Castro de Jesus, N.J.; Pinto, J.C. , *Processes* 2021, **9**, 2196.
14. A. Obradović, J. W. Thybaut and G. B. Marin, *Chem. Eng. Technol.*, 2016, **39**, 1996-2010.
15. L. Hu, D. Pinto and A. Urakawa, in *Catalysis: Volume 32*, The Royal Society of Chemistry, 2020, vol. 32, pp. 203-223.
16. K. Takanabe and E. Iglesia, *Angew. Chem. Int. Ed.*, 2008, **47**, 7689-7693.
17. X. Zhou, Y. Pang, Z. Liu, E. I. Vovk, A. P. van Bavel, S. Li and Y. Yang, *J. Energ. Chem.*, 2021, **60**, 649-659.
18. X. P. Dai, R. J. Li, C. C. Yu and Z. P. Hao, *J. Phys. Chem. B*, 2006, **110**, 22525-22531.
19. K. P. Peil, J. G. Goodwin and G. Marcelin, *J. Catal.*, 1991, **132**, 556-559.
20. R. Spinicci, *Catal. Today*, 1989, **4**, 311-322.
21. M. P. Rosynek, *Catal. Rev.*, 1977, **16**, 111-154.
22. M. Kotobuki, R. Leppelt, D. A. Hansgen, D. Widmann and R. J. Behm, *J. Catal.*, 2009, **264**, 67-76.
23. Q. G. Yan, W. Z. Weng, H. L. Wan, H. Toghiani, R. K. Toghiani and C. U. Pittman, *Appl. Catal. A: Gen.*, 2003, **239**, 43-58.
24. P. Fleming, R. A. Farrell, J. D. Holmes and M. A. Morris, *J. Am. Ceram. Soc.*, 2010, **93**, 1187-1194.
25. S. Bernal, F. J. Botana, R. García and J. M. Rodríguez-Izquierdo, *Thermochim. Acta*, 1983, **66**, 139-145.
26. Q. Mu and Y. Wang, *J. Alloys Compd.*, 2011, **509**, 396-401.
27. N. Khan, D. Dollimore, K. Alexander and F. W. Wilburn, *Thermochim. Acta*, 2001, **367-368**, 321-333.
28. L. De Almeida, S. Grandjean, N. Vigier and F. Patisson, *Eur. J. Inorg. Chem.*, 2012, **2012**, 4986-4999.
29. H. Liu, H. Wu and D. He, *Fuel Process. Technol.*, 2014, **119**, 81-86.
30. J. Li, G. Lu, G. Wu, D. Mao, Y. Guo, Y. Wang and Y. Guo, *Catal. Sci. Technol.*, 2014, **4**, 1268-1275.
31. A. Ekstrom and J. A. Lapszewicz, *J. Phys. Chem.*, 1989, **93**, 5230-5237.
32. M. Dixit, A. Menon, R. Baruah, A. Bhargav and S. Sharma, *React. Kinet. Mech. Catal.* . 2015, **115**, 611-624.

33. Y. Hinuma, T. Toyao, T. Kamachi, Z. Maeno, S. Takakusagi, S. Furukawa, I. Takigawa and K.-i. Shimizu, *J. Phys. Chem. C*, 2018, **122**, 29435-29444.
34. M. Caballero, G. Del Angel, A. Bonilla-Sánchez, I. Rangel-Vázquez, A. Arrieta, A. Vázquez-Zavala, L. Huerta and M. Salgado, *Int. J. Hydrogen Energy*, 2016, **41**, 23247-23259.
35. V. R. Choudhary, K. C. Mondal, A. S. Mamman and U. A. Joshi, *Catal. Lett.*, 2005, **100**, 271.
36. K. P. Peil, G. Marcelin and J. G. Goodwin, in *Methane Conversion by Oxidative Processes: Fundamental and Engineering Aspects*, ed. E. E. Wolf, Springer Netherlands, Dordrecht, 1992, pp. 138-167.
37. D. J. Driscoll, W. Martir, J. X. Wang and J. H. Lunsford, *J. Am. Chem. Soc.*, 1985, **107**, 58-63.
38. R. Schlögl, *Angew. Chem. Int. Ed.*, 2015, **54**, 3465-3520.
39. S. Huygh, A. Bogaerts, K. M. Bal and E. C. Neyts, *J. Phys. Chem. C*, 2018, **122**, 9389-9396.

Chapter 5

Operando investigation of simple oxide catalysts in oxidative coupling of CH$_4$

Abstract

Simple oxides as MgO and La$_2$O$_3$ possess the ability to selectively activate methane. However, during the oxidative coupling of methane (OCM), the selective conversion to ethane and following dehydrogenation to ethylene are threatened by the thermodynamically favoured partial and total oxidation reactions to form CO and CO$_2$, respectively. With the aid of spatially-resolved *operando* analysis of temperature and gas concentration along the catalytic bed, we demonstrated the relevance of highly exothermic reaction paths developed in the gas phase during OCM conditions at the front of the catalytic bed, largely determining the total C$_2$ yield obtained on those systems. At the light of the new insights provided by the analysis of the temperature and concentration gradients along the bed, we could redefine the positive effect of promoters (Li, Sr). By modifying the catalyst surface, they promote the suppression of the unselective exothermic oxidation paths, limiting the formation of hotspots and driving the reaction towards the desired C$_2$ products.

5.1   Introduction

Methane, the most abundant hydrocarbon in natural gas, is a potential candidate for the transition towards an oil-free chemical industry. Despite its abundancy, natural gas reservoirs are mainly located in remote regions and its price is still subjected to multiple variables, including transportation infrastructures and political stability of the producing countries. In addition, until today natural gas utilisation is limited to the generation of heat or power source, contributing to the global greenhouse gases emissions.[1] However, alternative and more valuable uses of methane are possible since it possesses a high potential to substitute oil in the synthesis of fundamental chemical commodities. Already industrially exploited are the production of hydrogen and syngas ($CO + H_2$) by steam reforming. Syngas can be further processed to target valuable products as methanol or higher hydrocarbons through Fischer-Tropsch process,[2] however such multi-step processes require higher investments to cope with the cost of transportation and storage.

Substantially more appealing is the opportunity to directly convert methane to added-value chemicals. Proposed strategies envisage one-step conversion of methane to ethylene, methanol, formaldehyde, halogenated compounds and aromatics.[3-6] Among those, the direct conversion of methane to ethylene is one of the most promising solutions, considering the market size of ethylene and its easier transportability in liquid form. Also, this strategy would help speed up the decarbonisation of the chemical industry. In fact, naphtha and ethane steam cracking are currently the main strategies for ethylene production. Energy demands of those processes are very high resulting in high CO_2 emissions, up to 1.8-2 ton CO_2/ ton ethylene when naphtha is employed as source.[7] The main challenge for the selective activation of methane is represented by the high-energy required to break the first C-H bond of the molecule (439 kJ mol^{-1})[8] and initiate the reaction. The use of oxidants can help overcome the thermodynamic limitations linked to the activation of the stable C-H bonds in the methane molecule, as in the case of oxidative coupling of methane (OCM).[9]

The reaction (Reaction 1) has attracted a lot of scientific interest with the promise of one-step valorisation of methane to ethylene.[10, 11]

$$2CH_4 + O_2 = C_2H_4 + 2H_2O \qquad \Delta H_{300K} = -281\ kJ\ mol^{-1} \qquad (5.1)$$

It is commonly agreed that the reaction proceeds via formation of methyl radicals, usually requiring high temperatures of operation to be generated (600-800 °C).[4, 12] Such radical species couple in the gas-phase to form ethane, which is finally dehydrogenated to ethylene. The oxidative coupling of methane takes place in a complex reaction network involving multiple interconnected reaction paths activated by the simultaneous presence of radical species and oxygen at high temperature (Scheme 5.1).[13] From a thermodynamic point of view, partial and total oxidation products (CO_x) formation is favoured in those conditions, limiting the total C_2 yield. In principle, heterogeneous catalysts can be utilised to kinetically drive the reaction towards the desired products and limiting the unselective routes. However, the minimum C_2 yield of 25-30%, estimated as a threshold to develop an industrially competitive ethylene production via OCM, has been only rarely approached.[14]
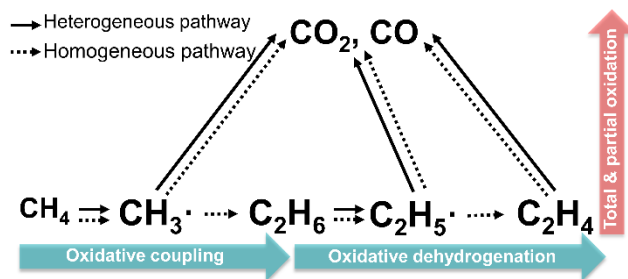
Scheme 5.1: Simplified reaction network under OCM condition

At the same time, complex catalyst formulations are frequently targeted to address higher catalytic performances, increasing the variables influencing the reaction network and mechanisms.[15] As a result, this complexity threatens the fundamental understanding of factors influencing OCM performances. A first step towards understanding the complexity of OCM reaction network is to isolate the role of the catalyst in selectively activating CH_4 conversion. To do so, simple metal oxides represent model systems which conveniently reduce the variables arising from complex catalytic systems. While providing high thermal and structural stability, such materials serve as oxidative templates on which CH_4 can be effectively activated.

Frequently employed in coexistence with promoters to enhance the catalytic properties, MgO and La_2O_3 possess already a remarkable activity towards coupling products in OCM conditions. It is recognised that they contribute to the OCM reaction path, activating the methane molecule on their surface by abstraction of an hydrogen atom and generating a methyl radical.[16, 17] The addition of alkali (Li), alkaline-earth (Sr, Ba) metals as promoters is known to significantly enhance the OCM activity of simple metal oxides in terms of C_2 selectivity.[18, 19] Literature reports on their effect on catalytic activity are abundant.[20, 21] In general, it is agreed to correlate the positive trend of C_2 selectivity with properties as the increased basicity and the increased lattice oxygen diffusivity introduced by the promoters.[22-25]

However, the fundamental role of simple oxides in promoting selective conversion of methane into C_2 products is still under question. In OCM reaction conditions, the nature of the interaction of the metal oxides with CH_4 is masked by the presence of gaseous oxygen and the activation of exothermic reaction paths. Isolating the intrinsic activity of MgO and La_2O_3 towards CH_4 activation, in absence of gaseous oxygen, can help elucidate the catalytic role of those oxides in the OCM conditions.[26]

Great research efforts have been put into the definition of the reactions involved in the catalytic OCM, with the aim of deriving kinetic data and depicting a reaction mechanism. Nonetheless, individuating the fundamental properties governing the selectivity towards C_2 products remains challenging. The accuracy of proposed kinetic models is threatened by the harsh conditions of OCM, which involve a complex chemical environment with a mixture of radical species, strong oxidants and high temperatures of operation.[27, 28] As for similar processes involving CH_4/O_2 mixtures, highly exothermic reactions are activated in an OCM reactor, resulting in the formation of hotspots.[13, 29] This unavoidably leads to temperature and concentration gradients along the reactor bed, complicating the identification of the fundamental catalyst role and the individuation of the active sites that guarantee the selective

conversion of methane.[30, 31] These observations directly question the conventional approaches for catalytic studies, based on the mere interpretation of reactor outlet composition and frequently ignoring the presence of temperature gradients. Instead, considered the influence of reaction temperature to the activation of methane[32] and oxygen[33], it appears necessary to investigate the temperature and concentration profiles along the reactor bed in order to derive realistic insights into the OCM reaction.

In this work, we investigate the catalytic OCM by means of temperature and species concentration data spatially-resolved along the reactor. Simple metal oxides (MgO, La_2O_3) are employed as basic catalytic systems, evaluating their intrinsic activity towards the selective activation of methane and their role played in OCM conditions. The contribution of the catalyst is discussed at the light of the unique information about the temperature and concentration gradients developed in the reactor bed. With the same approach, the catalytic effect of promoters (Li-promoted MgO, Sr-promoted La_2O_3) in OCM reaction is also investigated at the light of the new insights derived from spatially-resolved analysis.

5.2 Experimental

5.2.1 Catalyst preparation

MgO ($\geq$ 99% trace metal basis, Sigma Aldrich) and La_2O_3 (99.99%, Alfa Aesar) were used as simple metal oxide catalysts without any further treatment. The doped catalysts were prepared via a direct solid mixing method. The simple metal oxides and corresponding dopant metal carbonate salts ($SrCO_3$ for La_2O_3 and Li_2CO_3 for MgO) were mixed in an agate mortar with a certain amount deionized water (1 mL water per gram metal oxide). After that, the slurry was dried in the oven at 80 °C for 12 h, then calcined in the furnace at 800 °C for 4 h.

5.2.2 Catalyst characterization

Power X-ray diffraction (PXRD) was performed on D8 Advanced Powder Diffractometer (Bruker), with a germanium monochromator for Cu Kα1 radiation (λ=1.5406 Å), at a scan step of 0.02° per s from 10° to 80°.

5.2.3 Catalytic testing

The reaction setup is illustrated in Scheme D1 (Appendix D1). 200 mg of catalyst material (pelletised, crushed and sieved to the size range of 300-400 μm) was loaded into a quartz tube reactor, fixed between quartz wool layers. La_2O_3 was pretreated in O_2 (50 vol% in He, 50 mL/min) at 700 °C for 30 min before reaction, considering the high tendency of La_2O_3 to form hydroxides upon exposure to moisture in the air (See Figure D1, Appendix D3).[34]

A reactant mixture of CH_4 (40 vol%), O_2 (10 vol%), N_2 (13 vol%) and He (rest, 37 vol%) with a total flow rate of 80 mL/min was introduced into the reactor. The temperature of the catalytic bed was controlled by a Watlow heating control with a thermocouple inserted in the reactor and positioned at the end of the bed. The composition of the exhaust gas was analysed by gas chromatography (GC, Agilent 7890B, equipped with two FID and one TCD) after passing through a small water-condenser cooled by water circulation. For the experiment studying the effect of H_2, 1.5 vol% H_2 was added into the feed and N_2 volume portion was reduced to 11.5 vol%. For the unsteady-state catalytic reaction, alternation of the gaseous mixtures (CH_4, He

and 25 vol% O_2 in He) was implemented by a system of two 4-way switching valves controlled by software. The exhaust gas was analysed by combination of FTIR spectroscopy (Bruker ALPHA) and mass spectrometry (Omnistar Pfeiffer Vacuum).

5.2.4   Spatial analysis and visual inspection

For the temperature and catalyst bed visualization, the reactor furnace cover was modified by opening a ca. 3 cm × 1 cm window and the window was covered with a glass plate to avoid heat loss.. A USB digital microscope (800-1000× magnification) was used to visually observe color changes of the catalyst bed and particles. The infrared camera (Micro-SWIR 320CSX camera, Sensors Unlimited) was used to take IR radiation images that were converted to variations of temperature upon calibration. Details of space resolved gas sampling and temperature measurements are provided in Appendix D

5.3   Results and discussion

5.3.1   Unsteady-state oxidative coupling of CH_4

The intrinsic activity of MgO and La_2O_3 towards CH_4 activation was investigated by an unsteady-state catalytic reaction performed at different temperatures by alternation of O_2 (25 vol% in He) and pure CH_4 pulses separated by a He purge.

As previously observed in Chapter 4, a temperature of 900 °C was necessary to observe C_2 products, while CO and H_2 production was observed already at 700 °C. Figure 5.1 reports the products distribution obtained during exposure of La_2O_3 and MgO to the CH_4 pulse at 900 °C. In absence of gaseous oxygen, the total oxidation of CH_4 to CO_2 was strongly suppressed, as indicated by the absence of CO_2 signal below the detection limit (order of 100 ppm). At the same time, both catalysts were able to supply oxygen species from the lattice for the activation of CH_4. This finding indicates a high selectivity of lattice oxygen as oxidant, in accordance with other transient experiments.[35, 36]

MgO presents an intrinsic ability to activate methane and promote its dehydrogenation reactions, while participation of lattice oxygen species to the partial oxidation of CH_4 to CO takes place at a relatively slow rate compared to rare-earth metal oxides. Constant H_2 production, extensive coking and formation of C_2H_4 are products of dehydrogenation reactions involving CH_4 and C_2H_6.

The ability of MgO to provide lattice oxygen for reactions was already demonstrated by isotopic transient kinetics studies which revealed oxygen exchange from the surface layers of MgO.[37] This limited reducibility, probably circumscribed to the surface of the oxides, is a key property to balance between CH_4 activation and its selective oxidation. The present results shows that MgO possesses a unique intrinsic selectivity towards coupling products (Figure 5.1B). This superiority is often correlated to the high basicity of the alkaline earth metal oxides.[23, 38] In contrast, La_2O_3 manifested high initial activity towards partial oxidation of methane, as indicated by the matching peaks of CO and H_2 produced in the CH_4 pulse (Figure 5.1A). La_2O_3 is known for its high activity in producing gas phase methyl radicals.[39] However, in absence of gaseous oxygen, only limited C-C coupling ability is demonstrated. In rare-earth metal oxides, the prominent selectivity for partial oxidation products may derive from the

reducibility of surface oxygen species, which can actively participate in the conversion of methane.[40] In the case of La_2O_3, the high initial partial oxidation activity is abruptly lost, indicating quick deactivation of the catalytic surface, possibly by carbon deposition, somehow affecting the accessibility of lattice oxygen for the selective oxidation of methane to CO.
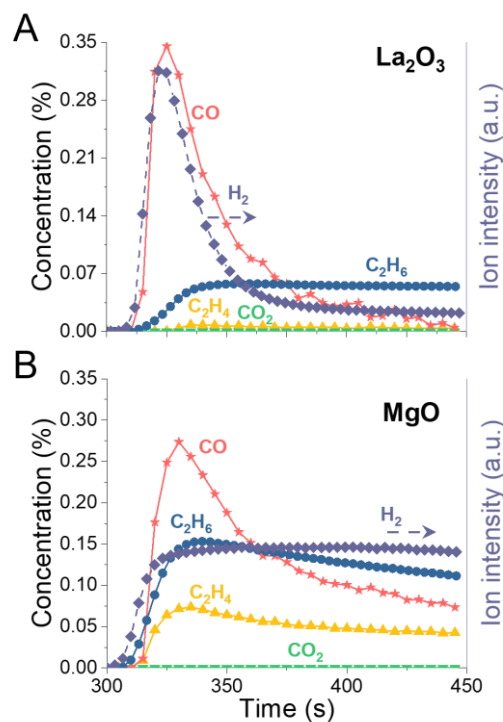

Figure 5.1: Concentrations of C_2H_6, C_2H_4, CO_2 and CO and ion intensity of H_2 (m/z = 2) in CH_4 pulse during OCM under unsteady-state operation on La_2O_3 (A) and MgO (B) at 900 °C. C_2H_4, CO_2 and CO concentration is quantified by IR and C_2H_6 concentration is quantified with mass spectrometry data which are calibrated with a simultaneous gas chromatography analysis. The values are averaged over multiple stable cycles of operation.

To further investigate the different behaviour of the MgO and La_2O_3 catalytic system, transient analysis of products evolved during unsteady-state CH_4 oxidation experiments is reported in Figure 5.2. Besides pure MgO and La_2O_3, two catalytic beds are prepared with a mixture of the simple oxides. In one configuration, a mixed bed containing equal amounts of the two simple oxides is loaded (50 wt% La_2O_3, 50 wt% MgO, physical mixture). In the other configuration, a layer of La_2O_3 is placed in front of a MgO catalytic bed (10 wt% La_2O_3, 90 wt% MgO), preventing mixing of the two oxides.
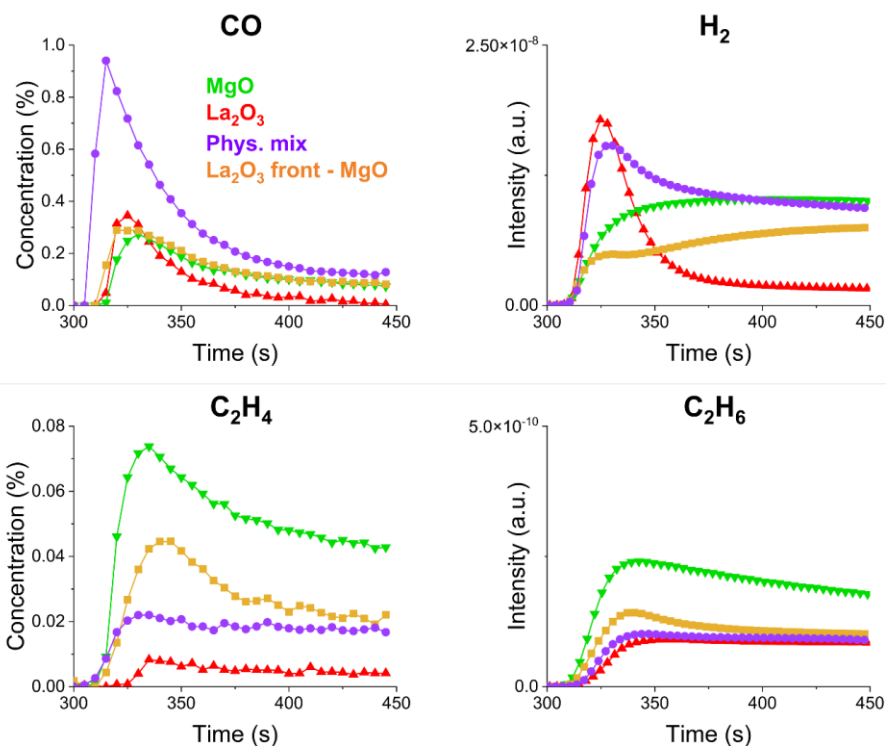
Figure 5.2: Transient analysis of products (FTIR + MS) during the CH_4 pulse (300-450 s) in unsteady-state OCM performed at 900 °C. The values are averaged over multiple stable cycles of operation. Results for La_2O_3 (red ▲), La_2O_3-MgO 50 wt% physical mixture (violet ●), MgO (green ▼), La_2O_3 (10 wt%, front of the bed)-MgO (yellow ■).

The results obtained for the 50 wt% physical mixture of the two catalysts reveal that CO and H_2 release are highly enhanced in this configuration. From a mechanistic point of view, those results confirm the intrinsic catalytic behaviour observed for the pure catalysts: on one hand, the ability of MgO in methane activation and dehydrogenation, on the other hand, the high reactivity of the oxygen species in La_2O_3 to promote partial oxidation to CO. MgO surface is very active for activation of CH_4 and $CH_3^{\bullet}$ radicals formation. However, in a pure MgO catalytic bed, the absence of highly reactive O species in the lattice limits their further oxidation to CO. The presence of La_2O_3 in the catalytic bed introduce this highly reactive oxygen species which promote the oxidation of CH_4, C_2H_6 and the respective methyl and ethyl radicals formed on MgO, resulting in the decrease of C_2 species and highly increased CO production compared to the pure MgO case.

To investigate the extent of coking, Figure 5.3 reports the profiles of CO_x species evolved from gasification of the carbon deposits during the oxidant pulse (O_2, 25 vol% in He). Pure La_2O_3 exhibited the lowest C deposition, while the highest accumulation of C deposits was found on MgO. For the 50 wt% mixture of MgO and La_2O_3, it would be reasonable to expect an amount of C deposited per g of catalyst close to the average value of the pure oxides. Interestingly, for the 50 wt% mixture of MgO and La_2O_3, CO_x species were released in comparable amount to the pure MgO catalytic bed. It is clear that, in presence of La_2O_3, the

mechanism of carbon deposition proceeded unaltered on the MgO surface, confirming the high dehydrogenation activity of the catalyst.
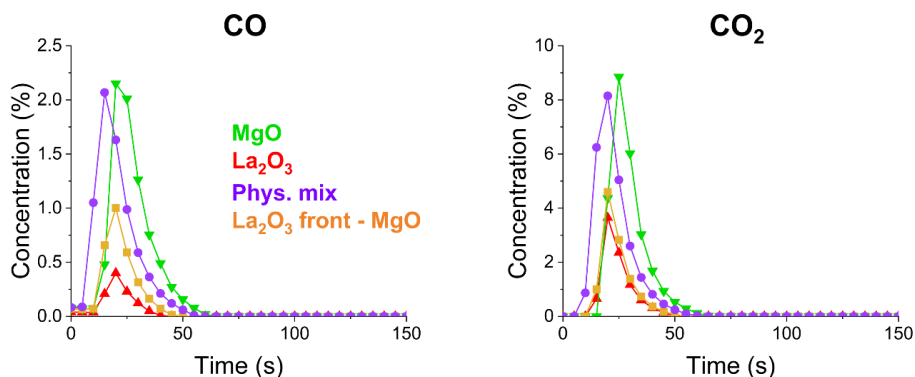

Figure 5.3: Transient analysis of products (FTIR + MS) during the O_2 pulse (0-150 s) in unsteady-state OCM performed at 900 °C. The values are averaged over multiple stable cycles of operation. Results for La_2O_3 (red ▲), La_2O_3-MgO 50 wt% physical mixture (violet ●), MgO (green ▼), La_2O_3 (10 wt%, front of the bed)-MgO (yellow ■).

A possible explanation for the high value of CO_x species found in the mixed catalytic bed is the presence of a concentration gradients, with a preferential accumulation of carbon deposits at the front of the reactor bed. To verify this, a catalytic bed was prepared by loading a limited amount of La_2O_3 at the front of the MgO catalytic bed (La_2O_3 10 wt%, MgO 90 wt%, 200 mg). For this catalytic bed, the synergy observed for the physically mixed bed (50 wt%) disappears. In fact, the separate contribution of the two catalysts can be recognised in the transient products profiles (Figure 5.2). The little amount of La_2O_3 at the front of the catalytic bed is responsible for the initial higher peak observed in CO and H_2 profiles. The rest of the bed, composed of MgO, is mainly responsible for the C_2 production and the continuous H_2 generation from dehydrogenation reactions. The absence of La_2O_3 particles in close vicinity allows the methyl radicals, generated on MgO surface, to couple in the gas phase and form C_2H_6, without undergoing further oxidation to CO.

The reduced amount of MgO in the catalytic bed reflected in the lower production of C_2 species, although the reduction clearly exceed the 10%, indicating that the front part of the catalytic bed may be responsible for a high share of the CH_4 conversion. *Operando* visualisation of the catalytic bed (Appendix D4, Figure D2) revealed that, at the end of the CH_4 pulse, the La_2O_3 catalyst placed at the front maintained its white colour, while MgO turned into a dark grey colour indicating formation of carbon deposits. However, the presence of La at the front of the catalytic bed also strongly suppressed carbon deposition, as observed in the amount of CO_x species developed in the O_2 pulse (Figure 5.3). The results suggest the relevance of possible concentration gradients in the conversion of CH_4 and confirm the preferential accumulation of C at the front of the catalytic bed.

5.3.2 Steady-state oxidative coupling of CH_4

The unsteady-state investigation of catalyst interaction with methane indicated peculiar selective conversion paths for the two oxidic systems. However, such prominent differences in the intrinsic catalytic behaviour are severely lost in steady-state OCM operation.

Catalytic activity of simple metal oxides, La_2O_3 and MgO, was evaluated by quantifying the gaseous concentration at the reactor outlet during OCM operation at different temperatures. The catalytic activity of La_2O_3 was found superior than that of MgO in terms of CH_4 conversion and C_2 yield (Figure 5.3A, C), more prominently at lower temperatures (550–650 °C). In such conditions, remarkably higher amounts of partial oxidation products (CO and H_2, Figure 5.4B, D) were detected for La_2O_3, reflecting what was observed for the unsteady-state catalytic results (Figure 1A). However, the higher activity towards C_2 products compared to MgO contrasts the consideration on the intrinsic selectivity of the oxides.

Even more strikingly, the two materials behaved similarly above 700 °C. The catalytic activity of the two systems were comparable in terms of conversion and selectivity, and a similar trend of decrease in catalytic performance above 850 °C is shown. The concentrations of CO_2 also confirmed those trends (Appendix D5, Figure D3).
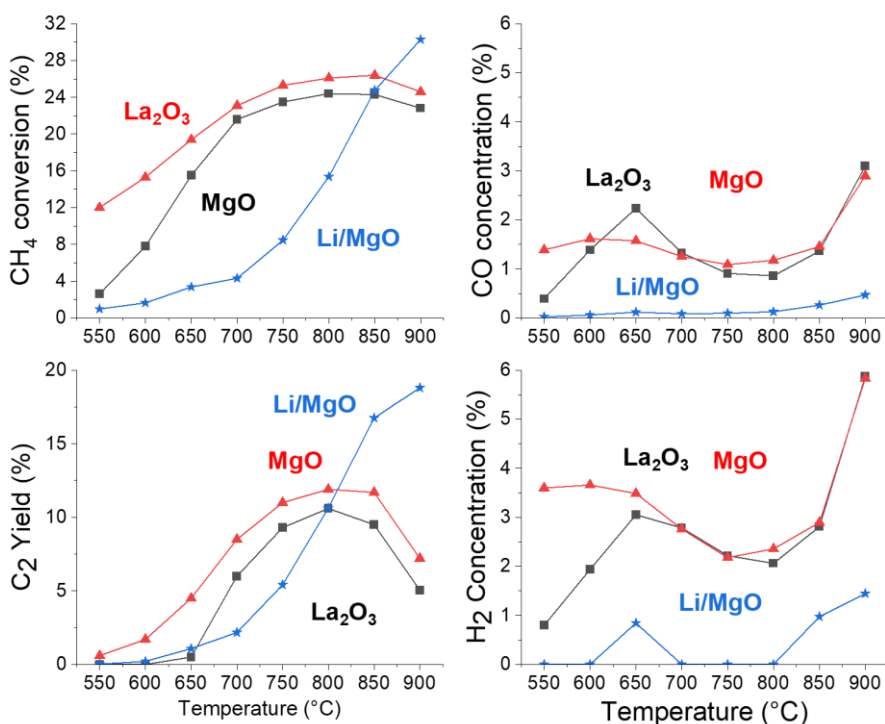
Figure 5.4: Catalytic performance of MgO (black), La_2O_3 (red) and 5 wt.% lithium doped MgO (Li/MgO, blue) in terms of CH_4 conversion (A), CO concentration (B), C_2 yield (C) and H_2 concentration (D) during OCM under steady-state operation ($CH_4/O_2 = 4$, 80 mL/min, He and N_2 diluted, N_2 is the internal standard for gas chromatography analysis) at different temperatures.

In this temperature range, O_2 is almost fully consumed and CH_4 total and partial oxidation products are detected in similar level (Figure 5.4 and Figure D3). This is an indication that exothermic reaction paths became predominant irrespectively of the catalytic system and reactions may be driven fully homogeneously. This given, it appears crucial to identify the extent of exothermic reaction paths for the two systems by investigating the distribution of heat in the catalytic reactor under reaction conditions.

5.3.3 Temperature and Concentration Gradients

A digital microscope and an infrared camera were used to qualitatively and quantitatively evaluate the temperature distribution along the catalytic bed. Remarkably, clear hotspots were observed (Figure 5.5A, B) only at the front of catalyst bed for both catalysts. To measure more precisely the catalyst temperature inside the reactor, additional spatial temperature measurements were performed using a movable thermocouple (Figure 5.5C). The measurements suggested that the temperature rise starts even before the catalyst bed, although differences in heat conductivity make a precise delimitation of the hotspot challenging. Nonetheless, the hot zone in La_2O_3 appeared to be shifted more to the front of the catalyst bed compared to that of MgO, indicating that the exothermic reactions might be activated at earlier position for La_2O_3.
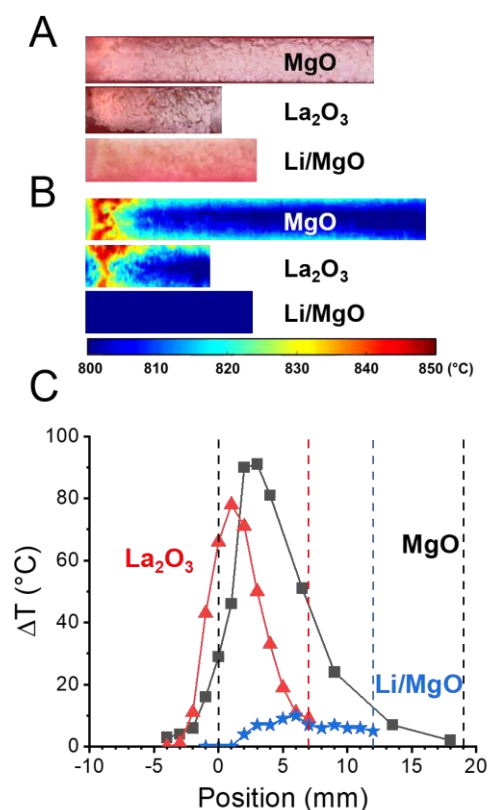
Figure 5.5: Visualization and quantification of hotspot formed during OCM under steady-state operation on MgO and La_2O_3 respectively at 800 °C: A, images of catalyst beds obtained by the digital microscope; B, images of catalyst beds acquired via infrared camera; C, spatial distribution of differential temperature of catalyst (ΔT). The temperature rise is calculated by subtracting the temperature measured with 10 vol% O_2 in N_2 at 800 °C from the temperature measured during OCM under steady-state operation (the same feed composition as in Figure 5.4) at 800 °C at respective positions on corresponding catalysts.

Considering the presence of hotspots in OCM conditions, it is necessary to investigating possible gradients in the products distribution along the catalytic bed. To this scope, space-resolved gas sampling was performed for the two catalysts. The profiles obtained during OCM at 700 °C are presented in Figure 5.6A, B.
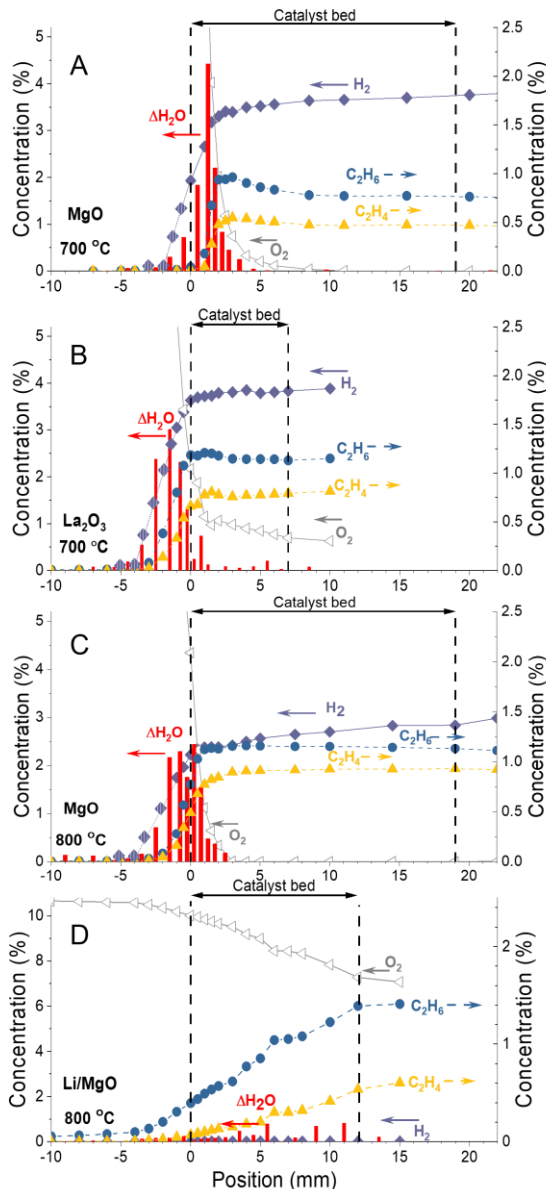

Figure 5.6: Space-resolved concentration profiles of O_2, C_2H_6, C_2H_4, H_2 and formed water between two data points (ΔH_2O) measured during OCM under steady-state operation on A) MgO at 700 °C, B) La_2O_3 at 700 °C, (C) MgO at 800 °C and (D) Li/MgO at 800 °C (same feed composition as in Figure 5.4)

The concentration profiles of oxygen clearly indicate that most of oxygen is consumed within a few mm from the front edge of the catalyst bed of MgO and La_2O_3 (note that the catalyst bed length of La_2O_3 is significantly shorter because of its higher mass density). There is residual oxygen present in the reactor towards the end of the catalyst bed for La_2O_3 (Figure 5.6B). Nevertheless, only looking at the oxygen profiles, it is evident that the reactions take place mainly at/near the front position of the catalyst bed in accordance with the temperature profiles (Figure 5.5) and with other spatial gas analysis.[30, 41, 42] In practice, the localized reaction zone does not seem to affect the OCM performance positively and rather it can be detrimental as evidenced from the decay of the C_2H_6 and C_2H_4 concentrations after the initial peak values near the front of the catalyst bed. Indeed, a slightly better catalytic activity was confirmed when a reduced amount of MgO was used (40 mg instead of 200 mg) up to 700 °C (Appendix D5, Figure D4). This shows that only a small portion of the catalyst at the front position positively contribute to OCM. C_2H_6 reforming reactions are suggested to take place according to spatial analysis of OCM on MgO at 850 °C (Figure D5).

To our great surprise, the reaction products appear in the gas phase even before the catalyst bed, with a more pronounced phenomenon observed in La_2O_3 than MgO at 700 °C. This observation was also reported for MgO when the reaction temperature was increased to 800 °C (Figure 5.6C, Figure D6.A-B). Back-diffusion of products and gas mixing may be at the origin of this phenomenon. In order to check these influences, SiC was added before the catalyst beds. The concentration profiles (Figure D7) confirms the identical observation, with an even more pronounced shift of the products towards the inlet direction, possibly due to higher gas temperature induced by the presence of heated SiC at the inlet position of the catalyst.

These observations pose a fundamental questions on the role of the catalyst in OCM. The catalyst is undoubtedly necessary since inert materials as SiC cannot efficiently catalyze OCM (Figure D8). As noted above, the presence of products before the bed was more prominently observed for La_2O_3. All products reached their maximum concentration values in the catalyst-free zone even at 700 °C. A careful comparison of the gas phase concentrations of the detected molecules indicates that H_2 concentration profile was significantly distinct from others and H_2 was observed at much earlier point along the flow direction. Given the Maxwell-Boltzmann distribution, lighter molecules as H_2 are in fact expected to back-diffuse faster at higher temperatures, explaining why H_2 was found at earlier positions before the catalytic bed. Here, the co-presence of H_2 and unreacted O_2 from the feed created the conditions for highly exothermic reactions, such as H_2 oxidation, to take place and to cause the formation of local hotspots. The analysis of the H_2O produced at different positions in the catalyst bed (Figure 5.6, red bars) suggests that increased H_2O detection was also associated with an increment in the formation of other products, including C_2 species (Figure 5.6). In fact, the increased temperature is known to enhance the rate of the homogeneous gas phase reactions in OCM.[43] In line with indications from homogeneous gas-phase OCM experiments, also the formation of C_2 products becomes relevant at T higher than 800 °C.[44] Due to highly exothermic reaction pattern, the reaction mixture was locally heated up significantly, probably at least by a few hundred degrees (the exact determination of the temperature profile measurement is limited by the spatial resolution of the thermocouple or IR camera), and unselective oxidation reactions took place in the gas phase. A complex homogeneous reaction network involving several radical species (H, OH, CH_3) is expected to control the distribution of products.[45]

Still, the production of H_2 itself reflects the role played here by the catalyst. As discussed previously, H_2 can be produced from partial oxidation and the lattice oxygen in La_2O_3 can more efficiently catalyze the reaction (Figure 5.1). This is in agreement with the observation from unsteady-state: at the front edge of the catalyst bed (at 0 mm), 3.6 vol% H_2 was observed for La_2O_3, which almost doubles the value observed for MgO (1.9 vol%) at 700 °C (Figure 5.6). The higher concentration of H_2 produced by La_2O_3 also explains its increased back-diffusion at the front of the bed. Higher concentration gives larger diffusion driving force, enhancing H_2 back-diffusing further away from the La_2O_3 catalyst bed. Moreover, the exothermicity of the partial oxidation reaction and the heat generated by concomitant hydrogen oxidation are expected to provoke gas expansion, contributing to the back-diffusion phenomenon. The presence of H_2 and consequent activation of exothermic reaction routes, positively influences the yield of OCM products. Such effect was confirmed by adding 1.4 vol% H_2 into the OCM feed using SiC, La_2O_3 or MgO as catalyst (Figure D9). Additional support to those hypotheses was provided by an experiment where a small portion of La_2O_3 was placed in front of MgO. In this case, La_2O_3 would generate more H_2, and MgO may efficiently catalyze OCM. As expected, we could confirm the significant enhancement of catalytic performance in this configuration of the catalyst compared to MgO (Figure D10).

It is clear that the function of the catalyst is to catalytically trigger the reaction by firstly activating methane on its surface. The local hotspots generated by highly exothermic reactions, including H_2 oxidation, provokes the activation of homogeneous gas phase reactions, which greatly control the products distribution. In such conditions, the majority of the reactions take place at the front of the catalyst bed, where oxygen is fast depleted. The higher activity of La_2O_3 over MgO at lower temperatures is attributed to the higher amount of H_2 produced by the former. However, the amount of produced H_2 seems to reach a similar level above certain temperatures (700 °C) indicating that, above this temperature, the specific impact of the metal oxide lose relevance in favor of the homogeneous gas-phase reaction steps, explaining similar activity and trends (Figure 5.4).

5.3.4 Catalytic effect of promoters

In OCM studies, it is common to add promoter(s)/dopant(s) to simple metal oxide to improve catalytic activity.[12] At the light of the previous insights about the role of simple metal oxides in OCM reaction conditions, it is now possible to investigate the catalytic effect of promoters in terms of spatial variation of products distribution and temperature. Figure 5.4 shows the catalytic performance of Li/MgO, which differs significantly from that of MgO. At first sight, CH_4 conversion and C_2 yield increase as the reaction temperature increases, in contrast to the trend observed in MgO (and La_2O_3). At the maximum temperature examined (900 °C), higher CH_4 conversion was observed for the Li-promoted sample compared to MgO, together with enhanced C_2 yield mainly due to the suppression of unselective oxidation reactions (CO and CO_2 formation, Figure D3).

An identical space-resolved concentration analysis was performed for Li/MgO at 800 °C (Figure 5.6D), clarifying drastic differences in the spatial profiles of gas phase species in the reactor. The amounts of detected H_2 as well as H_2O were negligible, indicating that the addition of lithium greatly suppresses H_2 formation and, consequently, its exothermic oxidation. This is also confirmed by the minor consumption of oxygen in the reactor (ca. 30% conversion). As a consequence, a clear hotspot was not observed for Li/MgO during OCM

126

(Figure 5.5C). The suppression of highly exothermic reactions at the front of the bed, together with the availability of oxygen throughout the whole catalytic bed, provoke a fundamental change in the catalytic behavior of the Li-promoted system. In fact, while most of the OCM activity was confined at the front or even before the catalyst bed for MgO (Figure 5.6A-C), concentration of C_2 species progressively increased along the Li/MgO catalyst bed.

For the strontium-doped La_2O_3 (Sr/La_2O_3) system, which showed significant suppression of the partial oxidation products (CO, H_2) compared to La_2O_3, the positive effect of the promoter was less prominent compared to Li/MgO. In fact, consistent formation of water was detected together with the fast depletion of oxygen at the front of the bed. (Figure D11 and Figure D6C in Appendix D).

The unicity of the lithium promoting effect is associated with the enhancement of the catalyst basicity.[38] Such property was found to be linked to the increased C_2 selectivity.[25] Another effect of Li promotion is the enhancement of the lattice oxygen mobility.[46] Considering the specific selectivity of lattice oxygen species observed for MgO, their increased mobility in presence of Li can positively influence the rate of formation of C_2 products. A closer look into the concentration profiles obtained for Li/MgO (Figure 5.6D) reveals a much higher selectivity to ethane than ethylene. This confirms that the Li-modified surface facilitates the coupling reaction, but at the same time does not promote the subsequent oxidative dehydrogenation of ethane (Figure D12). Also to be remarked, during the gas sampling experiment with Li/MgO, the outer surface of the capillary used to extract gases was coated with a material after the experiment, which was not observed for MgO. Loss of Li from the material in the form of LiOH has been reported for Li/MgO as a main cause of deactivation in OCM.[47] This implies a high mobility of the Li component over MgO, which was likely in a molten state under the reaction conditions and adhered to the capillary surface during the gas sampling experiment. This molten state of Li and its ability to cover the MgO support is expected to play an important role limiting the activity of the MgO lattice oxygen for partial and total oxidation, increasing the global selectivity towards C_2 formation.

5.4 Conclusions

In the complexity of the OCM reaction conditions, where radical species and oxidants coexist at high temperatures, the catalyst can play a fundamental role in driving the selectivity towards C_2 products. The primary role is to activate methane and form methyl radicals, but their selective coupling to ethane and following dehydrogenation to ethylene are threatened by the thermodynamically favoured partial and total oxidation reactions to form CO and CO_2. Simple metal oxides as MgO and La_2O_3, which possess intrinsically different ability to selectively convert CH_4, exhibited similar OCM performances in terms of CH_4 conversion and C_2 selectivity at high temperatures.

Space-resolved *operando* visualization, temperature measurement and gas sampling along the catalytic bed helped us demonstrate the relevance of highly exothermic reaction paths developed in OCM conditions over those catalysts. The formation of huge hotspots at the front of the catalyst bed derives from a pattern of highly exothermic reactions, including H_2 oxidation. Such hotspots greatly control the total C_2 yield, driving the selectivity towards partial and total oxidation products (CO_x) and narrowing the role of the catalyst to the mere activation of CH_4. The use of promoters, in particular Li on MgO, enhance the control on the selectivity by avoiding the formation of hotspots, quenching the unselective oxidation paths and activating the selective conversion to C_2 all along the catalytic bed.

Those insights demonstrated the importance of temperature and concentration gradients in catalytic OCM reaction, stressing the value of implementing spatially resolved analysis for a realistic investigation of the catalytic systems under operating conditions.

Appendix D

D1. Reaction setup
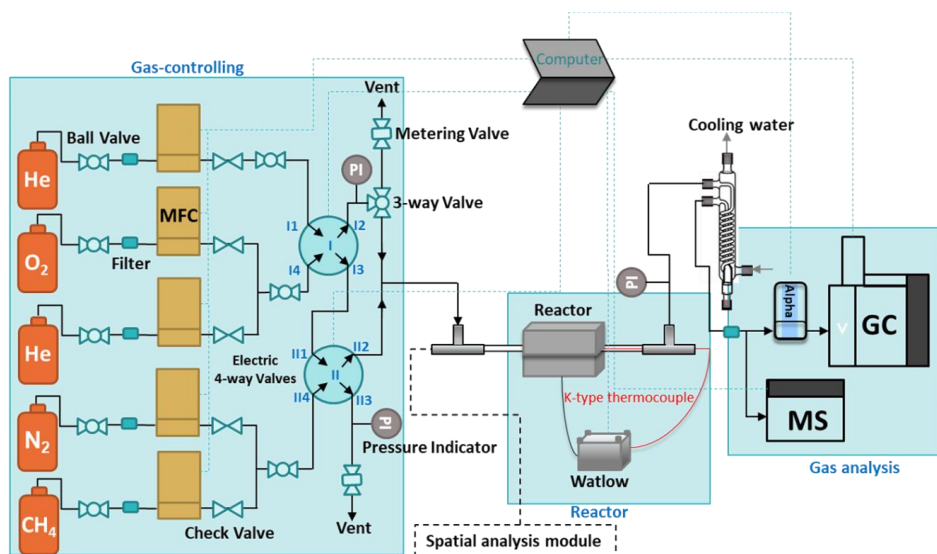
Scheme D1: Schematic of setup for catalytic reaction testing

D2. Spatial analysis module

The module for space-resolve gas analysis is depicted in Scheme D2. It consists of a base platform on which two metallic supports are placed, one fixed directly to the platform, keeping the tube in position, and the other one connected to the x-moving stage, controlled by computer. The system allows precise movements with minimum interval of 100 μm. A tubular channel, connected to the reactor longitudinally, contains the fused silica capillary (OD: 650 μm, ID: 150 μm) used for *in situ* gas sampling. A rubber bellow ensures the sealing while the distances between the two stages is changed. One end-tip of the capillary is placed at the end of the catalyst bed, another end-tip is connected to the detector, GC or MS. The capillary is inserted in the tubular channel and the connection ensured by a 1/16 inch female nut and graphite ferrule. When running the spatial-resolved gas sampling experiment, the gas is sucked from the end-tip inside the reactor and goes to the detector through the capillary. The spatial profile of the gas phase composition is obtained then by step movement of the x-moving stage, with the capillary end-tip sliding from the end to the front of the catalyst bed. To be noticed, when the gas analysis is performed by GC, a vacuum pump (Vacuumbrand) and a metering valve are connected to the outlet of the GC. The combination creates a mild driving force enabling to suck the gas with a flow rate of less than 5 mL/min. For measuring the spatial temperature profile, a K-type thermocouple replaces the capillary inserted into the catalyst bed. The thermocouple is connected to a temperature reader (Watlow).
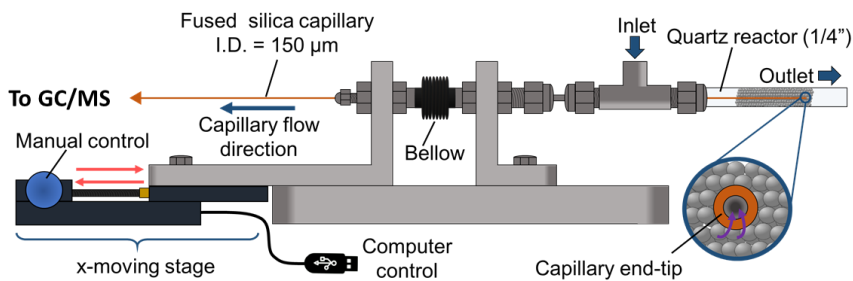
Scheme D2: Schematic of setup for catalytic reaction testing
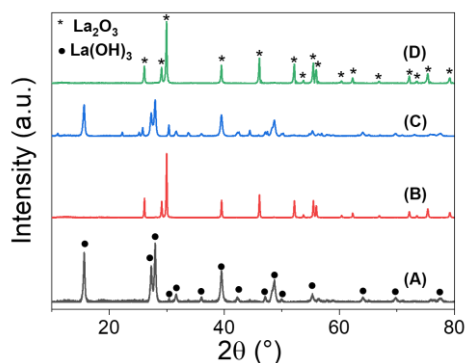
D3. Characterization of La₂O₃ sample

Figure D1: XRD profile of La₂O₃ sample with different treatment: (a) directly purchased La₂O₃; (b) after calcining (a) at 700 °C in air for 5 h; (c) after keeping (b) in a closed sample vial at room temperature for 1 day; (d) after calcine (a) in 50 vol% O₂ in He (50 mL/min) at 700 °C for 30 min.
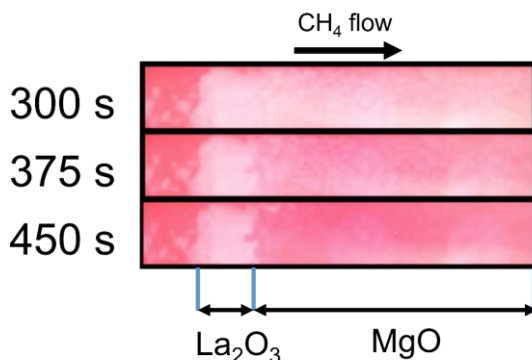
D4. Unsteady-state OCM activity

Figure D2: *Operando* visualisation of La₂O₃-MgO mixed catalytic bed (La₂O₃ 10 wt% at the front part of the catalytic bed) during CH₄ pulse in unsteady-state OCM reaction at 900 °C.

D5. Steady-state OCM activity
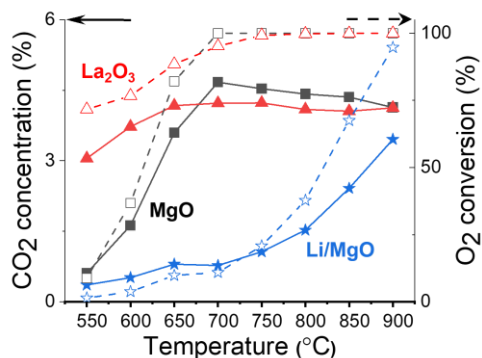
Figure D3: Comparison of OCM catalytic behaviour over MgO (black), La_2O_3 (red) and Li/MgO (blue) in terms of CO_2 concentration (solid lines) and O_2 conversion (dash lines).
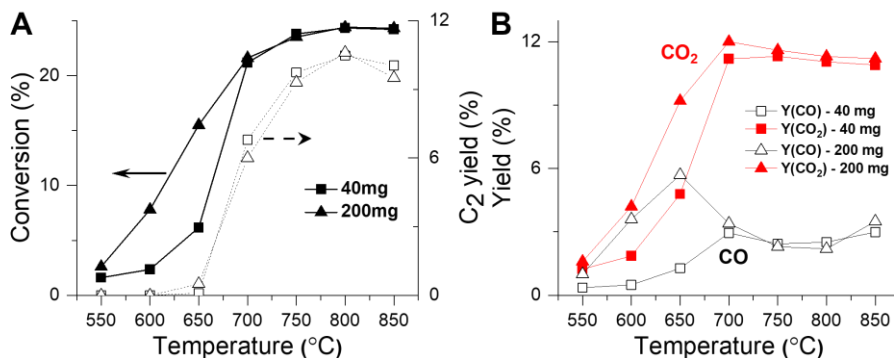

Figure D4: Comparison of catalytic performance over MgO with different amount (40 mg and 200 mg) in terms of CH_4 conversion & C_2 yield (A) and CO & CO_2 yield (B).
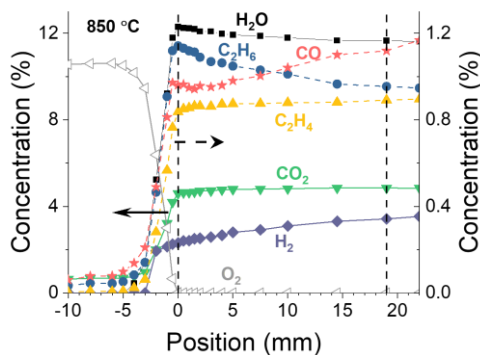

Figure D5: Spatial concentration profile of O_2, C_2H_6, C_2H_4, CO_2, CO, H_2O and H_2 during OCM under steady-state operation over MgO at 850 °C, H_2O is calculated by oxygen balance.
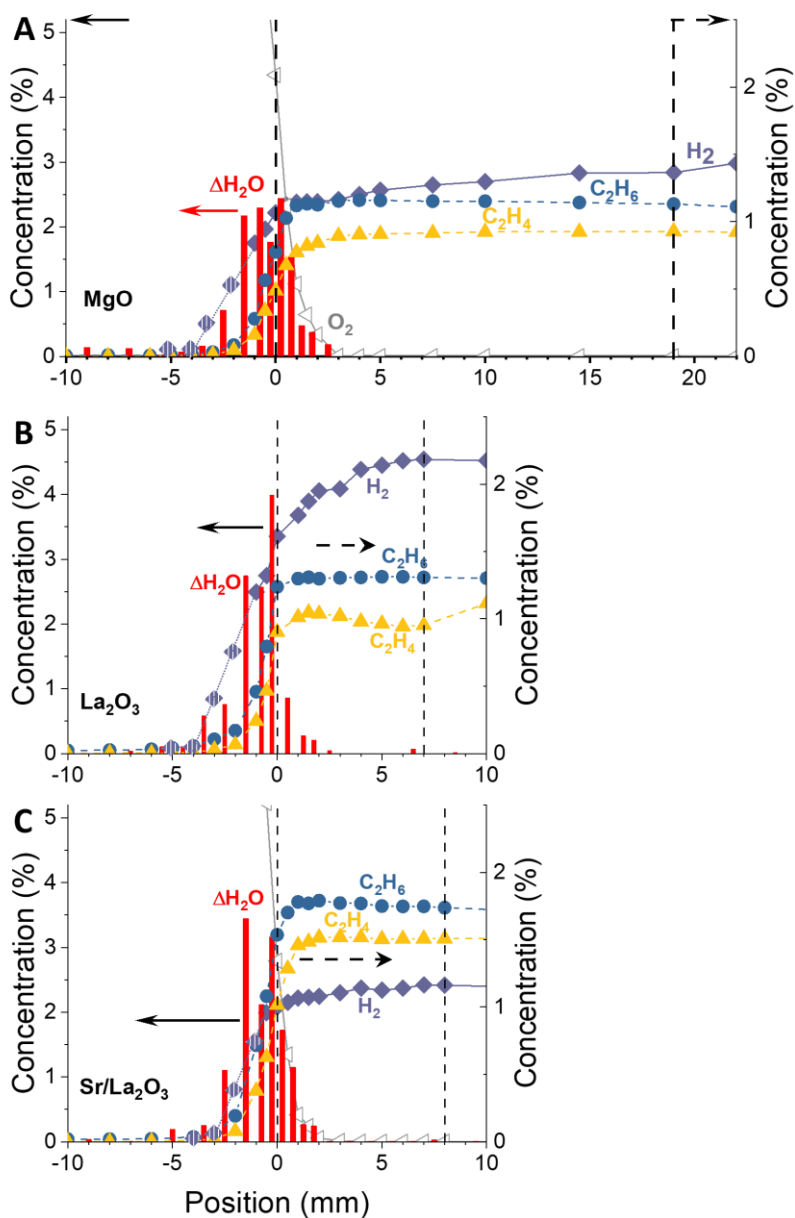
Figure D6: Spatial concentration profiles of O_2, C_2H_6, C_2H_4, H_2 and formed water between two data points (ΔH_2O) measured on MgO (A), La_2O_3 (B) and Sr/ La_2O_3 (C) during OCM under steady-state operation at 800 °C. ΔH_2O is the difference value between H_2O amount at one position and H_2O amount at previous position, H_2O amount is calculated by oxygen balance.
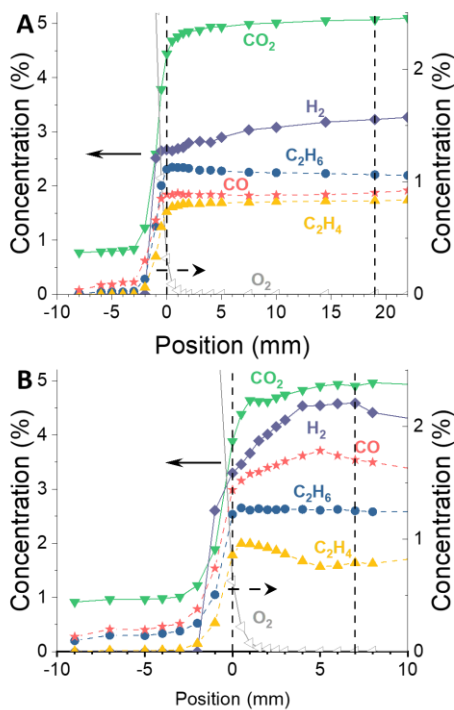
Figure D7: Spatial concentration profile of O_2, C_2H_6, C_2H_4, CO_2, CO and H_2 during OCM under steady-state operation over MgO (A) and La_2O_3 (B) with 4 mm SiC in front at 800 °C.
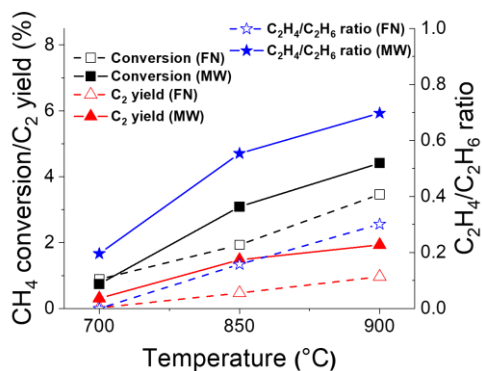

Figure D8: CH_4 conversion, C_2 yield and C_2H_4/C_2H_6 ratio during OCM on SiC with furnace reactor (open symbols) and microwave reactor (solid symbols) at 700 °C, 850 °C and 900 °C.
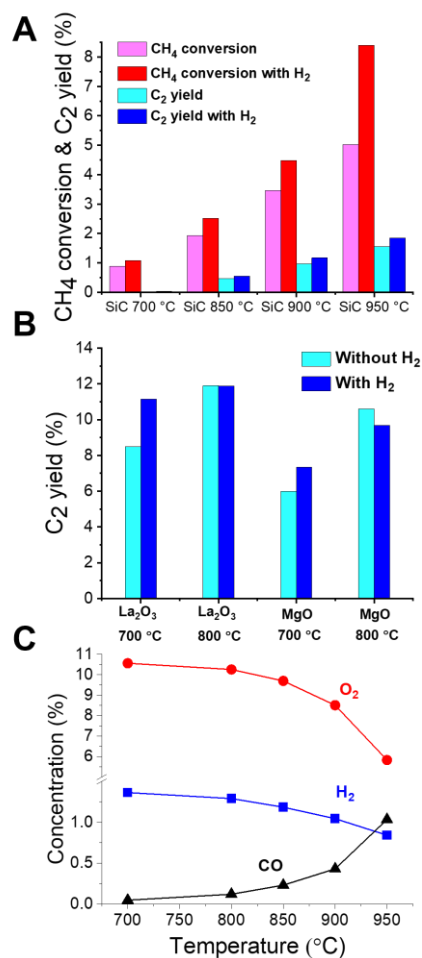
Figure D9: CH_4 conversion and C_2 yield during OCM over SiC (A) and C_2 yield during OCM over La_2O_3 and MgO (B) with/without H_2 in the feed under steady-state operation at different temperatures, and concentration of O_2, H_2 and CO during OCM over SiC with H_2 in the feed under steady-state operation (C). It shows H_2 addition participates in O_2 consuming and lifts up CH_4 conversion and C_2 yield when SiC is applied, and it enhances C_2 yield at 700 °C but lowers that at 800 °C when La_2O_3 and MgO are used. The harm to C_2 yield at high temperature of H_2 addition is because that the temperature rise caused by H_2 burning shifts the reaction system to its activity dropping range (≥ 850 °C).
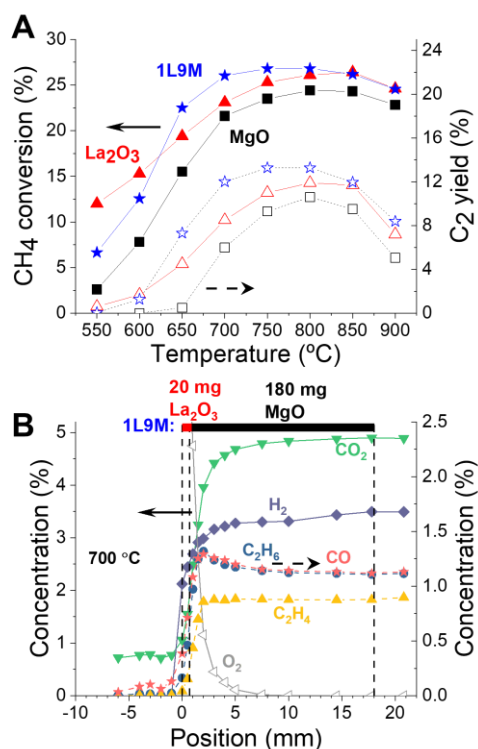
134

Figure D10: Comparison of OCM catalytic activity over La_2O_3, MgO and 1L9M (20 mg La_2O_3 + 180 mg MgO) under steady-state operation at different temperatures in terms of CH_4 conversion and C_2 yield (A), and spatial concentration profile of O_2, C_2H_6, C_2H_4, CO_2, CO and H_2 during OCM under steady-state operation over 1L9M (B).
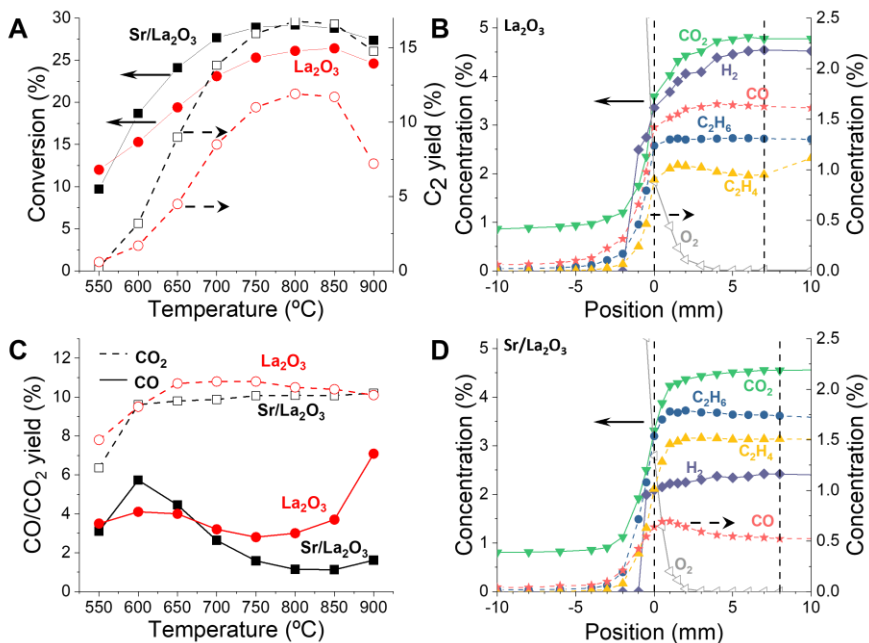
Figure D11: Comparison of La_2O_3 and Sr/La_2O_3 catalytic activity in terms of CH_4 conversion & C_2 yield (A), CO & CO_2 yield (C) and spatial gas concentration profile of O_2, C_2H_6, C_2H_4, CO, CO and H_2 during OCM under steady-state operation over La_2O_3 (B) and Sr/La_2O_3 (D) at 800 °C.
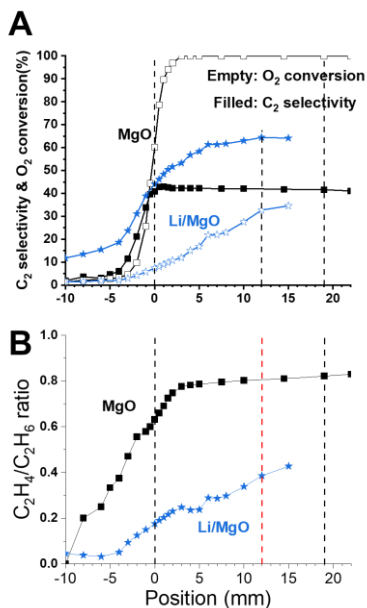

Figure D12: Comparison of MgO (black) and Li/MgO) spatial catalytic behaviour in terms of C_2 selectivity, O_2 conversion (A) and the ratio of C_2H_4/C_2H_6 (B) at 800 °C.

References

1. IEA, *Global Energy Review: CO₂ Emissions in 2021*, International Energy Agency, Paris, 2022.
2. K. Aasberg-Petersen, I. Dybkjær, C. V. Ovesen, N. C. Schjødt, J. Sehested and S. G. Thomsen, *J. Nat. Gas Sci. Eng.*, 2011, **3**, 423-459.
3. A. Holmen, *Catal. Today*, 2009, **142**, 2-8.
4. P. Schwach, X. Pan and X. Bao, *Chem. Rev.*, 2017, **117**, 8497-8520.
5. C. Karakaya and R. J. Kee, *Prog. Energy Combust. Sci.*, 2016, **55**, 60-97.
6. J. H. Lunsford, *Catal. Today*, 2000, **63**, 165-174.
7. T. Ren, M. Patel and K. Blok, *Energy*, 2006, **31**, 425-451.
8. S. J. Blanksby and G. B. Ellison, *Acc. Chem. Res.*, 2003, **36**, 255-263.
9. R. Franz, E. A. Uslamin and E. A. Pidko, *Mendeleev Commun.*, 2021, **31**, 584-592.
10. G. E. Keller and M. M. Bhasin, *J. Catal.*, 1982, **73**, 9-19.
11. J. H. Lunsford, *Angew. Chem., Int. Ed. Engl.*, 1995, **34**, 970-980.
12. E. V. Kondratenko, M. Schlüter, M. Baerns, D. Linke and M. Holena, *Catal. Sci. Technol.*, 2015, **5**, 1668-1677.
13. L. Hu, D. Pinto and A. Urakawa, in *Catalysis: Volume 32*, The Royal Society of Chemistry, 2020, vol. 32, pp. 203-223.
14. A. Cruellas, J. J. Bakker, M. van Sint Annaland, J. A. Medrano and F. Gallucci, *Energy Convers. Manage.*, 2019, **198**, 111789.
15. U. Zavyalova, M. Holena, R. Schlögl and M. Baerns, *ChemCatChem*, 2011, **3**, 1935-1947.
16. P. F. Nelson, C. A. Lukey and N. W. Cant, *J. Phys. Chem.*, 1988, **92**, 6176-6179.
17. T. Ito, T. Watanabe, T. Tashiro and K. Toi, *J. Chem. Soc., Faraday Trans. I*, 1989, **85**, 2381-2395.
18. J. M. DeBoy and R. F. Hicks, *Ind. Eng. Chem. Res.*, 1988, **27**, 1577-1582.
19. J. M. DeBoy and R. F. Hicks, *J. Chem. Soc., Chem. Commun.*, 1988, DOI: 10.1039/C39880000982, 982-984.
20. V. R. Choudhary, V. H. Rane and M. Y. Pandit, *J. Chem. Technol. Biotechnol.*, 1997, **68**, 177-186.
21. V. R. Choudhary, S. A. R. Mulla and V. H. Rane, *J. Chem. Technol. Biotechnol.*, 1998, **72**, 125-130.
22. V. R. Choudhary, V. H. Rane and S. T. Chaudhari, *Appl. Catal. A: Gen.*, 1997, **158**, 121-136.
23. J. A. S. P. Carreiro and M. Baerns, *J. Catal.*, 1989, **117**, 258-265.
24. Z. Kalenik and E. E. Wolf, *Catal. Lett.*, 1991, **9**, 441-449.
25. S. Arndt, G. Laugel, S. Levchenko, R. Horn, M. Baerns, M. Scheffler, R. Schlögl and R. Schomäcker, *Catal. Rev.*, 2011, **53**, 424-514.
26. O. V. Buyevskaya, M. Rothaemel, H. W. Zanthoff and M. Baerns, *J. Catal.*, 1994, **146**, 346-357.
27. C. A. Ortiz-Bravo, C. A. Chagas and F. S. Toniolo, *Journal of Natural Gas Science and Engineering*, 2021, **96**, 104254.
28. E. V. Kondratenko and M. Baerns, in *Handbook of Heterogeneous Catalysis*, Wiley, 2008, pp. 3010-3023.
29. F. Basile, G. Fornasari, F. Trifirò and A. Vaccari, *Catal. Today*, 2001, **64**, 21-30.
30. B. Zohour, D. Noon and S. Senkan, *ChemCatChem*, 2013, **5**, 2809-2812.
31. S. Pak, P. Qiu and J. H. Lunsford, *J. Catal.*, 1998, **179**, 222-230.
32. K. Otsuka and K. Jinno, *Inorg. Chim. Acta*, 1986, **121**, 237-241.
33. P. W. Wang, G. F. Zhao, Y. Wang and Y. Lu, *Sci. Adv.*, 2017, **3**, E130180.

34. P. Fleming, R. A. Farrell, J. D. Holmes and M. A. Morris, *J. Am. Ceram. Soc.*, 2010, **93**, 1187-1194.
35. V. Fleischer, P. Littlewood, S. Parishan and R. Schomäcker, *Chem. Eng. J.*, 2016, **306**, 646-654.
36. B. Benjiamin, F. Vinzenz, A. Sebastian, G. H. Miguel, U. Atsushi, H. Peter and S. Reinhard, *Catal. Today*, 2014, **228**, 212-218.
37. K. P. Peil, J. G. Goodwin and G. Marcelin, *J. Catal.*, 1991, **131**, 143-155.
38. J. A. S. P. Carreiro and M. Baerns, *React. Kinet. Catal. Lett.*, 1987, **35**, 349-360.
39. C. H. Lin, K. D. Campbell, J. X. Wang and J. H. Lunsford, *J. Phys. Chem.*, 1986, **90**, 534-537.
40. M. P. Rosynek, *Catal. Rev.*, 1977, **16**, 111-154.
41. B. Zohour, D. Noon and S. Senkan, *ChemCatChem*, 2014, **6**, 2815-2820.
42. C. Karakaya, H. Zhu, B. Zohour, S. Senkan and R. J. Kee, *ChemCatChem*, 2017, **9**, 4538-4551.
43. Y. Sekine, T. Nishimura and K. Fujimoto, *Energy Fuels*, 1998, **12**, 828-829.
44. J. W. M. H. Geerts, Q. Chen, J. M. N. van Kasteren and K. van der Wiele, *Catal. Today*, 1990, **6**, 519-526.
45. K. Takanabe and E. Iglesia, *Angew. Chem. Int. Ed.*, 2008, **47**, 7689-7693.
46. K. P. Peil, G. Marcelin and J. G. Goodwin, in *Methane Conversion by Oxidative Processes: Fundamental and Engineering Aspects*, ed. E. E. Wolf, Springer Netherlands, Dordrecht, 1992, pp. 138-167.
47. S. J. Korf, J. A. Roos, N. A. De Bruijn, J. G. Van Ommen and J. R. H. Ross, *Appl. Catal.*, 1990, **58**, 131-146.

Chapter 6

Enabling complete conversion of CH_4 and CO_2 in Dynamic Coke-Mediated Dry Reforming (DC-DRM) on Ni catalysts

Abstract

The substitution of steam by CO_2 as oxidising agent for CH_4 conversion to syngas has made dry reforming of methane (DRM) an attractive research area in catalysis. The harsh, high-temperature condition to activate the DRM is also harsh for the catalyst materials, often leading to fast deactivation of the catalyst. An additional limitation of conventional operation is the activation of the reverse water-gas shift reaction (RWGS), in which part of the H_2 is lost by reacting with CO_2 to form CO and H_2O. In this work, we define and illustrate the Dynamic coke-mediated dry reforming of methane (DC-DRM) based on unsteady-state operation as an effective strategy to overcome those limitations of steady-state DRM. In DC-DRM, the catalyst is periodically exposed to a redox cycle and interacts alternatingly with the reducing CH_4 pulse and oxidising CO_2 pulse, providing intrinsic separation of reactants and products feeds. Solid carbon species formed and deposited on the catalyst in the CH_4 pulse act as intermediate between the H_2 production from CH_4 decomposition and the CO formation upon gasification in the subsequent CO_2 pulse. This chapter proves the feasibility of DC-DRM on Ni-based catalytic systems, identifying suitable metal oxides supports and evaluating the role of metallic promoters. A La-promoted Ni/ZrO_2 catalyst exhibited excellent and stable catalytic performances at 800 °C approaching complete conversion of the CH_4 and CO_2 reactant pulses in the catalytic cycle, and separation of the H_2 and CO product streams. In addition, the involvement of the redox properties of reducible supports (TiO_2) in developing selective partial oxidation of methane is demonstrated as a powerful tool to enable formation of syngas in the reducing methane pulse with control on the H_2/CO ratio.

6.1   Introduction

Thanks to the abundant reserves of natural gas, its main component, methane, represents a readily available alternative to oil-based fossil fuels. In the last decades, dry reforming of methane (DRM, Reaction 6.1) attracted great scientific and technological interests.[1, 2] The reason is in the possibility of simultaneously convert methane and carbon dioxide to produce a syngas ($CO + H_2$).

$$CH_4 + CO_2 \ = \ 2H_2 \ + 2CO \qquad\qquad \Delta H_{298}^0 = 247 \ kJ \ mol^{-1} \qquad (6.1)$$

Compared to the conventional technologies for commercial syngas production involving steam or oxygen as oxidant (steam reforming of natural gas with large energy input as heat, autothermal reforming, partial oxidation), the direct utilisation of CO_2 as reforming agent of CH_4 in the DRM process can result in carbon footprint mitigation and potentially make it a 'greener' alternative.[3, 4] Compared to steam reforming in particular, the energy requirements to provide high-temperature steam are cut down. Moreover, a syngas with lower H_2/CO ratio can be obtained as product, which is a more favourable feedstock, for example, to promote chain growth reactions in Fischer-Tropsch synthesis of hydrocarbons or for the direct synthesis of dimethyl ether.[5-7]

DRM is a strongly endothermic reaction, requiring high temperatures to activate the highly stable chemical bonds of both CH_4 and CO_2 molecules. Thermodynamic equilibrium analyses of CH_4 and CO_2 mixtures show that high conversions can be obtained only at very high temperatures (T > 800 °C).[8] In such conditions, the global reaction proceeds via two main routes involving the decomposition of methane (Reaction 6.2) to form solid C and gaseous H_2, and the gasification of C by CO_2 to produce CO by the reverse Boudouard reaction (Reaction 6.3). At the same time, the endothermic reverse water-gas shift (RWGS, Reaction 6.4) can be activated. In this reaction route, the H_2 evolved from CH_4 decomposition is consumed by reacting with CO_2 from the feed. As a result, the syngas is enriched in CO, with H_2/CO ratio below 1, and contains undesired H_2O, demanding additional processing in order to meet the requirements of downstream operations, as methanol or hydrocarbon synthesis.
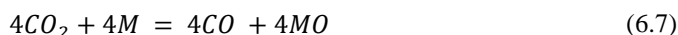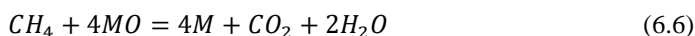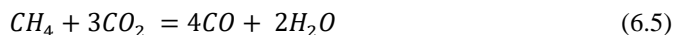
$$CH_4 \ = \ C \ + 2H_2 \qquad\qquad \Delta H_{298}^0 = 74.9 \ kJ \ mol^{-1} \qquad (6.2)$$
$$C + CO_2 = 2CO \qquad\qquad \Delta H_{298}^0 = 172.4 \ kJ \ mol^{-1} \qquad (6.3)$$
$$H_2 + CO_2 \ = \ H_2O + CO \qquad\qquad \Delta H_{298}^0 = 41 \ kJ \ mol^{-1} \qquad (6.4)$$

The extreme conditions required for achieving high conversions of CH_4 and CO_2 represent an hard proof for the catalyst materials. In fact, high temperatures usually translates into fast catalyst deactivation. The major causes of catalyst deactivation are sintering of the active metal and accumulation of stable carbon deposits, which can be accompanied by undesired pressure build-up in fixed bed reactors, abrupt changes in the thermal conductivity and catalyst fouling.[2, 9] In presence of a catalyst, the formation of stable carbon deposits becomes unavoidable when big particle sizes are involved.[10] Excellent activity in promoting DRM has been demonstrated over catalytic materials containing platinum-group metals (PGMs). Noble metal-based catalysts offer often outstanding performance in terms of reaction temperature and stability. Alternative catalytic systems containing more abundant transition metals as Fe, Co and Ni are also widely investigated. Compared to Co and Fe, the higher resistance of Ni

towards oxidation makes it more attractive in the formulation of highly active DRM catalysts.[1, 11-13]

The high rate of methane decomposition on Ni-based catalysts translates into fast coking and deactivation. In fact, CH_4 can be chemisorbed on Ni with direct cleavage of a C-H bond and stepwise dehydrogenation until deposition of a C atom. The C atoms can diffuse on/in the Ni particles so that carbon deposits grow in the form of whiskers with a Ni particle at the top. Thus the activity towards CH_4 decomposition is maintained while carbon deposits grow at a constant rate.[2] Partial passivation of the active Ni surface with sulfur was employed in SPARG process, sacrificing the overall activity to limit the growth of carbon deposits.[14] Bimetallic catalysts are recently investigated in order to mitigate the carbon deposition.[15-18] Combining Ni with traces of noble metals positively influences the activity while reducing the extent of coking.

Additional limitations to the exploitation of DRM derive from the intrinsic nature of conventional operational modes, which involve the co-feeding of the reactants leading to catalyst deactivation and difficulty in steady operation (*vide infra*). To overcome the limitations imposed by co-feed operation and the harsh reaction condition, a possibility is offered by unsteady-state processes, involving a paradigm change in the DRM operation mode. A first important benefit targeted by unsteady-state operation is feedstock and/or product separation, considering that separation is one of the most energy-intensive processes in chemical industry. An example is given by chemical looping operated processes,[19] which consist in the cyclical exposure of the catalytic material to the alternation of the separate gaseous reactants, commonly an oxidant and a reductant. Interconnected fluidised bed reactors, rotating reactors or alternating fixed bed reactors are required in order to expose the catalyst to the different atmospheres by either physically transporting the catalyst between the oxidising and the reducing reactors or switching the gaseous atmosphere of each reactor.[20] This operation mode has been successfully developed to improve the efficiency of catalytic combustion of hydrocarbon fuels.[21, 22]

In a similar fashion, chemical looping dry reforming of methane (CL-DRM) was proposed using oxygen-carrier catalytic materials that mediate between the reducing (CH_4) and oxidising (CO_2) reactant phases.[20, 23-25] Najera et al.[23] proposed a CL-DRM process as an alternative chemical looping combustion of CH_4 which enables utilisation of CO_2 as oxidant (Reaction 6.5). CH_4 is oxidised to CO_2 and H_2O (Reaction 6.6) by reaction with the oxygen of the carrier catalytic material (metal oxide 'MO'). After that, the carrier material is re-oxidised in CO_2 (Reaction 6.7), with simultaneous production of CO. In this process, CO is the only targeted product with no selectivity towards H_2, which is wasted during the total oxidation of CH_4 to CO_2 and H_2O by the oxygen carrier material.

$$CH_4 + 3CO_2 = 4CO + 2H_2O \qquad (6.5)$$

$$CH_4 + 4MO = 4M + CO_2 + 2H_2O \qquad (6.6)$$

$$4CO_2 + 4M = 4CO + 4MO \qquad (6.7)$$

Sorption-enhanced DRM processes based on calcium looping are also proposed to enhance the conversion of CO_2.[26] With the aim of intensifying CO_2 utilisation, Buelens et al.[27] combined the reforming (Ni), redox (Fe) and CO_2 sorption (Ca) functionalities in the catalytic

bed, defining a 'super-dry' reforming of CH_4. In this process, H_2 and CO deriving from CH_4 conversion are sacrificed to reduce the oxygen carrier material with formation of CO_2 and H_2O, a common trait of CL-DRM processes.[28] The presence of the CaO sorbent promotes *in situ* capture of CO_2 to form $CaCO_3$, while H_2O is removed from the reactor. Switching to an inert feed, regeneration of the CaO sorbent takes place with release of CO, which is thus inherently separated from the H_2O byproduct.

Several limitations can be pointed out for the CL-DRM. From operational point of view, achieving chemical looping operation requires circulating fluidised bed with high catalyst circulation rates. Additionally, sintering and degradation of the oxygen carriers materials represents an additional source of catalyst deactivation. Moreover, the employment of oxygen carriers typically results in the formation of total oxidation products (i.e. H_2O and CO_2) and low yields of H_2 and CO.

In this work, we present an unsteady-state DRM operation able to provide high conversions of CH_4 and CO_2 and intrinsic separation of the feed and product streams, while targeting high H_2 and CO yield. Inherent separation of both reactant and product streams is achieved by periodic switching of the gas feed at the inlet of a fixed-bed reactor. The global DRM reaction is thus divided in two stages (Scheme 1), the CH_4 decomposition (Reaction 6.2) and the C gasification by CO_2 (Reaction 6.3). Contrarily to conventional DRM operation, the carbon deposits (coke) represent here the targeted intermediate between the H_2 generation from CH_4 and the CO formation from CO_2. Accordingly, we coin this process as a Dynamic Coke-mediated Dry Reforming of Methane (DC-DRM). In DC-DRM the catalytic system undergoes substantial transformations during each reactant pulse, transitioning from a coke-free state in the CO_2 pulse to a coke-saturated state at the end of the CH_4 pulse. The irreversible accumulation of carbon deposits is tackled by the cyclic alternation of short reducing and oxidising reactant pulses in DC-DRM. This approach is expected to limit the irreversible accumulation of carbon deposits, favouring their complete gasification in each operation cycle and thus extending the stability of the catalyst performance. Additionally, an intrinsic advantage of the unsteady-state operation is the elimination of RWGS (Reaction 6.4) by precluding the mixing of the H_2 with the CO_2 feed. The result is a more valuable syngas, enriched in H_2, and the avoidance of undesired H_2O formation. In this perspective, it is decisive to select an optimal catalyst for DC-DRM operation able to provide fast decomposition of CH_4 with formation of carbon deposits that can be efficiently gasified in CO_2.

The work here presented proves the feasibility of DC-DRM operation and its potentiality towards full conversion of CO_2 and CH_4 reactant to CO and H_2, respectively. To this scope, Ni-based catalysts were synthesised and tested. The performance of different irreducible (SiO_2, ZrO_2, γ-Al_2O_3) and reducible (TiO_2) metal oxides supports was evaluated, together with the investigation of different metal promoters (La, Fe, K), with the aim of achieving full conversion of CH_4 and CO_2 in the catalytic cycle and providing stable operation in DC-DRM conditions.
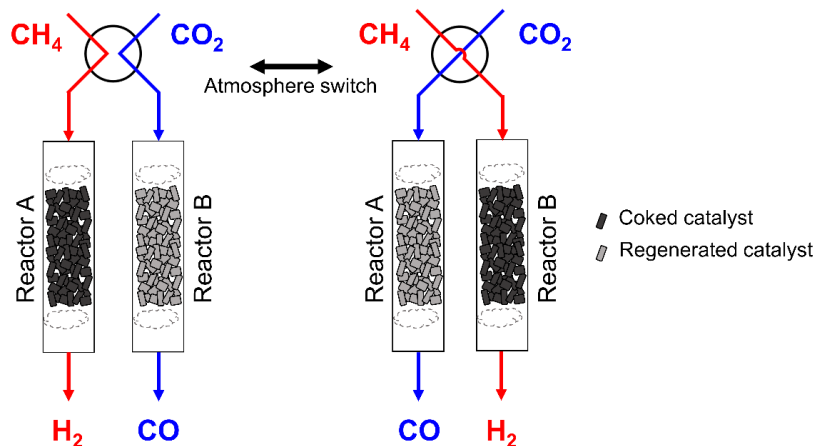
Scheme 6.1: Representation of Dynamic Coke-mediated Dry Reforming of Methane (DC-DRM) operated in alternating fixed bed reactors. For the purpose of this investigation, reactant feeds are alternated to a single fixed bed reactor and inert flushing phases (He) are interposed to eliminate possible influences to the catalytic results deriving from direct mixing of the reactants.

6.2   Experimental

6.2.1   Catalyst synthesis

Aluminum oxide (γ-phase, Alfa Aesar, 255 $m^2 g^{-1}$), silicon oxide (Alfa Aesar, surface area 261 $m^2 g^{-1}$) zirconium oxide (Alfa Aesar, 90 $m^2 g^{-1}$) and titanium dioxide (rutile, Alfa Aesar, > 99.5%) were employed as support material. For the TiO_2-ZrO_2 mixed oxide, ZrO_2 powder was impregnated in inert (N_2) atmosphere with a titanium (IV) isopropoxide solution (Sigma Aldrich, 97%) to obtain a 20/80 wt% TiO_2/ZrO_2 composition (Ti/Zr molar ratio = 15/85). The catalyst was then dried at 80 °C overnight and calcined in air at 800 °C for 5 h. Ni was added by incipient wetness impregnation using nickel nitrate hexahydrate (Alfa Aesar, >98%) as precursors on the different supports to synthesise the Ni/Al_2O_3 (15/85 wt%, NA), Ni/SiO_2 (15/85 wt%, NS), Ni/ZrO_2 (15/85 wt%, NZ) catalysts. For the promoted samples, aqueous solutions of potassium carbonate (Acros, >99%), lanthanum nitrate hexahydrate (Alfa Aesar, >99.9%) and iron (III) nitrate nonahydrate (Sigma Aldrich, ≥ 98%) were co-impregnated with the Ni precursor aqueous solution on the ZrO_2 support to synthesise the Ni-La/ZrO_2 (15/5/85 wt%, NLZ), Ni-Fe/ZrO_2 (15/5/85 wt%, NFZ) catalysts. After impregnation, the resulting mixture was dried overnight at 80 °C and then calcined at 500 °C for 5 h, if not stated differently. For Ni-K/ZrO_2 (15/5/80 wt%, NKZ), ZrO_2 was first impregnated with the Ni precursor, dried overnight at 80 °C and then calcined at 500 °C for 5 h. The resulting powder was further impregnated with an aqueous solution of K_2CO_3.

6.2.2 Catalyst characterization

Powder X-ray diffractograms were acquired on a Bruker D8 Advance Diffractometer with Bragg-Brentano geometry using monochromatic Cu Kα (λ=1.5406 Å) or Co Kα radiation (λ = 1.7902 Å). BET surface area of the catalysts was determined from N_2 adsorption isotherms at 77 K using a Micromeritics TriStar II 3020 instrument. Thermogravimetric analysis (TGA) of the spent samples was carried out in a METTLER TOLEDO SF/1100 thermogravimetric analyser by heating them up to 1000 °C at a rate of 10 °C min^{-1} under synthetic air flow. Transmission electron microscopy (TEM) of fresh and spent samples was carried out on a Jeol JEM1400 plus TEM instrument.

6.2.3 Catalytic testing

The configuration of the catalytic reactor setup was similar to the one described in previous works.[29, 30] The gas controlling part consisted of mass flow controllers (MFCs, Bronkhorst) and two electric 4-way valves to switch among different gas flows at the inlets. The catalyst powder was pelletised, crushed and sieved in 200-300 μm range. A tubular quartz tube reactor (0.4 mm ID, 0.6 mm OD) was filled with 200 mg of catalyst. Before reaction, the catalyst underwent a reducing pretreatement under 50 mL min^{-1} of pure H_2 at 500 °C for 1 h, unless stated differently. The temperature of the bed was controlled by a thermocouple inserted in the quartz reactor. Catalytic performance was evaluated under DC-DRM conditions at different temperatures (450 °C, 550 °C, 650 °C, 750 °C and 800 °C) and ambient pressure. The composition of the reactor effluent gas mixture was quantified by FT-IR spectroscopy (ALPHA, Bruker, 5s per spectrum). Valve switching and spectral acquisition were synchronised by LabView software. Each cycle of operation consisted of the alternation of 4 different phases (XFYF, where X= diluted CO_2 stream, F = He flush, Y = diluted CH_4 stream, F = He flush). The data presented were obtained from the average of at least 5 cycles of operation, after a stable and reproducible composition of the effluent was achieved. Conversion of CH_4 and CO_2 pulses were defined as

$$X = \frac{n_b - n_r}{n_b} \tag{6.8}$$

where n_b and n_r are the moles of reactant (CO_2 or CH_4) detected during a blank experiment and the reaction, respectively. Mass spectrometry (Omnistar, Pfeiffer Vacuum) was implemented to detect IR-transparent H_2 in the reactor effluent.

6.2.4 *Operando* thermal imaging of the catalyst bed

To investigate the spatial development of temperature gradients in the catalytic bed, an infrared thermal camera (IR camera, Micro-SWIRtm 320CSX Camera, Sensors Unlimited) is employed and placed on top of the reactor furnace. A glass-covered window opened at the top of the reactor furnace allow retrieving the IR radiation emitted by the hot catalytic bed and record its longitudinal temperature profile.

6.3   Results & Discussion

Unsteady-state operation for dry reforming of methane was achieved experimentally by exposing the catalytic bed to the pulsed alternation of a CH_4-containing and a CO_2-containing feed for several cycles of operation. The gas composition of the reactor outlet stream was analysed by infrared spectroscopy. Figure 6.1 reports the gas concentration profiles obtained for a blank experiment, employing a SiC bed. In a typical DC-DRM cycle, a CO_2 pulse (0-300 s) was initially sent to the reactor, followed by the reducing CH_4 pulse (405-510 s). For the purposes of this investigation, inert flushing phases (He, 300-405 s and 510-615 s) were introduced between the CO_2 and CH_4 pulses to avoid mixing of the reactants phases, to eliminate side reactions activated in co-feed conditions and thus isolate the role of the different catalytic materials.
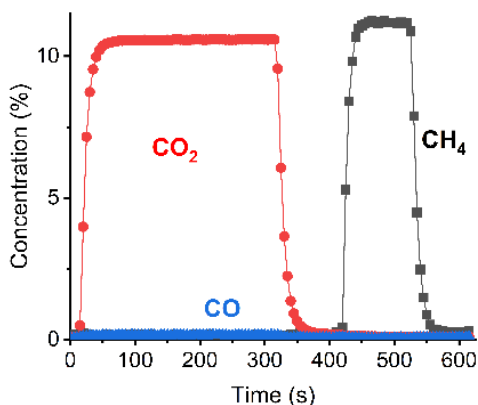

Figure 6.1: Reactor outlet gas concentrations obtained by FTIR spectroscopy during a blank DC-DRM experiment (SiC bed). DC-DRM cycle consists of the alternation of diluted CO_2 feed (10.6 vol% in He, 0-300 s), He flush (300-405 s), diluted CH_4 feed (11.2 vol% in N_2, 405-510s), He flush (510-615 s). Total flow rate was kept at 50 mL min^{-1}. Results are averaged over multiple stable cycles of operation.

6.3.1   Screening of irreducible metal oxide supports

First, SiO_2, ZrO_2 and γ-Al_2O_3 were screened as support materials for the catalytic system. The Ni precursor was added to the support via incipient wetness impregnation in order to obtain a final composition of 15 wt% Ni on the metal oxide support. X-ray diffractograms are of the synthesised samples are reported in supplementary information (Appendix E1, Figure E1). Considering the unsteady-state nature of the DC-DRM operation, an optimal catalyst should provide high activity in CH_4 decomposition and gasification of the carbon deposits by CO_2 with high efficiency. In this regard, the ratio between the converted CO_2 and the converted CH_4 (X_{CO2}/X_{CH4}) represents a useful descriptor to evaluate the catalytic performance. Considering the stoichiometry of the DC-DRM reaction, a catalyst with X_{CO2}/X_{CH4} ratio approaching 1 can provide high stability of the catalytic process by avoiding the accumulation of carbon deposits and at the same time guaranteeing the stoichiometric H_2/CO ratio of 1 in the product stream.

The screening of the support materials was conducted at mild reaction temperatures (550 and 650 °C), in order to highlight the contribution of the support to the reaction. At higher temperatures, extensive carbon deposition takes place and the peculiar role of the support in the reaction is less evident. Figure 6.2 reports the conversions of CO_2 (X_{CO2}) and CH_4 (X_{CH4}) obtained (Equation 6.8) and their ratio X_{CO2}/X_{CH4} for the different Ni-supported catalysts.

ZrO_2- and γ-Al_2O_3-supported catalysts displayed similar catalytic activity and, compared to
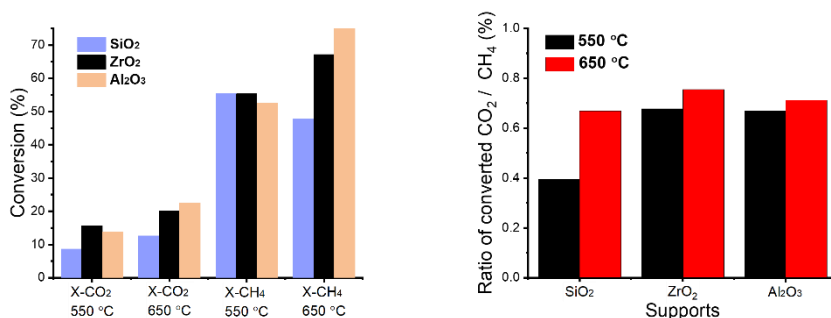

Figure 6.2: CO_2 and CH_4 conversion (X_{CO2}, X_{CH4}) obtained during DC-DRM at 550°C and 650 °C on different metal oxide-supported Ni catalysts (left, 15 wt% Ni) and ratio of converted CO_2/CH_4 (right). DC-DRM cycle consists of the alternation of diluted CO_2 feed (10.6 vol% in He, 0-300 s), He flush (300-405 s), diluted CH_4 feed (11.2 vol% in N_2, 405-510 s), He flush (510-615 s). Total flow rate was kept at 50 mL min^{-1}. Results are averaged over multiple stable cycles of operation.

the SiO_2-supported catalyst, they exhibited higher CO_2 conversion at both temperatures investigated and higher CH_4 conversion at 650 °C. The results clearly indicate a role played by the metal oxide support in the catalytic conversion of CO_2 and CH_4. Uncoordinated surface sites in metal oxides can exhibit acidic or basic character which directly influences the interaction with gaseous reactants. This is particularly of interest in the case of DRM catalysis. The adsorption of CO_2 molecule, a Lewis acid, can be favoured in presence of surface basic sites, while acid sites promotes the cracking of methane. Decreasing the acidity of the Ni/Al_2O_3 catalyst by addition of P, Bang et al.[31] observed a decrease in the initial CH_4 and CO_2 conversion. At the same time, the catalyst with lowest acidity showed limited deactivation by carbon deposition and more stable performances, indicating that C gasification by CO_2 is enhanced by the increased basicity introduced by P. It is recognised that SiO_2 support does not display prominent acidic or basic properties. At the contrary, ZrO_2 and Al_2O_3 can act as acid-base bifunctional catalyst.[32, 33]

Specifically for DC-DRM operation, the ability to provide both basic and acidic functionalities at the surface is fundamental to approach a ratio of converted CH_4 and CO_2 (X_{CO2}/X_{CH4}) close to 1, which is an important condition for the stability of the performances. The good performance in CH_4 and CO_2 conversions and the X_{CO2}/X_{CH4} ratio approaching 1 demonstrated the potential of ZrO_2 as a promising support for DC-DRM catalysts and thus it was chosen for the following investigations.

6.3.2 Reaction temperature

Figure 6.3 shows the reactor outlet stream composition during DC-DRM catalytic tests performed at different temperatures on the Ni/ZrO_2 catalyst. The results presented were obtained by averaging six cycles of stable operation. During the CH_4 pulse, solid carbon is deposited onto the catalyst, and in the subsequent CO_2 pulse, it serves as intermediate for the formation of CO via gasification reaction. For consistency, the concentration profiles during the CO_2 pulse is shown first in the Figures. In Ni-based catalysts, carbon nanofibers grow on the catalytic material as a result of the CH_4 decomposition. Importantly, the rate of gasification of carbon nanofibers by CO_2 is substantially higher compared to graphite or other carbon materials (carbon black, activated carbon).[34] When the temperature is sufficiently high, the CO_2 pulse could induce the carbon oxidation, thus complete regeneration of the activity towards CH_4 decomposition at each cycle, enabling the continuous DC-DRM operation.
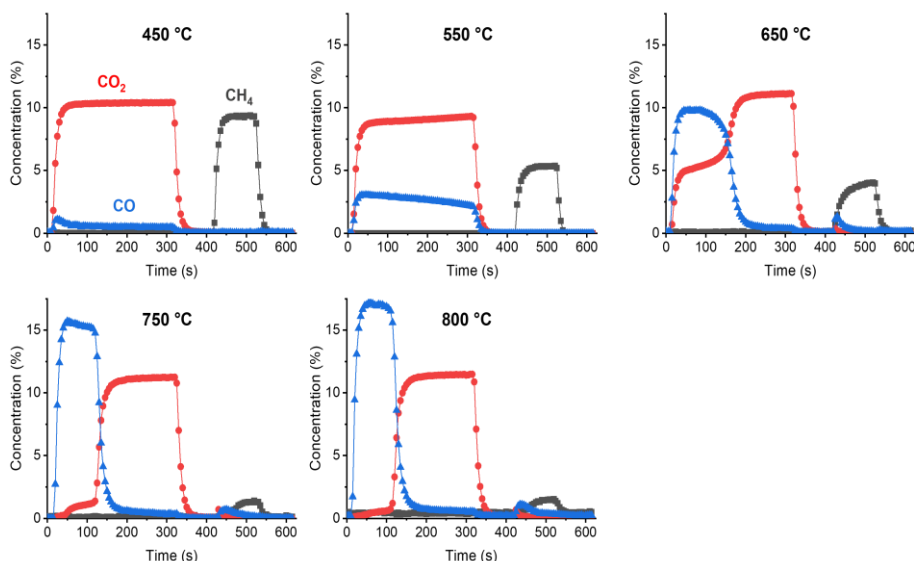

Figure 6.3: Reactor outlet gas concentrations obtained by FTIR spectroscopy during DC-DRM experiments on $Ni-ZrO_2$ catalyst (15 wt% Ni, NZ) at different temperatures. DC-DRM cycle consists of the alternation of diluted CO_2 feed (10.6 vol% in He, 0-300 s), He flush (300-405 s), diluted CH_4 feed (11.2 vol% in N_2, 405-510s), He flush (510-615 s). Total flow rate was kept at 50 mL min^{-1}. Results are averaged over multiple stable cycles of operation.

In agreement with the endothermic nature of the decomposition reaction (Reaction 6.2), the conversion of CH_4 is expected to increase with temperature. At the switch to the CH_4 pulse (405-510 s), the detection of CH_4 was immediate at temperatures between 450 and 650 °C. However, at 750 °C and 800 °C, the signal of CH_4 was detected with a delay, indicating that total conversion of the reactant feed was achieved at the beginning of the pulse. Such behaviour reflects the kinetic enhancement of CH_4 conversion at high temperatures and, accordingly, an increase in the rate of coking.

Above 650 °C, little CO and CO_2 formation was detected in the CH_4 pulse (405-510 s), revealing the ability of the catalyst to provide oxidising species. Considering the negligible

reducibility of the ZrO_2 support, oxidation of CH_4 to CO and CO_2 may be caused by the presence of NiO species, formed upon exposure to the CO_2 pulse. The coke gasification to CO takes place in the CO_2 pulse (0-300 s). At 450 and 550 °C, the coke gasification is limited, thus explaining the low CO_2 conversion profile observed. The concentration of CO in the product stream reached a maximum and then slowly decayed during the CO_2 pulse. However, at 650 °C, the formation of CO becomes favourable and most of the coke was removed in the first 120 s of the CO_2 pulse. At even higher temperatures, the kinetic of coke gasification is greatly enhanced bringing to fast and full conversion of CO_2. At 800 °C, the ZrO_2-supported catalyst was able to continuously provide high conversion of CO_2 and CH_4 in DC-DRM operation.

6.3.3 Promoters for DC-DRM catalysts

Fast deactivation of the catalyst in conventional DRM is commonly addressed to accumulation and uncontrolled growth of carbon deposits. Functionalisation of the catalyst material by addition of metal promoters is then a strategy to reduce the extent of coking and enhance the catalyst stability.[35] In the perspective of DC-DRM operation, fast coking is desirable when associated to the fast and complete conversion of the CH_4 pulse, as long as complete conversion of C deposits and regeneration of the activity is ensured in the CO_2 pulse. In this sense, an ideal catalyst should maximise the conversion of both CO_2 and CH_4 pulses, condition that also reduces the high costs of processing and separation of the product streams (i.e. CO and H_2). As a consequence, it is convenient to investigate the role of metal promoters in the catalytic system in terms of CO_2 and CH_4 conversions and their ratio. Promoted ZrO_2-supported Ni catalysts were prepared by addition of Fe, K or La metal promoters (15 wt% Ni, 5 wt% Fe, K or La). Figure 6.4 compares the DC-DRM performance obtained on the unpromoted and promoted catalysts at different temperatures.
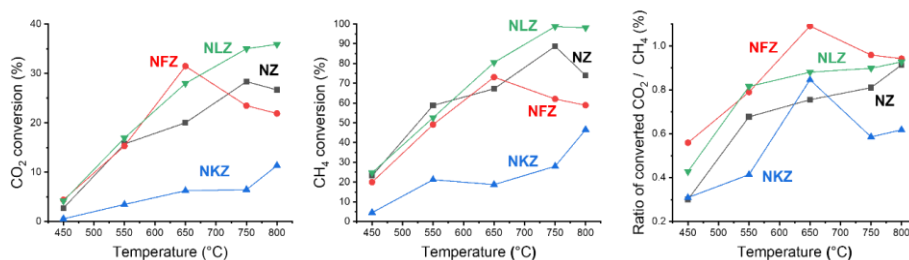

Figure 6.4: Comparison of CO_2 conversion (left), CH_4 conversion (middle) and ratio of converted CO_2/CH_4 (right) during DC-DRM performed at different temperatures over unpromoted Ni/ZrO_2 (15 wt% Ni) and promoted Ni/ZrO_2 catalysts ('NXZ' where 'X' is 'F' for Fe, 'L' for La and 'K' for K; 15 wt% Ni, 5 wt% X). DC-DRM cycle consists of the alternation of diluted CO_2 feed (10.6 vol% in He, 0-300 s), He flush (300-405 s), diluted CH_4 feed (11.2 vol% in N_2, 405-510 s), He flush (510-615 s). Total flow rate was kept at 50 mL min^{-1}. Results are averaged over multiple stable cycles of operation.

It is known that K addition increases the basicity of the catalyst, which favours chemisorption of CO_2 and enhances the gasification of carbon deposits.[36] Looking at Figure 6.4, the addition of K (NKZ) drastically reduced the DC-DRM catalytic activity in terms of both CO_2 and CH_4 conversion compared to the unpromoted Ni/ZrO_2 catalyst (NZ) at all temperatures investigated. At 800 °C, only 11% of the CO_2 and 46% of the CH_4 pulses were converted in

the K-promoted system. The concentration profiles obtained at 800 °C (Figure 6.5) revealed the presence of unreacted CO_2 and CH_4 in the corresponding pulses. In conventional DRM, it has been reported that K improves the catalyst stability by strongly suppressing coke formation.[37] This can be associated to a retarding effect of potassium on the methane decomposition steps (methane dissociation and carbon nucleation).[38] In DC-DRM, this functionality has a negative effect on the global catalytic performance in terms of both CH_4 and CO_2 conversion, with a substantially low X_{CO2}/X_{CH4} ratio. Rather, fast and extensive coking would be desirable as result of the complete CH_4 conversion, and the carbon deposits are expected to be efficiently removed in the CO_2 pulse.

Studies on bimetallic Ni-Fe catalysts reported a positive effect of Fe in DRM catalysis, which improves the gasification of carbon deposits and the resistance to intensive coking.[39] Theofanidis et al.[17] observed that Fe directly participates in the DRM mechanism, mediating the oxidation of C deposits by CO_2. Thanks to its redox properties, Fe gets easily oxidised by the gaseous CO_2 and in turn FeO_x species efficiently oxidise the carbon deposits to form CO and regenerate metallic Fe. Compared to the unpromoted Ni/ZrO_2 system, the tested Fe-promoted catalyst (NFZ in Figure 6.4) showed little improvement in terms of CO_2 and CH_4 conversion in DC-DRM. The increased CO_2 conversion at 650 °C can be explained by the enhanced oxidation of the iron present in the catalyst. By further increasing the reaction temperature, both CO_2 and CH_4 conversion declined, reaching 22% and 59% at 800 °C, respectively. From the gas concentration profiles obtained at 800 °C (Figure 6.5), it is possible to gain further insight about the effect of Fe as promoter. Analysing the CO_2 pulse region (0-300 s), a residual CO_2 signal was detected since the beginning of the cycle associated with a diminished activity in CO_2 conversion. After the initial coke gasification time (ca. 100 s), CO_2 was steadily consumed during the rest of the pulse producing CO. The total higher CO_2 consumption appears then to be linked to the oxidation of the Fe component which proceeded along the whole CO_2 pulse. As a consequence, in the CH_4 pulse, a strong increase in the concentration of the oxidation products (i.e. CO and CO_2) was registered, resulting from the partial and total oxidation of CH_4 by the catalyst lattice oxygen species.
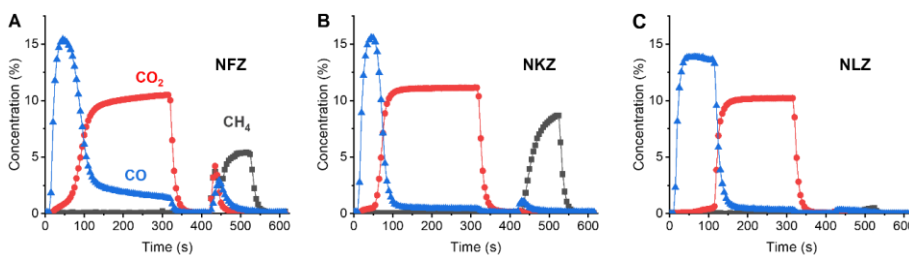

Figure 6.5: Reactor outlet gas concentrations obtained by FTIR spectroscopy during DC-DRM experiments at 800 °C on promoted Ni-ZrO$_2$ catalyst ('NXZ' where 'X' is 'F' for Fe, 'L' for La and 'K' for K; 15 wt% Ni, 5 wt% X). DC-DRM cycle consists of the alternation of diluted CO_2 feed (10.6 vol% in He, 0-300 s), He flush (300-405 s), diluted CH_4 feed (11.2 vol% in N_2, 405-510 s), He flush (510-615 s). Total flow rate was kept at 50 mL min^{-1}. Results are averaged over multiple stable cycles of operation.

As evident in Figure 6.4, the addition of La (NLZ) improved the CO_2 and CH_4 conversions in the whole temperature range, ensuring the best performance for DC-DRM operation among the studied catalysts. Looking at the profile obtained at 800 °C (Figure 6.5) on the NLZ catalyst, periods of almost complete CO_2 and CH_4 conversion are exhibited during the respective pulses. At this temperature and duration of the pulses, 36% of total CO_2 and 98% of total CH_4 fed to the reactor were converted. The ratio between the amount of CO_2 and CH_4 converted tended to 1, meaning that most of the carbon deposits can be removed in the CO_2 phase, a key condition for the long-term stability of the catalytic activity. La addition promotes Ni-based catalyst performance for DRM in terms of activity and catalyst stability. The formation of a La_2OCO_3 phase in DRM conditions mediates the interaction of the catalyst with CO_2 and enhances the gasification of deposited carbon.[40] Moreover, high dispersion of La demonstrated to protect Ni particles from oxidation and sintering.[41] In terms of protecting the active metallic Ni phase from oxidation, the promoting effect of La is evidenced in Figure 6.6. In DC-DRM reaction, the oxidative conditions of the CO_2 pulse promote oxidation of the Ni phase, which represents a well-known cause of catalyst deactivation towards CH_4 decomposition.[34, 42] In the case of unpromoted Ni/ZrO_2 catalyst (Figure 6.6A), water signal is detected in the reactor outlet stream during the CH_4 pulse. The water formation indicates the presence of an oxygen source in the catalyst, which can be identified in a partially oxidised Ni phase formed upon exposure of metallic Ni to the long CO_2 pulse. In the reducing pulse, the NiO species can be reduced by the H_2 produced or by the CH_4 itself, as indicates the small release of CO_2 at the beginning of the pulse. Keeping Ni in a reduced state is fundamental to maintain high CH_4 decomposition yields. DC-DRM operation intrinsically guarantees a limitation of the extent of Ni oxidation, thanks to the short oxidising pulse. By reducing the CO_2 pulse duration to the carbon gasification period (i.e. time of maximum conversion of
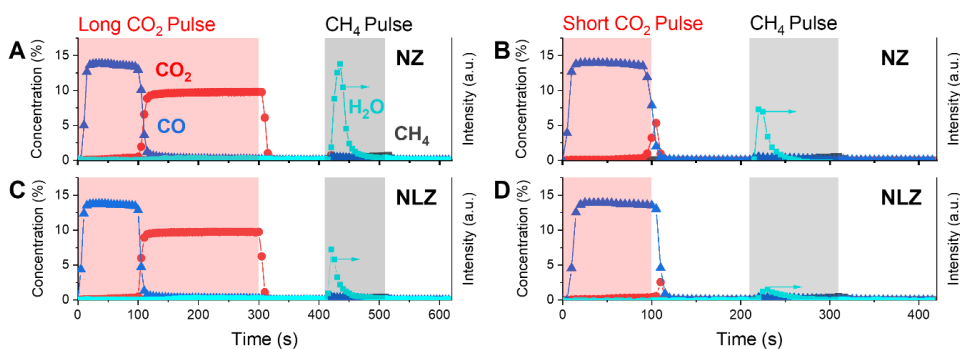

Figure 6.6: Reactor outlet gas concentrations obtained by FTIR spectroscopy during DC-DRM experiments at 800 °C on unpromoted Ni-ZrO_2 (A-C; 15 wt% Ni) and Ni-La/ZrO_2 (B-D; 15wt% Ni, 5 wt% La) catalysts with corresponding FTIR signal of water. Long CO_2 pulse experiments (A-C) consists of the alternation of diluted CO_2 feed (9.9 vol% in He, 0-300 s), He flush (300-405 s), diluted CH_4 feed (10.5 vol% in N_2, 405-510 s), He flush (510-615 s). Short CO_2 pulse experiments (C-D) consists of the alternation of diluted CO_2 feed (9.9 vol% in He, 0-100 s), He flush (100-210 s), diluted CH_4 feed (10.5 vol% in N_2, 210-310 s), He flush (310-420 s). Total flow rate was kept at 50 mL min^{-1}. Results are averaged over multiple stable cycles of operation. For this experiment, catalyst batches calcined at 800 °C were employed.

CO_2, 0-100 s in Figure 6.6A), the extent of Ni oxidation can be partially reduced, as shown in Figure 6.6B.

Ni oxidation by CO_2 is drastically prevented in the La-promoted catalyst, as shown by the decreased release of water in the CH_4 pulse (Figure 6.6C) compared to the unpromoted sample, likely due to a preferential interaction of CO_2 with the basic La-derived phase. By optimising the duration of the CO_2 pulse and limiting it to the carbon gasification period (0-100 s in Figure 6.6C), a minimum water release is detected in the CH_4 pulse, indicating the almost full suppression of the Ni oxidation phenomenon in presence of La (Figure 6.6D).This allows to obtain almost total conversion of the CO_2 pulse together with the prevention of Ni oxidation, thus improving the long-term stability of the catalyst performances.

In such operating conditions, it is possible to perform continuous DC-DRM operation on the NLZ system with about 99% conversion of CH_4 and 96% conversion of CO_2, having CO as main product in the oxidising pulse and H_2 as main product in the reducing pulse. Quantitative evaluation of the H_2 produced was conducted by implementing mass spectrometry during DC-DRM at 800 °C on NLZ (Appendix E2, Figure E2). The results confirmed the selective conversion of CH_4 to H_2 and its production in amounts comparable to the stoichiometry of decomposition reaction.

6.3.4 *Operando* IR thermal imaging

In DC-DRM, coke acts as intermediate between the H_2 production from CH_4 and the subsequent CO generation from CO_2. The alternation between the two short reactant pulses is expected to increase the stability of the process compared to conventional co-feed operation. Fast coking of the catalyst is targeted in the CH_4 pulse, then the reactant feed is switched to CO_2 to selectively and effectively gasify the coke to CO.

Since both CH_4 decomposition and C gasification by CO_2 are endothermic reactions, monitoring the temperature of the catalyst bed during reaction can provide insights about the coke-mediated mechanism of DC-DRM. Figure 6.7 shows the temperature profile of the catalyst bed obtained during the CO_2 and CH_4 pulses of DC-DRM at 800 °C on the NLZ catalyst (catalytic results shown in Figure 6.6D).

A clear temperature decrease was observed for both phases. During the CH_4 pulse, the reduction in temperature took place simultaneously from the front to the end of the catalytic bed until the end of the reduction pulse. This indicates that the catalyst is actively converting CH_4, releasing H_2 in the product stream and accumulating C over the surface of the whole catalyst bed. Considering the homogeneous activity of the bed, accumulation of carbon deposits at the front positions may be favoured in fixed bed configuration, resulting in spatial gradients of coke accumulation. High CH_4 conversion was maintained for the entire duration of the pulse, indicating that the reactant feed was switched before catalyst deactivation.
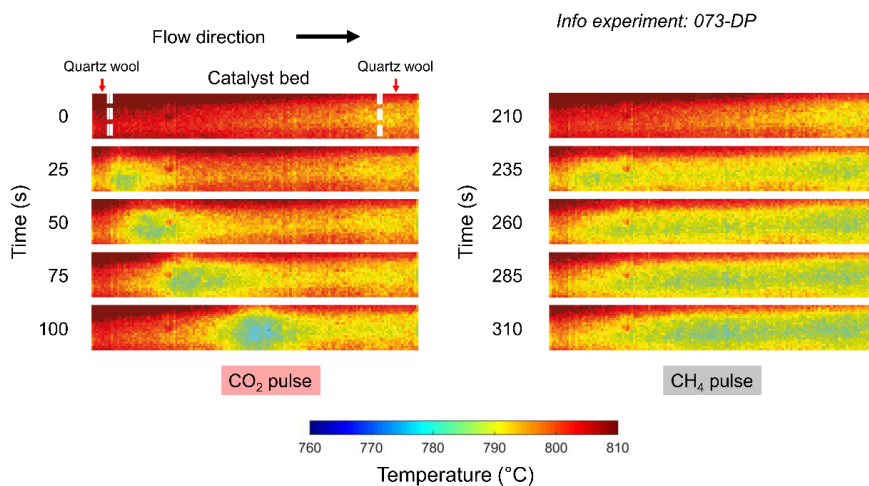
Figure 6.7: *Operando* IR thermal camera imaging of Ni-La/ZrO$_2$ (15wt% Ni, 5 wt% La) catalytic bed during DC-DRM operation at 800 °C. Images acquired during diluted CO$_2$ pulse (0-100 s, left) and diluted CH$_4$ pulse (210-310 s, right). Reactor outlet gas concentrations are reported in Figure 6.6D.

Interestingly, thermal imaging of the bed during the CO$_2$ pulse showed a clear 'cold spot' that propagated in the direction of the flow, reflecting the progress of the endothermic gasification reaction along the catalytic bed. The carbon deposits accumulated in the previous CH$_4$ pulse were gasified to CO resulting in high CO$_2$ conversions (96%). The cold spot represents a portion of the catalytic bed in which intense gasification of the C takes place, with CO$_2$ being largely converted. The removal of C species was completed progressively along the catalytic bed, as indicated by the 'cold spot' moving towards the end of the bed. At the end of the CO$_2$ pulse (100 s), the majority of the carbon deposits were gasified and unreacted CO$_2$ started to be detected in the reactor effluent stream.

6.3.5   Transmission electron microscopy (TEM)

The insights into the coke-mediated mechanism obtained by *operando* IR thermal imaging were further confirmed by Transmission Electron Microscopy (TEM). Figure 8 presents the TEM micrographs obtained for the fresh and spent NLZ catalyst samples. For the fresh NLZ sample calcined at 500 °C (Figure 6.8A-C), the absence of big agglomerates indicated a good dispersion of the Ni and La phases on the ZrO$_2$ support. In Figure 6.8C in particular, small particles (1-2 nm) were spotted on top of the ZrO$_2$ particles (10 nm), suggesting a high dispersion of the active phases obtained with the synthesis. To investigate the formation of coke and the effectiveness of its gasification during DC-DRM at 800°C, spent samples were collected after stopping the reaction at the end of the CH$_4$ pulse (Figure 6.8D-F) and at the end of the CO$_2$ pulse (Figure 6.8G-I). The high temperatures of reduction pre-treatment and DC-DRM reaction promoted the sintering of the metallic Ni phase, which tended to form agglomerates of size up to 100 nm. As expected, extensive coking of the catalyst took place in the CH$_4$ pulse, resulting in the pervasive growth of carbon-based structures on the catalyst (Figure 6.8D). In agreement with consolidated knowledge about the decomposition of light hydrocarbons on Ni, two main types of carbon structures were recognised, namely carbon

155

whiskers and graphitic layers.[38] Bigger Ni agglomerates above 50 nm were generally encapsulated in thin graphitic layers, while smaller Ni particles detached from the support and dynamically participated to the growth of carbon whiskers, forming filamentous hollow carbon structures of various diameters and lengths. TEM micrographs of the spent sample after the CO_2 pulse (Figure 6.8 G-I) shows that the majority of the carbon species were effectively removed to form CO and the catalyst was regenerated. A wide distribution of sizes for Ni phase was found, with sintered particles in the range of 50-80 nm. At reaction conditions, however, sintering did not cause deactivation of the catalyst performance.
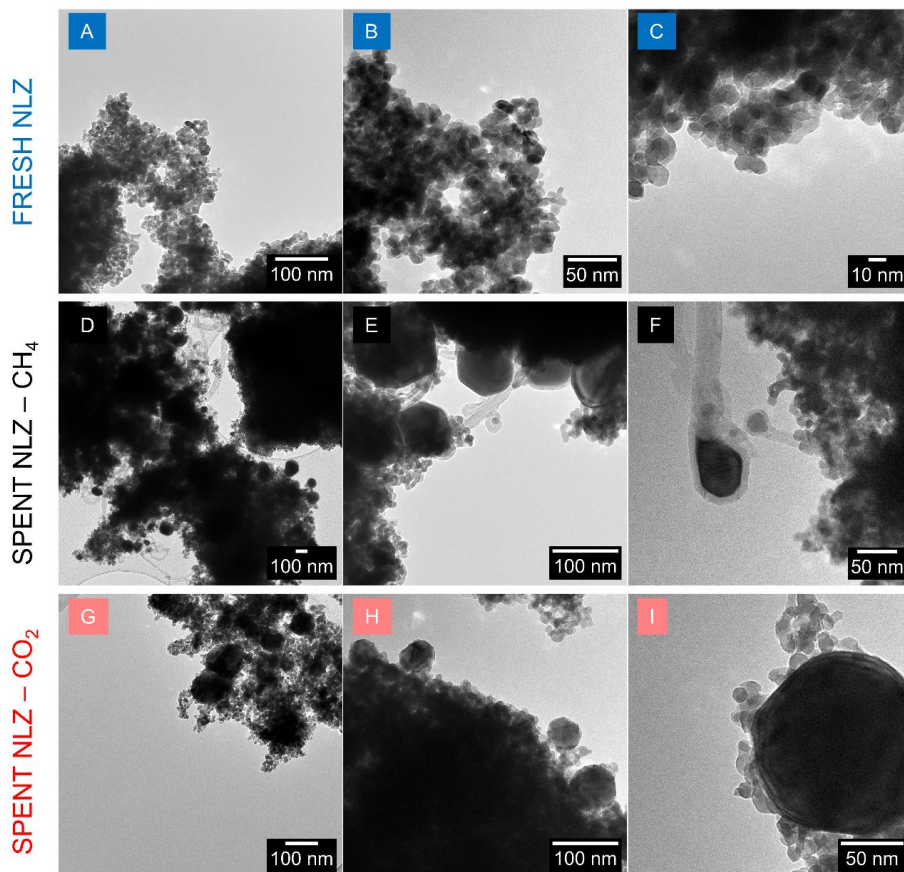

Figure 6.8: TEM micrographs of the fresh NLZ sample calcined at 500 °C (A-C) and spent NLZ samples after DC-DRM at 800 °C with reactions stopped at the end of the CH_4 pulse (D-F) and at the end of the CO_2 pulse (G-I). DC-DRM cycle consists of the alternation of diluted CO_2 feed (9.9 vol% in He, 0-100s), He flush (100-210 s), diluted CH_4 feed (10.5 vol% in N_2, 210-310s), He flush (310-420 s). Total flow rate was kept at 50 mL min^{-1}. After stopping the reaction, the catalysts were brought to room temperature in inert flush (He) at 10 °C min^{-1} cooling rate.

6.3.6 Stability of La-promoted Ni/ZrO$_2$

The accumulation of solid carbon deposits in catalytic DRM reactors leads to several complication, including catalyst fouling, pressure build-up and reactor blockage.[43] DC-DRM principle of exposing the catalysts to short reducing and oxidising pulses is expected to limit the irreversible accumulation of stable carbon deposits in CH$_4$, facilitating their complete gasification in CO$_2$ and regenerating the catalytic activity at each cycle. Figure 6.9 shows the results obtained for a NLZ catalyst during extended catalytic activity tests at 800 °C (45 reaction cycles). Comparing the catalytic activity of the initial cycles (2-10) with the last 15 cycles of operation (31-45), a remarkable stability of the performances was observed in terms of CO$_2$ and CH$_4$ conversion, with the absence of noticeable deactivation trends. These results indicates the ability of the NLZ system to provide high and stable conversion of CO$_2$ and CH$_4$ in DC-DRM conditions. After the last CO$_2$ pulse of the stability test, the reaction was stopped and the catalyst cooled down in He for ex-situ investigation.
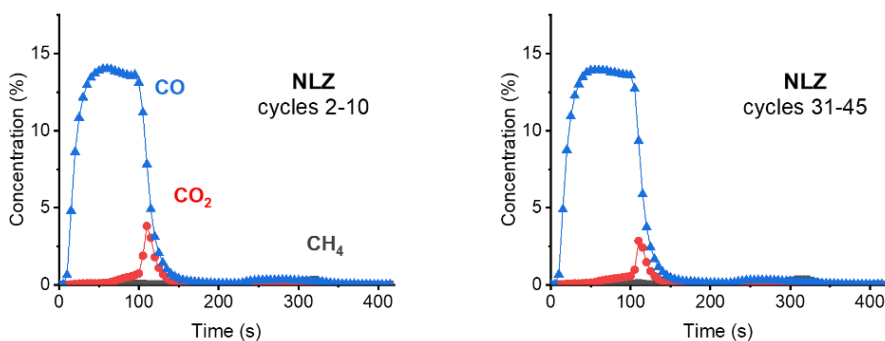

Figure 6.9: Reactor outlet gas concentrations obtained by FTIR spectroscopy during DC-DRM stability test at 800 °C on La-promoted Ni/ZrO$_2$ catalyst (15 wt% Ni, 5 wt% La, NLZ). DC-DRM cycle consists of the alternation of diluted CO$_2$ feed (9.9 vol% in He, 0-100 s), He flush (100-210 s), diluted CH$_4$ feed (10.5 vol% in N$_2$, 210-310 s), He flush (310-420 s). Total flow rate was kept at 50 mL min^{-1}. Results presented are averaged of cycles 2-10 (left) and cycles 31-45 (right) of operation.

The high reaction temperature and highly reducing conditions of DC-DRM are expected to promote the sintering of Ni particles. The changes observed in X-ray diffractograms before and after reaction (Appendix E3, Figure E3) indicated the presence of sintering phenomena involving both the Ni crystallites and the supports, as already shown in TEM micrographs of the spent NLZ sample (Figure 6.8). This is expected, considering that the reaction was performed at temperature substantially higher than the calcination conditions (500 °C, air). The Ni and support sintering at high temperatures was also evident from the drop of the BET surface area of the spent sample (Table E1). However, the activity of the catalysts in DC-DRM was not undermined by the observed formation of Ni crystallites, indicating that their growth is controlled on the ZrO$_2$ support. The exposure of the catalyst to short oxidative/reducing pulses seems to prevent fast and irreversible deactivation of the catalytic system. In fact, a NLZ catalyst synthesised with calcination at 800 °C showed similar catalytic behaviour (Figures 6.6B-D), despite the agglomeration of NiO in the fresh sample suggested by the increased degree of crystallinity for the NiO reflexes in XRD (Figure E3). Interestingly, no drops in the BET surface area after reaction was noticed for the NLZ catalyst calcined at 800 °C (Table E2). These results confirmed that the ZrO$_2$-supported catalytic system is able

to withstand DC-DRM reaction conditions and control the sintering of active metals and support without any noticeable deactivation trend in the first 4.5 hours of operation.

Extensive coking is another common cause for catalyst deactivation in DRM. When the NLZ catalyst was tested for conventional DRM (800 °C, 50 mL min^{-1}, CO_2 10 vol%, CH_4 10 vol%), a fast pressure build-up was registered in the reactor (> 0.5 bar), requiring to stop the reaction after 15 minutes of operation. Compared to the co-feed conditions, the separation of the CO_2 and CH_4 pulses in DC-DRM prevents the accumulation and uncontrolled growth of carbon deposits and allows the complete regeneration of the catalyst at each cycle. Similarly, no increase in pressure drop has been observed during cyclic alternation of CH_4 decomposition and C gasification by steam on Ni-based catalysts.[44] Notwithstanding, analysis of the NLZ catalyst after DC-DRM revealed the presence of a limited amount of carbon deposits after 45 cycles of operation at 800°C. Thermogravimetric analysis (Appendix E3, Figure E4) indicated the presence of solid carbon deposits in the spent NLZ catalyst, which were removed in air below 600 °C. Although the extent of carbon accumulation did not cause deactivation of the catalyst, optimising the catalytic material for complete carbon gasification can be beneficial for long-term operation. Extending the length of the CO_2 pulse can improve the gasification of coke, at the price of purity of the product stream and of the Ni oxidation enhancement. Engineering of several reaction parameters, including the volumetric flow rate and composition of reactant feeds, together with the optimisation of the catalyst composition can target the full removal of carbon deposits in view of long-term utilisation of the catalyst.

6.3.7   Reducible metal oxide supports for DC-DRM

Compared to irreducible metal oxides, the employment of a reducible metal oxide support offers the possibility of directly oxidising CH_4 in the reducing pulse thanks to the active participation of the lattice oxygen to the reaction. The introduction of an additional oxidant species, represented by the lattice oxygen species of the reducible oxide, is also expected to enhance the selective gasification of carbon deposits, thus limiting their accumulation. Employing TiO_2 rutile as support material, a La-promoted Ni catalyst (15 wt% Ni, 5 wt% La) was prepared by incipient wetness impregnation and tested for DC-DRM. The results of a long-term catalytic test (45 cycles) are shown in Figure 6.10.
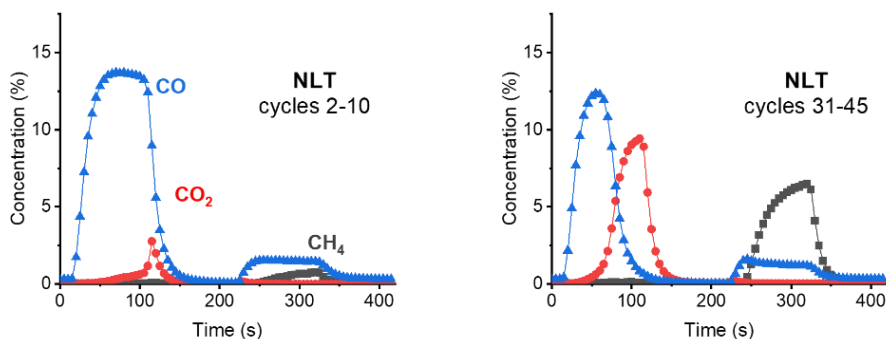
Figure 6.10: Reactor outlet gas concentrations obtained by FTIR spectroscopy during DC-DRM stability test at 800 °C on La-promoted Ni/TiO$_2$ catalyst (15 wt% Ni, 5 wt% La, NLT). DC-DRM cycle consists of the alternation of diluted CO$_2$ feed (0-100 s), He flush (100-210 s), diluted CH$_4$ feed (210-310 s), He flush (310-420 s). Total flow rate was kept at 50 mL min^{-1}. Results presented are averaged of cycles 2-10 (left) and cycles 31-35 (right) of operation.

In the first 10 cycles of operation, the TiO$_2$-supported system (NLT) exhibited high conversions of CO$_2$ and CH$_4$. Noticeably, the behaviour in the reducing CH$_4$ pulse was significantly different from the one observed in the ZrO$_2$-supported counterpart. Employing the reducible TiO$_2$ as support enabled a constant supply of lattice oxygen species for the selective oxidation of CH$_4$ or carbon deposits to CO. Direct participation of the TiO$_2$ lattice oxygen in the selective oxidation of CH$_4$ was already observed in Chapter 4. The high stability of surface oxygen vacancy in rutile TiO$_2$ is expected to favour the removal of lattice oxygen which can efficiently oxidise the carbon deposits on the catalytic surface.[45]

This contribution of lattice oxygen from the support to form CO directly changes the composition of the product mixture in the CH$_4$ pulse from pure H$_2$ to a H$_2$-rich syngas mixture (Appendix E4, Figure E5). By proper tuning of the lattice oxygen diffusion rate, as well as the composition of the reactant stream, a versatile and valuable syngas mixture can be targeted as direct product of the CH$_4$ pulse, bringing additional benefits to the process including the softening of technological requirements associated with pure H$_2$ streams (explosion limit, thermal conductivity, pipelines specifications). In the subsequent oxidative pulse, high CO$_2$ conversion were maintained, confirming the ability of the systems to provide efficient gasification of the carbon deposits together with the replenishment of the lattice vacancies and reoxidation of the metal oxide support.

However, after 45 cycles of operation, the TiO$_2$-supported catalyst showed a marked deactivation, with extensive loss in both CO$_2$ and CH$_4$ conversions (Figure 6.10). At the same time, the supply of lattice oxygen during the CH$_4$ pulse was preserved and the release of CO was not affected by the deactivation of the catalyst. Thermogravimetric analysis (Figure E4) of the spent catalyst revealed no weight loss trend under heating in air up to 1000 °C, indicating that the catalyst is able to efficiently remove the carbon deposits, also thanks to the contribution of oxygen species from the support lattice. Those findings excluded the contribution of solid carbon accumulation in the deactivation of catalyst observed for the TiO$_2$-supported catalyst. XRD of the spent catalyst (Figure E3) revealed that narrow metallic Ni reflexes with strong intensity were found in the spent NLT catalyst, indicating the

aggregation of Ni particles into big crystallites. Takenaka et al.[46] reported that at low Ni loadings (2.5 wt%), the Ni/TiO_2 system can provide stability of performances in cycles of CH_4 decomposition and regeneration by CO_2. However, a Ni loading of 10 wt% on TiO_2 led to fast deactivation of the catalyst towards CH_4 decomposition, due to agglomeration of the Ni particles in bigger aggregates. Considering the high loadings employed in this work (15 wt% Ni, 5 wt% La), the low surface area and porosity of the TiO_2-supported catalyst compared to the ZrO_2-supported counterpart (Table E1) clearly favoured the aggregation of the Ni particles and the deterioration of the catalytic activity observed.

The addition of TiO_2 to form binary oxides is known to strongly increase the number of surface acidic sites and their strength.[47] In the case of TiO_2-ZrO_2, both acidity and basicity are enhanced by incorporation of TiO_2.[48] In order to combine the stability of performances provided by an irreducible oxide as support (ZrO_2) with the possibility of tuning the product composition and introducing an additional route for coke gasification by a reducible support (TiO_2), a mixed oxide was synthesised targeting a surface doping of ZrO_2 with TiO_2.

For this purpose, ZrO_2 was impregnated with a Ti isopropoxide solution under inert atmosphere to ensure the dispersion of the Ti precursor in the pores of the ZrO_2 template. After this, the catalyst was dried at 80 °C and calcined at 800 °C in air to ensure the formation of the mixed oxide. XRD of the TiO_2-ZrO_2 support (Appendix E5, Figure E6, TZ) showed only reflexes associated to the ZrO_2 phase, suggesting the high dispersion of the Ti-derived phase.

A La-promoted Ni catalyst (NLTZ, Ni 15 wt%, La 5%) was then prepared by incipient wetness impregnation of the TiO_2-ZrO_2 mixed oxide support. Figure 6.11 shows the results obtained for CL-DRM at 800 °C on the NLTZ catalyst. Compared to the TiO_2-supported catalyst, the NLTZ system exhibited higher stability of the performances, with high CO_2 conversion maintained after 45 cycles and limited deactivation in terms of CH_4 conversion. Compared to the ZrO_2-supported catalyst, an additional oxidative route was activated by the insertion of TiO_2, which was able to provide lattice oxygen species and led to the formation of CO in the CH_4 pulse. The distinct catalytic functionalities introduced by ZrO_2 and TiO_2 materials were still recognised in the last 15 cycles of DC-DRM operation, although the slight increase of CH_4 signal detected at the outlet in the last 15 cycles suggests a possible weakening in the synergetic behaviour of the two oxidic phase.
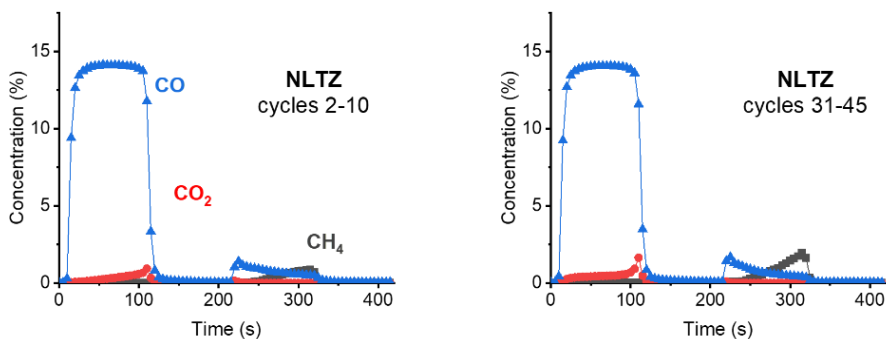
Figure 6.11: Reactor outlet gas concentrations obtained by FTIR spectroscopy during DC-DRM stability test at 800 °C on La-promoted Ni/TiO_2-ZrO_2 catalyst (15 wt% Ni, 5 wt% La, NLTZ). DC-DRM cycle consists of the alternation of diluted CO_2 feed (0-100 s), He flush (100-210 s), diluted CH_4 feed (210-310 s), He flush (310-420 s). Total flow rate was kept at 50 mL min^{-1}. Results presented are averaged of cycles 2-10 (left) and cycles 31-35 (right) of operation.

Functionalising the ZrO_2 support with a reducible oxide as TiO_2 can enhance the oxidation of the carbon deposits, while maintaining high stability of the catalytic performances and potentially leads the production of a H_2-rich syngas directly in the CH_4 pulse (Figure E7).

6.4   Conclusions

With the aim of overcoming the limitations of the conventional co-feed operation, we propose in this work an alternative unsteady-state process named dynamic coke-mediated dry reforming of methane (DC-DRM). In DC-DRM, CO_2 and CH_4 reactant pulses are alternatingly sent to the catalytic bed, targeting their complete conversion and achieving the complete separation of the H_2 and CO product stream. Separation of the H_2 and CO_2 streams also suppresses the undesired reverse water-gas shift reaction that, in co-feed operation, consumes valuable H_2 product to produce steam (H_2O). Exposure of the catalyst to short oxidising and reducing pulses can enhance the stability of the system, preventing accumulation of carbon deposits which brings to deactivation and catalyst fouling.

Ni-based catalyst for DC-DRM were synthesised and investigated. Among the irreducible metal oxides tested as support material, ZrO_2 acted as a stable template to the active metal component by containing sintering and ensuring high and comparable CO_2 and CH_4 conversion. On the Ni/ZrO_2 catalytic system, the effect of different metal promoters (La, Fe, K) on the conversion of CH_4 and CO_2 was also evaluated. The addition of Fe resulted in increased oxidation of the catalyst in CO_2 and resulted in total oxidation of CH_4 to undesired CO_2. The presence of K, and the increased basicity of the catalysts, provoked substantial loss in both CH_4 and CO_2 conversions. Distinctively, an enhancement of the DC-DRM performance was found for the La-promoted Ni/ZrO_2 system (NLZ), which enhanced the conversion of CO_2 and suppressed the oxidation of the Ni component. *Operando* IR thermal imaging of the catalytic bed gave relevant insights into the endothermic reaction routes involved in DC-DRM. Fast coking takes place homogenously along the bed during the decomposition of CH_4, while during the CO_2 pulse, a 'cold spot' representing the endothermic gasification of C progressively moves along the flow direction until complete removal of the carbon deposits. The $Ni-La/ZrO_2$ catalyst provided stable activity and approached complete conversion of the CH_4 and CO_2 reactant pulses to H_2 and CO, respectively, in 45 cycles of operation at 800°C.

Thanks to the flexibility of the DC-DRM process, specific functionalisation of the catalyst can directly enable tuning and control of the product stream composition. Including a reducible metal oxides as support (TiO_2 and mixed TiO_2-ZrO_2), the participation of lattice oxygen in the selective partial oxidation of methane is demonstrated. Apart from introducing a selective oxidation route that prevents coke accumulation, this specific catalytic functionality enables the production of syngas mixtures with high and tunable H_2/CO ratio directly in the CH_4 pulse, enhancing the versatility of the process and expanding the range of target downstream processes.

Appendix E

E1. X-ray diffraction of synthetised Ni catalysts

Powder X-ray diffraction patterns were acquired to determine the crystal structure of the synthesised catalysts and to verify the outcome of the synthetic procedure.

Figure E1 reports the result obtained for the Ni catalysts prepared on SiO_2 (NS), Al_2O_3 (NA) and ZrO_2 (NZ) supports, together with the promoted Ni/ZrO_2 catalysts with Fe (NFZ), La (NLZ) and K (NKZ). For all the samples, the diffraction pattern shows reflexes typical of NiO phase (PDF 22-1189) and the relative support materials. Additional crystalline phases were not detected, indicating the effectiveness of the synthesis method. For the promoted Ni/ZrO_2 samples, absence of reflexes associated with the metal promoters is related to the low loading (5 wt%) and indicates a high dispersion on the catalyst material.
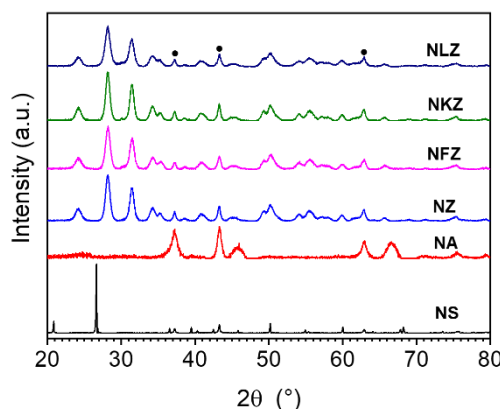

Figure E5. X-ray diffractogram of as-synthetised supported Ni catalysts (15 wt% Ni) on SiO_2 (NS), γ-Al_2O_3 (NA) and ZrO_2 (NZ) and promoted Ni/ZrO_2 catalyst with Fe (NFZ, 5 wt% Fe), K (NKZ, 5 wt% K) and La_2O_3 (NLZ, 5 wt% La). Reflexes from NiO phase (●) are found at around 44°, 51° and 75°.

E2. Catalytic activity – H_2 production on La-promoted Ni/ZrO_2

Quantitative evaluation of the H_2 was implemented by employing mass spectrometry (MS) of the associated fragment (m/z = 2) after calibration of the signal with H_2 flows of known concentration. Calibration was performed before and after the reaction to account for changes in the signal baseline. The obtained concentration values were confirmed by single point GC injections during reaction.

Figure E2 shows the concentration profiles obtained during DC-DRM operation on a La-promoted Ni/ZrO$_2$ catalyst. High conversion of CO$_2$ and CH$_4$ were obtained, resulting in a virtually pure product stream of CO and H$_2$ in the respective pulses.
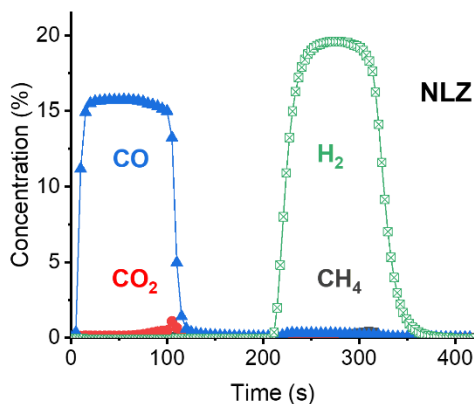

Figure E2. Reactor outlet gas concentrations obtained by FTIR spectroscopy and mass spectrometry during DC-DRM at 800 °C on La-promoted Ni/ZrO$_2$ catalyst (15 wt% Ni, 5 wt% La, NLZ). DC-DRM cycle consists of the alternation of diluted CO$_2$ feed (0-100 s), He flush (100-210 s), diluted CH$_4$ feed (210-310 s), He flush (310-420 s). Total flow rate was kept at 50 mL min^{-1}. Results presented are averaged of several stable cycles of operation.

E3. Characterisation of spent catalysts

To characterise the sample employed in DC-DRM stability test at 800 °C, the catalytic reaction was stopped at the 45th cycle of operation after the last CO$_2$ feed phase, bringing the reactor temperature down to ambient in inert flow (He). After that, the spent catalysts were removed from the reactor and employed for further characterisations.

Figure E3 shows the X-ray diffractograms obtained for La-promoted Ni/ZrO$_2$ (NLZ) and Ni/TiO$_2$ (NLT) catalysts, comparing the patterns of the fresh samples calcined at 500 °C before (black pattern) and after (red pattern) DC-DRM stability test at 800 °C. For both ZrO$_2$ and TiO$_2$ samples, NiO reflexes disappeared after reaction in favour of the formation of metallic Ni reflexes (53°, 61°). A strong increase in crystallinity was noticed in the TiO$_2$-supported sample after reaction. Only a small increase in the intensity of the reflexes was noticed for the NLZ catalyst, indicating that ZrO$_2$ as support can prevent sintering of the NiO particles ensuring high stability of the catalytic performances.

The NLT sample calcined at 800 °C displays new reflexes at 28°, 39° and 58° indicating the formation of a new crystalline phase assigned to nickel titanate (PDF 83-0198).
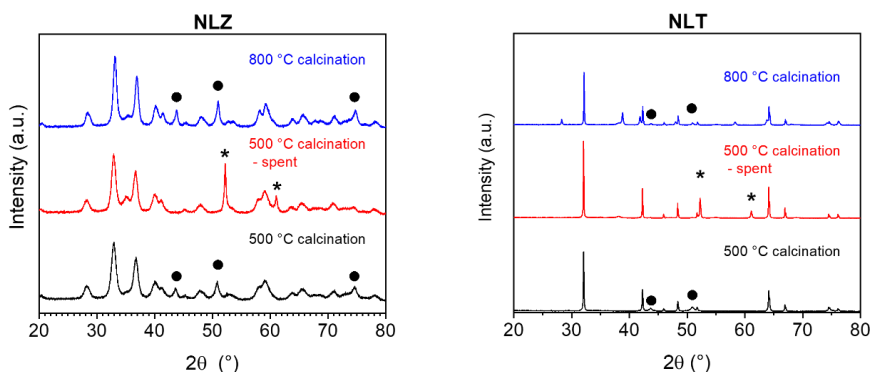
Figure E3. X-ray diffractogram of La-promoted Ni/ZrO$_2$ catalysts (NLZ, left) and Ni/TiO$_2$ catalysts (NLT, right). Reflexes from NiO phase (●) and metallic Ni (*) are highlighted.

Figure E4 shows the thermogravimetric analysis (TGA) profiles obtained on the NLT and NLZ spent samples employed in DC-DRM stability test at 800 °C. The reaction was stopped after the last CO$_2$ pulse, in order to ensure the completion of the C gasification reaction and investigate the ability of the catalyst to fully remove the carbon deposits. TGA was conducted by heating the spent catalyst up to 1000 °C (10 °C min^{-1} heating rate) under air flow. Both samples showed an increase in weight associated with the oxidation of the metallic Ni component by air. The derivative of weight change reported a peak at around 300 °C for NLZ and 500 °C for NLT, indicating the maximum rate of the Ni oxidation process. After that, a slight decrease in weight was observed in the NLZ, confirmed by the negative peak of the derivative weight change at around 500 °C. This loss in the catalyst weight was associated with the gasification of residual carbon deposits in air, which were not removed by CO$_2$. In the case of NLT, no weight loss phenomenon were individuated in the whole temperature range, indicating that the catalyst was be able to provide full gasification of the carbon deposits.
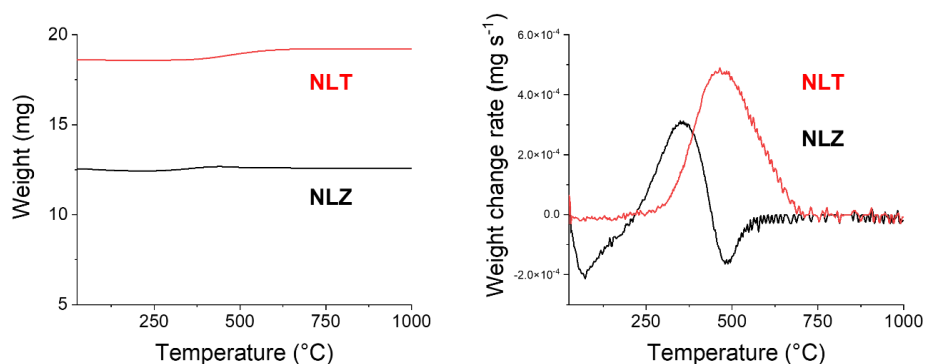

Figure E4. Thermogravimetric analysis of La-promoted Ni/ZrO$_2$ catalysts (NLZ) and Ni/TiO$_2$ catalysts (NLT). Relative weight change over temperature and (left) derivative of weight loss with respect to time over temperature (right). Samples were kept 10 min at room temperature then heated up at 10 °C min^{-1} rate until 800°C.

E4. Catalytic activity – H₂ production on La-promoted Ni/TiO₂

Figure E5 shows the concentration profiles obtained during DC-DRM operation on a La-promoted Ni/TiO$_2$ catalyst. High conversion of CO$_2$ and CH$_4$ were obtained. The redox ability of the TiO$_2$ support promoted an additional route in the CH$_4$ pulse, resulting in the selective partial oxidation of CH$_4$ to CO. As a result, a syngas with high H$_2$/CO ratio ($\approx$ 8) can be obtained.

Quantitative evaluation of the H$_2$ was implemented by mass spectrometry (See section S3).

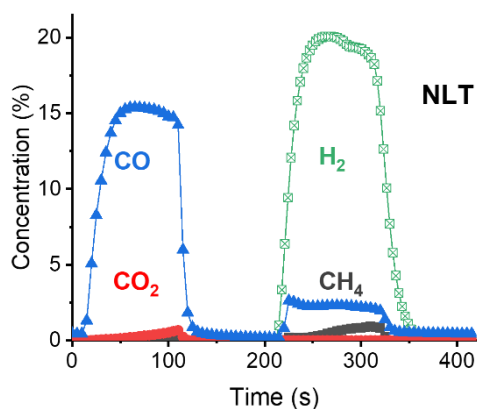**Figure E5.** Reactor outlet gas concentrations obtained by FTIR spectroscopy and mass spectrometry during DC-DRM at 800 °C on La-promoted Ni/TiO$_2$-ZrO$_2$ catalyst (15 wt% Ni, 5 wt% La, NLTZ). DC-DRM cycle consists of the alternation of diluted CO$_2$ feed (0-100 s), He flush (100-210 s), diluted CH$_4$ feed (210-310 s), He flush (310-420 s). Total flow rate was kept at 50 mL min⁻¹. Results presented are averaged of several stable cycles of operation.

E5. X-ray diffractograms – TiO₂-ZrO₂ mixed oxide

Figure E6 shows the X-ray diffractograms obtained for mixed TiO$_2$-ZrO$_2$ oxide (TZ, Ti/Zr molar ratio 15/85) and the La-promoted Ni/TiO$_2$-ZrO$_2$ catalyst (NLTZ, 15 wt% Ni, 5 wt% La). Apart from the NiO reflexes shown in the promoted sample, only reflexes of the ZrO$_2$ support were recognised in both samples, possibly indicating the high dispersion of the Ti-derived phase.
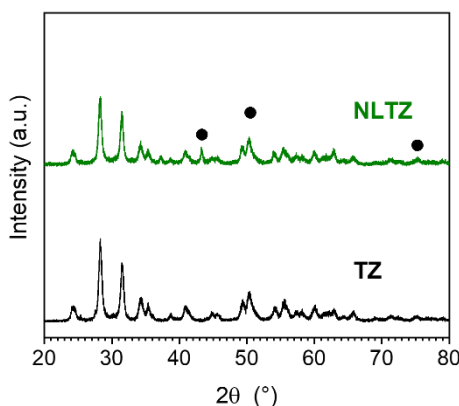
Figure E6. X-ray diffractogram of La-promoted Ni/ZrO$_2$ catalysts (NLZ, left) and Ni/TiO$_2$ catalysts (NLT, right). Reflexes from NiO phase (●) are highlighted.

E6. Catalytic activity – H$_2$ production on La-promoted Ni/TiO$_2$

Figure E 7 shows the concentration profiles obtained during DC-DRM operation on a La-promoted Ni/TiO$_2$-ZrO$_2$ catalyst (NLTZ, 15 wt% Ni, 5 wt% La). High conversion of CO$_2$ and CH$_4$ were obtained. The ZrO$_2$ support provided high dispersion of the Ni component and stable catalytic activity through the cycles. At the same time, the presence of Ti in the mixed oxide support promoted redox functionality in the catalyst, resulting in the selective partial oxidation of CH$_4$ to CO. However, the CO signal exhibit a decay trend in the CH$_4$ pulse, indicating that the limited amount of Ti introduced (Ti/Zr molar ratio 15/85) was not able to provide sufficient lattice oxygen species to achieve a stable production of CO.

Quantitative evaluation of the H$_2$ was implemented by mass spectrometry (See section S3).
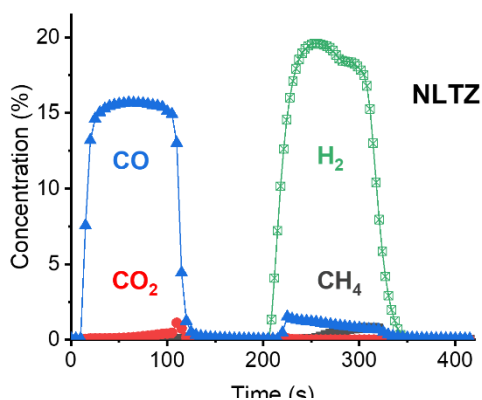
Figure E7. Reactor outlet gas concentrations obtained by FTIR spectroscopy and mass spectrometry during DC-DRM at 800 °C on La-promoted Ni/TiO$_2$ catalyst (15 wt% Ni, 5 wt% La, NLT). DC-DRM cycle consists of the alternation of diluted CO$_2$ feed (0-100 s), He flush (100-210 s), diluted CH$_4$ feed (210-310 s), He flush (310-420 s). Total flow rate was kept at 50 mL min^{-1}. Results presented are averaged of several stable cycles of operation.

Table E1 – BET surface area of catalysts calcined at 500 °C

Catalyst	BET Surface area $(m^2\ g^{-1})$
NLZ	63
NLZ spent (stability test at 800 °C)	21
NLT	6
NLTZ	29
NLTZ spent (stability test at 800 °C)	29

Table E2 – BET surface area of catalysts calcined at 800 °C

Catalyst	BET Surface area $(m^2\ g^{-1})$
NLZ	32
NLZ spent (stability test at 800 °C)	34
NLT	<4

References

1.   M. C. J. Bradford and M. A. Vannice, *Catal. Rev.*, 1999, **41**, 1-42.
2.   J. R. Rostrup-Nielsen, J. H. B. Hansen and L. M. Aparicio, *J. Jpn. Petrol. Inst.*, 1997, **40**, 366-377.
3.   A. Sternberg and A. Bardow, *ACS Sustain. Chem. Eng.*, 2016, **4**, 4156-4165.
4.   J. M. Lavoie, *Front. Chem.*, 2014, **2**, 81.
5.   A. M. Gadalla and B. Bower, *Chem. Eng. Sci.*, 1988, **43**, 3049-3062.
6.   C. Peinado, D. Liuzzi, M. Retuerto, J. Boon, M. A. Peña and S. Rojas, *Chem. Eng. J. Adv.*, 2020, **4**, 100039.
7.   G. Celik, A. Arinan, A. Bayat, H. O. Ozbelge, T. Dogu and D. Varisli, *Top. Catal.*, 2013, **56**, 1764-1774.
8.   K. Wittich, M. Krämer, N. Bottke and S. A. Schunk, *ChemCatChem*, 2020, **12**, 2130-2147.
9.   R. Mann, *Catal. Today*, 1997, **37**, 331-349.
10.   N. Abdel Karim Aramouni, J. Zeaiter, W. Kwapinski and M. N. Ahmad, *Energy Convers. Manage.*, 2017, **150**, 614-622.
11.   J. R. Rostrup-Nielsen, *Catal. Today*, 1993, **18**, 305-324.
12.   M. C. J. Bradford and M. A. Vannice, *Appl. Catal. A: Gen.*, 1996, **142**, 73-96.
13.   D. Pakhare and J. Spivey, *Chem. Soc. Rev.*, 2014, **43**, 7813-7837.
14.   J. R. Rostrup-Nielsen, in *Catalysis: Science and Technology Volume 5*, eds. J. R. Anderson and M. Boudart, Springer Berlin Heidelberg, Berlin, Heidelberg, 1984, DOI: 10.1007/978-3-642-93247-2_1, pp. 1-117.
15.   W.-J. Jang, J.-O. Shim, H.-M. Kim, S.-Y. Yoo and H.-S. Roh, *Catal. Today*, 2019, **324**, 15-26.
16.   Z. Bian, S. Das, M. H. Wai, P. Hongmanorom and S. Kawi, *ChemPhysChem*, 2017, **18**, 3117-3134.
17.   S. A. Theofanidis, V. V. Galvita, H. Poelman and G. B. Marin, *ACS Catal.*, 2015, **5**, 3028-3039.
18.   J. Zhang, H. Wang and A. K. Dalai, *J. Catal.*, 2007, **249**, 300-310.
19.   X. Zhu, Q. Imtiaz, F. Donat, C. R. Müller and F. Li, *Energy Environ. Sci.*, 2020, **13**, 772-804.
20.   M. Tang, L. Xu and M. Fan, *Appl. Energy*, 2015, **151**, 143-156.
21.   A. Lyngfelt, B. Leckner and T. Mattisson, *Chem. Eng. Sci.*, 2001, **56**, 3101-3113.
22.   J. Adanez, A. Abad, F. Garcia-Labiano, P. Gayan and L. F. de Diego, *Prog. Energy Combust. Sci.*, 2012, **38**, 215-282.
23.   M. Najera, R. Solunke, T. Gardner and G. Veser, *Chem. Eng. Res. Des.*, 2011, **89**, 1533-1543.
24.   S. Bhavsar, M. Najera and G. Veser, *Chem. Eng. Technol.*, 2012, **35**, 1281-1290.
25.   A. Löfberg, T. Kane, J. Guerrero-Caballero and L. Jalowiecki-Duhamel, *Chem. Eng. Process.*, 2017, **122**, 523-529.
26.   S. M. Kim, P. M. Abdala, M. Broda, D. Hosseini, C. Copéret and C. Müller, *ACS Catal.*, 2018, **8**, 2815-2823.
27.   L. C. Buelens, V. V. Galvita, H. Poelman, C. Detavernier and G. B. Marin, *Science*, 2016, **354**, 449.
28.   V. V. Galvita, H. Poelman, C. Detavernier and G. B. Marin, *Appl. Catal., B*, 2015, **164**, 184-191.
29.   L. Hu and A. Urakawa, *J. CO2 Util.*, 2018, **25**, 323-329.
30.   D. Pinto, V. van der Bom Estadella and A. Urakawa, *Catal. Sci. Technol.*, 2022, **12**, 5349-5359.
31.   S. Bang, E. Hong, S. W. Baek and C.-H. Shin, *Catal. Today*, 2018, **303**, 100-105.

32. K. Tanabe, *Solid acids and bases: their catalytic properties*, Elsevier,, 2012.
33. K. Tanabe, *Mater. Chem. Phys.*, 1985, **13**, 347-364.
34. S. Takenaka, E. Kato, Y. Tomikubo and K. Otsuka, *J. Catal.*, 2003, **219**, 176-185.
35. R. Franz, D. Pinto, E. A. Uslamin, A. Urakawa and E. A. Pidko, *ChemCatChem*, 2021, **13**, 5034-5046.
36. R. Roncancio and J. P. Gore, *Energy Conversion and Management: X*, 2021, **10**, 100060.
37. J. Juan-Juan, M. C. Román-Martínez and M. J. Illán-Gómez, *Appl. Catal. A: Gen.*, 2006, **301**, 9-15.
38. S. Helveg, J. Sehested and J. R. Rostrup-Nielsen, *Catal. Today*, 2011, **178**, 42-46.
39. I. V. Yentekakis, P. Panagiotopoulou and G. Artemakis, *Appl. Catal., B*, 2021, **296**, 120210.
40. R. Yang, C. Xing, C. Lv, L. Shi and N. Tsubaki, *Appl. Catal. A: Gen.*, 2010, **385**, 92-100.
41. H.-S. Roh and K.-W. Jun, *Catal. Surv. Asia*, 2008, **12**, 239-252.
42. M. Steib, Y. Lou, A. Jentys and J. A. Lercher, *ChemCatChem*, 2017, **9**, 3809-3813.
43. E. le Saché and T. R. Reina, *Prog. Energy Combust. Sci.*, 2022, **89**, 100970.
44. V. R. Choudhary, S. Banerjee and A. M. Rajput, *J. Catal.*, 2001, **198**, 136-141.
45. H. Li, Y. Guo and J. Robertson, *J. Phys. Chem. C*, 2015, **119**, 18160-18166.
46. S. Takenaka, Y. Tomikubo, E. Kato and K. Otsuka, *Fuel*, 2004, **83**, 47-57.
47. K. Shibata, T. Kiyoura, J. Kitagawa, T. Sumiyoshi and K. Tanabe, *Bull. Chem. Soc. Jpn.*, 1973, **46**, 2985-2988.
48. K. Arata, S. Akutagawa and K. Tanabe, *Bull. Chem. Soc. Jpn.*, 1976, **49**, 390-393.

Conclusions

In view of limiting climate change, undoubtedly the global efforts to abate CO_2 emission must aim at overcoming the present economy and industry, both heavily dependent on fossil fuels and, especially, oil derivatives. The transition towards carbon neutrality has to be characterised by the intense search for oil alternatives and the development of circular processes involving utilisation of cheap and renewable feedstocks. In this sense, CH_4 and CO_2 are ideal candidates as two abundant and easily-available C1 molecules that can be more valuably exploited in the near future. Clearly, peculiar challenges are associated with the utilisation of these two diverse chemical commodities. In terms of catalysis engineering, it is crucial to develop competitive reaction pathways for the direct or indirect conversion of CH_4 and CO_2 to valuable chemicals and fuels. Several challenges associated to their utilisation as chemicals and fuel feedstocks needs to be tackled by a combination of fundamental investigation on the catalytic reactions and development of effective reaction processes. This dissertation offers an exploration of the potential of unsteady-state operation both as a scientific tool to gain fundamental catalytic knowledge and as an alternative concept for advanced and flexible catalytic processes.

Integration of the capture of CO_2 from emitting sources with its direct conversion to more valuable molecules is the scope CO_2 capture and reduction (CCR) catalysis. In this isothermal, unsteady-state process, CO_2 is efficiently captured from diluted stream and selectively converted in H_2 stream thanks to unique properties of bifunctional catalytic materials. Chapter 2-3 offers a detailed investigation of a K-promoted Cu/Al_2O_3 system for the capture and selective conversion of CO_2 to CO. The catalytic role of K and Cu components has been clarified, the former responsible for the capture of CO_2 and the latter for the H_2 activation. Also, an important role is played by the y-Al_2O_3 support, which destabilises the K phase giving rise to the catalytically active state. Important insights into the CCR catalysis derived from *Operando* and spatiotemporal analysis, which permitted to elucidate the mechanism of CO_2 capture along the catalytic bed and to identify the catalytically active component in a KOH-type phase. The results reported here are considered relevant to catalytic systems employing alkaline metals and especially K as promoters for the CO_2 capture, also in view of expanding the scope of CCR process to different C1 products such as CH_4 and CH_3OH.

CH_4 is a decisive molecule for the transition towards an oil-free economy and industry. To expand its utilisation beyond the present combustion and H_2 production, extensive catalytic research is dedicated to overcome the limitations on its selective conversion. In Chapter 4 of this dissertation, transient analysis of products during unsteady-state experiments revealed a specific intrinsic selectivity of different simple metal oxides systems towards CH_4 conversion. At 900 °C, thanks to the direct participation of lattice oxygen, very different product selectivity has been observed, with preference to the partial oxidation to CO and H_2 in rare-earth metal oxides and to oxidative coupling products in MgO. The redox property of TiO_2 rutile directly intervenes in the activation of CH_4 ensuring a constant supply of lattice oxygen species for the formation of CO.

The fundamental insights obtained by unsteady-state experiments were applied to the investigation of the oxidative coupling of methane (OCM) to ethane and ethylene in Chapter

5. Inspired by the contrast between the similar steady-state activity trends and the different intrinsic selectivity towards CH_4 conversion in MgO and La_2O_3, a detailed investigation of the reaction with *in situ* analytic techniques has been conducted. The results showed that, in the oxidative conditions of steady-state OCM, highly exothermic routes are activated, generating a strong increase of temperature in the front part of the catalytic bed, which leads to the uncontrolled generation of unselective total oxidation products (CO_2, H_2O). The beneficial effect of specific catalytic promoters (Li-, Sr-) have been identified in the suppression of the total oxidation routes that significantly reduces the formation of hotspots and contributes to a substantial increase in C_2 selectivity. The observation reported are relevant to the design of efficient catalytic systems and favourably point towards advanced catalytic processes able to dose molecular oxygen to the reactor bed and avoid total oxidation conditions (e.g. unsteady-state conditions, membrane reactors).

Combined utilisation of CH_4 and CO_2 in the dry reforming process for H_2 and CO (syngas) production is an appealing catalytic strategy. The challenges of catalyst deactivation and coke accumulation, however, substantially limited its industrialisation in favour of the state of the art steam reforming process. Still, the interest in promoting CO_2 utilisation to mitigate the carbon footprint of the existing processes calls for the design of catalytic materials and processes able to withstand the harsh reaction conditions of dry reforming. In Chapter 6, an unsteady-state alternative to the traditional co-feed operation is presented in the name of dynamic coke-mediated dry reforming of methane (DC-DRM). By periodically alternating the reactant feeds to the catalytic bed, the process aims at fast and efficient decomposition of CH_4 in the reducing pulse and full gasification of the coke deposits in the CO_2 pulse. The results obtained on a La-promoted Ni/ZrO_2 system revealed the potential of such process targeting coke as the catalytic intermediate between the H_2 production in CH_4 and the CO production in CO_2, with inherent separation of reactant and product streams and elimination of unselective routes as reverse water-gas shift. The design of catalytic materials able to withstand long exposure to the reactant cycles can speed up the implementation of unsteady-state operation for the CO_2 reforming of CH_4, enabling utilisation of renewable feeds (e.g. captured CO_2, CH_4 from biomass) and, thanks to the flexibility of the process conditions, enable the production of tuned syngas mixtures.

CH_4 and CO_2 utilisation as C1 feedstock still faces multiple issues mainly concerning the thermodynamic stability of the molecules and the poor selectivity to valuable products in reactive conditions. Fundamental research on the mechanism of selective conversion is still necessary to guide the development of advanced catalytic materials and reaction pathways. Unsteady-state catalysis has the potential to overcome the thermodynamic limitations associated to CH_4 and CO_2 usage and design cutting-edge catalytic processes. It is indeed predictable that flexible and adaptable processes will constitute the new paradigm of a future carbon neutral chemical industry, due to the necessity of dealing with intermitting energy sources and renewable feedstocks.

Acknowledgments

Thanks to the committee members, Prof. **Christophe Müller**, Prof. **Vladimir Galvita**, Dr. **Vera Santos**, Prof. **Hans Geerlings** and Prof. **Evgeny Pidko**, for accepting my invitation and for dedicating precious time and energy to the evaluation of this dissertation. I greatly appreciate having the thesis evaluated by such successful and inspiring researchers. I would also like to thank my co-promotor, Prof. **Ruud J. van Ommen**, who granted me valuable and positive feedback during the whole PhD track, showing interest for the work and guiding me through the completion of the projects with suggestions and relevant questions.

The core of this dissertation is mainly made of flat molecules, inorganic materials and mechanical devices. Nonetheless, several stimulating researchers and skilled human beings surrounded me and helped me through the long probing path associated to it. Few words cannot settle the huge debt of gratitude, but I hope they can assist me in expressing my great esteem.

In a tentatively chronological order, I would like to start acknowledging the ones that made possible my entrance and development in the world of research. In this sense, I have to thank firstly Prof. Antonella Glisenti and all the amazing people of Impact Group that, during my Master internship and short research stay in the University of Padova, gave me the freedom, trust and chance to learn and build the start of my career. During this time, I also had the rare opportunity to be part of two synchrotron expeditions, under the guidance of Prof. Davide Ferri, that sparked my interest in *operando* spectroscopies.

Once the hazardous choice of pursuing a PhD was made, the possibility to be part of an inspired cutting-edge group as the Urakawa group in ICIQ was far beyond my initial expectations. Yet, most of my growth in the past years depends on the high level of challenges and uncommon possibilities I encountered here.

My biggest thank go to Prof. **Atsushi Urakawa**, who granted me the possibility of lifting my knowledge and capabilities by accepting me as PhD student, looking beyond my limited background and experience. It has been a privilege to witness your special way of challenging people by sparking their scientific interest, helping us to overcome our limits. You are an infinite source of opportunities for a PhD student and, no matter the craziness of your schedule, you also manage to share part of the life inside and outside the lab with us. I will always bring with me the memories and experiences of the frenetic lab/life moving from Spain to Netherlands, the never-ending shifts in crazy synchrotron projects, the long talks about science and life, together with the admiration for your unbeatable working pace and scientific attitude.

Although short, my experience in ICIQ could count on the meeting with amazing people and skilful researchers.

I have to start acknowledging Prof. Atul Bansode, who not only tolerated my frequent coffee visits to his office but also provided me a deep and constant know-how transfer which made me able to operate the ingenious in-house setup he firstly designed and built. Your unique skills constantly provided me technical support and your positive attitude has been essential to get me through all kind of problems and difficulties of research life.

A big *grazie* goes to Dr. Lingjun Hu, with whom I shared a twin experimental setup, a lot of writing and an important part of our PhD investigation and life. With your infinite patience and determination, you answered all my (many) daily questions and guided me in my first research steps, providing me an easy entrance in complicated topics and research questions. It has been a pleasure sharing this path with you and your hard work has been of great inspiration to me.

Huge thanks go to the Catalan crew, which welcomed me and taught me all the necessary for my short stay. Spending my days with you I could quickly understand castellano, getting to know the neoperreo divas with Juanjo, the traditional catalan songs with Marta and sharing the football suffering of Inter and Barça with Jordi. The nice time spent with you made the farewell to Tarragona even a bit more bitter.

Of course, a lot of thanks goes to the other members of the group, Sorin and Nat, that first welcomed me in Tarragona and then shared the adventurous moving to Netherlands, facing together the challenges of a different PhD track and getting used to the new environment and, especially, weather.

Coming to Delft has been a valuable experience for my life and career. Again, a lot of people were fundamental for my growth and path here in TU Delft.

I would like to thank all the Catalysis Engineering group for welcoming me in TU Delft and constantly helping me.

The technical staff of our section had an important role in my research, constantly providing help in the lab and feedback during my presentation at group meetings. Especially, I thank Bart for the infinite patience towards my help requests and for the passion towards my research problems, which granted me an expert eye to solve all kind of puzzles encountered in the work. Also huge thanks to Willy for her attentive guidance in the adsorption techniques and for her efforts to always accommodate my last minute requests, helping me meeting deadlines. Thanks also to Liliana for her assistance with GC and for the nice chats at the coffee machine, which in grey winter days could give me more energy than that poor quality coffee. Despite working in a different building during my PhD, I also need to thank Harrie for his assistance during and after the moving, his feedback during presentations and, last but not least, for showing us his performance in Korfball, getting us to know this interesting Dutch sport.

Thanks to Dimitrii Osadchii and Robert Franz, as last representative of the 'old' Catalysis Engineering group. You really made my transition toward the new reality easier and it was great to live the process of your PhD defenses as an early preparation for my turn. In particular, thanks to Robert for the fruitful collaborations among all the complaining talks, both in research papers and pizza making.

A big acknowledgment goes to all the bachelor and master students that (bad luck for them) got me as daily supervisor for their final projects. Thanks to Dean, Stefano, Meryl, Tjoep, Joris, Victor, Hugo and Jamie for instilling their unique and diverse qualities in this work, by actively contributing to the hard lab work, the data acquisition and analysis and by sharing the numerous headaches for interpreting non-intuitive results. I feel that my whole PhD in Delft took advantage not only from your daily work, but also from the multiplicity of perspectives and from the constant injection of motivation you brought.

Big thanks go to all the members of the Urakawa group in the Catalysis Engineering section. Min, Ahmad, Ezgi, Pratik, Tomone-san, Benjamin, Afreen and all the past members/visitors/students with whom we shared happy moments during these years.

A special acknowledgment goes to Disha and Thomas, who granted me a smooth access to the DRIFTS measurement and data analysis, accommodating all my time-consuming help requests.

Also a special acknowledgment to José, for regenerating my decayed Spanish and sharing the nostalgia for sunnier and warmer lands. Thanks for your constant help during the last steps of my PhD with constant advice and fruitful discussions. Your scientific accuracy and work application are not so common in the research world, I hope they will bring you far in a career in academia… or in Mercadona, as you like.

Thanks also to all the past and present members of the side of our section led by Prof. Monique van der Veen. Aside the countless presentations about MOFs I had to assist to (you will surely say the same about heterogeneous catalysis), I always appreciated the interaction in and outside the lab and the joyful moments spent together.

A special acknowledgement goes to Prof. Freek Kapteijn, Prof. Michiel Makkee and Rob Berger, for the interest shown in my research and the stimulating discussions had during my presentations in the CE group meetings.

Luckily, I could also enjoy an important share of these years outside the labs, where many people were precious to recover physical and mental energies, and where most of the motivation and ideas often generated.

I doubt that I could withstand more than 3 years of PhD life in Netherlands and, especially, in Delft, without the little family of the *symposium sofa*. I have to thank the spiritual founder of this little company, Giacomo, and then all the members for their diverse but precious contribution to my life. Davide for sharing common sources of deep suffering, PhD in Chemical Engineering and Inter matches. Silvia for her adventurous mind and daily supply of craziness, so much missed in this country. Giulia who, besides showing us what a real PhD should look like, constantly fed us in amazing Italian dinners. Ezgi and Tim for bringing their Erasmus knowledge to the group to spark every party. Despite being a typical milanese guy, Alessandro for the happiness of the year spent together. Carolina for holding strong against the Italian core of the group and for her hidden party potential. You helped me withstand even the most rainy days. Thanks also to all the (mainly Italian) late visitors, Michela, Andrea, Stefano, Michele e Chiara that filled many happy Dutch days and nights, despite my constant complaint about this country.

Especially thanks for all the people joining my 30s birthday party, officially the last party. There, I received the best present I could wish for. Thanks Joana for being part of my life since then. I was ready to leave Netherlands to follow the sun, but you shine love and care every day, constantly bringing me back to Portugal and making also the intensive writing times pass happily.

Mentioning Portugal, a big thanks to Fede and Cédric for hosting me during the frequent escapes to Lisbon, always contributing to my happiness sharing amazing brunches, cool nights

and unbeatable surfing days, and Mourad, for the short but intense nostalgic days lived between Padova and Portugal.

Thanks to all the members of the *esagono*: Longo for being a real friend despite the terrible people we are, Fallo for his unique classical culture and scary *terrone-veneto* mixture, Jolly for the numerous travels which, no matter the destination, constantly end in hell, Bipbip, who started the *al salto* plague and yet survived to keep high the puglia pride in the group, and Marcello, an inspirational mix of scientific and alcoholic excellence. While my liver will always curse you, my hearth cannot avoid acknowledging you for keeping alive the light of the old Padova times, for the infinite *scopone* tournaments in Covid times, for the moments still shared together. Thanks also to all the *consorti*, Federica for constantly laugh about the amazing people and experiences encountered in Bari and Padova years, Matilde for saving us from the terrible single-Longo and for always being an amazing host in Tuscany and Padova, Silvia for her cheerfulness and for safely limiting our dose of Jolly.

After many years of travelling and living abroad, it becomes difficult to clearly define where my home is. If I can still claim some identity from the Murgia lands, it is thanks to a bunch of life-long friends from the *goodness*. Even if the late years drastically reduced the time we used to spent together in uncommon travels as the *CTC*, we still share our grow path that from uncomfortable school chairs brought us to the adult world. Thanks to Marcello for sharing his PhD life from Italy, for the stimulating discussions and for the constant graphic advice, Michele for the frequent music updates and for hosting me during part of this writing, Gaetano and Giulio for the hilarious calls in improbable gaming nights, Luigi and Piero *alb.* for the unconventional travels that built unique memories for life, Pierpaolo for the (too short) surfing adventures, Piero for the engineering and altamuran pride, Alberto for storing and sharing precious material of our young ages. You bring me home faster than a private jet, constantly injecting nostalgia of our desert lands every time I am there.

Finally, yet importantly, thanks to my family, to which this thesis and any other achievement in my life is dedicated. *Grazie a Giusy, per aver condiviso la sua esperienza accademica e per essere sempre una fidata consigliera, ad Alfredo, che meglio di chiunque può capire i pro e contro di una vita in Olanda, e a Salvatore, vero sponsor culturale della mia infanzia senza il quale oggi probabilmente sarei solo un altro vuoto (e reazionario) contenitore di tecnicismi.*

Grazie mamma e papà per la libertà che mi garantite in ogni scelta di vita, anche quando queste mi portano molto lontano da casa. Spero che questo lavoro vi possa rendere fieri, essendo frutto soprattutto del vostro sostegno e supporto che mai mi sono mancati.

List of Publications

Publications within the scope of this thesis:

D. Pinto, S. Minorello, Z. Zhou, A. Urakawa, Role of γ-Al$_2$O$_3$ support, unique state of potassium and synergy with copper at the basis of the integrated CO$_2$ capture and reduction catalysis, *J. Environm. Sci.,* 2023, *accepted.*

D. Pinto, V. van der Bom Estadella, A. Urakawa, Mechanistic insights into the CO$_2$ capture and reduction on K-promoted Cu/Al$_2$O$_3$ by spatiotemporal operando methodologies, *Catal. Sci. Tech.,* 2022, **12**, 5349-5359.

D. Pinto, A. Urakawa, Specific selectivity of simple metal oxides towards CH$_4$ activation, *in preparation*.

L. Hu, **D. Pinto**, A. Urakawa, Active reactions and spatial gradients in oxidative coupling of methane, *Catalysis: Volume 32*, The Royal Society of Chemistry, 2020, **32**, pp. 203-223.

L. Hu, **D. Pinto**, A. Urakawa, Catalytic oxidative coupling of methane: heterogeneous or homogeneous reaction?, *ACS Sustainable Chem. Eng.*, 2023, *accepted.*

D. Pinto, L. Hu, A. Urakawa, Enabling complete conversion of CH$_4$ and CO$_2$ in Dynamic Coke-Mediated Dry Reforming (DC-DRM) on Ni catalysts, *in preparation*.

Publications outside the scope of this thesis:

R. Franz, **D. Pinto**, E.A. Uslamin, A. Urakawa, E.A. Pidko, Impact of promoter addition on the regeneration of Ni/Al$_2$O$_3$ dry reforming catalysts, *ChemCatChem*, 2021, **13**, 5034-5046.

D. Pinto, A. Glisenti, Pulsed reactivity on LaCoO$_3$-based perovskites: a comprehensive approach to elucidate the CO oxidation mechanism and the effect of dopants, *Catal. Sci. Tech.,* 2019, **9**, 2749-2757.

Curriculum Vitae

Donato pinto was born on 12th August, 1992 in Altamura, Italy. In July 2011, he received his high school diploma at Liceo Classico Cagnazzi (Altamura, Italy). In September 2011, he enrolled in the Materials Science course in the University of Bari (Italy). Here, with a thesis about 'Photocatalytic activity of titanium dioxide nanocrystals: role of size, shape and surface chemistry' under the supervision of Dr.ssa Elisabetta Fanizza, he obtained his BSc in December 2014. In September 2015, he enrolled in the Materials Science course in the University of Padova (Italy). Between September 2016 and February 2017, he participated in the Erasmus + mobility programme with an international exchange in the Universidade de Aveiro (Portugal). After that, he joined the IMPACT group in the University of Padova (Italy) under the supervision of Prof.ssa Antonella Glisenti. In September 2017, he had the chance to participate in a beamtime experiment at ESRF synchrotron facility (Grenoble, France - Project code MA 3625) in collaboration with Dr. Davide Ferri (PSI – Switzerland). He obtained his MsC in December 2017 with a thesis on 'Effect of doping on the reactivity of $LaCoO_3$-based perovskites: catalytic activities and kinetics by pulsed reaction analysis'. After that, he continued in the IMPACT group as Assistant Research Fellow (March 2018 – August 2018), participating in a second beamtime experiment at ESRF synchrotron facility (Grenoble, France - Project code MA 3927). In October 2018, he started a PhD in the Urakawa group at the Institut Català de Investigació Quimica in Tarragona (Spain) as part of the Barcelona Institute of Science and Technology PhD Fellowship Programme EU's Horizon 2020 research and innovation programme (Marie Skłodowska-Curie grant agreement No. 754558). In May 2019, he joined Prof. Atsushi Urakawa at the Technische Universiteit Delft (Netherlands) as PhD in the Chemical Engineering department. His PhD project focused on heterogeneous catalytic strategies for CH_4 and CO_2 utilisation by unsteady-state operation, investigated with the aid of *in situ/operando* analytic techniques.